Surface-Initiated Polymerization and Janus Membrane Synthesis from Graphene and Poly(dopamine)

DISSERTATION

zur Erlangung des akademischen Grades

Doctor rerum naturalium

(Dr. rer. nat.)

vorgelegt

dem Bereich Mathematik und Naturwissenschaften

der Technischen Universität Dresden

von

M.Sc. Daniel Hafner

geboren am 14.06.1989 in Karabulak/Kasachstan

Eingereicht am 10.12.2020

Verteidigt am 26.03.2021

Gutachter: Prof. Dr. rer.nat. habil. Rainer Jordan (TU Dresden)

Priv.-Doz. Dr. rer. nat. habil. Alla Synytska (IPF Dresden)

Die Dissertation wurde in der Zeit vom Januar 2015 bis zum Juni 2019 an der Professur für Makromolekulare Chemie an der Technischen Universität Dresden angefertigt.

„Es hat sich bewährt in solchen Lagen

Das Orakel von Delphi zu befragen.“

- Bodo Wartke, ***Antigone***

Contents

Contents I

Abbreviations and Symbols III

1. Introduction 1

2. State of Knowledge 3

2.1 Janus materials ... 3

2.1.1 Design and fields of application ... 4

2.1.2 Synthesis of Janus membranes ... 8

2.2 Polymer surface modification ... 11

2.2.1 Polymer brushes ... 11

2.2.2 Photoinitiated free radical polymerization and SIPGP ... 14

2.2.3 Copper-catalyzed controlled radical polymerization and SI-CuCRP ... 17

2.2.4 Poly(dopamine) (PDA) ... 23

2.3 Graphene ... 30

2.3.1 Geometrical and electronic structure ... 32

2.3.2 Strain-engineering of graphene ... 33

2.4 Polymer carpets ... 37

2.4.1 Synthesis of polymer carpets ... 38

2.4.2 Fields of application ... 42

3. Motivation and Objectives 45

4. Results and Discussion 48

4.1 Surface-initiated Cu(0)-mediated controlled radical polymerization on poly(dopamine) modified surface ... 48

4.1.1 Synthesis of initiating layer ... 48

4.1.2 SI-CuCRP on PDA/BiBB ... 51

4.1.3 Polymer brush synthesis on different substrates ... 55

4.1.4 Grafting block copolymer on surface ... 59

4.2 Fabrication of Janus polymer carpets ... 62

4.2.1 Transfer and flipping of polymer brushes ... 63

4.2.2 Fabrication of Janus polymer carpets by second grafting ... 68

4.2.3 Fabrication of Janus polymer carpets by transfer 73
4.2.4 Patterned Janus polymer carpets 76
4.3 Strain-engineering of graphene by polymer grafting 79
4.3.1 Grafting of polymer brushes on graphene 82
4.3.2 Grafting of polymer bottle-brush brushes on graphene 88
4.3.3 Patterning of graphene based polymer carpets 96
4.3.4 Janus polymer carpets based on graphene 104
5. Summary **113**
6. Zusammenfassung **117**
7. Experimental **122**
7.1 Materials 122
7.2 Methods and devices 123
7.3 Procedures and Syntheses 124
7.3.1 Transfer of graphene 124
7.3.2 Self-assembled monolayer (SAM) of APTES on SiO_2 wafer 124
7.3.3 SAM of ODS on SiO_2 wafer 125
7.3.4 Deposition of PDA on different substrates 125
7.3.5 Binding of BiBB-initiator on surface 125
7.3.6 Surface-initiated Cu(0)-mediated controlled radical polymerization (SI-CuCRP) 125
7.3.7 Self-initiated photografting and photopolymeriaztion (SIPGP) 126
7.3.8 Grafting of block copolymer brushes on PDA/BiBB 126
7.3.9 Patterning of polymer brushes 126
7.3.10 Synthesis of poly(2-oxazoline) (POx) bottle-brush brushes 127
7.3.11 Fabrication of polymer carpets and Janus polymer carpets from PDA 127
7.3.12 Fabrication of Janus polymer carpets from graphene 128
Bibliography **129**
Danksagung **143**

Abbreviations and Symbols

0 - 9	1.BZ	first Brillouin zone
	2D, 3D	two dimensional, three dimensional
	4VP	4-vinylpyridine
A	ACN	acetonitrile
	AFM	atomic force microscopy
	APTES	3-aminopropyltriethoxysilane
	A(R)GET	activator (re-)generation by electron transfer
	ATR	attenuated total reflection
	ATRP	atom transfer radical polymerization
	a.u.	arbitrary units
B	b	block
	BBB	bottle-brush brush
	BDE	bond dissociation energy
	BiBB	2-bromoisobutyryl bromide
	BuOx	2-butyl-2-oxazoline
C	CA	cellulose acetate
	CNT	carbon nanotube
	CRP	controlled radical polymerization
	CuCRP	Cu(0)-mediated controlled radical polymerization
	CVD	chemical vapor deposition
D	d, d_0	thickness, initial thickness
	D	distance
	$DA^{\cdot}$(HCl)	dopamine (as HCl salt)
	DCM	dichloromethane
	δ	deformation
	DHI	5,6-dihydroxyindole
	Đ	dispersity
	DMAEMA	N,N-dimethylaminoethyl methacrylate
	DMSO	dimethyl sulfoxide
	DOPA	3,4-dihydroxyphenylalanine
E	*e*	electro
	EA	ethyl acrylate
	EHMA	2-ethylhexyl methacrylate

	ε	strain or strain axis
	EtOx	2-ethyl-2-oxazoline
F	FRP	free radical polymerization
	FT-IR	Fourier transform infrared spectroscopy
G	g	graft
	G	graphene
	GO	graphene oxide
	rGO	reduced graphene oxide
H	HEA	2-hydroxyethyl acrylate
	HEMA	2-hydroxyethyl methacrylate
I	I_D, I_G, I_{2D}	intensity of D-, G-, 2 D-band of graphene
	iBA	isobutyl acrylate
	IC	inner conversion
	ICAR	initiators for continuous activator regeneration
	iPOx	2-isopropenyl-2-oxazoline
	iPrOH	isopropanol
	iPrOx	2-isopropyl-2-oxazoline
	ISC	intersystem crossing
	ISET	inner sphere electron transfer
K	k_p, k_t	rate constant of propagation, termination
L	λ	wavelength
	LbL	layer-by-layer
	LB	Langmuir-Blodgett
	LCROP	living cationic ring-opening polymerization
	LCST	lower critical solution temperature
M	Mefp	*Mytulis edulis* foot protein
	MeOTf	methyl triflate
	MeOx	2-methyl-2-oxazoline
	MMA	methyl methacrylate
N	N	degree of polymerization
	nBA	n-butyl acrylate
	NiPAAm	N-isopropyl acrylamide
	NMP	nitroxide-mediated polymerization
	NMR	nuclear magnetic resonance

	nPrOx	2-propyl-2-oxazoline
	ν_{as}, ν_s	asymmetric or symmetric stretching
O	ODS	octadecyltrichlorosilane
	OEGMA	oligo(ethylene glycol) methacrylate
	OSET	outer sphere electron transfer
P	***P***	polarization
	P3HT	poly(3-hexylthiophene)
	PDA	poly(dopamine)
	PEG	poly(ethylene glycol)
	PEI	poly(ethylene imine)
	Pip	piperidine
	PMDETA	1,1,4,7,7-pentamethyldiethylentriamine
	PMeOx-MAA	poly(2-methyl-2-oxazoline) methacrylate
	PMT	photo multiplier tube
	POx	poly(2-oxazoline)
	ppm	parts per million
	PRE	persistent radical effect
	PTFE	poly(tetrafluoro ethylene)
	PVA	poly(vinylalcohol)
R	R·	radical
	R_a, R_{comp}, R_{dis}	rate of activation, comproportionation, disproportionation
	RAFT	reversible addition fragmentation chain transfer
	R_g	radius of gyration
	RMS	root mean square
	ROP	ring-opening polymerization
	rt or RT	room temperature
S	S_0, S_1	singlet state, first excited singlet state
	SAM	self-assembled monolayer
	SARA	supplemental activator and reducing agent
	SBMA	sulfobetaine methacrylate
	SERS	surface-enhanced Raman spectroscopy
	SET-LRP	single electron transfer living radical polymerization
	SI-ATRP	surface-initiated atom transfer radical polymerization
	SI-CuCRP	surface-initiated Cu(0)-mediated controlled radical polymerization

	σ	grafting density
	SIP	surface-initiated polymerization
	SIPGP	self-initiated photografting and photopolymerization
	SI-RAFT	surface-initiated reversible addition fragmentation chain transfer
	SPMA	3-sulfopropyl methacrylate
	St	styrene
T	T_1	triplet state
	tBMA	tert-butyl methacrylate
	TEM	transmission electron microscopy
	Tg	glass transition temperature
	θ_S	static water contact angle
	Tol	toluene
	t_R	reaction time
	Tris	trishydroxymethyl aminomethane
U	UV	ultraviolet
V	vis	visible
X	XPS	X-ray photoelectron spectroscopy

The official unit symbols of the International Unit System (SI) apply through the entire work.

Abbreviation of the polymer names constitutes as follows: the acronym for respective monomer is taken and the letter "P" for *poly* (Greek for "many") is prefixed. For example, a polymer from methyl methacrylate (MMA) – i.e. poly(methyl methacrylate) – will be abbreviated as PMMA.

This rule also applies for surface-bound polymer chains. If polymers are grafted on top of another polymer layer, the resulting structure will be further denoted with a "g" between the names. Accordingly, PMMA grafted to poly(dopamine) (PDA) will be denoted as PDA-g-PMMA. Likewise, the letter "b" will be used if the resulting structure exhibits block-like architecture; e.g. PDA-g-PMMA-b-PtBMA.

1. Introduction

"…this tells us that poking in new directions, even randomly, is more rewarding than is generally perceived." – Andre Geim, ***Random Walk to Graphene***

It might not be entirely without sentiment to begin this work citing a winner of the Nobel Prize.[1] Negating the validity of his words, however, would entirely underestimate the power of human curiosity. This inner drive to explore the unknown and his inventive nature has marked the evolution of men and civilization since time immemorial. Discovery of new materials and development of innovative tools and technologies has therefore constantly proceeded paving the way to modern society. Since the beginning of the 20th century, exploitation of silicon has led to a rapid progress in semiconductor technology. As an example, the invention of small transistors, microchips and computers has promoted changes in almost every aspect of life and coined the term of "digital revolution".[2–4] Daily used devices like notebooks, tablets or smartphones are products of these developments and have become indispensable in our lives. Applications in the areas of medicine, energy harvesting or production profit from digitalization.[5] While silicon might have had the highest impact in that context within the last century, other kinds of emerging materials like Janus membranes and graphene lead the way into future.

The term "Janus object" (or "Janus material") was introduced by Cassagrande *et al.* in the end of 1980s;[6] it refers to materials exposing two separated compartments with different surface properties. "Janus membranes" are two-dimensional (2D) materials fulfilling this criterion. Their potential to enhance and optimize performance in several nanomembrane technologies is enormous.[7,8] Due to the unequal surfaces, Janus membranes can generate a strong directional thrust useful for transport processes.[7] Therefore, environmental applications like water collection or nanofiltration have been proposed. Likewise, Janus membranes can be integrated in energy harvesting and conversion applications, since catalytic contact or selective ion flow can be drastically improved.[8] Despite these promising perspectives, research interest has only started growing within the last 10 years. In fact, no general bottom-up routes for Janus membrane synthesis exist up to date. Such routes could contribute to a better fundamental understanding of occurring transport processes and allow for proper adjustment in respect to desired implementation.

The use of surface-initiated polymerization (SIP) might be one option to realize this goal. SIP methods like surface-initiated photografting and photopolymerization (SIPGP)[9–11] and

surface-initiated Cu(0)-mediated controlled radical polymerization (SI-CuCRP)[12–14] enable the synthesis of polymers with different functionality and architecture. The SI-CuCRP especially bears huge potential for surface modification and exact tuning of properties, due to the high control over reaction, applicability to a wide variety of monomers and the possibility to synthesize patterns and gradients. Thus, it might open the door to Janus membranes with tunable compartmentalization and surface characteristics. It further permits formation of polymer brushes at high grafting density and thereby induction of chemo-mechanical force. Zhang *et al.* reported on the strong steric repulsion in so grafted polymer brushes even leading to detachment from rigid substrates.[12] Such use of SI-CuCRP can even become crucial for the concept of "strain-engineering", i.e. change of electrical properties by application of mechanical stress, and especially prompt development in technology based on graphene.

First isolated in 2004, the 2D graphene presents a unique set of electronic, mechanical and optical features.[15,16] Its superior charge carrier mobility (~ 142 times higher than Si), thermal conductivity and gigantic intrinsic strength (5 - 10 times higher than Si) have labelled it as material of superlatives.[17,18] Being an atomically thin layer, it further provides ultralow weight, high flexibility and transparency. Due to this extraordinary properties, graphene was already integrated in flexible solar cells, foldable touch-screens and organic light emitting diodes or energy storage devices.[18,19] Yet, a direct implementation in optoelectronics or for the fabrication of microchips remains difficult. The reason for that is the absence of a measurable electronic band gap required for such typical semiconductor applications. Consequently, research has been focused on generating a band gap by the above mentioned strain-engineering.[20] Among other phenomena, strain was demonstrated to shift and split Raman signals, improve electron-phonon coupling or enhance superconductivity.[20] However, no sufficient deformation was achieved to generate a band gap. Grafting of polymer brushes on graphene *via* SI-CuCRP could fulfill this task. Polymer brushes attached to thin cross-linked 2D sheets – so-called polymer carpets – were shown to undergo reversible change in morphology depending on environment.[9] This is possible because the underlying 2D sheet allows for collective release of chemo-mechanical stress by strong deformation. Synthesis of densely grafted, graphene based polymer carpets might be therefore the key to successful strain-engineering of a band gap.

Clearly, Janus membranes and graphene can both define a new era of technology and even address worldwide problems like ever growing energy demand or water pollution. Still, the described issues with the materials´ limitations have to be overcome. So, it is time to start – not so randomly – "poking in new directions".

2. State of Knowledge

2.1 Janus materials

Major interest in scientific research has been drawn to Janus materials because of their unique feature of combining different properties at two distinct sides. Their name springs from the bi-faced roman god Janus **(Fig. 2.1)**[21], since Janus materials often hold contrary chemical character or functionality facing in opposite direction. For example, they can be organic/inorganic[22], hydrophobic/hydrophilic[23–25], magnetic/non-magnetic[26] or ionic/non-ionic[25,27].

Figure 2.1: Bust of Janus, roman god of beginnings and endings, past and future.

Break of symmetry and combination of different properties has been long known from molecules like tensides or block copolymers and used to promote self-assembly processes into aggregates such as micelles, vesicles or polymersomes. Janus materials, however, can be regarded as a bridge between this classic molecular interaction and colloidal/nanoparticle chemistry. They enable the design of supramolecular structures on larger length scale and integration of desired physical properties provided by the micro- or nanoparticle, i.e. magnetism, different mechanical or optical features, conductivity and others. Therefore, development in synthesis and application of Janus particles has progressed significantly since de Gennes popularized the term in his Nobel lecture in 1991.[28] High diversity in shapes has been reached including spherical, rod- or disc-like forms or even capsules **(Fig. 2.2)**. Different degrees of anisotropy are accessible and compartmentalization can be attained through the core of the particle or through its surface.

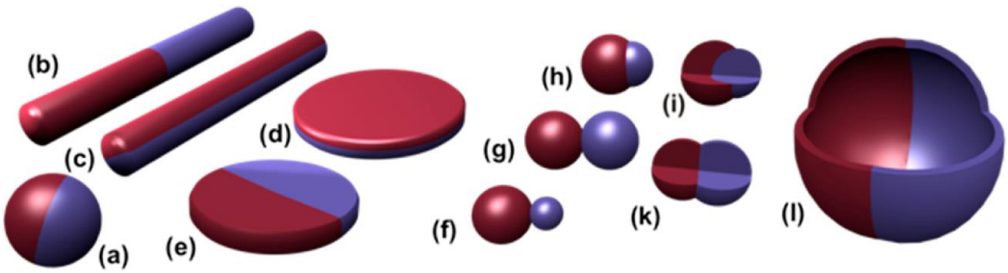

Figure 2.2: Representative overview of different Janus material shapes. Spherical (a), cylindrical (b, c), and disc-shaped (d, e) Janus particles are displayed. Various kinds of dumbbell-shapes with asymmetric character (f, h, i), symmetric appearance (g, k) as well as Janus vesicles or capsules (l) are realizable. Taken from Ref.[29] and modified.

2.1.1 Design and fields of application

Janus materials can be exploited as a platform for side-selective chemistry[30] and catalysis[31], stabilization of colloidal solutions[25,32,33], controlled self-assembly[22,34,35] or defined change of macroscopic properties upon application of an external stimulus[33,36–38]. An example for the latter was given by Yin *et al*. who produced Janus spheres from polymer/Fe_2O_3 nanoparticles and polymer/CdS quantum dots by co-jetting in a simple microfluidic device.[39] Thus, a magnetically induced fluorescent switch was developed **(Fig. 2.3 b)**. Analogously, switching by electric field is possible by mixing different charge properties (carbon black and TiO_2 in **Fig. 2.3 a**) into the polymer matrix.[40] Beside integration of such Janus particles into displays and E-panels, the technique allows for scale-up, high throughput production and precise tailoring of shapes and compartment.[41]

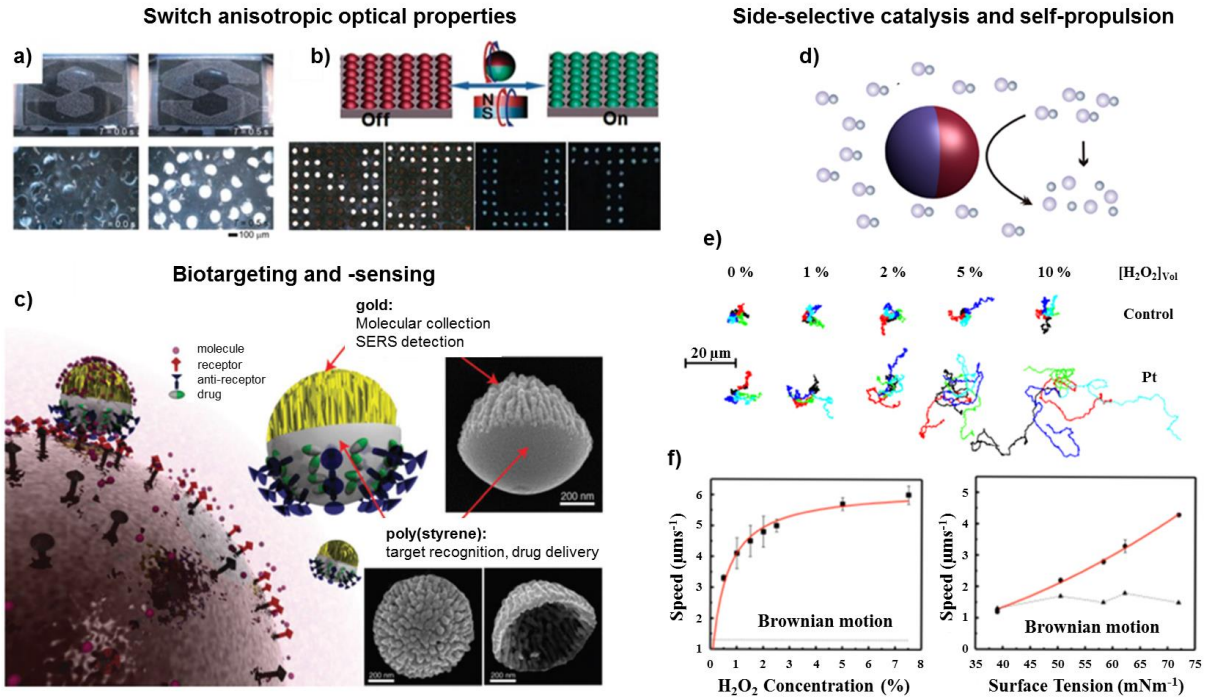

Figure 2.3: Selection of possible applications for (spherical) Janus particle. Switchable optical devices can be realized with conductive (a) or magnetic (b) Janus particles. Biosensing and active drug targeting can be achieved with functionalized Au/PSt Janus particles (c). Side-selective catalysis allows for generation of movement (d - f). Trajectories of five Pt-coated Janus particles (e) and speed increase (f) are dependent on H_2O_2 concentration. Taken from Refs.[31,39,42,43] and modified.

Synytska and coworkers reported on the synthesis of "hairy" Janus spheres from poly(acrylic acid) and poly(styrene) (PSt) for immobilization of inorganic nanoparticles and subsequent anisotropic catalysis.[44] The received system enables stabilization and adjustment of emulsions and inherits high interfacial activity making it advantageous for emulsion

polymerization. On the other hand, such side-selective reaction may be used for self-propulsion of the particles **(Fig. 2.3 d - f)**. Howse *et al*. calculated the trajectories of Pt-Janus particles catalyzing reduction of H_2O_2 **(Fig. 2.3 e)**.[42] The directed nature of O_2 evolution generates accelerated movement, which overcomes otherwise dominant Brownian motion **(Fig. 2.3 f)**. Such an increase of the diffusion coefficient is of specific interest for self-motile carriers in nanomedicine, since larger volumes can be screened and drug delivery may become more efficient.

Other applications of Janus particles in biological context include *in vivo* imaging, sensing and drug targeting. Especially, optically active or magnetic materials offer high contrast and the option of cell manipulation. For example, Hu and Gao incorporated fluorescent pyrene into polymer beads and decorated one side with superparamagnetic ferrous oxide.[45] Thus, fluorescent cell imaging was enabled after facilitated attachment in a magnetic field. In addition, oscillation of the magnetic field and resulting spinning of the Janus particles can induce mechanical forces sufficient to cause cell death. The group of Sun even combined imaging techniques with cell-specific labeling using Fe_3O_4/Au dumbbell particles.[46] Receptor antibodies specific to epithelial cancer cells were bound to the oxide part enabling simultaneous cell targeting and imaging through magnetic resonance (Fe_3O_4) and optical reflectivity (Au) without fluorescence labeling. Wu *et al.* and Hsieh *et al*. further extended the concept of synchronous biotargeting and -sensing to include drug delivery **(Fig. 2.3 c)**.[43,47] PSt beads were roughened with oxygen plasma and one hemisphere was subsequently coated with thin layers of gold. The so created large surface area of noble metal serves two main purposes, which are high capacity analyte collection and effective surface-enhanced Raman spectroscopy (SERS).[43] The organic hemisphere on the other hand, allowed for functionalization with cell-specific CD44 antibodies and binding of drugs *via* biodegradable disulfide linkers. Up to 12-fold recognition was observed on MCF-7 and HeLa cancer cells in comparison to normal cells. Efficient cleavage of the used linker was realized in cytoplasm to permit drug release.[47]

Beside the advances in the chemistry of three dimensional (3D) Janus particles, the field of two dimensional (2D) Janus objects has been growing in recent years.[7,8,48–50] As often, one of the most representative examples of such interface materials comes from nature: the lotus leaf exhibits a superhydrophobic surface on one side and is hydrophilic on the other.[48] This asymmetric wettability makes it self-cleaning in air and anti-oil-fouling in water. In principle, such 2D materials can have two different configurations: either the layers (and therefore properties) are definite or somewhat interconnected by a gradient from one surface to the

other. For precise differentiation Xu *et al*. further define the term "Janus membranes" as interface materials with opposing surface properties and structure that "allows the opposing properties at the interface to work collaboratively and leads to the distinctive transport behaviors within the membrane".[7] These transport behaviors bear outstanding potential for a series of separation and harvesting processes **(Fig. 2.4)**, as the asymmetric properties create an inner driving force along the transport direction. If a water drop is put on the hydrophobic side of a Janus membrane with opposing wettability, it will be pulled by gravity and eventually permeate to the hydrophilic side. If it is put on the hydrophilic side, however, it will spread through the membrane but cannot cross the hydrophobic barrier. Hence, the transmembrane resistance is much lower on the hydrophobic than on the hydrophilic side in that case.

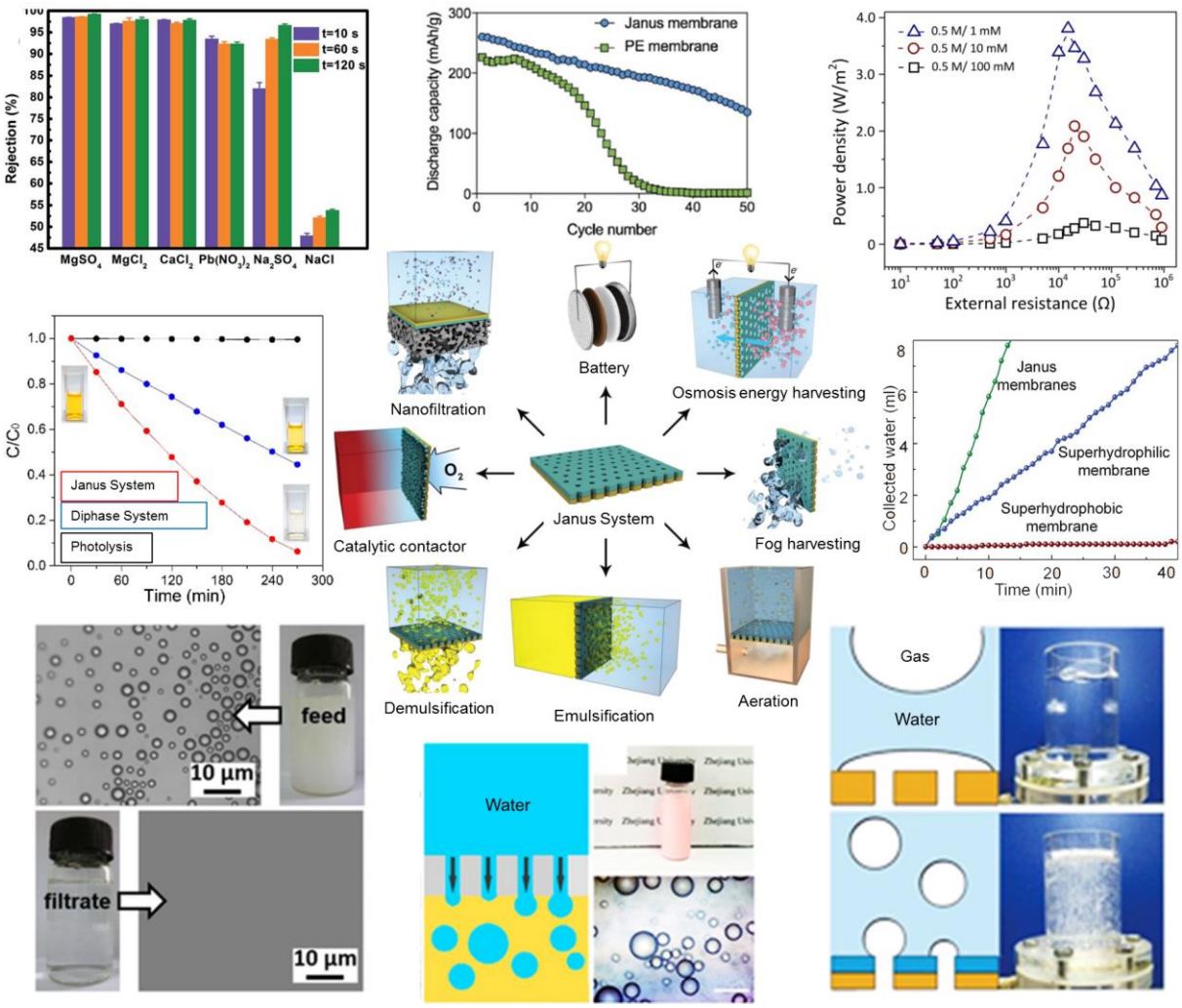

Figure 2.4: Potential applications of Janus membranes. Directed transport allows for efficient harvesting or separation processes. Furthermore, increase of interface compatibility can enhance performance of directed transport and catalysis. Taken from Refs.[8,50–53] and modified.

Accordingly, a lot of research concentrates on unidirectional liquid transport for controlled and efficient filtration or emulsification.[23,24,54] Grafting of polymer on carbon nanotubes (CNTs) was used in the group of Chen to synthesize a hydrophobic/hydrophilic membrane for quantitative removal of different alkanes and benzene derivatives from water **(Fig. 2.4)**.[24] While such membranes are generally useable for oil/water separation, the organic phase can effectively foul the hydrophobic side and increase transmembrane resistance. Therefore, Janus membranes for oil transport should rather be oleophobic/oleophilic to increase permeation flux. A special approach is to fabricate a membrane with one side being superamphiphobic (i.e. superhydrophobic and superoleophobic) and one side being oleophilic.[55] In that way, not only undesired fouling can be prevented, but also possible blocking by water. As result, the efficiency of oil separation from water can reach up to 99 %. Likewise, application of Janus membranes in emulsification or aeration **(Fig. 2.4)** can significantly enhance the performance of the process.[54,56] Due to lower transmembrane resistance energy, costs and deterioration are minimized making Janus membranes ideal candidates for gas and water collection or purification.

In addition to the transport and separation processes described above, membranes play a crucial role in energy conversion and battery technology. Here, Janus membranes can facilitate the required mass transfer, improve contact for catalysis and function as charge filter. For example, thin poly(amide) films with opposing charges at different sides can be applied for nanofiltration **(Fig. 2.4)**, since they reject divalent cations and anions and simultaneously allow for water permeation.[51] Selectivity of charge or ion transport can also be applied to prolong longevity of Li-ion batteries. While these are one of the most used power sources nowadays, dissolution of heavy metals (i.e. Mn^{2+}, Ni^{2+} and Co^{2+}) from the electrodes´ materials during charge/discharge cycles remains a major problem. As they can pass through the typically used polyolefin separator, following diffusion and reduction at the anode lead to drastic capacity loss. That was circumvented by integration of a Janus membrane with a chemically active thiolated side, which can effectively trap these metal ions and still allow for Li^{+} cross-flow.[57] The second side consisted of poly(ethylene imine) (PEI) nanofibers and conductive CNTs for effective electron transport and current generation. Eventually, these Janus membranes not only enabled a faster rate of charging/discharging than conventional separators, but also an improvement of long-term performance of the fabricated batteries **(Fig. 2.4)**.

Gao *et al*. reported on the application of Janus membranes with asymmetric surface charge polarity from mesoporous carbon and macroporous alumina for osmotic power generation.[58]

Salinity difference in water is regarded as a renewable and sustainable energy source because of high accessibility and reserves. So far, conventional membrane-based osmosis harvesting processes suffer from high ion transport resistance, poor ion selectivity and surface polarization. Thus, the achievable power densities created by ion diffusion are economically unattractive. The values obtained by Gao and colleagues, however, outperform commercially available ion exchange membranes by a factor of ten due to outstanding rectification ratio even with high ion concentration **(Fig. 2.4)**.

The research progress in 3D Janus materials has been flourishing since the end of 20th century. The potential of Janus membranes, however, has been only recognized within the last decade. While research interest has been slowly growing, examples in possible fields of application apart from directed liquid transport are limited and require further exploration. Likewise, the actual mechanisms of transport as well as the contributions of each layer, their thickness or the configuration of the Janus membrane are not thoroughly understood. One of the reasons is that main focus in studies lies on the performance enhancement of established processes and adjustment of the Janus properties to that specific application. Therefore, investigations on further synthetic strategies offering a rather general approach of Janus membrane fabrication are still required.

2.1.2 Synthesis of Janus membranes

As discussed above, Janus membranes often find application in directed transport and separation[23,24,49] or even as responsive 2D materials[7,49]. Hence, different approaches have been developed to create Janus membranes to suit different demands.

Generally, synthesis approaches can be categorized as asymmetric fabrication or asymmetric decoration **(Fig. 2.5)**. In the first, the Janus structure is generated during synthesis by sequential double layer formation or through controlled phase separation. A simple strategy reported by Ionov and coworkers is the use of dip-coating process of different polymers on top of each other followed by cross-linking.[36] Combined with structuring techniques they were able to produce effective actuators from responsive N-isopropyl acrylamide (NiPAAm) **(Fig. 2.6 a)**. Wu *et al.* produced a hydrophobic/hydrophilic nanofibrous membrane by sequential electrospinning of poly(urethane) and cross-linked poly(vinylalcohol) (PVA).[59] Analogously, sequential filtering on porous substrates was applied to obtain Janus membranes with thicknesses between 50 nm and 120 nm.[60] However, for these fabrication methods a critical consideration of compatibility between the used components is of great importance,

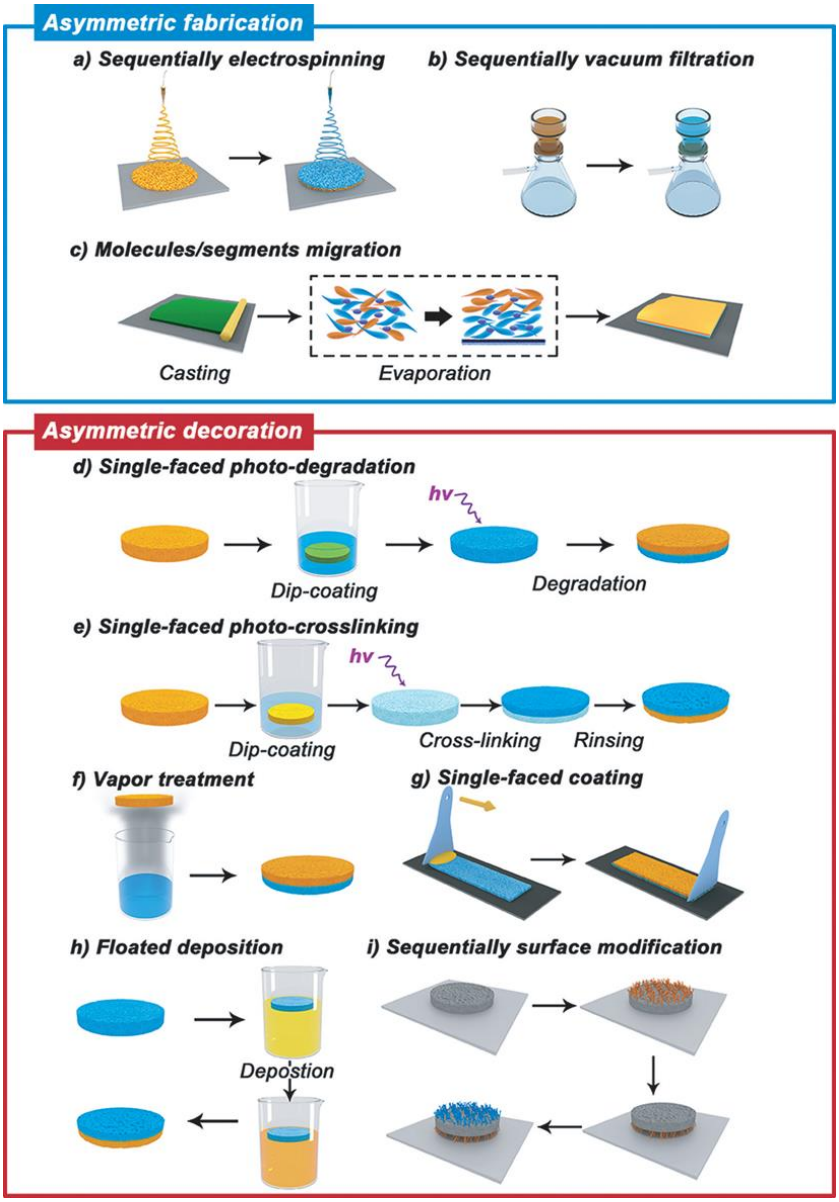

Figure 2.5: Schematic illustration of synthetic routes to Janus membranes. The methods can be categorized as asymmetric fabrication or asymmetric decoration of existing membranes. Each relies either on sequential or single-faced processes. Taken from Ref.[7] and modified.

since it is crucial for the resulting stability of the Janus material. Contrary, phase segregation of polymeric blends from a casting solution may be applicable, but is strongly dependent on the used solvent.[61]

The asymmetric decoration approaches rely on single-face modification of existing or pre-synthesized membrane materials **(Fig. 2.6)**. Here, photochemistry is of particular interest for side selective treatment. Chen *et al.* first decorated a copper mesh with TiO_2 and hydrophobic dodecanthiol and then recovered the hydrophilicity on one side by UV exposure.[62] Liu´s group on the other hand used UV-induced cross-linking and subsequent extraction and polymerization to produce asymmetric wettability on a cotton fabric.[63]

Furthermore, one-face vapor deposition and wet process modification are useful strategies. However, problems with the membrane´s wettability leading either to functionalization on both sides or unsatisfying coverage and inhomogeneous layers have to be overcome. Mussel-inspired poly(dopamine) (PDA), known to be an universal coating agent able to stick to hydrophobic surfaces, can be used in such case.[54,56] Floating a hydrophobic membrane on a dopamine (DA) solution results in one-sided formation of a hydrophilic layer **(Fig. 2.6 b)**, which can be tuned in penetration depth by co-deposition PEI.[56]

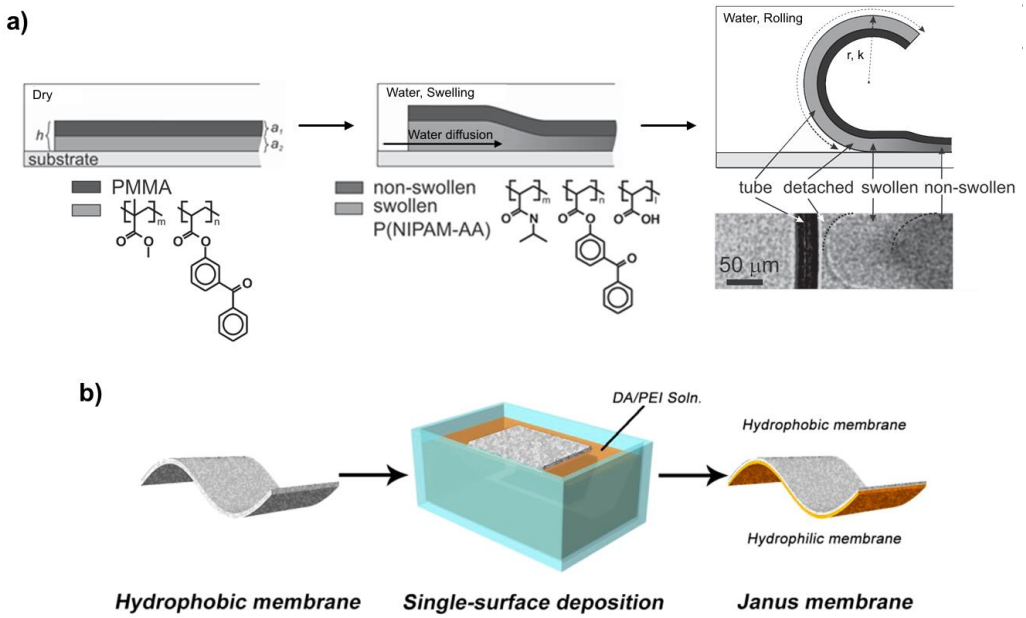

Figure 2.6: Examples of Janus membrane synthesis by sequential coating of polymers (a) and one-sided deposition DA/PEI on poly(propylene) (b). The latter was used for emulsification while the system in a) enabled stimuli-responsive folding. Taken from Refs.[36,54] and modified.

As outlined, all these methods either combine two components into one Janus membrane or modify existing 2D materials. An actual bottom-up synthesis route has not been reported up to date and would be a completely new strategy for membrane design. In the latest review on Janus membranes, Darling *et al*. convincingly point out that such approach can provide a higher control of interfacial compatibility and bear the potential of precise tailoring of surface properties.[8] This will also include application of new (2D) materials like organic frameworks, graphene or layered transition metal chalcogenides and oxides. Emerging surface modification techniques will likewise contribute to this development. Especially, the above mentioned PDA as universal adhesion promoter and controlled synthesis of polymer brushes may provide a functionality-rich toolbox for accurate construction of Janus membranes with desired thickness, dimension, wettability, charge and other tailor-made surface characteristics.

2.2 Polymer surface modification

Surface functionalization plays a key role in many technical and everyday areas. Be it the coating of non-biocompatible materials for medical applications[64], the construction of sensors [64] or the application of a film to reduce friction[65]. Therefore, a variety of techniques have been developed to introduce desired functionality on the surface. Well known approaches are the production of layer-by-layer (LbL)[66,67] and Langmuir-Blodgett (LB)[68] films, spin coating[69,70] or chemical vapor deposition (CVD)[71]. Also, self-assembled monolayers (SAMs) have been widely used as they form dense and uniform layers.[14,72,73] Unfortunately, surface modification with low molecular substances as well as the use of non-covalent methods like dip or spin coating may struggle with a lack of solvolytical or thermal stability.[74,75] Use of polymer grafts and surface-initiated polymerization (SIP) methods can counteract these challenges.

Polymer brushes are especially promising as they allow for introduction of high functional density. Their versatility in chemical structure and architecture as well as tailorable properties has therefore turned them into a field of focus in polymer chemistry. Polymer brushes are intrinsically dynamic systems adaptable to the environment, which makes them interesting for precise surface chemistry, adjustment of wettability or control of adhesion. Successful implementations of polymer brushes were already demonstrated for anti-fouling surfaces[76], cell culturing[77,78], stimuli-responsive release[79,80], sensing[81], catalysis[44], colloidal stabilization[44,82] and actuation[49] or deformation[9,10,83]. Likewise, several SIP approaches have been developed to realize the synthesis.

2.2.1 Polymer brushes

Polymer brushes are macromolecular chains which are end-tethered to a surface or interface at high grafting density (σ).[84] In general, such polymer grafts can possess different architecture, chemical composition and degree of polymerization. The physical conformation, however, will strongly depend on the proximity of attachment points on the substrate (i.e. grafting density) and solvent quality. When grafting density is low the chains are isolated and build random coils. The resulting thickness (d) only scales with the degree of polymerization (N) in that case and depends on the radius of gyration (R_g) in the respective solvent **(Fig. 2.7)**. The polymer exhibits the so called “mushroom” or even “pancake" regimes **(Fig. 2.7)**, if the chains adsorb firmly to the surface. This changes drastically, when grafting density rises.

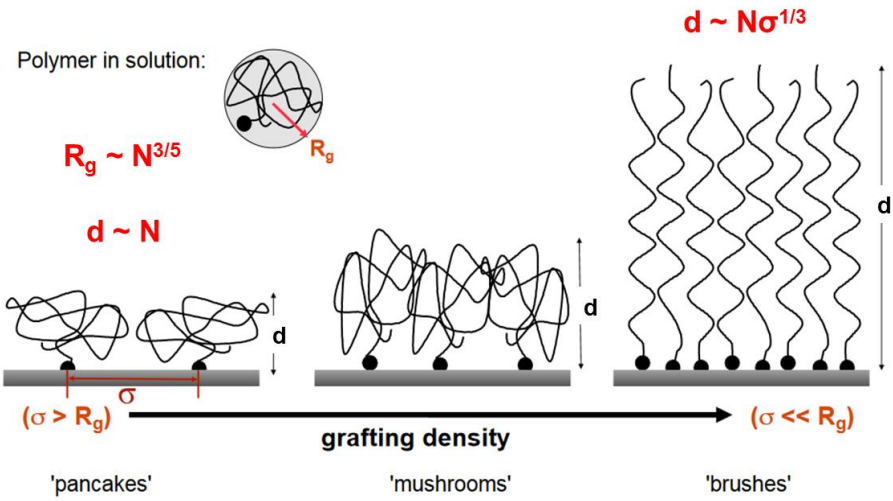

Figure 2.7: Schematic illustration of end-tethered polymer chains on surface. The resulting thickness (d) is dependent on degree of polymerization (N) and grafting density (σ). The displayed scaling laws apply for good solvent conditions.

When the distance between anchoring points decreases and becomes smaller than R_g, the polymers begin to overlap. Consequently, steric repulsion enforces extension of the chains forming the eponymous "brush" regime **(Fig. 2.7)**. In that case, the final brush height scales with both N and σ.

Detailed theoretical description of brush behavior can be found in the works of Alexander[85], de Gennes[86] and Milner[84]. In the Alexander-de Gennes model the polymer chains are considered to be surrounded by hard spheres, so-called "blobs" **(Fig. 2.8 a)**. These blobs represent the excluded volume, i.e. space occupied by a given chain segment. In this most basic description the equilibrium thickness of the brush scales as

$$d \sim N(w\sigma)^{v} \qquad (1)$$

, where w is the excluded volume and v is the Flory parameter, exhibiting 1/3, 1/2 or 1 for a good solvent, a θ-solvent and a poor solvent, respectively. From equation (1) it becomes obvious that the brush dimension is increasing linearly with the degree of polymerization, which is much larger than in solution, where R_g increases with $N^{1/2}$ (in θ-solvent). Furthermore, the model suggests that segment density rapidly drops to zero, when the distance from the substrate reaches beyond d and free chain ends are exposed to the edge of the brush. However, this description was found to be flawed due to strong simplification. Polymer brushes can undergo surface reconstruction and bury their head groups beneath the surface to reduce free energy.

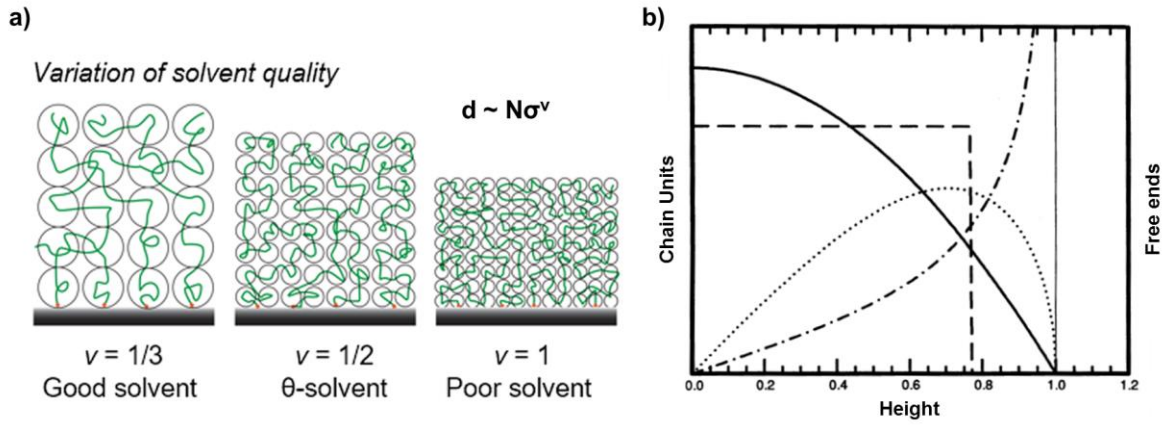

Figure 2.8: Illustration of polymer brush conformation with respective scaling law (a). The brush is surrounded by "blobs" to account on the excluded volume. Self-consistent field calculation (b) describes the brush density profile as a parabola (solid line). The chain end density displays a maximum beneath the edge of polymer brush in the presence of solvent (dotted line) to reduce free energy. Taken from Refs.[84,87] and modified.

Milner *et al.* applied self-consistent field calculations to describe the polymer brush conformation at moderate grafting density.[88,89] Their results show that the brush density profile is a parabola, basically describing a "fraying" of the polymer chains as distance from the substrate increases **(Fig. 2.8 b)**. The maximum concentration of free chain ends is not found at the outer edge of the layer anymore, which represents a more realistic picture of polymer brushes. More advanced models describing conformation and thickness at high grafting densities[90], on non-planar substrates[91] and for charged brushes[92–94] can be found in literature, giving a deeper insight into the behavior of surface-bound polymer chains.

For the realization of polymer binding on surface two general methods are distinguishable: "grafting to" and "grafting from". In the "grafting to" approach the polymer chains are synthesized prior to grafting and subsequently covalently bound or adsorbed to the substrate **(Fig. 2.9)**. That necessitates the incorporation of a suitable chemical group or property into the polymer, which ensures interaction or reaction with the functionality exposed at the surface of the substrate. Utilization of this route enables thorough characterization of the chemical structure, molecular weight or dispersity (Đ) of the synthesized molecules before the actual grafting. Hence, precise adjustment of these characteristics and highly uniform polymer coatings can be realized by "grafting to". However, major drawbacks are the values for d and σ achievable *via* this method. Since the attachment is carried out in solution, the polymer forms random coils occupying space, which corresponds to their dimension (R_g). In that way, a high diffusion barrier is built for other chains.[95] Further polymer can only bind at a distance farther than R_g. As result, σ remains low and the polymer chains stay in the mushroom regime **(Fig. 2.9)** with thickness of 10 nm at maximum.[96]

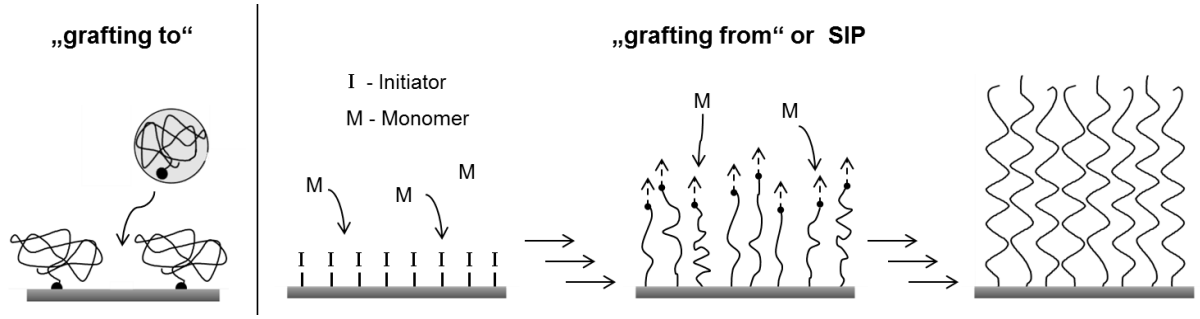

Figure 2.9: Two general approaches to bind polymer on surface. In “grafting to” readily synthesized polymer chains are bound by use of an appropriate functional group. In “grafting from” polymerization is initiated at the surface and polymer chains grow directly on the substrate.

In the “grafting from” (or SIP) approach the polymer is synthesized directly from initiator bearing substrate. Consequently, only much smaller monomer molecules have to diffuse to the substrate enabling chain growth in close vicinity **(Fig. 2.9)**. Due to the resulting high σ the individual polymer chains have less space available and stretch away from surface forming polymer brushes. In contrast to “grafting to”, SIP can produce layer thicknesses of several hundred nanometers. However, characterization in regard to classical polymer properties (e.g. N, Đ) becomes difficult, since the polymer chains are anchored to the substrate and most common techniques rely on solution based analysis. Therefore, the brushes would have to be selectively cleaved at the binding site for controlled detachment from the surface beforehand.
Immobilization of initiator is often achieved *via* SAM formation, leading to well defined reaction mechanisms. Though, other techniques mentioned above are also applicable. Once an adequate initiating moiety is bound, almost every polymerization type can be adapted to SIP including living anionic[97,98] or cationic polymerizations[99], free radical (FRP)[9,10,76] or controlled radical polymerizations (CRP)[12,14,100,101] and ring-opening polymerizations (ROP)[98,99,102]. In the following chapters two specific, radical SIP methods will be presented, which are the self-initiated photografting and photopolymerization (SIPGP) and the surface-initiated Cu(0)-mediated controlled radical polymerization (SI-CuCRP).

2.2.2 Photoinitiated free radical polymerization and SIPGP

Synthetically, FRP is one of the common methods applied to graft polymer chains on surface. Alike all chain-growth polymerizations it consists of initiation (by initiator dissociation into active radical species), propagation (by successive addition of monomer to the active chain end), termination (by disproportionation or recombination) and transfer reactions. Even though the radical character can lead to unspecific chain end functionalization and wide

dispersity, it also allows for the use of almost every vinyl monomer opening the door to diverse adjustment of substrate properties. In addition, FRP systems are advantageous due to their simplicity and relatively high tolerance towards contamination.

The surface-bound radical (R·) can be generated by different approaches including UV-light irradiation[9–11,96], thermal initiation[103,104] and treatment with peroxides[105,106], plasma[107] or even ultrasound[108]. Among these, photoinitiation offers an up-scalable grafting option with low experimental demand and cost. Furthermore, polymerization is restricted to light irradiated space so that straight forward synthesis of patterned surface is accomplished by use of an appropriate mask. This so-called negative photolithography is a well-known procedure and useful to introduce different properties or reactivity in confined area (µm-scale).

Generally, photoinitiated polymerizations rely on addition of a photosensitizer (e.g. benzophenone), which can absorb the UV-light. Thus, an electron from its π-system is excited from the ground state S_0 to the higher energy singlet state S_1 **(Fig. 2.10)**. Subsequently, the excited electron can undergo intersystem crossing (ISC) and form the triplet state T_1, which can be regarded as a bi-radical form due to unpaired electrons. As proposed by Yang and Rånby for their system with benzophenone, the next step is a photoreduction of the sensitizer by abstraction of hydrogen from the substrate. Thereby, a reactive R· is generated at the surface and an inert (benzhydrol) radical in solution.[109] The former will eventually initiate grafting following the FRP mechanism.

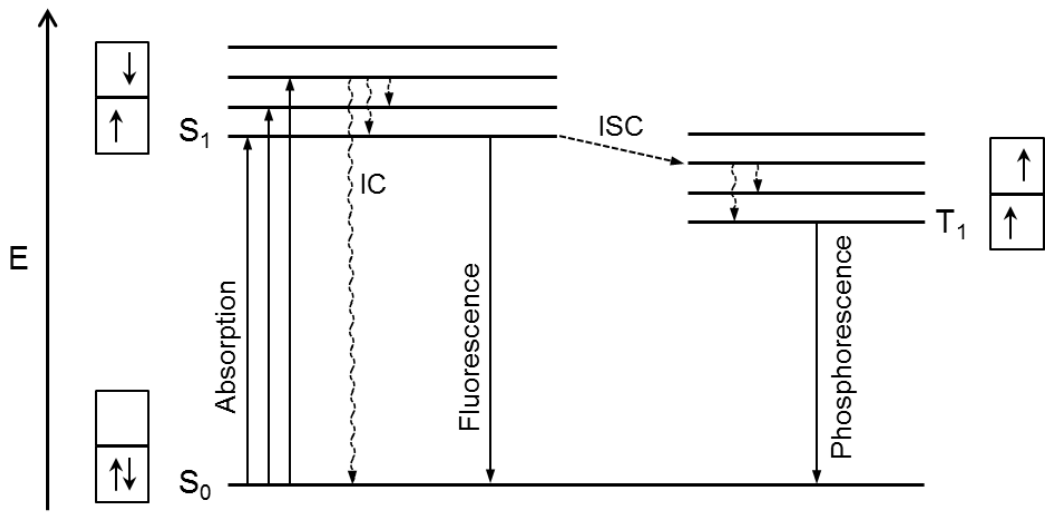

Figure 2.10: Jablonski diagram of possible electron transitions induced by radiation absorption. An electron in excited state (S_1 or T_1) can fall back to the ground state (S_0) and lead to radiation emission through fluorescence or phosphorescence. Besides, vibrational relaxation (or inner conversion, IC) can lead to non-radiative transition. Inter-system crossing (ISC) leads to a triplet state (T_1) *via* spin inversion. The respective electron configuration is schematically depicted for S_0, S_1 and T_1.

Further investigations revealed that the application of a photosensitizer is not obligatory and acrylic and styrene monomers can likewise form the bi-radical and start grafting after UV absorption **(Fig. 2.11 a)**.[110,111] Li *et al.* were the first to propose the mechanism for this process only relying on the auto-initiation by the monomer itself **(Fig. 2.11 b)**.[110] They termed it self-initiated photografting and photopolymerization (SIPGP). As can be drawn from the name, not only the desired grafting is initiated, but also unavoidable polymerization in solution or bulk. Since H-atoms can be abstracted from monomer molecules as well, this side-reaction is common in all surface-initiated radical photopolymerizations. When using photosensitizers, the process can be inhibited, if the bond dissociation energy (BDE) of the substrate is significantly lower than that of the monomer. SIPGP on the other hand is more susceptible to it because the monomer radical definitively remains as side-product after H-abstraction **(Fig. 2.11 b)**.

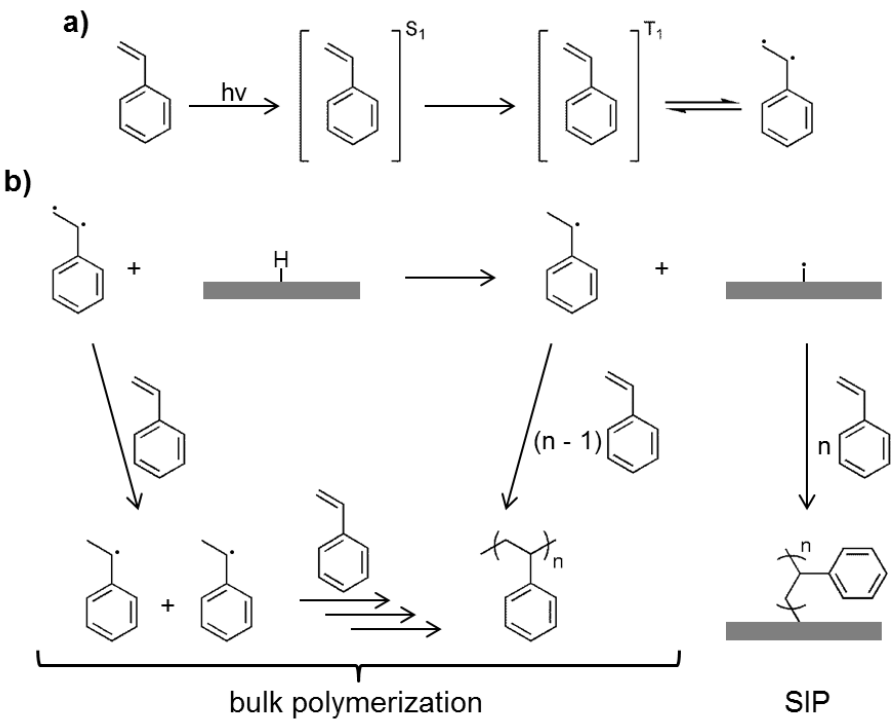

Figure 2.11: Illustration of the SIPGP mechanism with styrene as model monomer. UV irradiation leads to formation of a monomer bi-radical (a), which can abstract hydrogen from surface (b). The remaining surface-bound radical will initiate grafting (SIP). Furthermore, styrene radicals are built, which results in unavoidable bulk polymerization.

The bulk polymerization presents the main limitation of SIPGP because of the resulting monomer consumption and increasing viscosity, which decrease the grafting rate and overall efficiency. Furthermore, the FRP mechanism will lead to a certain amount of branching and cross-linking within the growing polymer chains. Still, Rånby and coworkers reported a

grafting efficiency of over 50 % for styrene[111] and final layer thickness can reach hundreds of nanometers[112]. Since only monomer and substrate are required for the reaction, SIPGP is probably the simplest experimental procedure to synthesize polymer brushes. As long as a hydrogen atom with sufficiently low BDE is present, the respective surface can be grafted with a broad variety of monomers. Hence, SIPGP was utilized to polymerize on different organic substrates[109,111] and SAMs[73], diamond[112], glassy carbon[81,113], graphene[11] and for the synthesis of polymer carpets[9–11,76].

2.2.3 Copper-catalyzed controlled radical polymerization and SI-CuCRP

Beside FRP approaches, CRP is one of the mostly used types for SIP because it ensures linear polymer brush architecture and gives dispersities close to living polymerizations (Đ = 1.05 - 1.30). In comparison to ionic polymerizations, CRP methods are less prone to termination by impurities in reaction solution and especially water. Therefore, experimental realization becomes considerably easier, since monitoring of reaction conditions does not require being as strict.

All CRP approaches achieve the desired control by reversible deactivation of the propagating chain ends with a persistent radical and formation of a so called “dormant species”. Due to the predominant bimolecular termination in the early stages of reaction, higher levels of deactivator are built. This persistent radical effect (PRE) shifts the equilibrium to the side of the dormant species and R· concentration is drastically reduced. Thus, termination is rather kinetically suppressed (reaction constant $k_t \sim [R\cdot]^2$) than the propagation ($k_p \sim [R\cdot]$). Following that principle three main methods of CRP were established with the deactivator being nitroxides (nitroxide-mediated polymerization, NMP)[114], dithioesters (reversible addition-fragmentation chain-transfer polymerization, RAFT)[101] and transition metal complexes (atom transfer radical polymerization, ATRP)[115].

Concerning polymer brush grafting, most attention was drawn to surface-initiated atom transfer radical polymerization (SI-ATRP).[116] Since its development by Matyjaszewski in 1995, ATRP has been labeled a useful tool for the synthesis of complex architecture due to excellent control of structure under mild reaction conditions, applicability to various monomers and tolerance against impurities as well as functional groups.[100,117,118] In principle, a transition metal complex is used as catalyst to activate an alkyl halide and form the propagating species. Additionally, the higher oxidation state metal complex is built and mediates the PRE. As shown in **Figure 2.12**, Cu(I) is applied for catalysis in most cases, while the generated Cu(II) complex acts as deactivator. The equilibrium constants for such

systems are extremely low ($K_{ATRP} = 10^{-11} - 10^{-2}$) and depend on the reaction´s milieu (i.e. T, solvent, type of ligand and monomer).[119] However, sufficiently high concentrations of the catalyst have to be used and addition of Cu(II) salts is necessary to ensure good control of polymerization.[120,121] Therefore, several techniques have been developed to minimize the amount of Cu catalyst. All of them rely on the reduction of excess Cu(II) back to the activating species **(Fig. 2.12)**; either *via* additional azo-initiator (initiator for continuous activator regeneration, ICAR)[122], chemical reducing agents (activators (re)generated by electron transfer, A(R)GET)[100], electrical current (*e*ATRP)[123] or photochemistry (Photo ATRP)[118]. Additionally, these approaches improve the oxygen tolerance of the polymerization.

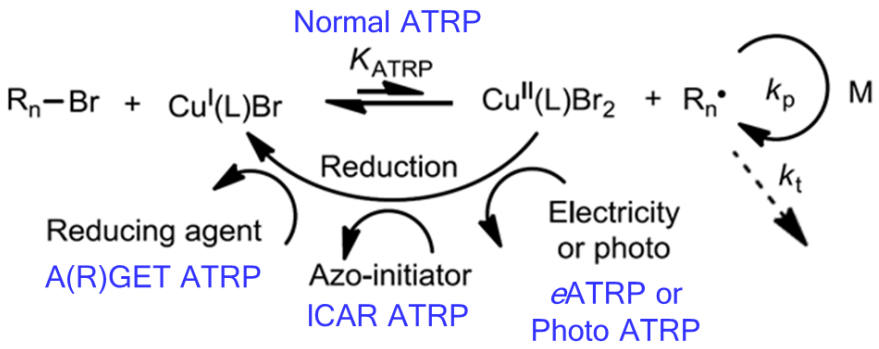

Figure 2.12: Reaction scheme of copper catalyzed ATRP. Cu(I) complexes can activate alkyl halides and generate radicals (R·), which will start polymerization with monomer (M). The equilibrium is strongly shifted to the side of educts so that R· concentration remains low. Other ATRP variations make use of different reduction processes to regenerate the activating copper species. Taken from Ref.[124] and modified.

Another important ATRP variation is performed in the presence of elemental copper, which is introduced as powder or Cu-wire. Hence, concentration of the soluble species is low and unsolved catalyst can be isolated and reused. In 2006, Percec and coworkers published on highly efficient and ultrafast synthesis by such Cu(0)-mediated controlled radical polymerization (CuCRP).[125] Popularity of CuCRP has been growing since and its robustness and living character has been demonstrated even under ambient conditions[126] and in exotic solvents such as alcoholic beverages[127]. Furthermore, well-defined complex polymers have been synthesized including hyperbranched, decablock copolymers, pentablock star polymers, and dendritic structures.[128]

With their publication on CuCRP, Percec *et al.* also postulated a new reaction mechanism called single electron transfer living radical polymerization (SET-LRP, **Fig. 2.13**).[125] Likewise, Matyjaszewski *et al.* developed the supplemental activator and reducing agent

(SARA ATRP) mechanism[129] to describe the polymerization process, which lead to lively discussions in literature. In both mechanisms the same components are considered; however, different roles are assigned to each. SET-LRP suggests that alkyl halides are mainly activated by highly reactive "nascent" Cu(0) particles through an outer sphere electron transfer (OSET). No considerable catalytical contribution comes from the generated Cu(I) species. If N-containing, multidentate ligands are used, Cu(I) disproportionates in polar solvents like dimethyl sulfoxide (DMSO) or water. Thus, Cu(0) and the main deactivator Cu(II) are regenerated **(Fig. 2.13)**.

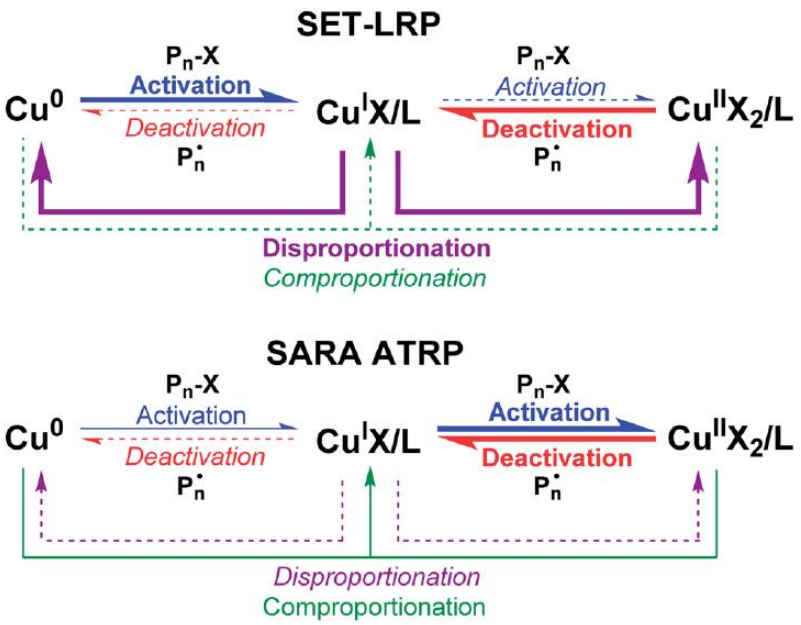

Figure 2.13: Proposed mechanisms for ATRP in the presence of Cu(0) with major contributions indicated with bold arrows and minor/negligible contributions with thin/dotted arrows. In the SET-LRP mechanism zerovalent copper is the main activator of alkyl halides and Cu(I) rapidly disproportionates regenerating Cu(0).In the SARA ATRP mechanism Cu(0) acts as supplemental activator and reduces Cu(II) species back to the main activator Cu(I). In both cases the Cu(II) species functions as main deactivator. Taken from Ref.[129].

SARA ATRP on the other hand proposes a typical ATRP equilibrium with Cu(0) acting as an additional catalyst. By comproportionation with Cu(II) it also regenerates the main activator Cu(I). However, the activation rate of the alkyl halides by elemental copper is sufficiently lower than that of Cu(I). The initiation occurs by an inner sphere electron transfer (ISET) and disproportionation is regarded as negligible **(Fig. 2.13)**.

The assumptions of both mechanistic views are supported with experimental and theoretical investigations. For example, the disproportionation of SET-LRP can be easily visualized and quantified *via* UV/Vis measurements.[130–132] Furthermore, the removal of Cu(0) particles from polymerization solution lead to ceasing of reaction, loss of end group fidelity and control

over molecular weight.[128] Polymerization in non-disproportionating solvents like acetonitrile (ACN) resulted in poor end group functionality. Monitoring of $CuBr_2$ absorbance showed that concentration of Cu(II) species was not reduced during reaction.[133] Since ^{1}H-nuclear magnetic resonance (^{1}H-NMR) spectroscopy displayed end group preservation of 100 %,[134] bimolecular termination could be ruled out. Hence, higher amounts of Cu(II) species could not be ascribed to an established PRE, as it would be required in ATRP. Finally, theoretical consideration of activation energies suggests a heterolytic rather than a homolytic dissociation of the halide, which would be the case of OSET.[125,135] High-level *ab initio* calculations performed by Matyjaszewskiet *et al.*, however, demonstrate that catalysts favor ISET in the presence of monomers containing electron withdrawing groups (e.g. acrylates, etc.).[136,137] They further argue that rate acceleration can be attributed to polarity change in the reaction medium which was verified by polymerizations in ACN and DMSO giving comparably high control.[129] Similar results were achieved with non-disproportionating ligands. Moreover, determination of rate constants as well as calculation of actual rates (R) showed that comproportionation ($R_{com} = 2 \times 10^{-7}$ Ms^{-1}) dominates over disproportionation ($R_{dis} = 2 \times 10^{-10}$ Ms^{-1}) throughout reaction.[138] Still both were comparably slow and could not compete with the activation by Cu(I) species ($R_a = 6 \times 10^{-3}$ Ms^{-1}), which was revealed to be the main contribution to the control of polymerization.[129,138]

More recent reports from Haddleton and coworkers elucidate the fate of the reaction components in organic[139] and aqueous media[140]. In fact, their results suggest that polymerization mechanisms may be different in different solvents and even dependent on the experimental protocol. While obtained rate accelerations and control proved Cu(0) to be crucial for the reaction in both cases, “nascent” particles were found to be rather inactive in DMSO and only 31 % of Cu(I) underwent disproportionation.[139] This value even dropped to 10 %, when monomer was present in solution. These observations contradict the proposed mechanism of SET-LRP. Contrary, in water disproportionation reached 85 - 96 % within minutes even when the solution contained monomer.[140] By comparison of typical ATRP and SET-LRP protocols it was further revealed that both Cu(0) and Cu(I) species can equally effective catalyze polymerization. If the ATRP is performed in pure water, however, good control over dispersity could be only achieved with addition of $CuBr_2$. Therefore, the assumption of SET-LRP mechanism is supported for aqueous environment.

All in all, the CuCRP mechanism remains a matter of discussion as it involves several components and homogeneous as well as heterogeneous processes, which have to be carefully evaluated. The number of presented literature is large, often appearing “to be conflicting for

the general audience and it is noted that in many times the conditions utilized are not directly comparable"[140]. Still, CuCRP presents a versatile approach for polymerization with unmatched reaction rates and control over dispersity and functionality.

Despite significant progress in the methodology, only limited preservation of endgroup fidelity is possible, when ATRP is employed on surface. That becomes obvious from the fact that attempts of block copolymerization result in diblocks at maximum.[100] Besides, first efforts to transfer the promising CuCRP on surface were beneficial for polymerization rate, but still limited by catalyst diffusion from the used copper wire to the substrate.[141] Introduction of Cu-powder to generate the catalytic species is likewise not applicable, since it can lead to contamination of the polymer brushes or damage of the surface.[142]

It was therefore not until 2015 that the surface-initiated Cu(0)-mediated controlled radical polymerization (SI-CuCRP) was reported by the group of Jordan.[14] A copper plate was fixed above the substrate in a simple "sandwich" set-up with TiO_2 wafer fragments serving as separators **(Fig. 2.14 a)**. Then, this assembly was immersed into reaction solution (monomer, ligand and solvent). Due to the native oxide layer on the plate, copper in all possible oxidation states may be dissolved and introduced into the reaction mixture. In their mechanistic consideration the authors consequently take into account all possible catalytic paths described in SET-LRP and SARA ATRP.[14] The activating species has to diffuse from Cu-plate to the initiator, which is immobilized on the substrate. In such case reaction takes place in between the facing surfaces. Since the Cu-plate is the only source of catalyst, its distance (D) is of crucial importance for the grafting process **(Fig. 2.14 c - e)**. Highest polymer brush thicknesses are generally produced at D = 0.5 - 0.7 cm, while direct contact with substrate prohibits grafting.[12–14] These findings lead to the assumption that bulk copper is not responsible for activation and the main catalyst is formed in solution. However, if the distance becomes too large, diffusion becomes a limiting factor again.

Since its publication, the SI-CuCRP has offered new opportunities for polymer brush synthesis. Polymerization was found to be restricted to the initiator bearing substrate, so that reaction solution and copper plate can be reused and only µl-amounts of solution are needed.[12,14] Furthermore, this method not only has enabled synthesis of polymer brushes with unmatched growth rates (d = 80 - 468 nm for acrylates and methacrylates after 1 h)[13], but was shown to be also applicable on wafer-scale[12] and under ambient conditions[13,143] **(Fig. 2.14 b)**. In addition, the low amounts of solution required for reaction enabled the production of polymer brush arrays in one single polymerization step **(Fig. 2.14 f)**.

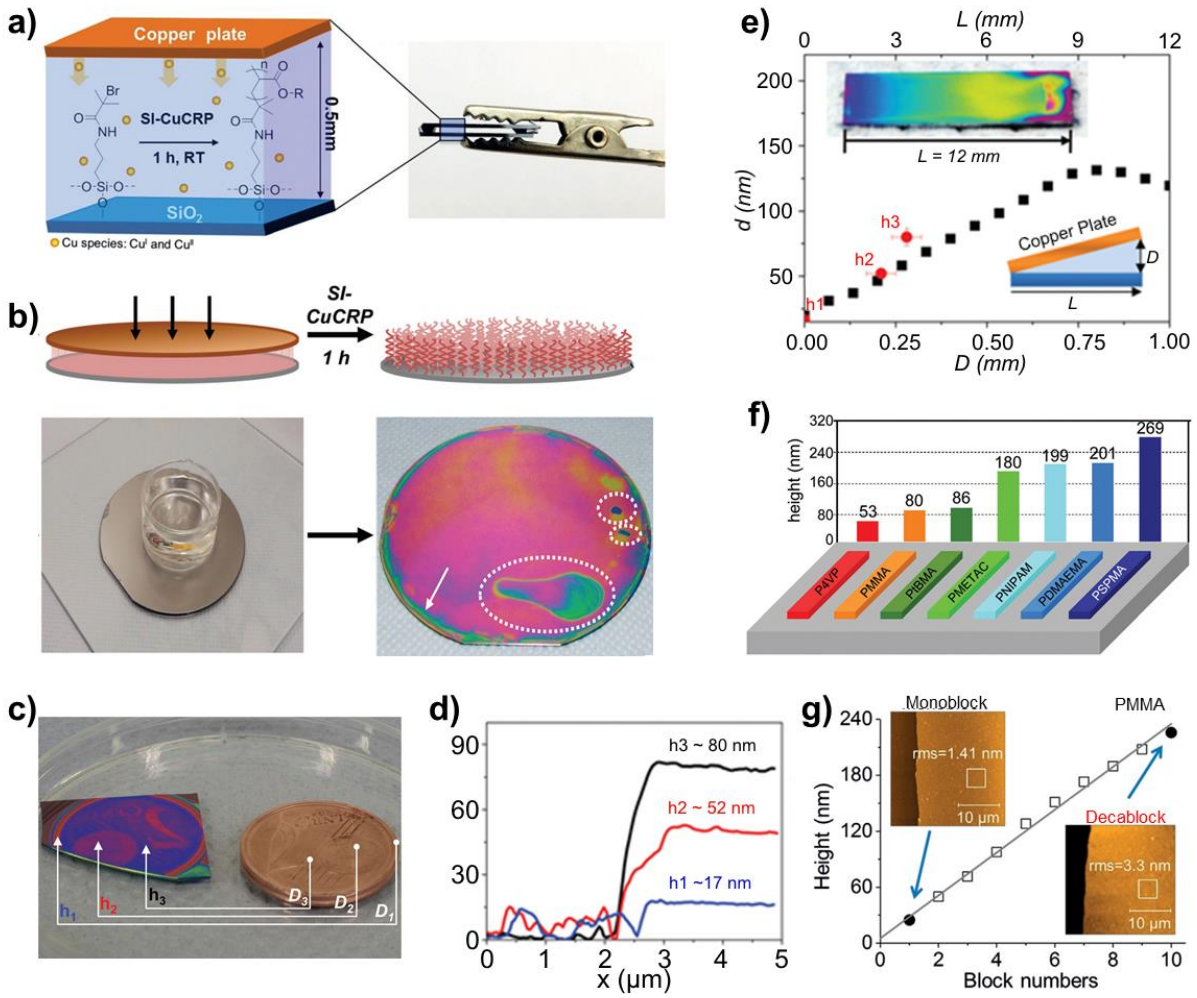

Figure 2.14: Illustration of experimental set-up (a) and new synthetic possibilities of SI-CuCRP. Synthesis in ambient conditions allows for polymer brush grafting on wafer-scale (b). Furthermore, proximity printing (c, d) and gradient fabrication (e) becomes feasible by use of different substrate-to-copper plate distance D. Polymer brush arrays can be produced in one step (f) and outstanding end group fidelity enables synthesis of blockpolymer brush to give unmatched blocknumbers (g). Taken from Refs.[12,14,143] and modified.

The above described distance dependency of grafting opened new doors for sample patterning. For example, the copper plate proximity printing was introduced.[12] Here, a Cu-plate providing an engraved shape with defined height profile (e.g. a copper coin, **Fig. 2.14 c,d**) is used to generate the negative image on the substrate. Fabrication of polymer brush gradients can also be achieved by simply tilting the plate above the substrate **(Fig. 2.14 e)**.[12,14,144]

Finally, one of the main advantages obtained by SI-CuCRP is its highly living character. Synthesis of tetrablock copolymers verified the excellent endgroup fidelity provided by this SIP approach.[12] A recent report further extends the concept of SI-CuCRP by grafting various hydrophobic brushes from monomer traces in water phase.[143] This "on-water" grafting allowed for synthesis of decablock (homo)polymer brushes **(Fig. 2.14 g)**; a block number yet

to be surpassed on surface. It is especially remarkable that height growth followed a strictly linear trend, although each layer of polymer was thoroughly washed and analyzed between grafting steps. These results clearly demonstrate the robustness of the method. Taking into account its versatility and applicability to different monomers the development of SI-CuCRP can be therefore rendered a major breakthrough for controlled surface chemistry.

2.2.4 Poly(dopamine) (PDA)

No matter what kind of SIP is employed, the introduction of an initiating layer prior to the polymerization itself is necessary since most substrates only show insufficient reactivity or do not provide the required functionality.[72,73] However, techniques like LbL, LB or CVD often demand tedious preparation, complex experimental set-up or are time consuming procedures. Hence, more straightforward approaches are desirable.

In 2007, PDA was established as "mussel-inspired" coating by a publication of Lee *et al.*[145] Mussels are well-known fouling organisms able to attach to nearly any kind of organic or inorganic surfaces **(Fig. 2.15 a)**. The key to these excellent adhesive properties was found in the *mytilus edulis* foot protein 5 (Mefp-5), which contains high amounts of 3,4-dihydroxyphenylalanine (DOPA) and lysine **(Fig. 2.15 b - d)**.

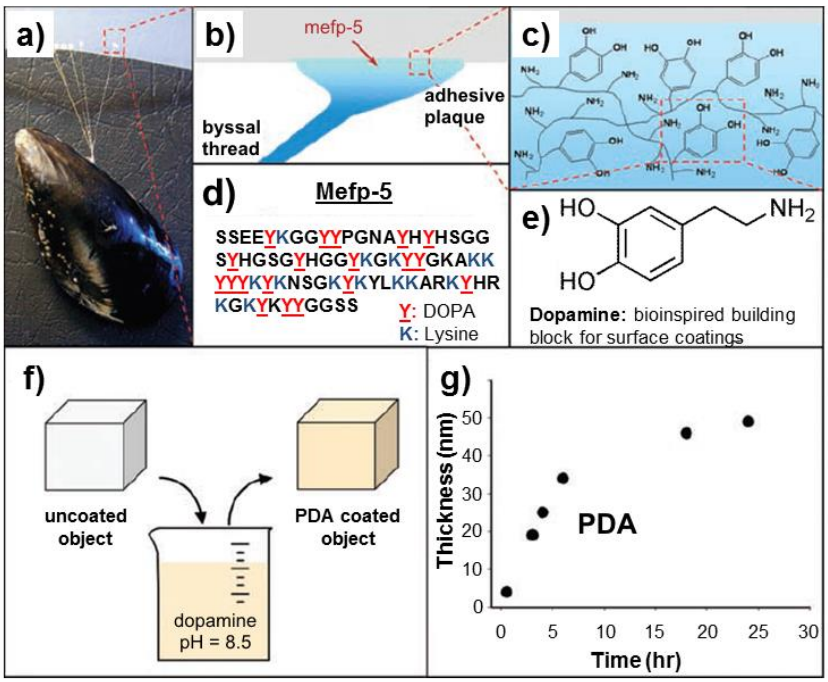

Figure 2.15: Photograph of a mussel sticking to a surface (a) and schematic illustrations of the interfacial location (b) and amino acid sequence (d) of Mefp-5. The amino and catechol groups exposed through lysine and DOPA (c) can be mimicked by dopamine (e). Immersion of an object into DA solution leads to formation of a PDA layer on its surface (f, g). Taken from Ref.[145] and modified.

Lee *et al.* came up with the small molecule compound dopamine (DA) **(Fig. 2.15 e)** to mimic the two main functions of Mefp-5, i.e. the catechol group of DOPA and the amino group of lysine. It was found that DA undergoes spontaneous self-polymerization/self-cross linking in slightly alkaline water (pH = 8.5) and ambient conditions. If a substrate is immersed into solution, PDA layers can be controllably obtained on surface reaching up to 50 nm **(Fig. 2.15 f,g)**. As speculated, such deposition was performable on a wide range of materials independent from their original surface nature. Especially these outstanding adhesive properties at minimum experimental effort make PDA an universal mediating agent for surface modification offering new strategies for simple material functionalization.[145–147] Within the first decade after its publication, PDA was therefore deposited on all types of materials, shapes and sizes; these include glass[145], Si_3N_4[145], (noble) metals and metal oxides[145,148], steel[149], CNTs[150,151], nanoparticles[152,153], poly(tetrafluoroethylene) (PTFE)[145,154] and various organic fibers and membranes[155].

Along the success of PDA as a surface coating there have been a number of publications dealing with its formation mechanism and final structure. Generally, oxidation is regarded as the first step in the polymerization, since lack of O_2 in solution drastically inhibits the process. Likewise, different oxidizing agents may be used to initiate and improve the synthesis or deposition of PDA.[156] The first oxidation product dopamine-quinone **(Fig. 2.16)** can further form 5,6-dihydroxyindole (DHI) by cyclization and rearrangement. Then, these two components and non-oxidized DA undergo several branching and assembly processes to finally compose cross-linked PDA. However, different pathways have been proposed in literature regarding the nature of cross-linking. Initially, an eumelanin-like structure was suggested mainly consisting of covalently connected indole units **(Fig. 2.16)**.[149] Other studies argue that PDA comprises rather different components including catechols, quinones and amines and verify the covalent cross-linking theory.[157] Contrary, it was also postulated that non-covalent assembly of mono- and oligomers is dominant within PDA.[158,159] Importantly, all claims are supported by detailed studies using advanced analysis techniques like solid state[158] or magic angle spinning NMR[157], Fourier-transform infrared spectroscopy (FT-IR)[149] or mass spectrometry[157] and theoretical calculations[149,159]. Therefore, contributions of covalent and noncovalent pathways are both plausible and may be present in comparable measure. Additionally, the reaction conditions were shown to have influence on the final structure of PDA. Della Vecchia *et al.* observed that a higher starting concentration of DA can lead to effective “trapping” of non-cyclized units and molecules from buffer

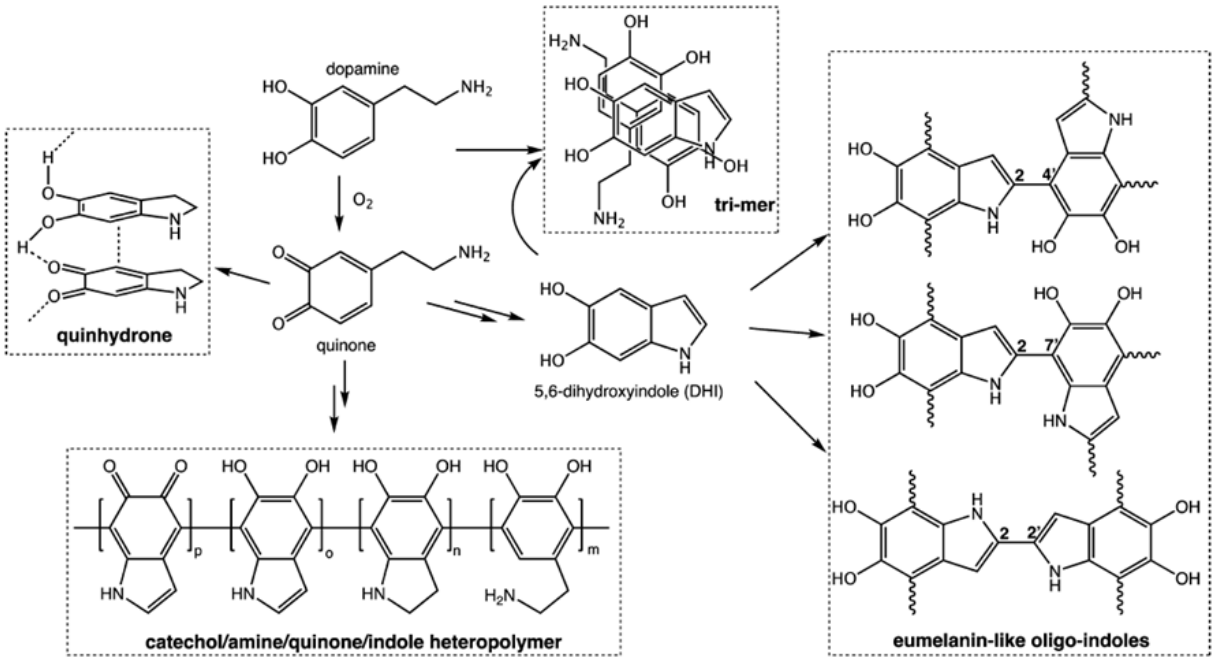

Figure 2.16: Simplified illustration of hypothesized polymerization processes of DA. Dopamine-quinone is produced in the first step by auto-oxidation. Next, cyclization and rearrangement leads to formation of 5,6-dihydroxyindole. Several paths for following steps are proposed in literature, which include covalent cross-linking, non-covalent assembly as well as formation of different oligomeric or heteropolymer structures. Taken from Ref.[155].

solution are also incorporated within the polymer.[160,161] Moreover, they found evidence for the presence of pyrrole and carboxylic groups, which hints towards partial degradation during polymerization. Similar to natural melanin, PDA exposes a partly radical character and paramagnetism stabilized by the extended π-system.[162,163] Electron spin resonance signals obtained for PDA further suggest an irregular network, where the radical is located at single quinone groups. Ju *et al.* have confirmed that PDA can be therefore used as an effective radical scavenger.[163]

The nature of adhesion remains comparably undefined. While its remarkable ability to robustly stick to all kind of materials is independent from surface properties, the actual binding mechanism seems to vary for different types of substrate. For instance, the catechol functionality can attach to metals and metal oxides *via* coordination interactions[164,165], while Michael addition/Schiff base reaction may allow for covalent binding on amine or thiol containing substrates[166]. However, various interactions between substrate and PDA can be present at once, as in the case for Mefps sticking to surface **(Fig. 2.17)**. Zhang *et al.* used PDA coated colloidal AFM probes for investigations on the adhesion on surfaces with different wettability.[167] Their study revealed strong contribution of dispersive interactions to the sturdy adhesion. In addition, interlayer attraction can arise from hydrogen bonding and charge

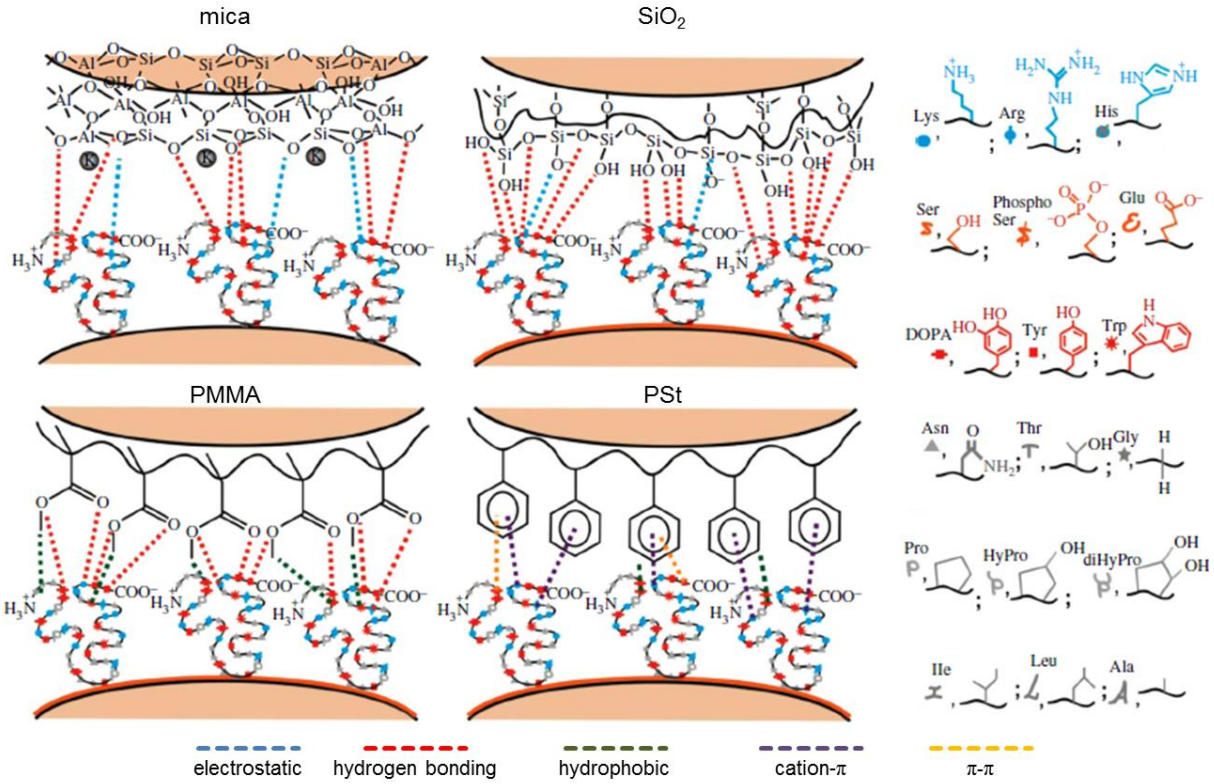

Figure 2.17: A schematic illustration of the chemical groups within Mefps and their interplay with four different substrate surfaces. The highlighted interactions between the Mefps (Mefp-3 as example) and the different surface types may likely be present, when PDA is used as coating. Taken from Ref.[168] and modified.

transfer[157] as well as π-π-stacking and cation-π-stacking[169]. A recent report by Maier *et al.* re-emphasizes that amino as well as hydroxyl groups synergistically contribute to the robust adhesion of PDA to minerals by surface salt displacement.[170]

Although the actual polymerization and adhesion mechanism as well as its structure are still a topic of discussion, it seems certain that PDA provides rich functionality; this includes carboxylic units, primary and secondary amines, aromatic rings, quinones and hydroxyl groups.[149,157,158,160] This quantity and variety of functions has already been further extended by ad-layer formation *via* Michael addition/Schiff base reaction[171], immobilization of nanoparticles[172,173] or different SIP approaches like SIPGP[76,154], SI-ATRP[147,148] or surface-initiated reversible addition fragmentation chain transfer (SI-RAFT)[174,175]. Furthermore, thermal treatment can induce carbonization building N-doped structures similar to graphene, graphene oxide (GO) or reduced graphene oxide (rGO).[176–178] The possibility of incorporating sheer endless chemical properties bears huge potential for precise material engineering. The simple experimental approach, ubiquitous applicability and low cost of PDA, hence, have incited scientific enthusiasm towards exploration of “mussel-inspired” materials and their implementation despite the lack of structural clarity. Various review

articles can be found giving detailed overviews on integration of PDA in biomedical[179] and environmental[180] context, for self-healing materials[181] or energy and sensing applications[182]. Since the advantages provided for the respective field are manifold and often very specific to the actual application, a complete presentation would be beyond the scope of this work. However, a short outline of PDA coated and derived materials and their application is given in **Table 2.1**.

Table 2.1: List of materials functionalized with PDA, further modification procedures and applications thereof.

Material	Substrate form	Modification	Application
(PDA)	particles	Cu^{2+} chelating	antibacterial capsule
		Fe^{3+} /carbonization	oxygen reduction catalyst
		thiol coupling of doxorubicine	drug delivery
SiO_2	-	SIPGP/SiO_2 etching	antifouling polymer carpet
	mesoporous scaffold	-	enhancement of cell attachment/ proliferation
	microspheres	carbonization	oxygen reduction catalyst
	nanoparticle	Ag deposition/ fluorination	oil/water seperation
Si/SiO_2	nanoparticle	carbonization/ SiO_2 removal	anode for Li^+ batteries
glass	-	microcontact printing	cell/bacteria/protein printing
Fe_3O_4	microsphere	Au growth	reusable catalyst
	nanoparticle	carbonization	anode for Li^+ batteries
CeO_2	sheets	$CaCO_3$ mineralization	light-mediated dye degradation
MnO_2	nanowire	Mn^{2+} incorporation/ carbonization	supercapacitor
SnO_2	nanoparticle	carbonization	anode for Li^+ batteries
TiO_2	electrode	-	low cost solar cell

Table 2.1: List of materials functionalized with PDA, further modification procedures and applications thereof.

Material	Substrate form	Modification	Application
$Ni(OH)_2$	nanowire	thermal treatment	supercapacitor
steel	mesh	Michael addition of dodecylmercaptan	oil/water seperation
Pt	nanoparticle	cross-linking of antibodies	immunosensor
Ag	nanoparticle	plating on nanomaterials	oxidation catalyst
Au	-	microcontact printing	cell/bacteria/protein printing
	nanorods	-	photothermal cancer treatment
	electrode	cross-linking of antibodies	bacteria detector
CdSe	quantum dot	-	reduction of *in vivo* toxicity
CdSeTe	quantum dot	aptamer conjugation	targeted cell imaging
graphene	-	hydrogel formation	metal adsorption for water treatment
	scaffold	Ag deposition	inhibition of bacteria growth
	quantum dot	-	stabilization of *in vivo* luminescence
GO	sheets	Michael addition of proteins	tissue with enhanced biocompatibility
rGO	-	-	increased blood compatibility
CNT	-	Pd/Pt deposition	oxygen reduction catalyst
	-	SI-ATRP/binding ethylene diamine	uranium removal from water
silicone	-	microcontact printing	cell/bacteria/protein printing
		poly(carbonate) hydrogel formation	antibacterial surface
poly(lactic acid)	film	-	improvement of biointegration

Table 2.1: List of materials functionalized with PDA, further modification procedures and applications thereof.

Material	Substrate form	Modification	Application
PSt/poly(lactic acid)	scaffold	Michael addition of growth factors	differentiation of stem cells
poly(amide)	membrane	-	oil/water separation
poly(caprolactone)	nanofiber	-	tissue engineering
poly(carbonate)	-	Ag deposition	antibacterial surface
poly(methyl methacrylate) (PMMA)	powder	-	improvement of biointegration
poly(sulfone)	membrane	LbL of GO	oil/water seperation
poly(urethane)	-	-	enhancement of cell attachment
poly(vinylidene fluoride)	powder	-	increase in dielectric constant
cellulose	nanofiber	magnetite/Ag	reusable antibacterial surface
cotton fabric	scaffold	Ag deposition	antibacterial surface
collagen	fiber	hydroxyapatite mineralization	dentin regeneration
yeast	-	-	immobilization/ protection of yeast cells

To sum up, PDA offers a unique combination of substrate independent adhesion and compatibility with a broad variety of subsequent modification techniques. In contrast to other coating techniques, the type of surface functionality has not to be considered and synthesis of specially tailored molecules is not required (as it is the case for LbL). The possibilities of one-step synthesis, simultaneous incorporation of other components, versatile intrinsic reactivity and controlling of layer thickness further add to the attractiveness of PDA. Therefore, it is no surprise that the plethora of applications **(Tab. 2.1)** is rapidly growing and over 5900 PDA related articles have been published since 2007 (as found on SciFinder under the term “poly(dopamine)” in February 2019). There is little doubt that this number will further increase in coming years.

2.3 Graphene

Graphene is an ideal, atomically thin, but laterally quasi infinite hexagonal lattice of sp^2-hybridized carbon **(Fig. 2.18 a)**. In fact, it was the first real 2D material to be isolated and stable at room temperature, which was widely regarded as impossible because of thermal fluctuations inhibiting long range order within such 2D lattice. In 2004, Novoselov and colleagues, however, were able to mechanically exfoliate the material using adhesive tape on graphite.[15] Small undulations within the layer **(Fig. 2.18 c)** were found to compensate the thermally induced instability allowing for the existence of graphene.

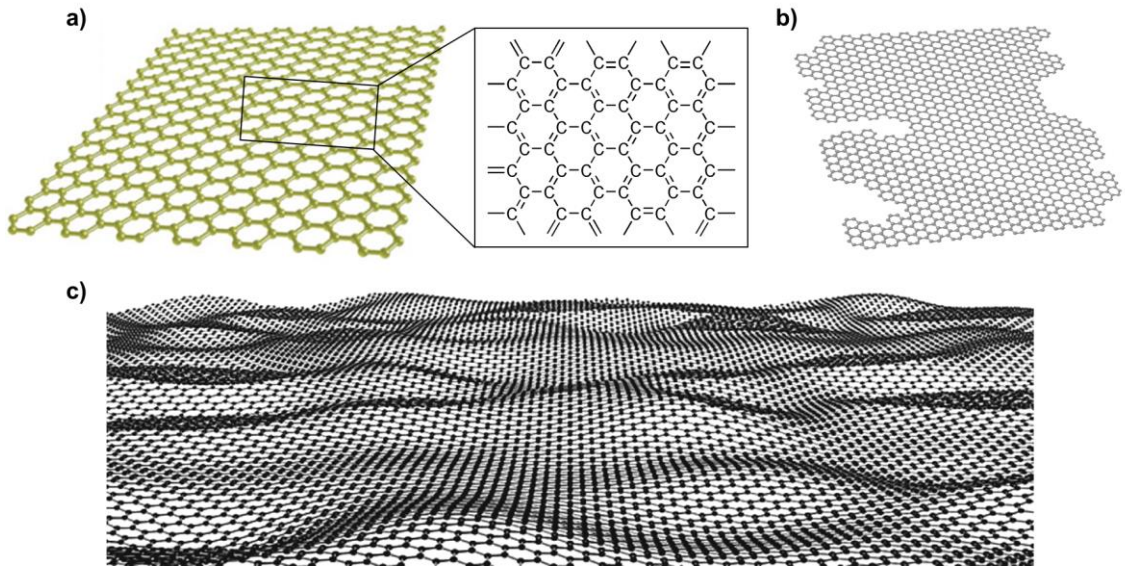

Figure 2.18: Illustration of an ideal hexagonal 2D structure of graphene and its chemical composition (a). However, real graphene always possesses defects and irregular edges (b). Additionally, the C-atoms are not perfectly in plane; the structure is somewhat corrugated (c). Taken from Refs.[183,184] and modified.

Since that discovery, graphene has sparked tremendous scientific interest due to outstanding mechanical and electronic properties provided by its structure. More precisely, it owns the highest Young´s modulus ever determined for a 2D material (1 TPa) while being flexible and sustaining elastic strain up to 25 %.[185] At room temperature the electron (and hole) mobility within graphene exhibits 200 000 $cm^2\ V^{-1}\ s^{-1}$; [186] a value that is approximately 142 times higher than in the typically used semiconductor silicon. In addition, it is able to withstand current densities up to 10^8 A/cm^2, which is one million times higher than that of copper.[187] In combination with high thermal conductivity, impermeability to gases and high transparency (~ 98 %) these features make graphene promising for integration in smart and flexible electronic devices and optoelectronics as well as sensing or environmental applications.[18,20]

In the light of these perspectives, Novoselov and Geim were awarded the Nobel Prize for their work on the most prominent 2D material in 2010.[1,16]

Along different approaches to realize implementation, research has been concentrated on production of pure and large area graphene. Top-down methods, i.e. exfoliation processes, have been used to receive single or few layer sheets. Here, separation of individual sheets from graphitic compounds is achieved by decomposition with chemical agents (chemical exfoliation) or solvent intercalation (liquid phase exfoliation).[18] In most cases an additional external force is introduced by ultrasonication (shear force) or thermal treatment (expansion) to trigger the exfoliation.[188] Similarly, electrochemical exfoliations have been reported.[189] Furthermore, several techniques have been developed to prepare graphene nanoribbons by controlled cutting of CNTs.[190,191] However, all these methods are only suitable for synthesis of flakes in the range from nanometers to some micrometers. Another major drawback is the lack of control over the synthesis so that no high quality product is obtainable. Chemical exfoliation, for example, can be performed by oxidation of graphite with strong acids.[192,193] In that way, GO sheets exposing a considerable amount of O-containing groups (e.g. OH, COOH, epoxides, etc.) are produced in the first step. Subsequent reduction is applied to form rGO and hence minimize the number of chemical functionalities on the material´s surface. Still, synthesis of pristine, highly conjugated graphene is not possible this way.

In bottom-up methods small molecule compounds are deposited under controlled conditions to grow graphene directly on a substrate.[18] These methods allow for adjustment of synthesis parameters to minimize defects or regulate number of layers. While different bottom-up approaches exist (e.g. molecular beam deposition, epitaxial growth)[194,195], CVD is most commonly used because it enables high through-put and purity of product. CVD of graphene involves vaporization of precursor molecules, transport to a metallic substrate (Cu, Ni), pyrolysis to carbon and formation of the desired structure.[196,197] Deposition has to be heterogeneously catalyzed at the metal surface to prevent clustering. The type of substrate will therefore determine the exact growth mechanism. As the produced carbon atoms start to interconnect, small isles of graphene begin to grow. Finally, single layer graphene is synthesized on large area. Yet, it should be noted that the obtained sheet is not a continuous 2D crystal, but composed of domains with grain boundaries.[198] Since the CVD kinetics can be fine-tuned by change of temperature, flow rate, cooling rate, pressure and concentration of involved gases, the process has been researched and refined in the hunt for high quality graphene.[196,197,199] Nonetheless, no defect-free, monocrystalline single layer is existent on large scale up to date **(Fig. 2.18 b)**.

2.3.1 Geometrical and electronic structure

The outstanding properties of graphene are closely related to its geometrical and electronic structure. The carbon forms σ-bonds to three neighboring atoms in plane through sp^2-hybridized orbitals.[200] Orthogonally to that plane free p_z-orbitals build π-bonds with electrons delocalized through the entire 2D lattice. This results in an atomic honeycomb structure with short interatomic distance (~ 1.42 Å) of covalent C-C bonds. The unit cell of graphene contains two inequivalent C-atoms A and B **(Fig. 2.19)** and can be described with vectors $a_1 = a_2 = 2.46$ Å. The vectors δ_1 - δ_3 are used to describe the relative position to the closest neighbors. Their proximity towards each other can be explained by the strong bonds involved and is the reason for the enormous intrinsic strength of 130 GPa (i.e. maximum applied stress before material failure)[185].

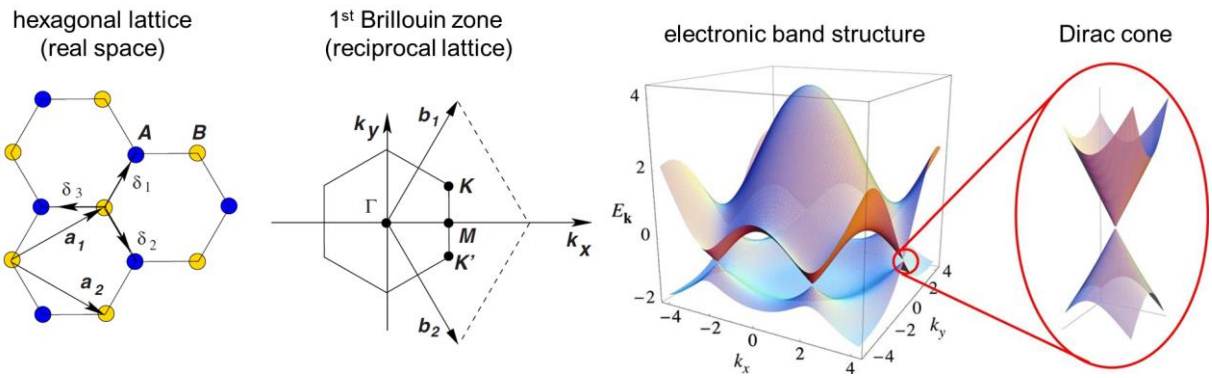

Figure 2.19: Crystal lattice of graphene comprised of atoms A and B with the unit cell described by vectors a_1 and a_2. The electronic energy structure can be calculated by construction of the first Brillouin zone (1.BZ) in the reciprocal lattice. The hexagonal 1.BZ presents the points K and K´, which are discrete connection points of valence and conduction band. In the vicinity of K-points the energy dispersion of electrons can be described with so-called Dirac cones. Taken from Ref.[200] and modified.

From the geometric composition and the given values the electronic band structure can be calculated by projection of the reciprocal lattice (denoted with vectors b_1 and b_2 in **Fig. 2.19**). Due to the high symmetry of the graphene lattice, the tight-binding model can then be applied.[20] That means electron wave functions and energies are calculated by linear combination of atomic orbitals under the assumption that they tightly bind to the respective atom and hopping occurs only between nearest neighbors.[200] As result, a symmetric energy spectrum is obtained **(Fig. 2.19)** with valence and conduction band only in contact at discrete points. These points are located at the corners of the 1.BZ and called K and K´ (or Dirac points). In their proximity, i.e. low energy state, the electronic band structure is well described as cones with linear energy dispersion (Dirac cones). Following the quantum mechanical

equations behind this description, it can be concluded that the electrons can move through the layer with an effective mass of zero. That explains the unmatched electronic properties in graphene. In addition, charge carrier concentrations can reach up to 10^{13} cm^{-2}.[18]

Finally, the population in the band structure has to be addressed. The situation in graphene resembles a state somewhere in between metal and semiconductor. While the valence band is completely filled with electrons, the conduction band is completely empty.[18,20,200] The connection of valence and conduction band in the K-points is located at Fermi level. Due to the cone-like structure, the density of states in these points is zero. Consequently, conductivity in pristine graphene is low, as no states can be occupied. Still, high electric conductivity can be achieved by doping, hence, shifting the Fermi level. Therefore, graphene is regarded as a zero band gap semiconductor.

2.3.2 Strain-engineering of graphene

Despite all attractive features of graphene, the absence of a band gap makes direct application in (opto-)electronics difficult, since typical semiconductor features are required. Thus, there has been a strong ambition to introduce a band gap and enable exploitation of the excellent electron mobility for a long time. One way to achieve this goal is the controlled change of electronic properties by induction of strain, which is also known as “straintronic effect”. Since the mechanical durability and flexibility of graphene allow for strong deformation, a new field of “strain-engineering”, or “straintronics”, has been established in that pursuit.[20]

As already mentioned, graphene is theoretically stretchable up to 25 %. However, compressive strain of ca. 0.1 % is enough to form ripples and wrinkles in the 2D layer.[201] Such application of strain have been reported to shift Dirac cones and Raman signals of graphene as well as stabilize atom adsorption, enhance coupling between electrons and phonons (collective lattice vibration) and prompt other phenomena.[20] Stronger electron-phonon coupling, for example, would facilitate superconductivity making it realizable at comparably high temperatures of 20 - 30 K. The shift of Dirac cones can result in band gap opening **(Fig. 2.20)**. Under uniaxial or shear strain the Dirac cones at K and K´ start to move into opposite direction. If the applied strain is sufficient they will eventually merge and open the desired band gap. As calculated, threshold values for uniaxial strain lie at ~ 20 % of strain to realize this goal.[202,203] For deformation *via* shear force, on the other hand, a threshold of ca. 16 % was reported by Cocco *et al.* and a maximum band gap of 0.72 eV was found at 20 % shear strain.[204] Biaxial strain, however, does not change geometry so that neither Dirac cones are merged nor a band gap opened.

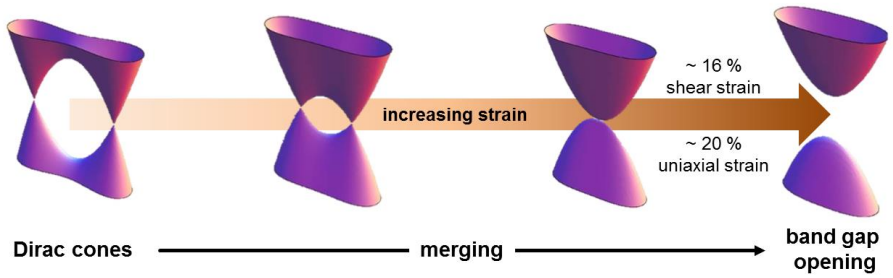

Figure 2.20: Band gap opening upon application of strain. Dirac cones begin to move towards each other and start to merge. When threshold values are overcome, a measureable electronic band gap opens. Taken from Ref.[193] and modified.

The distortion within the crystal lattice and band gap opening can be monitored and quantified with Raman spectroscopy. In the single layer graphene Raman spectrum two prominent signals can be found **(Fig. 2.21 a)**; the G-band at ~ 1580 cm^{-1} and the 2 D-band at ~ 2680 cm^{-1}.[20] The former originates from photon absorption by sp^2-hybridized carbon. An electron is excited into a higher energy state forming an exciton **(Fig. 2.21 c)**. Subsequently, a phonon scattering leads to recombination and thus emission of light. In simpler words, the G-band arises from light scattering by C=C bond group vibrations. The 2 D-band is a consequence of a double resonance scattering **(Fig. 2.21 d)**. First, an excited electron (or hole) is inelastically scattered by a phonon to a neighboring Dirac cone. Then, a second phonon scatters back the electron before final recombination occurs. The form, exact position and relative intensity of the 2 D peak can be used to estimate the number of layers within graphene. For example, intensity in relation to the G-band is much lower in a double layer or graphite **(Fig. 2.21 a)** as compared to a single layer graphene. Scattering caused by defects within the graphene structure give rise to the D-band (~ 1350 cm^{-1}). Hence, the ratio between intensities of D- and G-band (I_D/I_G) is a measure for disorders within the structure.

Since application of uniaxial strain breaks the hexagonal symmetry of the graphene lattice **(Fig. 2.21 b)**, the vibrations of C=C bonds lose their degeneration. As result, the G-band red shifts and splits into G^+ and G^- modes **(Fig. 2.21 e)**.[205,206] It was found that the intensity ratio between these two signals depends on the polarization of the incident light. Likewise, the loss of symmetry in the 1.BZ brings about different paths for the double resonance phonon scattering. As shown in **Figure 2.21 b** the distance to one of the nearest Dirac cones will be elongated (blue arrows), while the other two will be shortened (red arrows) if graphene is stretched along armchair direction. For stretching along the zigzag axis the case is vice versa. In any case, the scattering paths become energetically inequivalent. Therefore, the 2 D-band also splits into 2 D^+ and 2 D^- signals **(Fig. 2.21 f)**.[207]

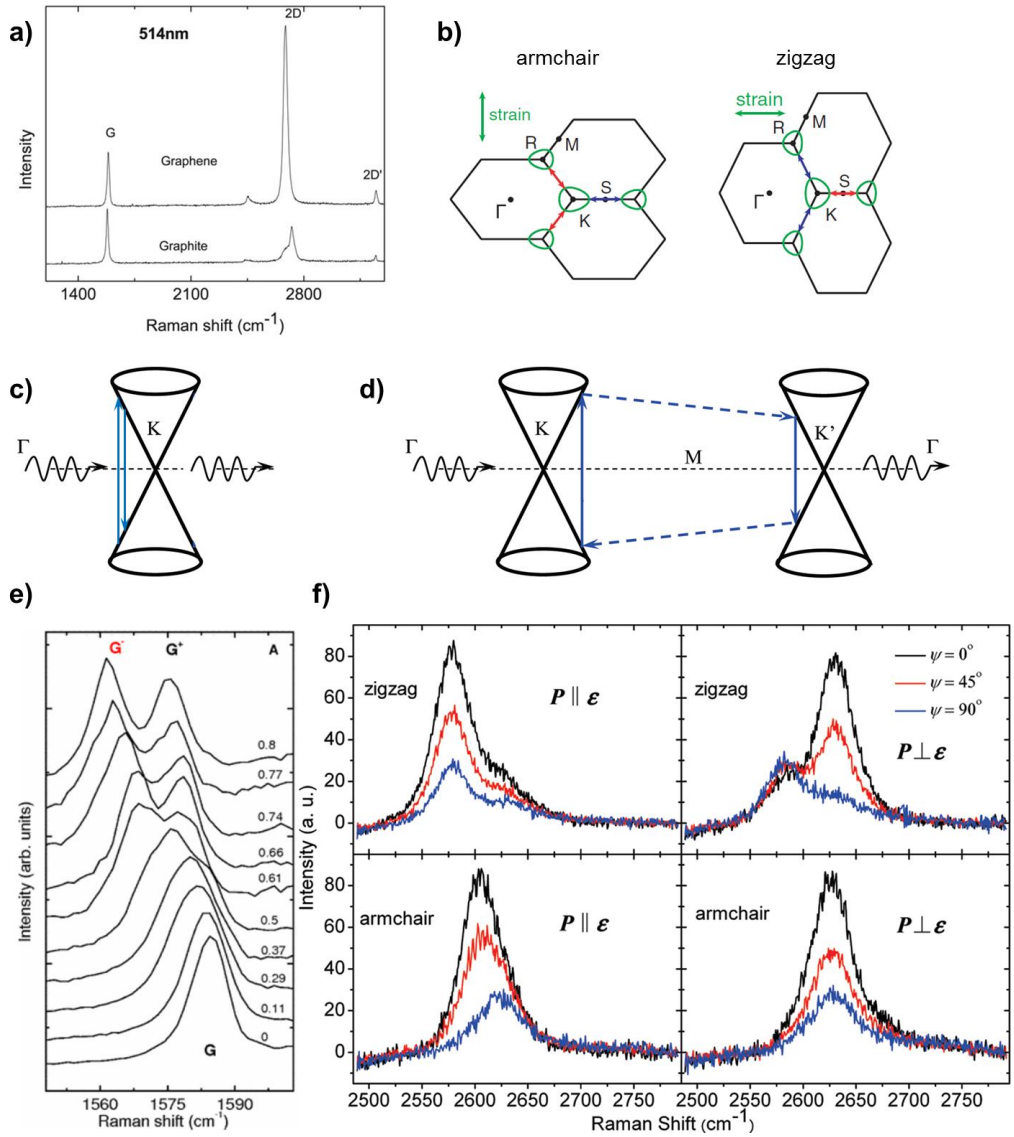

Figure 2.21: Typical Raman spectrum of unstrained single layer graphene (a) and schematic illustration of phonon scattering processes leading to the characteristic G-band (c) and 2 D-band (d). Stretching in armchair or zigzag direction (b) breaks symmetry forming inequivalent scattering paths. As result, the signals split into G^+ and G^- (e) as well as 2 D^+ and 2 D^- (f). The degree of splitting and intensity is dependent on strain axis ($\boldsymbol{\varepsilon}$) and its relation to incident light polarization (***P***). Taken from Refs.[206–209] and modified.

The degree of signal splitting can be used to quantify effective strain. Yoon *et al.* found that 2 D^+ and 2 D^- shift rates for strain along the armchair axis are - 44 cm^{-1}/% and - 63 cm^{-1}/%, respectively.[210] However, the values are different for deformation in the zigzag direction exhibiting - 26 cm^{-1}/% and - 68 cm^{-1}/%. Still, the degree of splitting and intensity ratio I_{2D}^+/I_{2D}^- are strongly dependent of the polarization angle in relation to strain axis **(Fig. 2.21 f)**.[207] No band splitting can be observed within the Raman spectrum, when biaxial strain is applied due to the preservation of symmetry. However, a redshift of G- and 2 D-band will occur because of the strain induced phonon softening (hindrance of vibration).[211]

Though theory clearly points out the potential of strain-engineering, its realization is complicated. Naturally, intrinsic strain exists in graphene at the edges of the layer leading to twisting.[184] In addition, mismatch between the layer and substrate can form ripples and small wrinkles. To introduce strain intentionally, controlled expansion and shrinking of substrate is applied. Flexible substrates can be directly deformed to transfer force onto the graphene sheet. Ferrari and coworkers reported on strains up to 1.3 % using polymeric substrates and bending them in two different set-ups **(Fig. 2.22 a)**.[206] In a comparable approach Huang *et al.* transferred graphene on poly(dimethyl siloxane) reversibly introduced uniaxial strain up to 3 %.[205] Pre-stretching of elastic substrates prior to synthesis or transfer of graphene and subsequent relaxation is also applicable **(Fig. 2.22 c)**. As demonstrated for MoS_2 flakes, wrinkles can be induced within the layer on µm-scale.[212] Another possibility is the utilization of piezoelectric substrates to trigger longitudinal deformation by voltage.[211] Thermal expansion mismatch can similarly lead to tension within the layer. For instance, heating and cooling of graphene on SiO_2 or SiC substrate achieved between 0.1 % and 0.8 % of strain.[209,213] Mi *et al.* published on the promotion of strain by SiO_2 nanopillars.[214] A single layer graphene was transferred onto the substrate forcing the sheet to adapt to the topology **(Fig. 2.22 b)**. The result was a strain of ca. 0.2 % calculated from Raman shift.

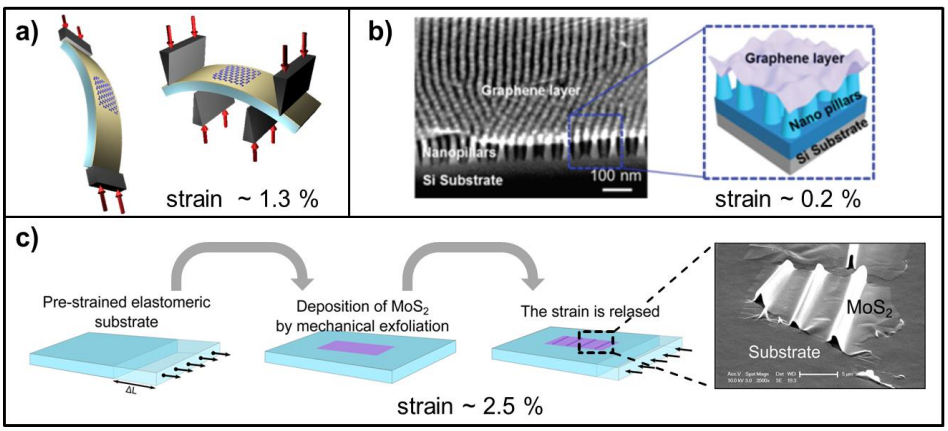

Figure 2.22: Approaches of strain application and achievable strain values. Flexible substrates can be used to stretch adhering graphene by bending (a) or pre-stretching and relaxation after deposition (c). Defined surface topology can be used to ripple graphene sheets (b). All methods reach 3 % of strain at maximum. Taken from Refs.[16,191,206] and modified.

From the examples above it becomes obvious that established straining procedures are not sufficient to open a band gap in graphene. Although analytical and mathematical methods would allow for precise detection and quantification, actual strain of at least 16 % is still to be reported. Consequently, a system is required providing enhanced coupling between the single layer and applied force or stimulus – just, as it is the case in polymer carpets.

2.4 Polymer carpets

Polymer carpets are ultrathin freestanding membranes comprised of a cross-linked 2D sheet exposing polymer brushes at its surface **(Fig. 2.23 a)**. Their name arises from the morphological similarity to an actual floor carpet and was introduced in a seminal work by Amin and others in 2010.[9] Ideally, the 2D sheet is atomically thin or exhibits heights of several nanometers (≤ 10 nm) at maximum. The attached polymer layer, however, can reach hundreds of nanometers, while the lateral extension of the carpet may range from micrometers to centimeters.[10,215,216] Thus, aspect ratios in between 10^3 and 10^7 are attainable.

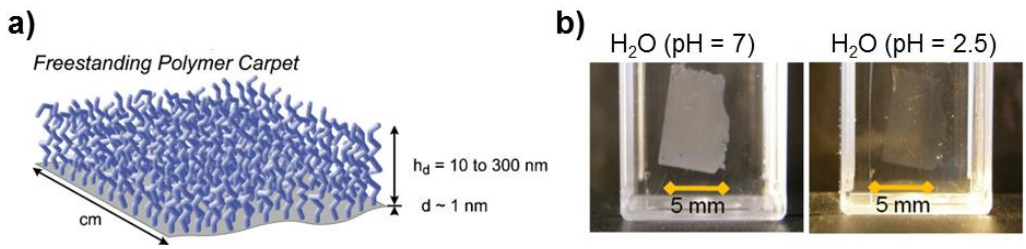

Figure 2.23: Schematic illustration of the general structure of freestanding polymer carpets (a) and photographs of a poly(4-vinylpyridine) (P4VP) carpet as transferred on glass (b). Immersion in good (H_2O, pH = 2.5) and bad solvent (H_2O, pH = 7) induces morphology switch and thus change in optical character. Taken from Ref.[9] and modified.

The most remarkable feature of this new class of material is the preservation of polymer brush conformation providing high sensitivity and responsiveness, while simultaneously being robust, flexible as well as mechanically and chemically stable. In contrast to other nanomembrane systems, polymer carpets can therefore react to external stimuli faster, since the interaction between polymer chains is not inhibited by strong cross-linking. Due to the absence of a rigid substrate the entire carpet undergoes cooperative changes of physical properties like wettability or transparency **(Fig. 2.23 b)**.[9] Furthermore, access to a broad variety of polymer brush functionality and various SIP methods (see **chapters 2.2.1** and **2.2.3**) enables precise tailoring of thickness, elasticity, reactivity or responsive behavior of the polymer carpet. As shown by Amin *et al.* patterning can even lead to anisotropic and directed buckling and wrinkling of the layers.[10] Accounting on their huge aspect ratio, implementation of polymer carpets into devices coupling minor changes to large scale effects was proposed by the researchers. For instance, microsensors and actuators could directly profit from the aforementioned directed/anisotropic transformation of morphology. Equally,

integration in all kind of (nano-)membrane technologies or as biomimetic tissues could become employable to enhance the respectively required effects.

Despite their unique characteristics only a very limited amount of research has been dedicated to the topic of polymer carpets. Further exploration is still needed to extend on synthetic possibilities (e.g. for gradient or Janus-type polymer carpets) and variety of usable 2D materials.

2.4.1 Synthesis of polymer carpets

In their initial report Amin and colleagues applied e-beam induced cross-linking of biphenyl SAM and afterwards performed SIPGP. The so synthesized polymer brush layers can be detached from the substrate to give freestanding polymer carpets. While this four-step approach (SAM formation, cross-linking, SIPGP, lift off) is rather straight forward, the variety of competing surface modification techniques allows for a wider range of possible pathways **(Fig. 2.24)**. Apart from SIP, which is required to graft polymer and ensure brush morphology, fabrication of polymer carpets can be subdivided into two major synthetic challenges. First, an ultrathin cross-linked 2D sheet or scaffold has to be produced, which generally will be realized on a substrate or support. The so obtained 2D structure should provide chemical functionality directly compatible for SIP or enabling initiator immobilization for polymer brush synthesis. Second, the readily formed nanolayer has to be lifted off the substrate/support to receive the freestanding polymer carpet.

In principle, all coating techniques may be applicable to generate a thin molecular or polymeric film on surface to serve as precursor for 2D sheet synthesis. Similar to Amin *et al.*, the Gölzhäuser group reported on synthesis of freestanding or transferable carbon nanomembranes based on aromatic SAMs.[217–219] While it is possible to use the cross-linked SAM itself as the 2D scaffold **(Fig. 2.24)**, bond formation between the molecules has to be induced by e-beam or extreme UV-light. Therefore, the instrumentation effort is comparably high. Another approach to use SAMs was reported by Whitesides and colleagues.[220,221] They formed Au-thiol monolayers to mediate fabrication of 5 nm thin polymer sheets. For that, a thin PEI layer was immobilized by ionic, covalent or hydrophobic adsorption on the SAMs and cross-linked by reaction with polymeric anhydride. After release from surface freestanding films with micrometer lateral size were obtained. Grafting of a thin polymer layer on SAM and cross-linking can give similar results. Furthermore, sequential filtering and dip- or spin-coating have been performed to build polymer nanomembranes.[69,219] Simple spin-coating, for example, was used to build an amino terminated poly(ethylene glycol)

(PEG) layer on gold.[69] Chemical cross-linking was achieved by use of epoxy terminated PEG to synthesize polymer sheets of 10 - 300 nm, which were stable after detachment from substrate. Goedel *et al.*, on the other hand, used poly(isobutene) with ionic head groups to create LB films on copper grids.[222,223] These films were shown to be robust when cross-linked physically during drying process or chemically by UV exposure.

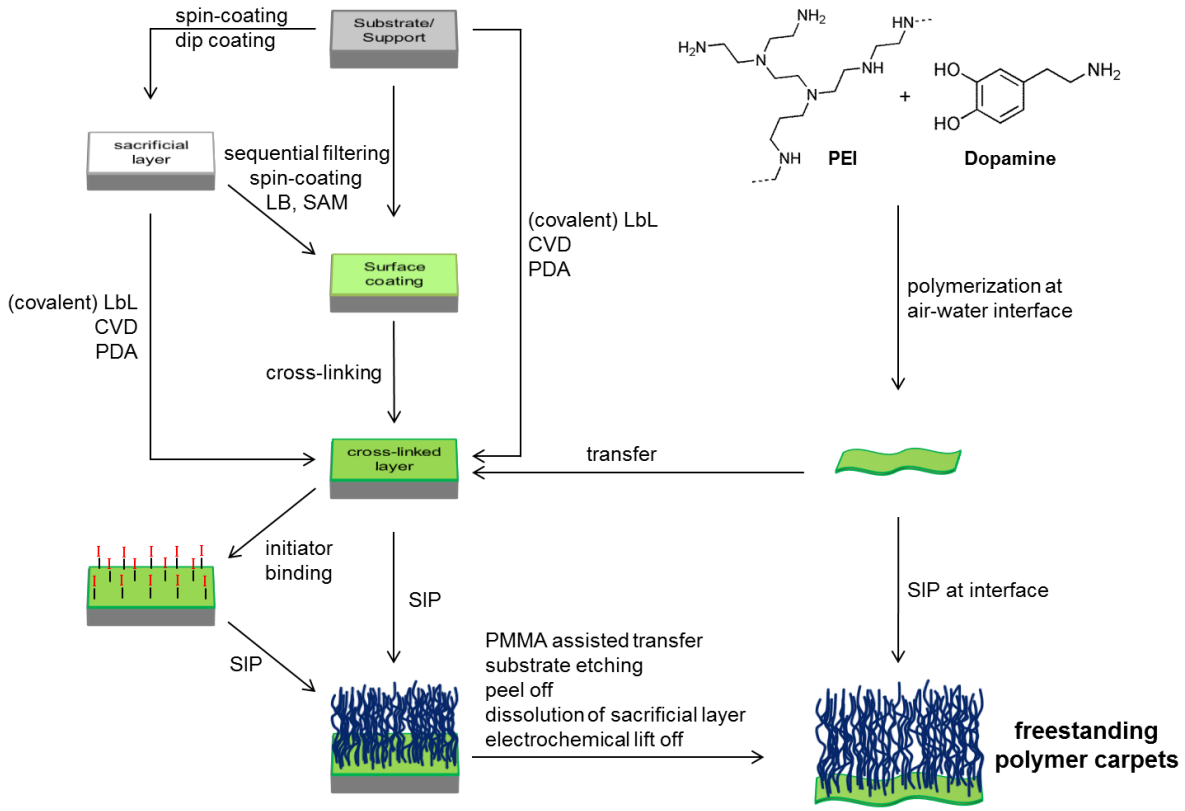

Figure 2.24: Overview of possible synthetic routes for fabrication of freestanding polymer carpets. Prior to SIP, a thin cross-linked 2D layer can be produced on substrate/support by various competing techniques. After SIP, the synthesized polymer brush is detached from supporting surface *via* etching or dissolution. Alternatively, use of sacrificial layers or synthesis at air-water interface is applicable.

To circumvent the additional step of cross-linking, LbL assembly can be used **(Fig. 2.24)**. Several reports on LbL and subsequent polymer carpet fabrication were published by Advincula and Estillore.[67,224] Layer thickness between 6 nm and 30 nm were reached by alternating dip coating of cationic and anionic ATRP macroinitiators. As the single layers in such systems are held together by strong electrostatic interactions, following lift off procedures gave stable freestanding films. Polymer carpets could therefore be synthesized using SI-ATRP. Moreover, covalent LbL of poly(vinyl dimethylazlactone) and PEI has been demonstrated to be suitable for synthesis for 2D nanofilms, as the two components undergo

rapid "click"-type reaction.[66] Another elegant approach is the use of mono- or few layer 2D materials (or 2D polymers) deposited or directly synthesized on substrate. As example, CVD graphene monolayers can be grafted with polymer *via* SIPGP.[11,216,225] The polymerization occurs on the already present defect sites in graphene and sp^3 to sp^2 ratio remains constant.[11] Hence, the chemical and electronic structure is not affected by the grafting. Since CVD graphene is commercially available, this strategy can be even regarded as one-step synthesis of polymer carpets. In addition, such synthesis can be realized on comparably large scale determined by the size of support (i.e. cm-size Cu-foil), while the monolayer provides the lowest possible thickness of a 2D sheet. Other 2D materials like hexagonal boron nitride, exfoliated MoS_2, GO or rGO were also demonstrated to be compatible for initiator binding and polymerization.[226–229] This palette has been further extended by C_3N_4, $MoSe_2$, WS_2, WSe_2 in the PhD thesis of Wenbo Sheng.[230] Emerging synthetic routes and growing interest in 2D material science will further add to this list in future.[231–234]

PDA surface chemistry is of particular interest for polymer carpet synthesis considering its experimental ease and low cost (see **chapter 2.2.4**). Kohri *et al.* were the first to report on PDA based freestanding polymer brushes.[147] Prior to deposition, dopamine was converted with 2-bromobutyryl bromide (BiBB) so that Br was present within the final PDA layer (Edmondson-method). Thereby, a 6 nm thin coating was achieved and SI-ATRP was enabled. Contrary, SIPGP was used in another publication by Amin *et al.* to graft various monomers on unmodified PDA.[76] In both cases the produced polymer brushes could be detached from substrate to result in colorless polymer carpets. These retained lateral integrity as well as smoothness and adhered robustly to the new support, when transferred. The self-polymerization of PDA was also exploited for copolymerization with PEI at the air-water interface.[235] Even though the achieved thickness of the so synthesized 2D membrane was relatively high (80 nm), such systems might be suitable for grafting reactions at interface making a lift off procedure obsolete.

So far, many strategies to detach polymer brushes rely on the pre-coating of the substrate with a sacrificial layer **(Fig. 2.24)**. As such, PVA and cellulose acetate (CA) are of particular interest because of their solubility in water. The reports of Advincula[67] and Kohri[147] mentioned above demonstrate the simple dissolution of CA to receive the desired polymer carpets. While PVA can be used in the same way[70], Ober and Ohm spin-coated the polymer to perform SIP on the formed layer[236]. Due to entanglement of PVA chains and the grafted PSt, slipping apart of polymer brushes is prevented during dissolution. Thus, the PVA layer acts as cross-linked nanoscaffold and exposure to water resulted in release of micrometer size

polymer carpets. Additionally, PVA can serve as a promoter for peeling off the synthesized polymer brush layer.[224,237,238] In that case, it is casted and dried on the sample. Then, the whole layer can be mechanically removed from substrate with the help of tweezers. After dissolution of PVA the freestanding polymer carpet is obtained. However, the substrate-to-2D sheet interaction has to be considerably weak to ensure clean peel off in this approach. Systems covalently bound to the substrate are therefore not applicable.

In contrast, most metal or metal oxide substrates and supports can be etched away to release the polymer carpets from its surface and allow for all kinds of preceding 2D sheet formation (i.e. SAM, LbL, CVD, etc.). For instance, gold is one of the best studied systems for binding of SAMs and can be simply oxidized by KI/I_2 solution in ambient conditions. The initial report of Amin and works by Gölzhäuser demonstrate the feasibility for polymer carpet fabrication.[9,215,217] Similarly, often used substrates like Cr or Cu are applicable for release from surface by mild etching with $Ce(NH_4)_2(NO_3)_6$ or $NH_4S_2O_8$, respectively.[11,239–241] Furthermore, a comparably fast process is the lift off from SiO_2 with the help of HF-solution. As reported by Ober and Welch, hydrofluoric acid is capable of etching oxides, while polymers remain unharmed.[242,243] Therefore, this system was chosen a number of times for the detachment of polymer brushes and fabrication of PDA based polymer carpets.[76,242] It is noteworthy that for any of these procedures sufficient stability on macroscopic scale is only achieved with thick polymer brushes (~ 100 nm). Otherwise, PMMA assisted release has to be applied; a PMMA film is spin-coated on the polymer brush prior to detachment and dissolved after transfer. That way, even SAMs can be directly transferred on different support. Finally, electrolytic lift off can be considered as another option. Edmondson and Huck built an electrolysis cell with the gold substrate acting as cathode.[244] By passing current through an aqueous NaCl solution the beforehand grafted and cross-linked poly(methacrylate) was released from surface.

All in all, plenty of possible synthetic routes are available to attain polymer carpets using different kinds of underlying 2D sheets, substrates/supports and several detachment procedures. However, only a handful of the above described examples actually represent the class of this material. Furthermore, only two reports exist on patterned or gradient polymer carpets up to date, although SIP methods like SI-CuCRP provide synthetic access. Janus-type polymer carpets are likewise imaginable and would combine the best of two worlds: improved selectivity and transport with enhanced sensitivity. At the same time, the number of applications – so far, just as limited as number of publications on polymer carpets – could be further extended.

2.4.2 Fields of application

As a representative of the family of freestanding nanomembranes, polymer carpets are promising for several areas in 2D related nanotechnology. Development of (bio)-sensors[239], micromechanical devices[219,241] and flexible electronics[245,246] could benefit from the highly dynamic, soft polymer brush layer. Moreover, polymer carpets could contribute to typical membrane processes like gas or liquid separation[247,248] and tissue engineering for biomedical applications[249].

One of the first integrations of polymer carpets into a biosensing application was reported by Hess and coworkers.[216] N,N-Dimethylaminoethyl methacrylate (DMAEMA) and tert-butyl methacrylate (tBMA) were copolymerized on graphene *via* SIPGP. The resulting polymer carpet was incorporated in a field effect transistor and the attached poly(tert-butyl methacrylate) (PtBMA) ester group was modified with the enzyme acetylcholinesterase. Thus, an acetylcholine sensitive system was obtained able to induce enzymatic degradation of the molecule. During reaction H^+ is produced and can be bound by the amino group of DMAEMA. As effect, charge doping is introduced and the transistor current is effectively modulated allowing for detection of acetylcholine concentrations as low as 0.5 µM. In a similar approach Gao *et al.* synthesized graphene based polymer carpets as transferable DNA sensing arrays.[239] First, single stranded DNA was bound to the polymer. Then, hybridization with the complementary strand was performed and visualized by observing fluorescence change in UV-spectroscopy. Furthermore, the potential of graphene polymer carpets for energy harvesting was demonstrated.[250] After grafting a thin layer of poly(4-bromostyrene), Tao *et al.* synthesized poly(3-hexylthiophene) (P3HT) brushes by Kumada-coupling reaction. Being a conjugated polymer, P3HT displays excellent electronic and photonic properties.[251] In fact, the photoluminescence intensity was enhanced in the polymer carpet compared to spin-coated P3HT because of improved inter-chain absorption and resulting higher charge carrier mobility. However, energy conversion by emission has to be reduced to harvest the absorbed light for electric work. Therefore, heterostructures with MoS_2 were fabricated to quench the luminescence by efficient separation of electron-hole pairs. As result, generation of photocurrent became feasible **(Fig. 2.24)**. Although the current density could not compete with conventional solar cells, such P3HT carpets are highly promising for flexible, large area optoelectronic devices.

The publication of Amin *et al.* on PDA polymer carpets is an example for utilization as antifouling tissue.[76] Since cells prefer soft materials for growth, transferred PDA nanosheets aided attachment of mice embryonic fibroblasts (44 % more cells than on grafted PDA) due to

lower Young´s modulus **(Fig. 2.25)**. Poly(3-sulfopropyl methacrylate) (PSPMA) carpets, on the other hand, inhibited cell growth (75% fewer cells) and effectively promoted cell death because of the negatively charged chain rejecting the likewise negatively charged fibroblasts. Preliminary results on PDA based carpets exposing poly(2-oxazoline) (POx) bottle-brush brushes (BBBs) further prove the capability of cell adhesion and growth control. In that case, all POx BBBs were beneficial for cell adhesion when grafted on PDA modified surface (black columns in **Fig. 2.25**). However, the cell number grew significantly larger, if respective carpets were used for the attachment tests (red columns in **Fig. 2.25**).

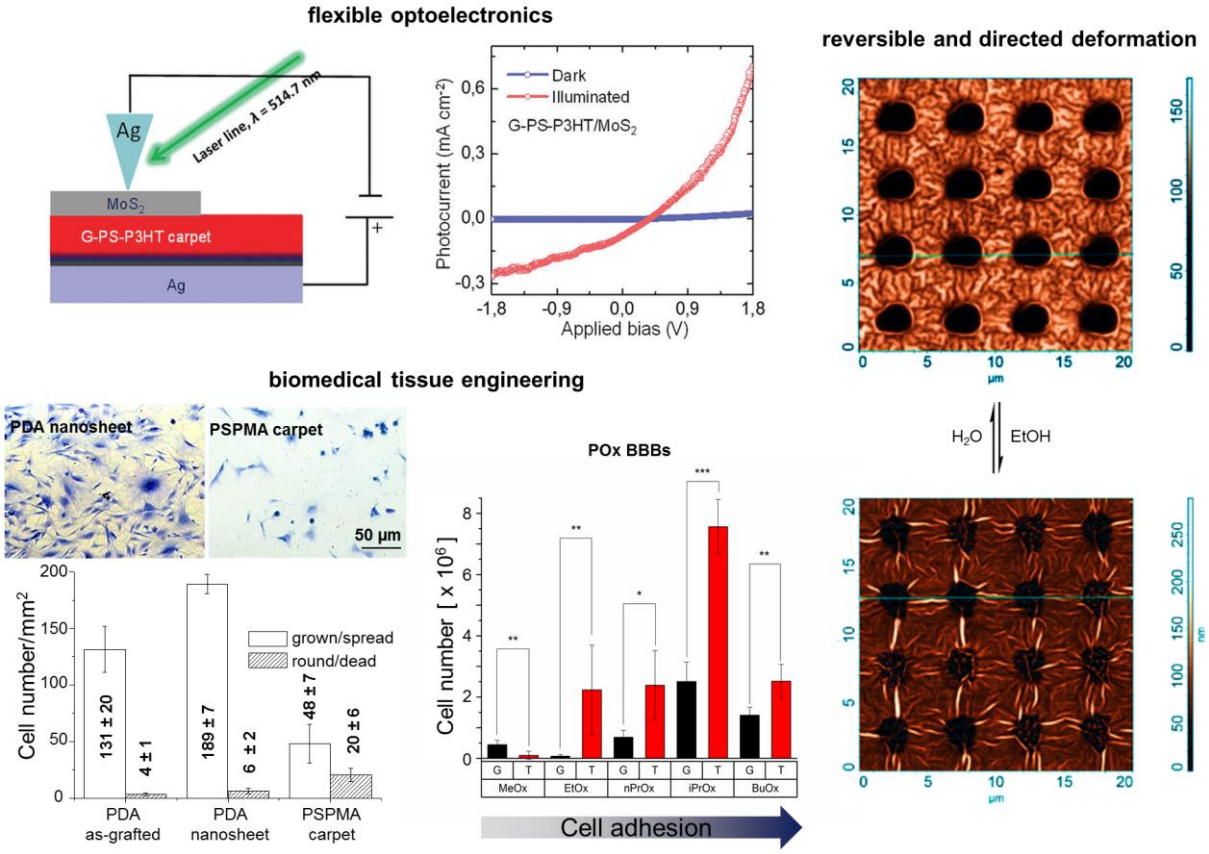

Figure 2.25: Applications making direct use of polymer carpets. Beside implementation in biosensors and optoelectronics, polymer carpets can be tailored as biomedical tissue to control cell adhesion. The soft and flexible nature enables fast, reversible and possibly directed deformation. Taken from Refs.[10,76,250] and modified.

The cooperative change of physical properties induced by variation of environment and resulting switch in morphology may become one of the most useful features of polymer carpets. As pointed out by Huck *et al.*, fast and collective response behavior can potentially add to the fundamental understanding of folding processes in nature.[241] Patterned polymer carpets exhibit defined and directed wrinkling due to anisotropic stress relief.[10] In addition, morphology can be reversibly changed in different solvents, pH or temperature, when stimuli-

responsive polymers like P4VP are used **(Fig. 2.25)**. Therefore, these systems could be ideal to study nanoscale folding in dependence of material stiffness, pattern size or external stimulus. Furthermore, microstructure bending was suggested to be suitable for tunable optical gratings, actuators or cell alignment.[252] Even electronic devices for directed response could be fabricated making use of the wrinkling profile. For example, silver nanoparticles can be immobilized and reduced within polymer brushes from DMAEMA.[81] If a patterned polymer carpet from DMAEMA is used as template, such deposition could be exploited to form a conductive layer directed by the arising wrinkles. Greco *et al.* demonstrated that such strongly wrinkled metallic surface possess higher and possibly unidirectional conductance.[253] Other applications profiting from complex buckling topologies were summarized by Rodríguez-Hernández *et al.* and include smart displays or windows, organic light-emitting diodes, electrochromic devices, solar cells or SERS.[254]

While some examples of polymer carpet integration and utilization exist, it can be concluded that their full potential is far from being exhausted. Especially, their ability to build complex surface topology and macroscopically change properties has not been exploited yet. An intriguing approach would be to capitalize on the wrinkling in the polymer carpet for precise deformation of the underlying 2D sheet. In other words, an efficient and switchable strain could be applied if the morphology transformation affects the 2D material. Following the principle of strain-engineering described in **chapter 2.3.2**, synthesis of polymer carpets from graphene might therefore induce band gap opening. Grafting of gradient or patterned polymer brushes could even allow for the tuning of optoelectronic properties on µm-scale in that case. Likewise, Janus-type polymer carpets could help to control or increase mismatch of mechanical properties and responsive behavior. Moreover, these Janus polymer carpets could become beneficial for implementations as described in **chapter 2.1.1**, since they can provide selective mass or charge transfer, improve contact and are highly sensitive due to the polymer brush layer. Along the way, the bottom-up tactic of SIP enables exact tailoring of polymer brush characteristics. Tuning compartment thickness or configuration of Janus polymer carpets in that manner can contribute to a better understanding of general transport processes within Janus membranes. Consequently, additional research in this area is still required and structural variety of polymer carpets needs to be broadened.

3. Motivation and Objectives

Surface-initiated polymerization (SIP) has become a popular approach for the synthesis of polymer grafts allowing for the introduction of chemical functionality, adjustment of wettability and surface energy or control of bioadhesion.[255,256] All types of polymerization have been adapted to this approach, since it ensures advantageous polymer brush conformation by high grafting density. In 2015, Zhang *et al.* presented a new method for grafting polymer brushes from surface that they termed surface-initiated Cu(0)-mediated controlled radical polymerization (SI-CuCRP).[14] In contrast to other approaches no copper halides or powders, but a Cu(0) plate fitting the geometrical demand of the substrate was used to catalyze reaction. As a result, they obtained the fastest surface-initiated controlled/living polymerization with highest grafting densities ever reported. It enabled synthesis of block copolymer brushes, defined patterns and gradients, polymer brush arrays as well as wafer-scale grafting with minimal amounts of reactants.[12,14] As a high potential method, SI-CuCRP can be also exploited for synthesis of polymer carpets from poly(dopamine) (PDA) and graphene to pave the way for Janus membrane fabrication and effective strain-engineering.

The first part of this work aims to extend on the possibilities of surface modification and material synthesis by merging SI-CuCRP and mussel-inspired PDA surface chemistry **(Fig. 3.1)**. The outstanding adhesive properties of PDA label it an universal mediating agent for surface polymerization, as deposition is possible on any kind of surface.[145,146,148–153] Therefore, combination of both methods can allow for controlled functionalization of various substrates independent of its original surface properties.

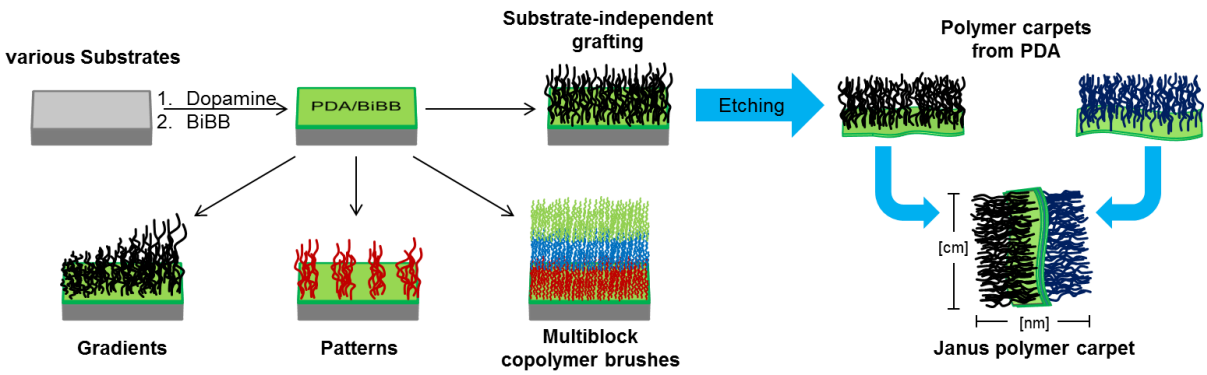

Figure 3.1: Schematic illustration of the synthetic goals to be achieved with SI-CuCRP on PDA surfaces. After deposition of PDA and conversion with Br-initiator (BiBB) different surfaces can be controllably functionalized with polymer brushes. Etching of substrate enables fabrication of polymer carpets and Janus membranes (Janus polymer carpets).

For that, it has to be proven that PDA does not limit control of SI-CuCRP due to its partly radical character. Hence, a comparison of grafting on typical SI-CuCRP initiator and PDA-bound initiator has to be carried out. In addition, it is aimed to synthesize block copolymer brushes to demonstrate the level of control achievable with SI-CuCRP on PDA.

Furthermore, use of PDA should enable the fabrication of Janus membranes holding different properties at two distinct sides. As published by Amin *et al.*, PDA retains lateral integrity upon detachment from substrate to give nanosheets and polymer carpets, which consist of a thin cross-linked PDA scaffold exposing polymer brushes.[76,147] Once these polymer carpets are transferred onto another support, they can robustly adhere again due to the nature of PDA. It is obvious that PDA will just as strongly attach to itself, when two of such freestanding structures are combined **(Fig. 3.1)**. In another approach, the functional groups within the PDA should also enable grafting of a second polymer brush from the other side of the polymer carpet. The resulting Janus polymer carpets will exhibit thicknesses of nanometers while being centimeters in lateral size. SI-CuCRP can ensure synthesis of polymer brushes with well-defined architecture for high sensitivity and responsivity in possible applications of the resulting membrane.[14] It also will open the door to the fabrication of various patterned Janus polymer carpets, since simple photolithographic process can be applied. Ultimately, a general and sizeable method should be attained for precise tailoring of surface properties and novel 2D Janus materials for side-selective and directional chemistry.

In the second part of this work the received SIP method will be used for modification and strain-engineering of single layer graphene **(Fig. 3.2)**. Due to its high flexibility, transparency and high charge carrier mobility, graphene is often regarded as the future material of optoelectronics. However, the absence of an electronic band gap makes integration into control and switching devices impossible. While theoretical calculations show that application of strain (ε) effectively modulates electronic structure to induce band gap opening, the practical realization of such "strain-engineering" remains a big challenge. Most reported approaches do not reach over 3 % of strain for graphene or other 2D materials.[209,212,213,257] Polymer brushes on the other hand might bear the potential to accomplish higher values by inducing chemo-mechanical force because of high grafting density (σ). As observed by Zhang *et al.* synthesis of thick and dense polymer brushes *via* SI-CuCRP leads to partial degrafting from rigid SiO_2 due to strong steric repulsion between the polymer chains.[12] Contrary, Amin *et al.* observed pronounced wrinkling (AFM in **Fig. 3.2**) upon synthesis of polymer carpets from flexible precursor, which can be assigned to compensation of lateral stress caused by grafting and subsequent washing procedure.[9,10] Polymer carpets from

4-vinylpyridine (4VP) even offered the option of reversible buckling. A major breakthrough in strain- and band gap-engineering will be achieved if similar behavior can be observed after synthesis of graphene based polymer carpets. As strain threshold values (16 % - 20 %)[20] can be overcome, new paths of material design will open and graphene integration into optoelectronic devices, sensors or transistors will become feasible.

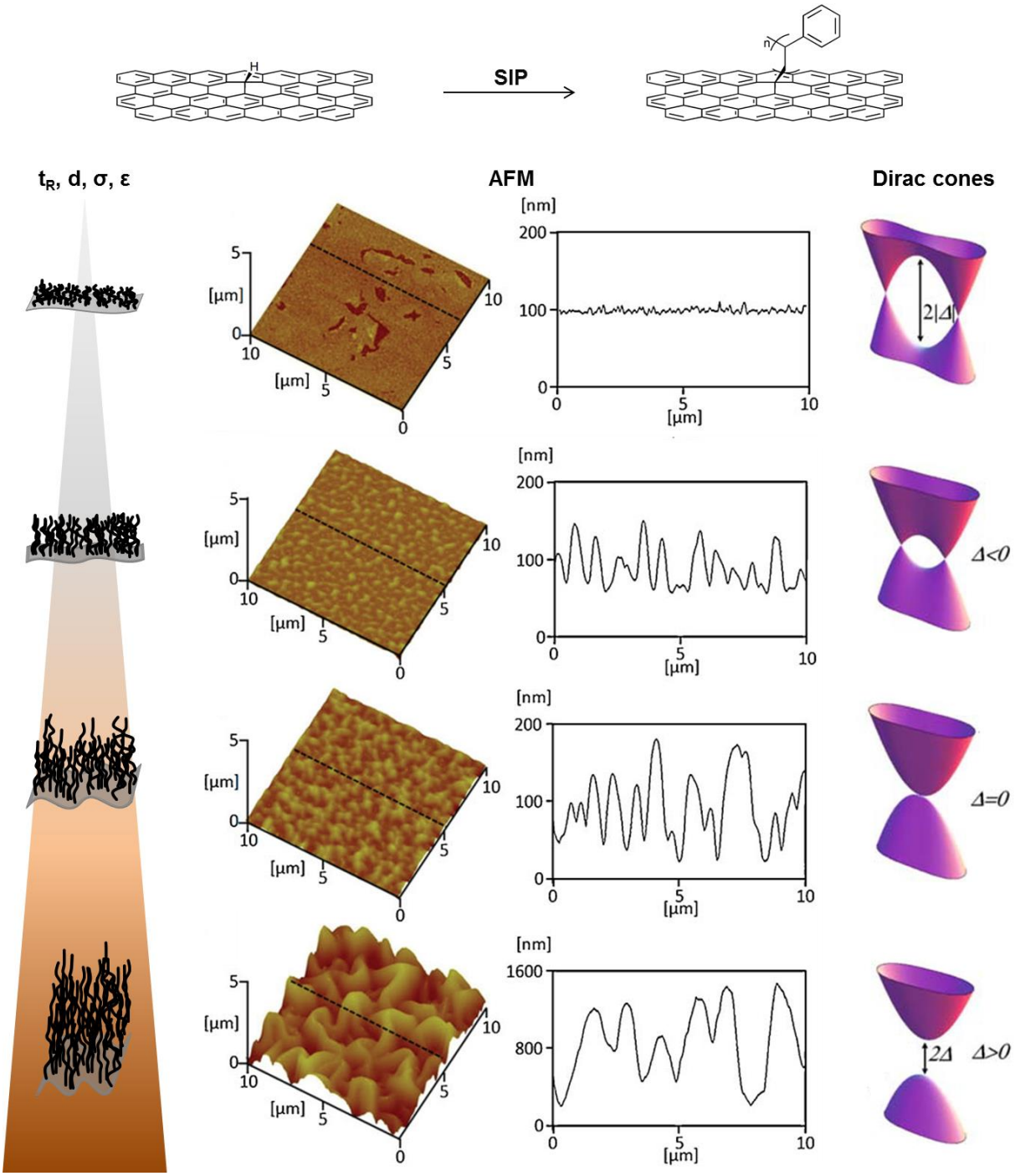

Figure 3.2: Schematic illustration of strain- and band gap engineering in graphene by SIP. When reaction time (t_R) is prolonged polymer brush thickness (d) and grafting density (σ) rise and result in strong steric repulsion. Thus, strain (ε) is chemo-mechanically induced causing deformation in the graphene sheet and shift of Dirac cones in the energetic structure. As they start merging, a band gap opens. Pictures are taken from Refs.[9,193] and modified.

4. Results and Discussion

4.1 Surface-initiated Cu(0)-mediated controlled radical polymerization on poly(dopamine) modified surface

As surface-initiated Cu(0)-mediated controlled radical polymerization (SI-CuCRP) was never before performed on poly(dopamine) (PDA) surface, a series of experiments were dedicated to establish the combination of both as a versatile method for surface modification. Starting from PDA deposition, substrates were prepared for further polymerization steps by subsequent binding of initiator. Then, SI-CuCRP was performed to graft polymer brushes on SiO_2 and several other substrates to exploit PDA chemistry. Furthermore, grafting of block copolymer brushes was accomplished to demonstrate the method´s robustness.

4.1.1 Synthesis of initiating layer

PDA was deposited on a silicon wafer (SiO_2 300 nm) in a previously reported manner by placing the substrate into a freshly prepared solution of dopamine in 10 mM trishydroxymethyl aminomethane/HCl buffer (Tris/HCl, pH = 8.5).[76] Then, 2-bromoisobutyryl bromide (BiBB), a typical initiator for atom transfer radical polymerization (ATRP), was reacted with the PDA layer following the procedure of Zhang *et al.* to give PDA/BiBB **(Fig. 4.1)**.[14] For comparison initiator was also bound to 3-aminopropyltriethoxysilane (APTES) to give APTES-BiBB. Immobilization of APTES on the SiO_2 wafer was realized by ultrasonication of a 5 % solution in acetone.

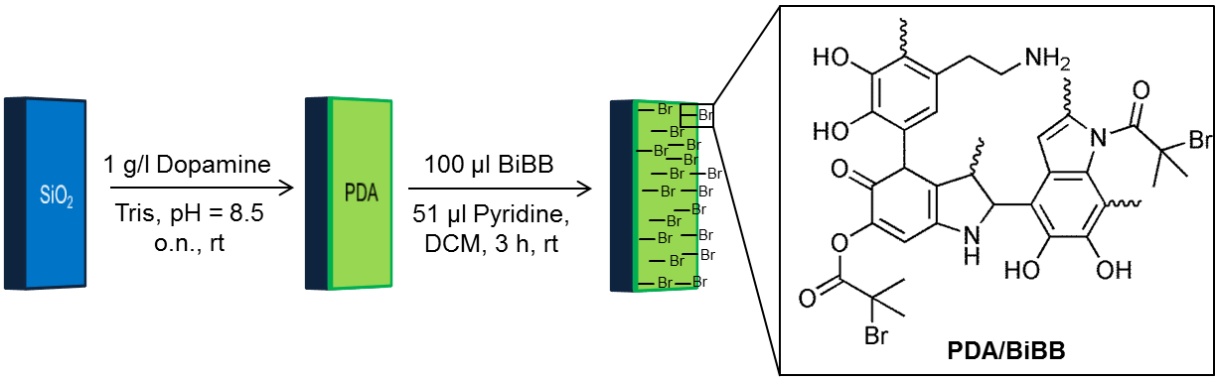

Figure 4.1: Schematic illustration of the synthesis route to PDA/BiBB. After PDA deposition the initiating Br-groups are bound to the surface *via* conversion with BiBB. Amino- and hydroxyl groups offer binding sites for the reaction. APTES-BiBB was synthesized analogously.

Successful conversion of PDA and APTES surface with BiBB was confirmed by the change of static water contact angle (θ_S) from 36 - 45° for PDA to 63 - 68° for PDA/BiBB and from 50 - 55° for APTES to 68° for APTES-BiBB **(Tab. 4.1)**. These values are in good agreement with values in literature.[14,76]

Table 4.1: Surface characteristics before and after modification of SiO_2 substrates. Formation of SAM, PDA and subsequent conversion with BiBB lead to change of θ_S, representing the respective functional group exposed at the surface.

Surface	$d_{ellipsometry}$ [nm]	d_{AFM} [nm]	θ_S [°]
SiO_2	270 - 310	-	< 10
APTES	1 - 2	-	50 - 55
APTES-BiBB	~ 2	-	68
PDA	20 - 35	20 - 35	36 - 40
PDA/BiBB	20 - 35	20 - 35	63 - 68

The ellipsometrically determined thickness (d) of APTES-BiBB and PDA/BiBB typically lay at ~ 2 nm and 20-35 nm, respectively. Neither ellipsometry nor atomic force microscopy (AFM) showed significant change of thickness or surface roughness (root mean square, RMS = 1 - 2 nm) for PDA samples after conversion with BiBB. Considering that the PDA layer thickness is already over 20 times higher than an additional BiBB layer this observation is expected. Even if little swelling might occur because of BiBB diffusion into the porous PDA, the effect is negligible, since the process is probably limited by the sterically demanding tertiary carbon.

Furthermore, X-ray photoelectron spectroscopy (XPS, **Fig. 4.2**) was performed on both APTES-BiBB and PDA/BiBB. Besides the expected peaks of oxygen, nitrogen and carbon on both samples a weak Br 3d signal is detected on APTES-BiBB at a binding energy of 69.0 eV.[258] The low intensity can be explained with a gradual loss of bromine during the measurements due to the continuous exposure of energy. Additionally, three carbon species can be distinguished and assigned to C-C, C-N/C-Br and C=O at a binding energy of 284.6 eV, 286.0 eV and 288.3 eV, respectively.[12,258] Similarly, a peak originating from Br appears at 70 eV for PDA/BiBB.[12,258] Furthermore, the signals of C-C, C-N/C-Br and C=O can also be found at 284.7 eV, 286.2 eV and 288.1 eV, respectively.

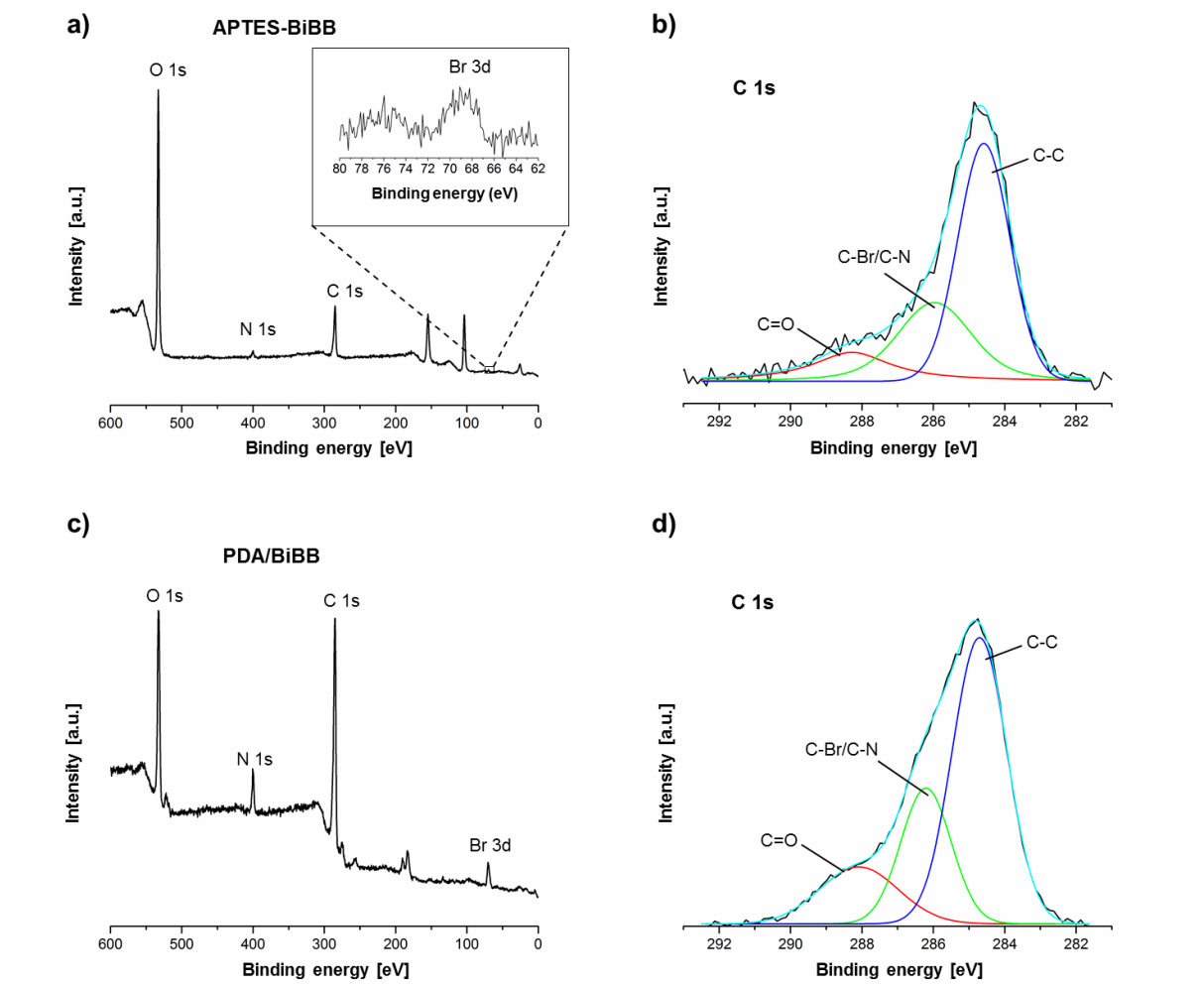

Figure 4.2: XPS spectra of initiator modified SiO_2: APTES-BiBB (a) and its core-level spectrum (b). PDA/BiBB (c) and its core-level spectrum (d). Appearance of a Br 3d signal can be seen in the spectra of both samples.

All in all, the data clearly prove the binding of bromine initiator to both APTES and PDA modified SiO_2. Especially, this procedure proved to be advantageous in comparison to the method reported by Edmondson *et al.*, where dopamine is reacted with BiBB in the first step and deposition is carried out directly afterwards.[259] While that provides the possibility of a one-pot reaction, the so fabricated initiating layers are comparably thin (1 - 10 nm). Most importantly, very inhomogeneous layers are formed with thickness reaching up to 30 nm at single spots in samples with a mean layer height of ca. 3 nm. Additionally, not all dopamine molecules converted with BiBB will be incorporated into the deposited layer. Thereby initiating efficiency and SI-CuCRP is negatively affected. Consequently, it is no surprise that subsequent polymerization yields equally heterogeneous polymer brushes and hardly reproducible results. This approach of initiator binding was therefore not further used and the protocol described in **Figure 4.1** was applied throughout the entire work.

4.1.2 SI-CuCRP on PDA/BiBB

First, a series of monomers (methacrylates and styrene) were grafted on an initiator bearing surface *via* SI-CuCRP **(Fig. 4.3)**. The substrate was covered with a copper plate at a distance D of 0.5 mm and immersed into a degassed solution of monomer, solvent and ligand (1,1,4,7,7-pentamethyldiethylendiamine, PMDETA) at room temperature. Analogously, SI-CuCRP was carried out on APTES-BiBB.

Figure 4.3: Schematic illustration of the synthesis of polymer brushes on PDA/BiBB *via* SI-CuCRP. A Cu(0)-surface is clamped at a distance D = 0.5 mm over the PDA/BiBB substrate and the assembly is immersed into degassed reaction solution.

After SI-CuCRP the resulting polymer brushes were analyzed with ellipsometry and contact angle measurements. All polymer brushes exhibit a typical contact angle **(Tab. 4.2)** showing the successful grafting of each monomer on both APTES-BiBB and PDA/BiBB. Considering that reaction time (t_R) did not exceed 1 h **(Tab. 4.2)**, remarkable brush thicknesses were reached with every monomer.

Table 4.2: Results of SI-CuCRP of different monomers on modified SiO_2. Ligand: PMDETA; monomers: 2-hydroxyethyl methacrylate (HEMA), N,N-dimethylaminoethyl methacrylate (DMAEMA), methyl methacrylate (MMA), tert-butyl methacrylate (tBMA), styrene (St). The values of d represent the respectively obtained polymer brush thickness.

Monomer	Solvent	t_R[min]	APTES		PDA	
			d [nm]	θ_s [°]	d [nm]	θ_s [°]
HEMA	H_2O	60	238 ± 15	52 ± 3	250 ± 20	56 ± 2
DMAEMA	10%(v/v)-H_2O in iPrOH	60	58 ± 6	58 ± 5	45 ± 5	59 ± 5
MMA	DMSO	60	127 ± 10	69 ± 2	79 ± 5	68 ± 4
St	DMSO	60	25 ± 5	90 ± 1	29 ± 6	87 ± 2
tBMA	DMSO	20	41 ± 8	95 ± 6	51 ± 5	101 ± 2

Especially hydrophilic monomers reacted with high rates reaching up to 250 nm for poly(2-hydroxyethyl methacrylate) (PHEMA) after only 60 minutes of reaction. Even with only small amounts of water in otherwise unsuited solvent isopropanol (iPrOH), thicknesses

of 58 nm and 45 nm were achieved for poly(N,N-dimethylaminoethyl methacrylate) (PDMAEMA). Hydrophobic monomers display slower growth of polymer brush. These results are not very surprising, as radical polymerizations in the presence of Cu(0) are known to proceed faster in H_2O than in dimethyl sulfoxide (DMSO).[129,260] However, styrene was still polymerizable in DMSO and reached a polymer brush height of around 25-30 nm after 60 minutes. Furthermore, it is remarkable that for tert-butyl methacrylate (tBMA) thicknesses of 41 nm and 51 nm were reached even after reducing reaction time to 20 minutes.

Motivated by this results a macromonomer of poly(2-methyl-2-oxazoline) (PMeOx) end-functionalized with methacrylic acid (PMeOx-MAA) was grafted using SI-CuCRP **(Fig. 4.4 a)**. Such grafting through approach allows for the synthesis of poly(2-oxazoline) (POx) bottle-brush brushes (BBBs) with highly crowded side-chains and thereby prolonged polymeric backbones and high density of functional groups.

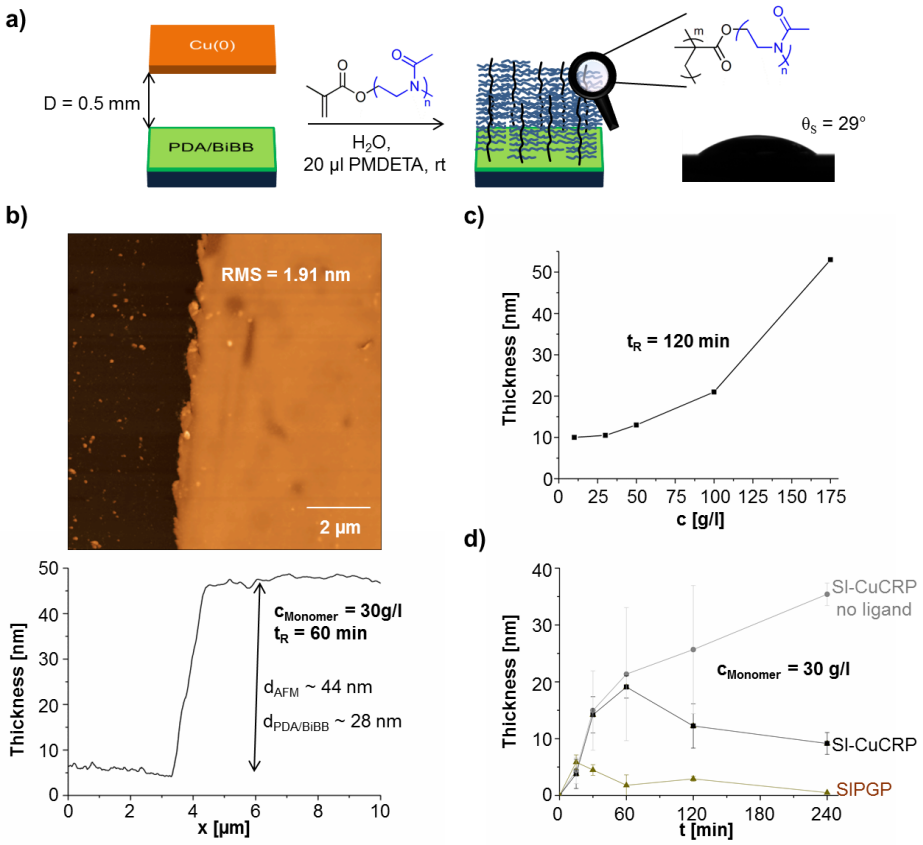

Figure 4.4: Schematic illustration of PMeOx BBB synthesis by SI-CuCRP (a). Besides hydrophilic θ_S, the BBBs have smooth surface as displayed in AFM of a sample polymerized for 1 h (b). The grafting rate is strongly dependent on concentration (c) and polymerization time (d).

UV-induced polymerization, i.e. self-initiated photografting and photopolymerization (SIPGP), did not provide satisfying layer thickness in earlier experiments **(Fig. 4.4 d)**. With

SI-CuCRP ca. 20 nm PMeOx BBBs can be synthesized within 1 h using a concentration of 30 g/l of monomer. This means an almost threefold increase in comparison to the highest thickness achieved by SIPGP (~ 6 nm, **Fig. 4.4 d**). The main reason for this difference lays in the grafting efficiency of the SI-CuCRP and the fact that polymerization is restricted to the initiator bearing substrate. In contrast, SIPGP leads to polymerization in solution consuming monomer, increasing viscosity and hence decreasing PMeOx-MAA accessibility by hindering its diffusion to the substrate. Therefore, it was suspected that concentration increase during SI-CuCRP might analogously affect grafting, because viscosity strongly increases, when high amounts of macromonomer are dissolved in water. Contrary, thicker BBBs were achieved by use of higher concentration of macromonomer in water reaching up to 53 nm at 175 g/l and 2 h of reaction **(Fig. 4.4 c)**. It seems that diffusion of activating Cu-species is not hindered by the viscosity increase and accessibility of PMeOx-MAA is enhanced by the higher concentration. Furthermore, the macromonomer contains nitrogen which can act as electron donor and can be therefore regarded as a polydentate N-ligand. Thus, a high amount of PMeOx-MAA could even facilitate the dissolution, stabilization and transport of different Cu-species. To test this hypothesis SI-CuCRP was carried out without addition of PMDETA (c = 30 g/l). As result, grafting of PMeOx BBBs is successful and even more efficient (ca. 25 nm and 35 nm after 2 h and 4 h, respectively, **Fig. 4.4 d**). It is obvious that the macromonomer is acting as ligand in SI-CuCRP. Still, a final conclusion whether it is actually beneficial for the grafting rate cannot be drawn because of the low number of samples (two for every experiment), different reaction profiles and great error bars for samples without PMDETA. Additionally, a slight decrease in thickness can be observed, when polymerization time is longer than 1 h for SI-CuCRP with use of PMDETA. This growth pattern can be explained by a relatively fast polymerization and grafting of the PMeOx-MAA resulting in thick BBBs. Strong steric repulsion is caused by the high grafting density of polymeric side-chains, which might lead to detachment of the bottle-brushes similar to the observations of Jordan and coworkers.[12] That would mean higher BBB thickness is obtained because height was not sufficient enough to induce degrafting or rupture within the time frame of polymerization. Therefore, lack of ligand and high viscosity (i.e. high concentration) decrease grafting rate. At this point, it cannot be concluded which of the assumptions is correct. Anyhow, SI-CuCRP proves to be suitable to directly graft monomers with more complex architecture (PMeOx-MAA) on PDA/BiBB, which so far was not possible with SIPGP.

Eventually, patterned and gradient polymer brushes were synthesized **(Fig. 4.5)**. As outlined by Tao *et al*. and Dehghani *et al*. the distance of the Cu(0)-plate to the substrate plays a key

role for the polymerization rate and the grafting density of the resulting polymer brush.[14,144] Therefore, a gradient in brush thickness can be obtained by tilting the copper plate relative to the initiator surface **(Fig. 4.5 a)**. In that way a gradient poly(methyl methacrylate) (PMMA) brush was synthesized on PDA/BiBB with optical thickness ranging from 52 - 79 nm over a substrate length L of 1.5 cm **(Fig. 4.5 c)**. Similar to the finding of Tao *et al*. an off-leveling in brush height can be observed at a Cu(0)-plate distance of ca. 0.6 mm. This kind of profile is expected from the literature and arises mostly because of a grafting density gradient.[144]

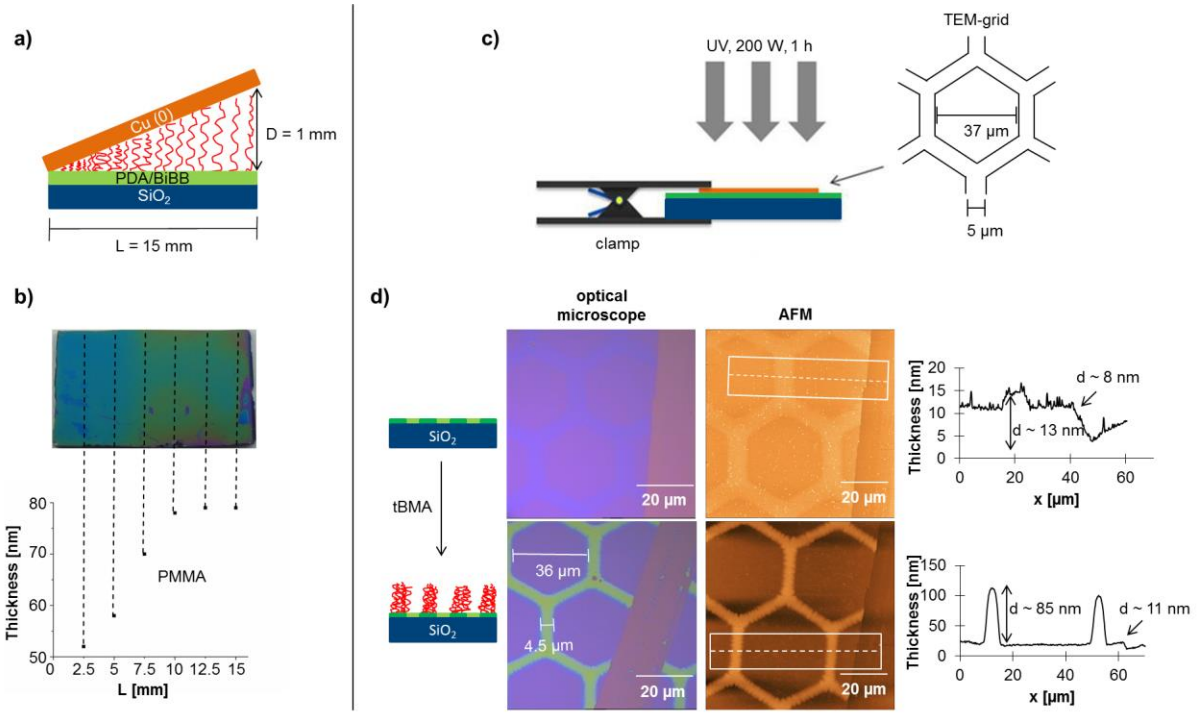

Figure 4.5: Schematic illustration of the synthesis of gradient (a, b) and patterned (c, d) polymer brushes on PDA/BiBB *via* SI-CuCRP. A slope in the Cu(0) distance D from 0 to 0.5 mm leads to a thickness gradient in the PMMA brush (c). Selective UV induced cleavage of Br through a photomask (TEM-grid) leads to well-defined polymer brushes with pattern of the used photomask after SI-CuCRP (d).

Dehghani and coworkers detected a higher concentration of Cu(I) species on the substrate, when the used Cu(0) plate was close to the surface in aqueous solution.[144] Following the SARA ATRP mechanism, they conclude that correlating to the Cu(I) concentration and huge ATRP equilibrium constant a high amount of radicals is present in these areas. As only low control of ATRP process can be achieved in water without addition of salts, a low local concentration of deactivating Cu(II) complex will therefore lead to a high degree of termination. This explains why grafting density is low at a short distance D and thicker brushes can be obtained, when the copper plate is placed further away from the substrate. On

the other hand, SET-LRP mechanism might explain the observed results by a low concentration of "nascent" Cu(0) particles in close distance to the substrate. Since Cu(0) is the main activator in SET-LRP, this would lead to a slow polymerization rate and inefficient initiation. However, it should be kept in mind that the activation and polymerization also could proceed differently depending on used solvents.[139,140] Thus, the gradient formation mechanism might be different for systems in aqueous and organic media.

Finally, a patterned sample was prepared by selectively cleaving Br from PDA/BiBB by UV-light and subsequent SI-CuCRP. As photomask a transmission electron microscopy grid (TEM-grid) was placed on the initiator surface and fixed with a clamp **(Fig. 4.5 b)**. After UV exposure (200 W, 1 h), AFM scans revealed a slight decrease in thickness of ca. 5 nm for the uncovered areas **(Fig. 4.5 d)**. In regard to the high intensity and exposure time this result demonstrates the robust nature of PDA, as the PDA/BiBB layer is only partly destroyed by the UV-light. Furthermore, additional UV-induced cross-linking within PDA might lead to shrinking of the layer. More importantly, SI-CuCRP on the so prepared substrate resulted in polymer brush growth only in the previously covered regions giving the expected pattern of the used TEM-grid. This proves that polymerization is limited to areas with still bound initiating moieties and patterning can be achieved by well-known photolithographic process.

It is of particular interest that all these results of SI-CuCRP are similar for both surface-bound initiator systems making PDA/BiBB an alternative to the common APTES-BiBB without restriction of polymerization and providing new options for surface modification.

4.1.3 Polymer brush synthesis on different substrates

As PDA is well known for its strong adhesion on any kind of substrates, SI-CuCRP can be exploited to graft polymer brushes on different surfaces in a facile, fast and controlled way. Therefore, polymerization was carried out on several substrates including metals (Au, Cu), oxides (Al/Al_2O_3, SiO_2) and repellent organic surface (PTFE) **(Fig. 4.6)**.

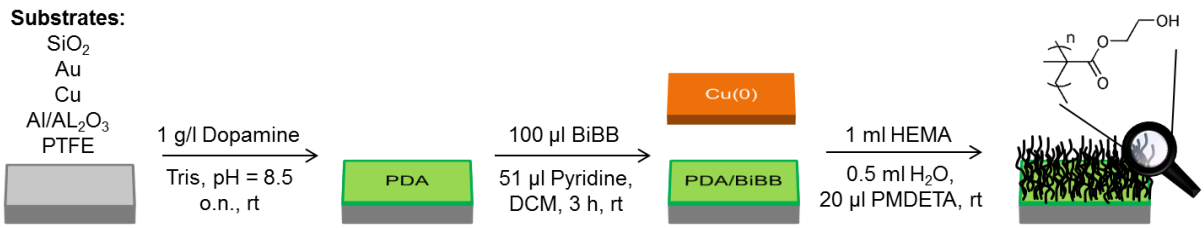

Figure 4.6: Schematic illustration of the synthesis of polymer brushes on different substrates *via* SI-CuCRP. After deposition of PDA on each substrate the surface is functionalized with BiBB and SI-CuCRP of HEMA is performed.

The experimental procedure remained as described above. However, reaction time was decreased to 15-30 minutes since the used monomer (HEMA) showed high polymerization rates.

The grafting of PHEMA on the different substrates was confirmed by contact angle measurements and Fourier transform infrared spectroscopy (FT-IR). While static contact angles **(Fig. 4.7)** ranged from very hydrophilic (SiO_2, $\theta_S < 10°$) to very hydrophobic (PTFE, $\theta_S = 112°$) for the pure substrates, it changed strongly upon deposition of PDA ($\theta_S = 29 - 42°$) and subsequent conversion with BiBB ($\theta_S = 68 - 74°$) indicating successful modification on all substrates. After SI-CuCRP typical θ_S for PHEMA was observed on every surface exhibiting similar value of 54° and 57° on Al/Al_2O_3 and Cu, respectively **(Fig. 4.7)**. SiO_2 and gold both had a contact angle of 51° after SI-CuCRP.

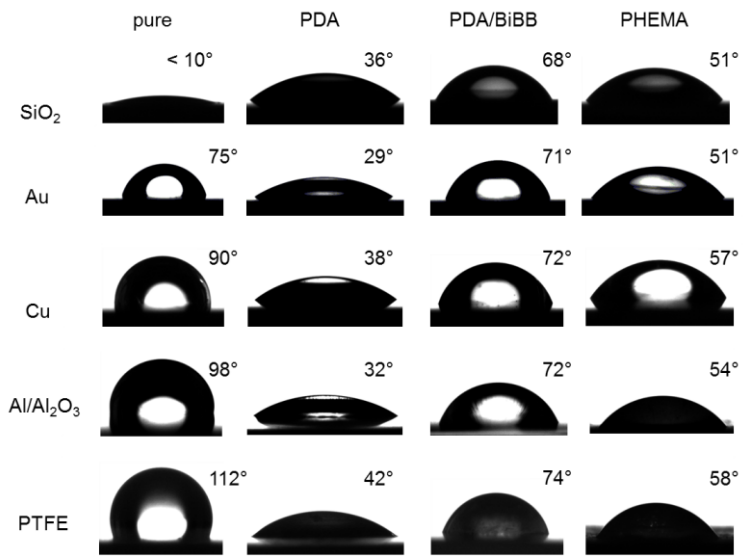

Figure 4.7: Photographs of static water contact angle on pure substrate and substrates grafted with PDA, PDA/BiBB and PEHMA. Each substrate can be modified and exhibits the typical θ_S value for the respective layer after each modification step.

Interestingly, while polymerization worked well on every surface, binding of BiBB on PDA grafted PTFE led to a successive destruction of the PDA layer within 1 hour. This was not observed on the other substrates. After all, it seems that adhesion of PDA on PTFE is not as robust as expected, so that reaction time had to be reduced to 20 minutes. Still, subsequent polymerization of HEMA decreased the contact angle to 58° due to the hydrophilicity of the resulting polymer brush on the PTFE substrate. It is necessary to point out that the functionalization of PDA with initiator on PTFE is the only occasion, where destruction of PDA was observed. No indication of PDA weakness was observed after polymerization even

after grafting multiple blocks of polymers up to 270 nm (see **chapter 4.1.4**). A partial destruction of PDA would lead to a sudden decrease of thickness after grafting due to rupture of polymer brushes. However, such behavior was never detected. As reported by Jordan et al., even small amount of polymer chain detachment could be otherwise seen in the AFM.[12]
Moreover, FT-IR spectra taken after surface polymerization clearly display successful functionalization of PTFE **(Fig. 4.8)**. Although signals of C-F stretching (1100-1300 cm^{-1}) originating from the substrate are dominating the spectrum **(Fig. 4.8 e)**, a broad signal of O-H stretching from PHEMA can be observed between 3680 cm^{-1} and 3050 cm^{-1} **(Fig. 4.8)**. In addition, vibrations of the polymeric backbone, i.e. ν_{as} (CH_2, CH_3) at 2946 cm^{-1}, ν_s (CH_2, CH_3) at 2884 cm^{-1} and δ (CH_2) at 1468 cm^{-1}, as well as characteristic stretching of the ester group, i.e. ν (C=O) at 1722 cm^{-1} and ν (C-O-C) at 1080 cm^{-1}, are visible.

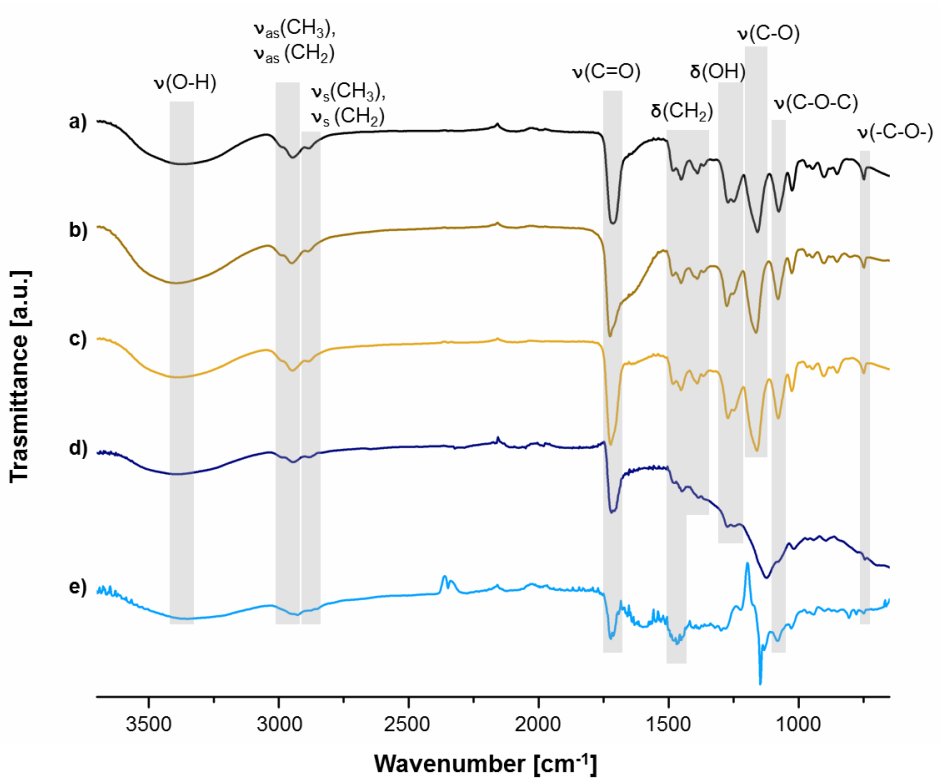

Figure 4.8: FT-IR spectra of PHEMA on Al/Al_2O_3 (a), Cu (b), Au (c), SiO_2 (d) and PTFE (e). All samples display characteristic PHEMA vibrations after immobilization of PDA/BiBB and following SI-CuCRP.

Same signals prove the grafting of PHEMA on the other substrates **(Fig. 4.8 a-d)**. Furthermore, additional signals of OH deformation (1276 - 1248 cm^{-1}), twisting and rocking of CH_2 (1389 - 1365 cm^{-1}) and several stretching vibrations of C-O bonds were detected. Stretching of Si-O-Si is very prominent in the spectrum of PHEMA on SiO_2 at 1122 cm^{-1} **(Fig. 4.8 d)** even though the same kind of surface was used as background. However, all

signals mentioned above can still be distinguished. Therefore, it is evident that grafting of PHEMA was accomplished on all used substrates.

Following the same protocol even natural membranes, i.e. egg shell membrane as well as skin from pomelo fruit and onions, can be functionalized with polymer brushes **(Fig. 4.9)**. For example, egg shell membrane is a natural biomaterial composed of collagens that is biocompatible because of its similarity to native extracellular matrix.[261] It was shown to promote wound healing[262], wound protection and pain relief[263]. Blending with poly(urethane) was applied for wound dressing[264], while hydrolyzed membranes on phosphorylcholine polymer provided an extracellular matrix environment for adhesion and growth of human dermal fibroblasts[265]. Therefore, a combination of such biomaterials with polymer brushes could become highly interesting for biomedical application. Due to the rough and soft nature of the membranes, neither height determination nor wettability experiments could be performed after deposition of PDA and following reactions. Still, it can be seen by bare eye that a brown film builds on the membranes after deposition of PDA **(Fig. 4.9 a)**.

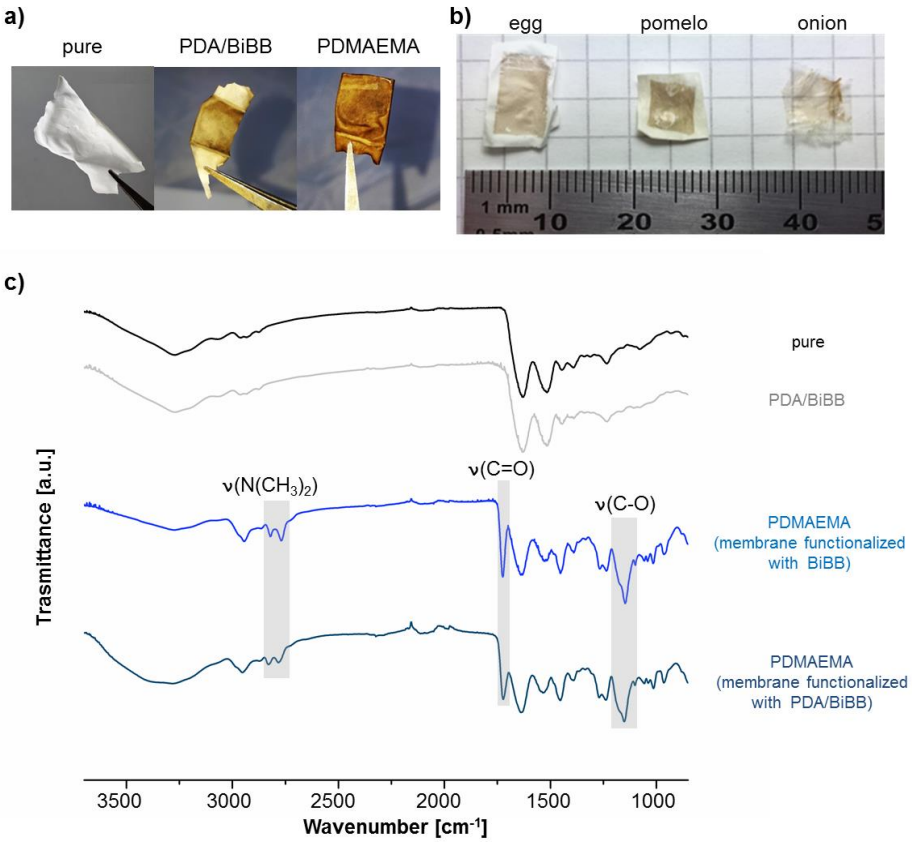

Figure 4.9: Photographs (a) and FT-IR spectra (c) of egg shell membranes functionalized with PDA/BiBB and PDMAEMA brushes. Signal appearance of ester stretching and amino group proves the successful grafting of the polymer even without use of PDA layer. Transfer of PDMAEMA carpets enables functionalization of natural membranes without modifying its chemical structure (b).

Besides that, FT-IR signals arising from stretching of the ester group (1724 cm^{-1}, 1147 cm^{-1}) and amino group (2820 cm^{-1}, 2769 cm^{-1}) are detected after SI-CuCRP of DMAEMA **(Fig. 4.9 c)**. Hence, it can be concluded that the experimental set-up is suited for modification of such biological systems. However, use of PDA is not obligatory in that case. Since the proteins in the membranes already possess amino acids which can be directly functionalized with initiator, polymerization was also feasible without prior deposition of dopamine **(Fig. 4.9 c)**. On the other hand, a PDA based system provides the option of transferring readily synthesized and defined polymer brushes onto the biomaterial **(Fig. 4.9 b)**. This approach not only enables thorough characterization of the polymer brush, but also functionalization of the membranes surface without affecting its chemical structure. In addition, denaturation due to solvent treatment is minimized.

In conclusion, combination of SI-CuCRP and PDA chemistry offers a general method for controlled polymerization on all kind of surface including noble metal (Au) as well as repellent, unreactive surface (PTFE) and natural membranes (e.g. egg shell membrane).

4.1.4 Grafting block copolymer on surface

To demonstrate the high end group fidelity of SI-CuCRP on PDA modified surface grafting of block copolymer brushes was carried out **(Fig. 4.10)**. A silicon surface was chosen as model substrate and functionalized with PDA/BiBB as described above. Then, the polymerization procedure was performed and the resulting polymer brush was washed and dried. Subsequently, another layer of polymer was grafted *via* SI-CuCRP on the same sample. The whole process was repeated several times without further functionalization with initiator between polymerizations.

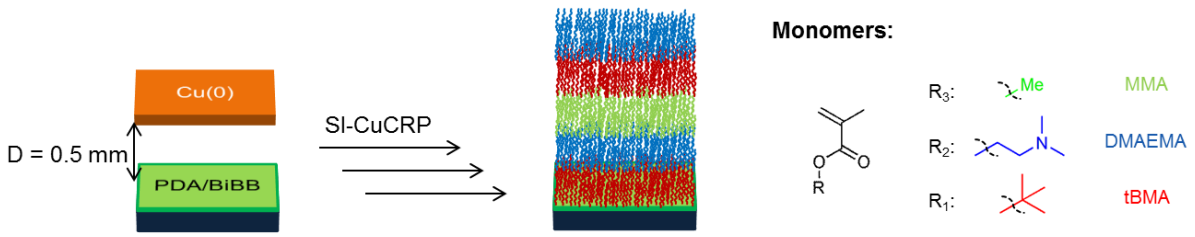

Figure 4.10: Schematic illustration of the synthesis of block copolymer brushes on PDA/BiBB *via* SI-CuCRP. A Cu(0)-surface is clamped at a distance D = 0.5 mm over the PDA/BiBB substrate and the assembly is immersed into degassed reaction solution. After reaction the sample is washed and SI-CuCRP is repeated several times.

As can be seen in **Table 4.3** a five block copolymer brush was synthesized with alternating hydrophilic and hydrophobic blocks. The first block of poly(tert-butyl methacrylate) (PtBMA)

gave a comparable brush thickness as in previous experiments **(Tab. 4.3)** and a contact angle of 96° owing to its hydrophobic nature. Before polymerizations a double scratch was made on the PDA/BiBB layer so that AFM scans could always be measured at the same spot.

Table 4.3: Results of block copolymerization on PDA/BiBB modified SiO_2 by SI-CuCRP. Ligand: PMDETA.

Block	Monomer	Solvent	t_R [min]	d_{Block} [nm]	θ_s [°]
1	tBMA	DMSO	15	46 ± 1	96 ± 4
2	DMAEMA	10%(v/v) H_2O in iPrOH	15	11 ± 2	52 ± 5
3	MMA	DMSO	20	61 ± 4	61 ± 7
4	tBMA	DMSO	25	52 ± 7	100 ± 5
5	DMAEMA	10%(v/v) H_2O in iPrOH	25	86 ± 12	76 ± 8

After the following polymerization of DMAEMA a height increase of 11 nm was detected **(Fig. 4.11)**. The static contact angle dropped to 52° **(Fig. 4.11)**. Analogously, PMMA and further layers of PtBMA and PDMAEMA were grafted resulting in consecutive brush growth and exhibiting 61°, 100° and 76° for θ_s, respectively.

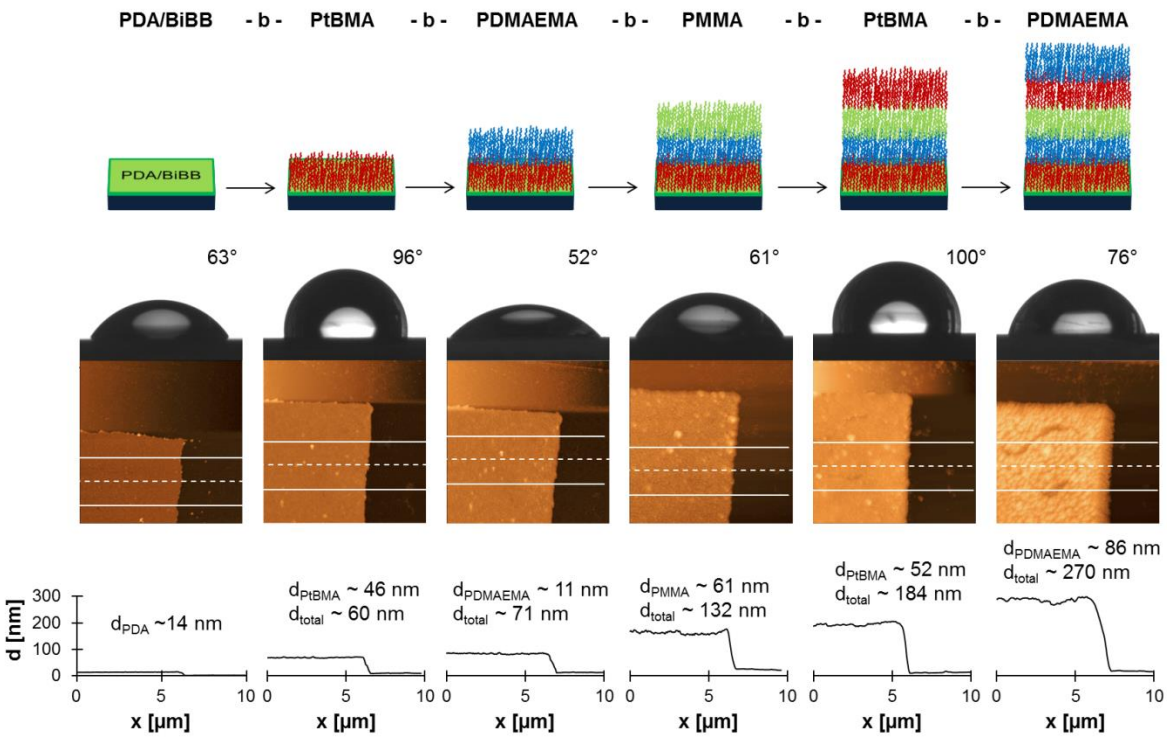

Figure 4.11: Block copolymerization of different monomers: development of contact angle depending on polymer brush (top) and the corresponding AFM image (below) with respective profile (bottom). AFM images are 10 x 10 μm^2.

Since the grafting of the second block (PDMAEMA) resulted in a thickness gain of only 11 nm, the polymerization time of following polymerizations was prolonged for 5 min or 10 min. This resulted in sufficiently higher thickness increases of 61 nm for PMMA, 52 nm for PtBMA and 86 nm for another layer of PDMAEMA **(Fig. 4.11)**.

All these values confirm successful polymerization of the used monomers. As all contact angles match to the respective polymer brush, it can be concluded that each polymerization step results in an extra layer of polymer rather than in a system with mixed polymer brushes on surface. In case of mixed (not block-like) brushes a value resembling both brushes would be expected. For a hydrophobic/hydrophilic brush mixture, the hydrophobic brush will collapse and the contact angle will represent the hydrophilic layer. This is not the case in our results. The slightly higher θ_s for the last PDMAEMA block ($\boldsymbol{\theta_s}$ = 76°) can be explained by enhanced surface roughness, as can be seen from the higher deviation from the mean thickness (**Tab. 4.3**). Therefore, it can be assumed that a block-like structure is attained.

Furthermore, this explains the stepwise increase of the polymer brush from 60 nm after the first SI-CuCRP to 270 nm after the last step. Such a gain in thickness as well as height increase after each polymerization (52-86 nm, **Fig. 4.11**) is unlikely to be caused by only higher grafting density. Especially, it has to be taken into account that grafting density was calculated to be very high for SI-CuCRP already after one polymerization.[12] Therefore, a further growth will occur on top of the previously grafted brush. Still, a certain interpenetration depth cannot be completely excluded.

Only after grafting of the fifth block no further growth of polymer brush was possible. It is suspected that initiating moieties are lost to a certain amount during the experimental procedure. Furthermore, a drop in accessibility of Br-groups due to surface reconstruction or mismatch in wettability between polymer brush and used monomer-solvent mixture might be a reason. Still, the synthesized pentablock represents the highest block number reached for copolymer brushes on surface up to date and demonstrates the high level of control and robustness of the SI-CuCRP on PDA. Hence, the presented combination of both bears great potential for material synthesis.

4.2 Fabrication of Janus polymer carpets

Since Janus particles and membranes are often regarded as a great platform for directed chemistry, the synthesized polymer brushes on PDA were used as starting material for the fabrication of 2D Janus structures. In particular, the so prepared Janus membranes have lateral expansion of centimeters (determined by substrate size) and thicknesses of only nanometers **(Fig. 4.12)**. In addition, they expose highly dynamic polymer chains adaptable to environmental change and high density of functional groups on both sides of the membrane.
Two main methods of synthesis were applied **(Fig. 4.12)**. For both, a polymer brush was made freestanding to give a polymer carpet, which then was turned around to expose the PDA side.

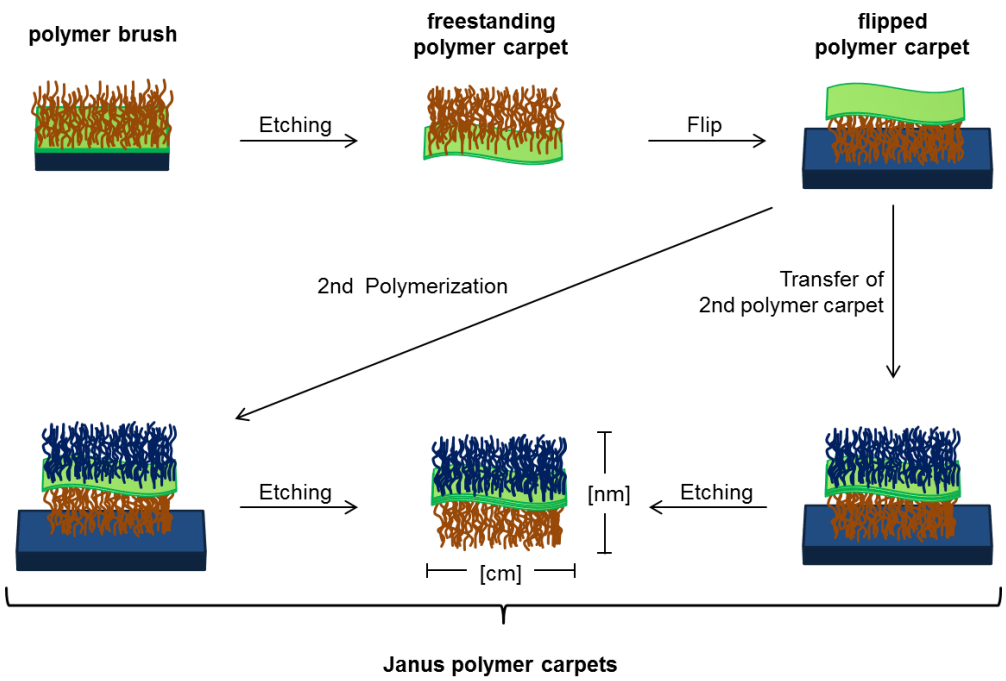

Figure 4.12: Schematic illustration of used synthetic strategies for the fabrication of Janus polymer carpets. First a polymer carpet is flipped around onto a support. Then, either a second polymerization or transfer of another polymer carpet is performed to result in Janus membrane.

In the first approach a functionalization with BiBB and subsequent SI-CuCRP was applied to give a second polymer brush on the flipped carpet (2nd Polymerization, **Fig. 4.12**). The second approach involved the transfer of a different polymer carpet on top of the previously flipped one (Transfer, **Fig. 4.12**). In that way, facing PDA sides can adhere to each other overcoming issues with different wettability and compatibility. Because of their morphology and as they are formed from polymer carpets, the so fabricated membranes are also referred to as Janus polymer carpets.

4.2.1 Transfer and flipping of polymer brushes

For the synthesis of Janus polymer carpets polymer brushes (PDA-g-polymer) were detached from the SiO_2 substrate and turned around to expose PDA side ("Flip" in **Fig. 4.13**). First, a series of polymer brushes were synthesized *via* SI-CuCRP and SIPGP to test stability against substrate etching and flipping process of the resulting polymer carpet.

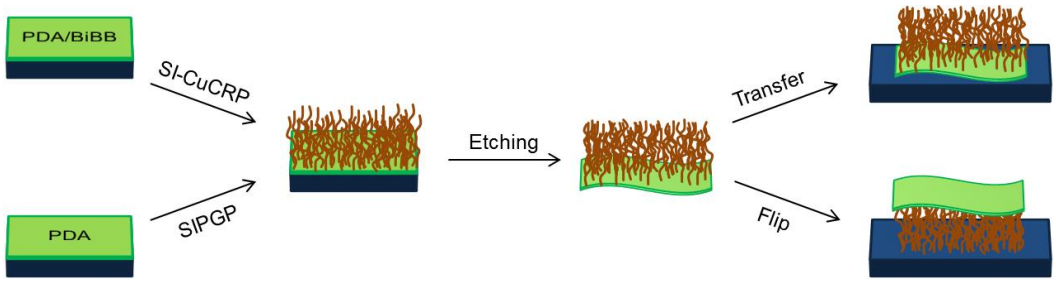

Figure 4.13: Schematic illustration of synthesis and transfer processes. After polymerization the polymer brush is detached from SiO_2 by etching. Then, the resulting polymer carpet is fished with another support or flipped.

Same monomers were used as in previous experiments. Additionally, N-isopropylacrylamide (NiPAAm), 3-sulfopropyl methacrylate as K-salt (SPMA) (both not used for SIPGP) and 2-ethylhexyl methacrylate (EHMA) were polymerized for structural variety. Furthermore, 2-hydroxyethyl acrylate (HEA), ethyl acrylate (EA), isobutyl acrylate (iBA) and n-butyl acrylate (nBA) were used. These monomers were chosen as their glass transition temperature (Tg) is below 0°C. According to theoretical calculations by Xia and Keten a low bulk Tg is beneficial for strong adhesion of polymer to a substrate, since intermolecular interactions between polymer chains decrease.[266] As intermolecular interaction weakens, adhesion energy of thin films to substrate rises. Therefore, the chosen acrylates are expected to provide polymer brushes and carpets suitable for the flipping approach.

Like before, the surfaces of the polymer brushes display typical θ_s values after SI-CuCRP **(Tab. 4.4)**. NiPAAm showed rapid grafting rates comparable to those found in literature[12,14] resulting in thick polymer brushes after short reaction time of 60 min. Even EHMA, which cannot be dissolved in typical SI-CuCRP solvent, is polymerizable in a mixture of toluene (Tol) and DMSO giving 90 nm thick brushes after 30 min. The only exception is the polymerization of SPMA, which only gave 20 nm after one hour of polymerization. However, this might be explained with the high repulsion forces caused by the negative charge in the monomer leading to a partial rupture of the polymer brushes during the polymerization as well as during the washing process. Such behavior was already observed for thick polymer brushes at high grafting densities.[12] Still the contact angle of the

sample was found to be below 10° what can be clearly assigned to the hydrophilic nature of the poly(3-sulfopropyl methacrylate) (PSPMA) brush. For polymerization of the acrylates reaction time had to be strongly reduced (5 - 20 min), as grafting of these monomers was outstandingly fast (d = 105 nm after 5 min for iBA, **Tab. 4.4**) and the thick polymer layers were already destroyed by rinsing with solvent. Short reaction times and use of DMSO or DMSO/Tol mixture on the other hand gave polymer brushes with thicknesses roughly between 50 nm and 150 nm, which could be used further.

SIPGP for all of the monomers was performed in substance and was expectedly successful. Typically polymer brush thicknesses between 50 nm and 150 nm are achieved, if polymerization is carried out until strong viscosity increase necessitates the abort of reaction.

Table 4.4: Results of SI-CuCRP of further monomers on PDA/BiBB for following transfer and flipping experiments. Ligand: PMDETA.

Monomer	Structure	Solvent	t_R [min]	d [nm]	θ_s [°]
NiPAAm	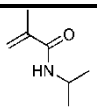	iPrOH in H_2O (1:2)	60	58	56
SPMA	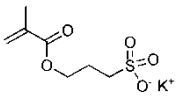		60	20	< 10
EHMA	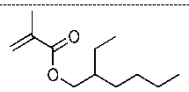	Tol in DMSO (0.75:1)	30	90	98
EA			10	63	80
HEA	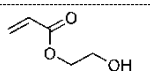	DMSO	20	34	50
iBA	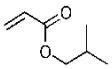		5	105	101
nBA	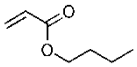		20	144	100

The detachment from substrate was achieved by etching away the SiO_2 layer with aqueous 5 - 10 % HF-solution resulting in freestanding polymer carpets. It is important to note that this process is performed with a spin-coated layer of PMMA to mechanically stabilize the hydrophilic polymer carpets (i.e. polymer brushes with $\theta_s < 90°$). This is required to prohibit swelling and destruction of the nanosheets. The only exceptions are brushes from PMMA. In that way all polymer brushes could be made freestanding polymer carpets and transferred onto another support (mainly SiO_2). Similar to the results reported by Amin *et al.*, the polymer

carpets retained their lateral integrity and robustly adhered to the new support (data not shown).[76]

In the following flipping step, the freestanding polymer carpets were fished from a water container and a second SiO_2 wafer was placed on top of them as support **(Fig. 4.14)**. Then, this SiO_2 support was carefully slid off to receive flipped polymer carpets.

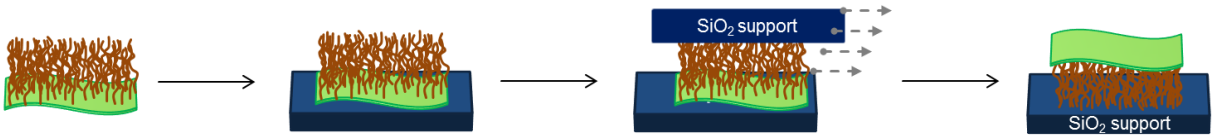

Figure 4.14: Schematic illustration of the process to turn around a freestanding polymer carpet. A SiO_2 support is placed on top of a freshly fished polymer carpet and carfully slid off (dashed arrows) to be flipped.

Poly(2-ethylhexyl methacrylate) (PEHMA) brushes on PDA not only show lateral integrity upon detachment from its original substrate, but also remain intact after the transfer and flip **(Tab. 4.5)**.

Table 4.5: Results of transfer and flipping experiments after SI-CuCRP and SIPGP. All polymer brushes are transferable onto different support. Polymer brushes from EHMA and acrylates can be flipped independent of applied polymerization technique.

Monomer	**SIPGP**		**SI-CuCRP**		**Tg [°C]**[267]
	Transfer	**Flip**	**Transfer**	**Flip**	
HEMA	✓	✗	✓	✗	57
DMAEMA	✓	✗	✓	✗	19
NiPAAm	-	-	✓	✗	85 - 130
MMA	✓	✗	✓	✗	105 - 120
tBMA	✓	✗	✓	✗	118
St	✓	✓	✓	✗	100
EHMA	✓	✓	✓	✓	**- 10**
HEA	✓	✓	✓	✓	**- 15**
EA	✓	✓	✓	✓	**- 24**
iBA	✓	✓	✓	✓	**- 24**
nBA	✓	✓	✓	✓	**- 54**

Polymers from EHMA are already known to be excellent adhesives while also being flexible and chemically resistant.[268] The long alkyl side chain of PEHMA allows for the formation of strong dispersive interaction and thereby sufficient adhesion to the support. Moreover, if its Tg of -10 °C is considered, the success of the flipping is not surprising according to Xia and Keten.[266] . As hypothesized, all brushes with low Tg (< 0 °C) could be turned over as well **(Tab. 4.5, Fig. 4.15)**. Results were comparable to the flipping experiments for PEHMA brushes and independent of the used grafting technique. Small scratches and holes in the carpets are often present after the flipping procedure **(Fig. 4.15)**. These can be mainly ascribed to rupture because of high forces during placing and off-sliding of the support. Especially, building of little bubbles beneath the carpet and their subsequent bursting, when the support is pressed on top of the carpet may enhance this effect. However, the main part of the membranes stays intact and retains lateral integrity.

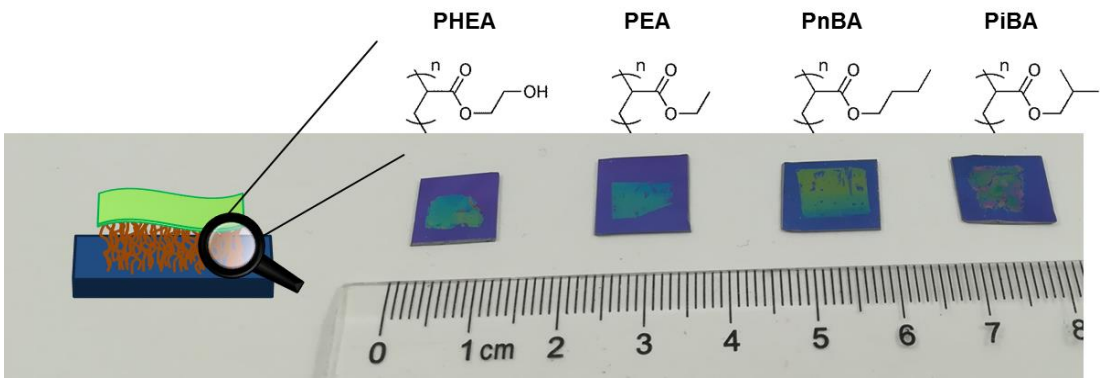

Figure 4.15: Photograph of flipped polymer carpets from PHEA, PEA, PnBA and PiBA. All of the carpets withstand the procedure. Small defects can be seen arising from the mechanical forces during the flipping.

As can be seen from the AFM scan thickness of PEHMA polymer carpets synthesized by SI-CuCRP is not affected by the procedure **(Fig. 4.16)**. The θ_s of 60° expectedly resembles the hydrophilic nature of PDA/BiBB and not that of PEHMA (θ_s = 100°, **Fig. 4.16**). However, comparison of the AFM scans before and after the flipping reveals a higher surface roughness (root mean square, RMS = 11 nm) for the flipped PDA-g-PEHMA carpets and introduction of regular wrinkles mostly ranging between 15 - 20 nm. In general, RMS after the flipping lies within a range of 6 nm to 11 nm. The building of wrinkles in the polymer carpet can be ascribed to the stress during transfer and flipping steps. Similar results were obtained for PEHMA carpets synthesized by SIPGP. After turning around the carpet θ_s exhibits a value of 46°, which is typical for PDA surface. Since fabrication of Janus polymer carpets is later

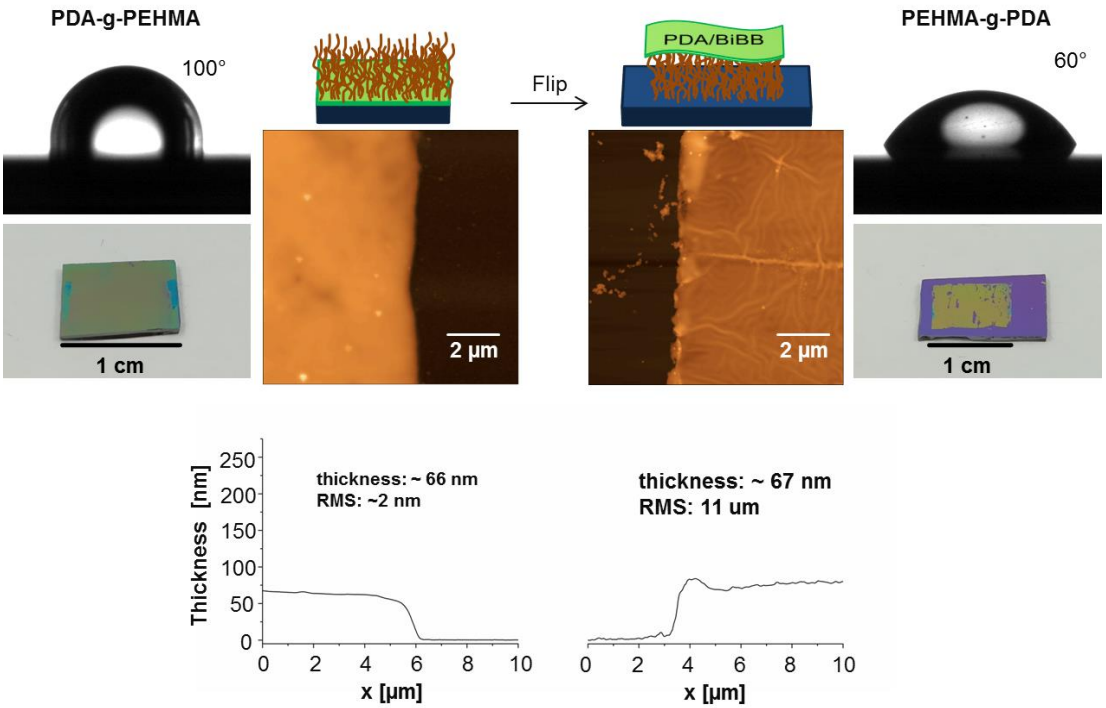

Figure 4.16: AFM scans and optical pictures of PDA-g-PEHMA sample and its θ_S before (left) and after the flip (right). The procedure of flipping causes wrinkling and small defects due to the applied mechanical forces. Contact angles resemble the respective polymer facing up on the substrate.

easily achieved by transferring another polymer carpet onto the flipped structure or by further polymerization, the observed wrinkles will obviously affect the surface of the final Janus polymer carpets. Still, PEHMA brushes on PDA offer a system for a reproducible flipping process onto SiO_2 support.Analogously, poly(styrene) (PSt) carpets could be flipped around after SIPGP. PSt carpets synthesized by SI-CuCRP on the other hand were not stable enough to withstand the procedure. This can be explained by low polymer brush thickness and thus low mechanical stability, when styrene is used as monomer in SI-CuCRP (compare **Tab. 4.2**). Additionally, SI-CuCRP is highly controlled and therefore the growing polymer brush is not affected by cross-linking. In contrast, such cross-linking during SIPGP leads to a higher stability within the polymer layer enabling the flipping of the PDA-g-PSt sheets.

The approaches to flip PMMA spin-coated samples failed as all of them crumbled strongly due to the thickness of the PMMA layer (ca. 400 nm) and a lack of compatibility with the support. Similarly, polymer brushes from tBMA, and MMA (all not spin-coated with PMMA) do not provide enough stability and were mostly destroyed during the procedure **(Fig. 4.17 a)**. Supports of PMMA and PSt were used to circumvent these problems. However, later experiments proved these organic materials as disadvantageous, as then readily formed Janus polymer carpets could not be made freestanding again. Instead, strong swelling and

roughening of the substrates during dissolution resulted in destruction and crumbling of the carpets, which made further processing impossible **(Fig. 4.17 b)**.

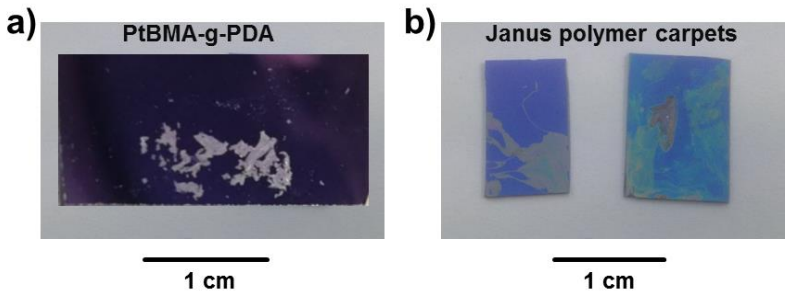

Figure 4.17: Photographs after attempt of flipping tBMA carpet (a) and Janus polymer carpets after transfer from PMMA support (b). PtBMA brushes are destroyed by the flipping procedure and Janus polymer carpets crumble strongly during dissolution of the organic support.

Since both SI-CuCRP and SIPGP can be applied for the polymerization of EHMA and acrylates on PDA based systems and the resulting polymer brushes are robust enough to be turned around, these monomers are the optimal choice for the synthesis of Janus polymer carpets. The hypothesis that polymer carpets from low bulk Tg polymers will lead to strong adhesion able to endure flipping process is therefore reaffirmed. Additionally, polymer brushes from polymers with high bulk Tg (i.e. Tg > 0°C) were not robust enough for the procedure. PDA-g-PSt brushes synthesized *via* SIPGP are the only exception and could be considered for structural variety. In the following experiments, however, PEHMA was chosen as main model polymer brush for further steps as application of SI-CuCRP ensures synthesis of well-defined, linear structure and grafting rate is moderate in comparison to acrylates.

4.2.2 Fabrication of Janus polymer carpets by second grafting

The first approach of Janus membrane fabrication involved a polymerization of EHMA *via* SIPGP followed by flipping and subsequent functionalization of the up-facing PDA layer with BiBB **(Fig. 4.18)**. Before flipping, a self-assembled monolayer (SAM) of octadecyltrichlorosilane (ODS) was bound to the surface *via* chemical vapor deposition (CVD) to exclude direct functionalization of the SiO_2 wafer with initiator. In the last step SI-CuCRP was performed to receive a Janus polymer carpet. This procedure ensures that the second grafting is initiated only from PDA/BiBB layer and no polymerization occurs on the previously grafted polymer brushes.

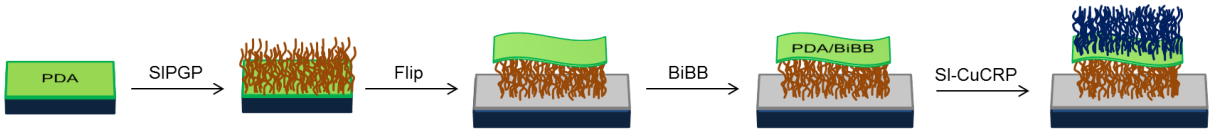

Figure 4.18: Schematic illustration of Janus polymer carpet synthesis by two grafting methods. After SIPGP of EHMA the polymer brushes are flipped and functionalized on unreactive SAM of ODS (gray layer). Then, a second polymer brush is grafted *via* SI-CuCRP.

As previously, the flipping of PDA-g-PEHMA was successfully performed onto the ODS monolayer. The surface roughness was comparable with the results obtained earlier (RMS = 6 - 8 nm, **Fig. 4.19**). After subsequent functionalization with BiBB the surface of flipped PDA-g-PEHMA displays strong wrinkling and high RMS values of about 65 nm. Obviously, swelling and deswelling of the polymer brushes in the used solvent (dichloromethane, DCM) will cause stress within the carpet. In addition, the reaction itself might lead to a higher stiffness within the PDA layer. Different behavior in swelling and different mechanical properties of PDA and PEHMA brushes will result in a strong formation of wrinkles and buckles to release the built up stress. This is possible because the polymer carpet is only loosely attached to the SAM surface by the PEHMA brushes and not strongly bound to the rigid substrate. Importantly, the thickness was not affected and stays the same **(Fig. 4.19)** meaning the structure is stable enough to withstand the treatment.

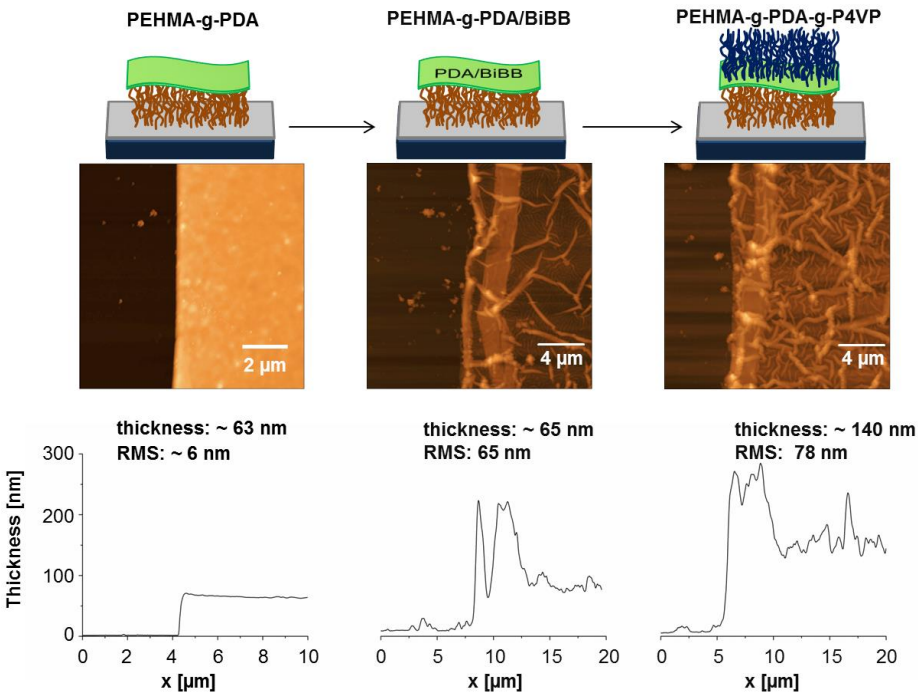

Figure 4.19: AFM images of flipped PEHMA carpet before (left) and after (middle) functionalization. The reaction leads to strong building of wrinkles. Subsequent polymerization *via* SI-CuCRP results in thickness gain (ca. 75 nm) and enhances wrinkling (right).

SI-CuCRP was performed with the so freshly prepared flipped carpets. 4-Vinylpyridine (4VP) was used as monomer as it contains characteristic functional groups which can be spectroscopically distinguished from the PEHMA brushes. As can be seen in the AFM images **(Fig. 4.19)** the SI-CuCRP was successful and a thickness of 140 nm was obtained after 1 h of polymerization. This corresponds to a poly(4-vinylpyridne) (P4VP) brush height of ca. 75 nm. Due to the influence of solvent, monomer and reaction discussed above a further increase in RMS from 65 nm to 78 nm is observed. FT-IR further confirmed the grafting of P4VP **(Fig. 4.20)**, as characteristic signals of aromatic ring stretching and C=N stretching appear at 1600 cm^{-1} and 1558 cm^{-1}, respectively.

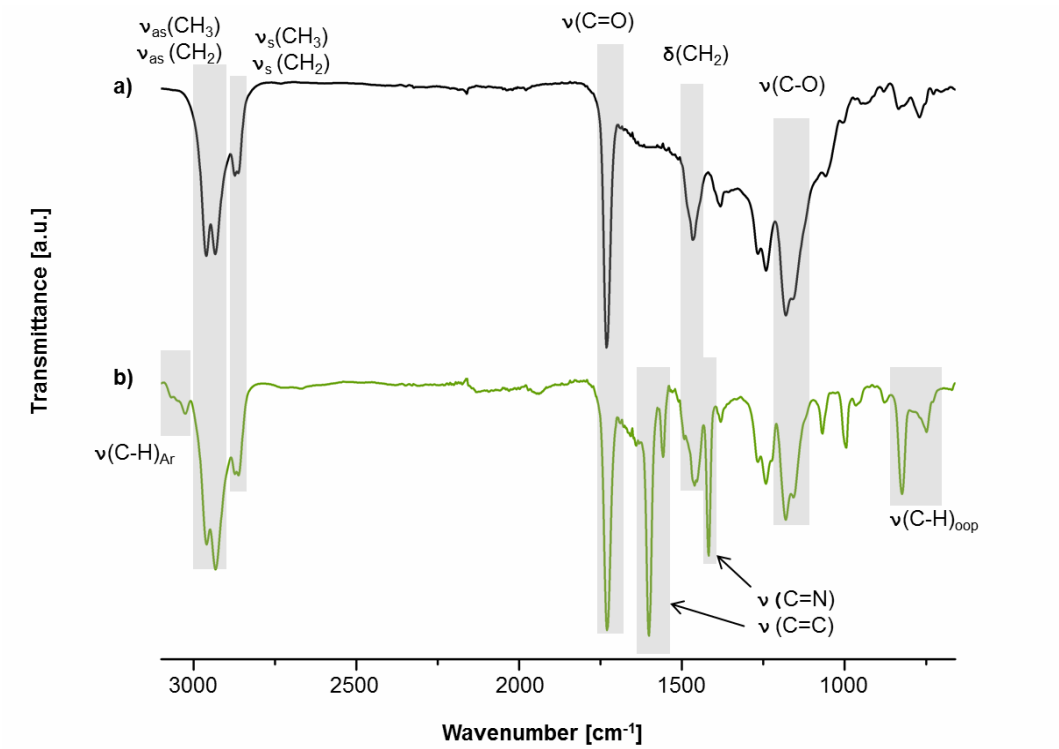

Figure 4.20: FT-IR spectra of PDA-g-PEHMA after flipping (a) and after functionalization and SI-CuCRP of 4VP (b). Appearance of signals from aromatic stretching modes and C=N stretching prove successful grafting.

Furthermore, aromatic C-H stretching (3080 - 3008 cm^{-1}) and bending (822 cm^{-1}, 748 cm^{-1}) arise in addition to signals of the PEHMA ester group (ν (C=O) at 1731 cm^{-1}, ν (C-O) at 1180 cm^{-1}) as well as the typical signals for CH_3 and CH_2 stretching **(Fig. 4.20)**.

Since all the data clearly prove that the used procedure is applicable for the synthesis of a second polymer brush after flipping, a series of other monomers was grafted in the same manner **(Fig. 4.21)**. All received polymer carpets exhibit a higher thickness after SI-CuCRP with results for PSPMA and poly(sulfobetaine methacrylte) (PSBMA) comparable with those

achieved for P4VP brushes. PDMAEMA and poly[oligo(ethylene glycol) methacrylate] (POEGMA) even reach overall heights of 820 nm and 740 nm after 1 h and expose dramatically enhanced surface roughness (RMS = 234 nm for POEGMA), even though wrinkling is not as clearly developed as on the other samples. Moreover, the water contact angles of all samples match the expected values of the respective structure **(Fig. 4.21)**.

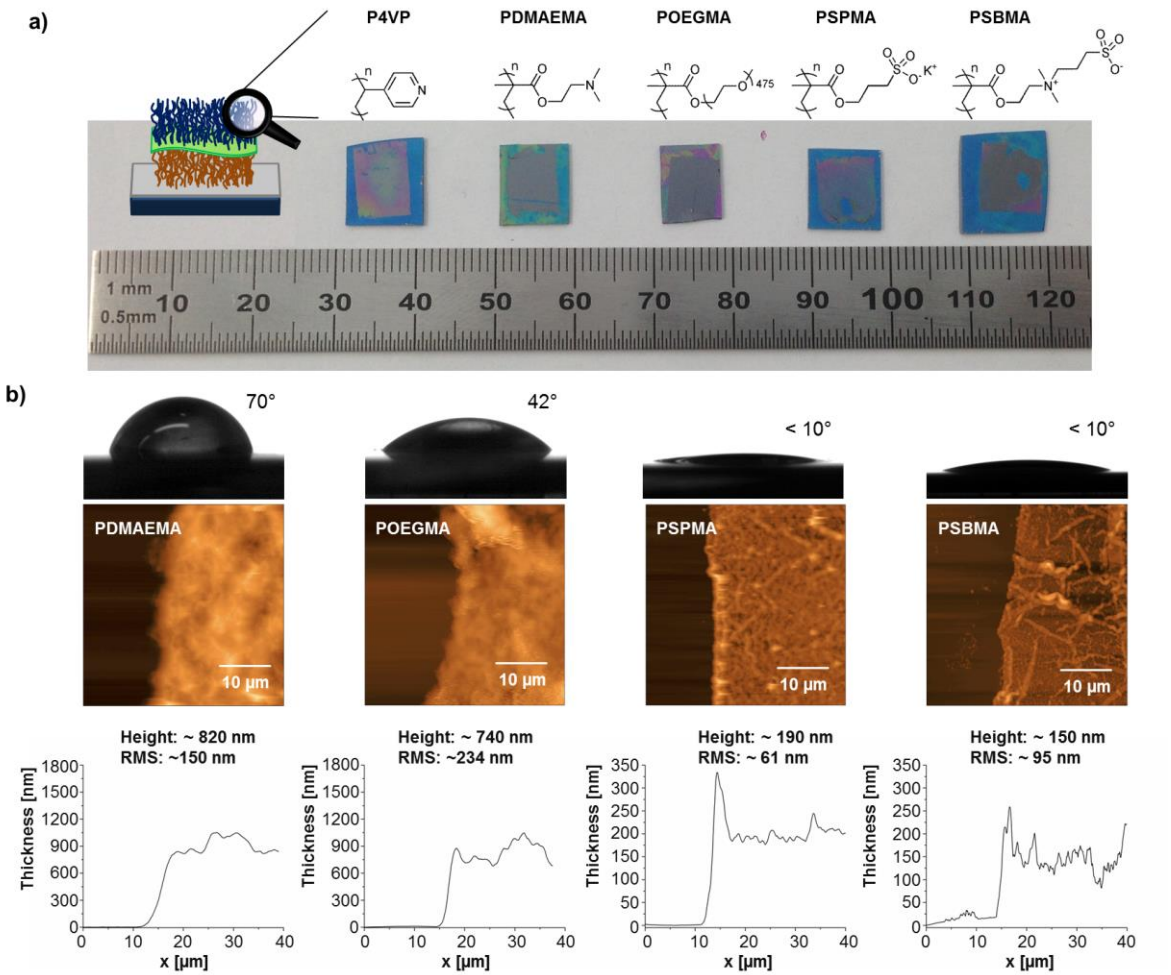

Figure 4.21: Photograph of the synthesized Janus polymer carpets (a) with the respective chemical structure of the up-facing polymer brush. All AFM images (b) show very rough surfaces and high polymer thickness after SI-CuCRP. Static water contact angles correspond to the respective polymer brush.

Although the SI-CuCRP was carried out in aqueous solution and polymerization was therefore expected to be rapid, the found thicknesses are quite surprising. Compared to the previous results obtained from SI-CuCRP on still grafted PDA/BiBB (see **chapter 4.1.2, Tab. 4.2**), DMAEMA shows a grafting rate 8 - 15 times higher. It has to be stated that reaction solvent mixture in this case was different (67 % (v/v)-H_2O in iPrOH) from the one used in the **chapter 4.1.2** (10 % (v/v)-H_2O in iPrOH). Still, such a fast growth cannot be explained by change of solvent only. One possible reason for the enhancement of grafting

could be the accessibility of reactive sites in the PDA/BiBB layer. This might be better in the flipped polymer carpet than in the still grafted PDA/BiBB due to a higher flexibility and stronger swelling in the solvent. As mentioned above SI-CuCRP was done directly after conversion of PDA with BiBB, which was not necessarily the case for the previously synthesized samples. Consequently, aging of the initiator, i.e. loss of Br moieties, cannot occur, since it is immediately used. Therefore, a higher initiating efficiency because of a higher amount of Br at the surface might also explain the observed. Furthermore, the porous nature of PDA has also to be considered. Monomer can be taken up into the structure and grafting can be initiated within **(Fig. 4.22)**.

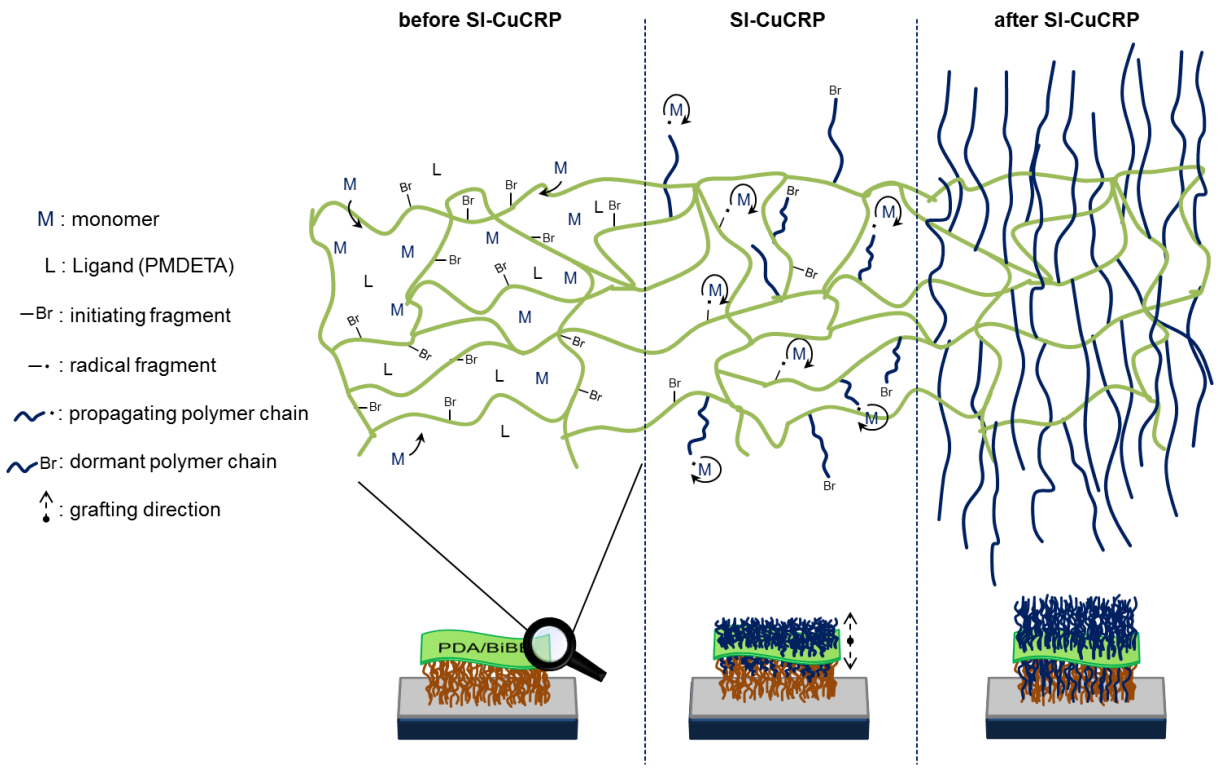

Figure 4.22: Schematic illustration of polymerization on flipped initiating polymer carpet. Monomer can start grafting within PDA/BiBB and polymer brushes can grow into two directions. For the sake of clarity possible participating Cu-species are not shown.

Even if BiBB is not incorporated to a considerable amount into the PDA, the growing polymer chain most probably can dig through the layer. In consequence, it cannot be ruled out that grafting of polymer brushes takes place in two directions, i.e. on top of the flipped polymer carpet towards solution and through the initiating layer toward the substrate **(Fig. 4.22)**. Eventually, this will lead to mixed polymer brushes at the bottom part of the polymer carpet. Hence, no clearly separated sides are synthesized and the obtained membrane cannot be considered a Janus type material. This kind of progress of polymerization can also

explain the outstanding thickness gain, since growth in both directions "doubles" the increase. All in all, the functionalization of flipped PDA-g-PEHMA carpet with initiator and following SI-CuCRP can be regarded as successful. All of the used monomers can be grafted on top of the flipped carpets. In principle, this series of experiments gives membranes with two different sides, being hydrophobic/hydrophilic (all), non-aromatic/aromatic (P4VP), non-responsive/T-responsive (PDMAEMA, POEGMA) and non-ionic/ionic (PSPMA) or non-ionic/zwitter-ionic (PSBMA) **(Fig. 4.21)**. However, a confirmation of such Janus type structure (by θ_S measurement) is difficult, since it would require another flipping which is not achievable with the polymer brushes exposed on top. Either way a distinct separation of the two polymer brushes is not guaranteed with this approach.

4.2.3 Fabrication of Janus polymer carpets by transfer

For the assembly of Janus polymer carpets two different polymer brushes were detached from the SiO_2 substrate and put together with the PDA sites facing each other **(Fig. 4.23)**. PEHMA carpets were flipped as described above and a second polymer carpet was transferred on top. SI-CuCRP was used for synthesis of the polymer brushes in this approach.

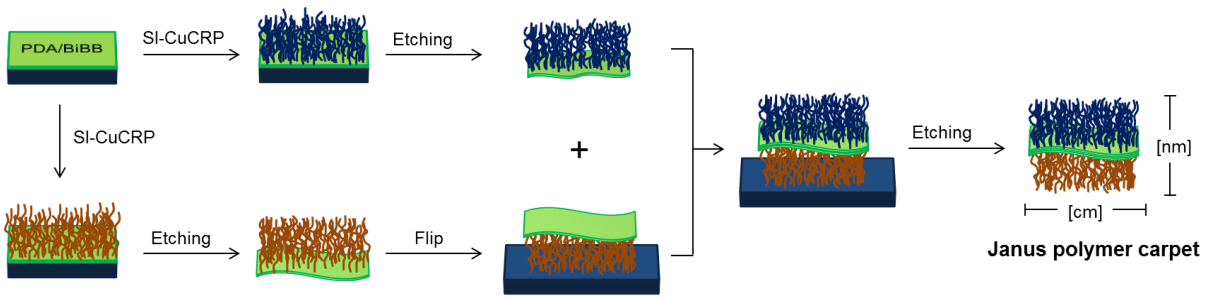

Figure 4.23: Schematic illustration of the synthetic pathway to Janus polymer carpets. One freestanding polymer carpet is flipped on a support and a second polymer carpet is transferred on top.

Purposely the single carpets were put together in a way that characteristics of the individual polymer brushes could be also determined. The area of overlapping polymer brushes appears yellow/red because of the overall thickness of ca. 126 nm which can be seen in the AFM scan **(Fig. 4.24)**. From the AFM scans in the spots of the individual polymer carpets it is obvious that the overall thickness is almost exactly the sum of single polymer carpet heights (PDA-g-PDMAEMA = 70 nm, PDA-g-PEHMA = 63 nm). The small deviation of 7 nm can be explained by small inhomogeneity in polymer brush thickness in both carpets, but also by certain interpenetration at the interface of the facing PDA layers. Moreover, the determined

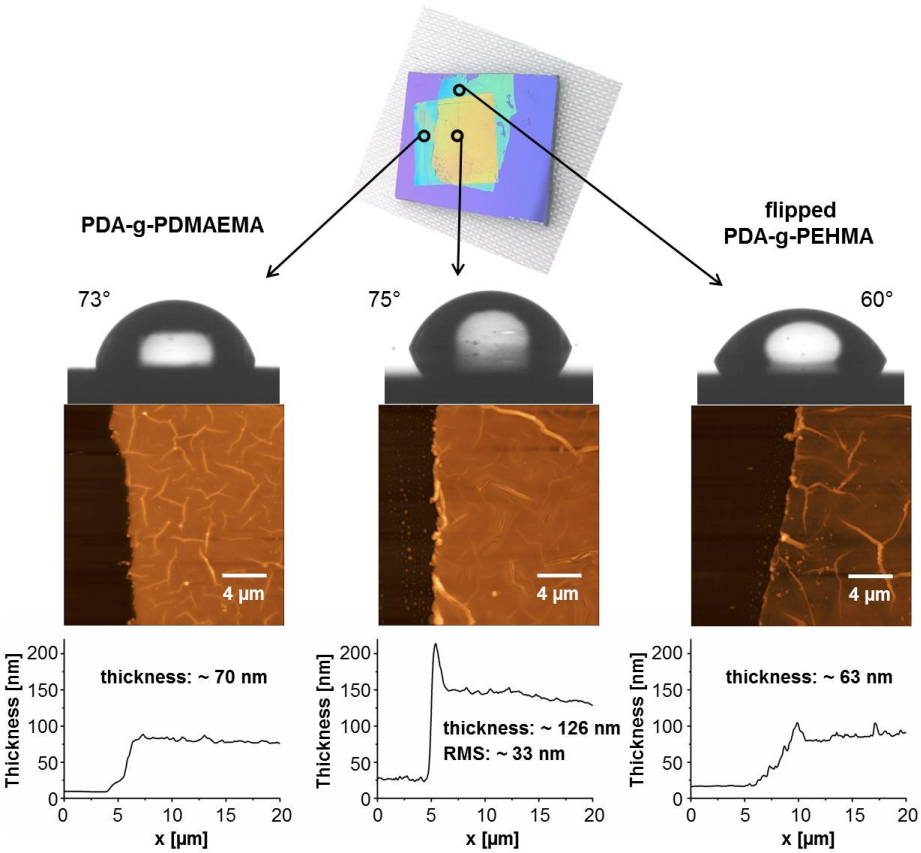

Figure 4.24: Image of Janus polymer carpet from PDA-g-PDMAEMA and flipped PDA-g-PEHMA on SiO_2 with corresponding surface characteristics. Left: static water contact angle and AFM image with height profile of PDMAEMA carpet. Right: static water contact angle and AFM image with height profile of flipped PEHMA carpet. Middle: surface properties of the overlapping area of transferred polymer carpets.

high surface roughness (RMS = 33 nm) contributes to the difference. This also explains that PDMAEMA brush exposing areas revealed θ_s of 73° and 75°, which is slightly higher than before the transfer ($\theta_s \sim 59°$). As mentioned before, the high RMS and the building of wrinkles (**Fig. 4.24**, AFM) in the polymer sheet most probably arise from the stress during transfer steps. Same could be observed for the area of flipped PDA-g-PEHMA, where the θ_s of 60° expectedly resembles the hydrophilic nature of PDA/BiBB and not that of PEHMA ($\theta_s = 98°$, **Tab. 4.4**). In addition to the mechanical stress during the flipping and transfer as well as different swelling behavior of the polymer brushes may also play a role in the formation of the wrinkles. Since the transfer of PDA-g-PDMAEMA was conducted with the help of PMMA, acetone was used to dissolve it afterwards. Different degree of extension or collapsing of the polymer brushes in the solvent might induce additional tension into the sheets. Moreover, PDA based polymer carpets transferred on SiO_2 were shown to retain smooth surface[76], since the rigid substrate prohibits reduction of the inherent steric stress of polymer brushes. In the Janus systems, however, the softer nature of the underlying PDA-g-PEHMA carpet most probably allows stress release resulting in higher RMS and

stronger wrinkling. Still, the applied procedure is clearly suited to produce a variety of Janus polymer carpets based on flipped PDA-g-PEHMA **(Fig. 4.25 a)**. The PDA-g-PEHMA based Janus carpets, could also be detached by simply floating them on HF-solution again. In that manner a series of different freestanding Janus polymer carpets were fabricated with the previously synthesized polymer brushes **(Fig. 4.25 b)**.

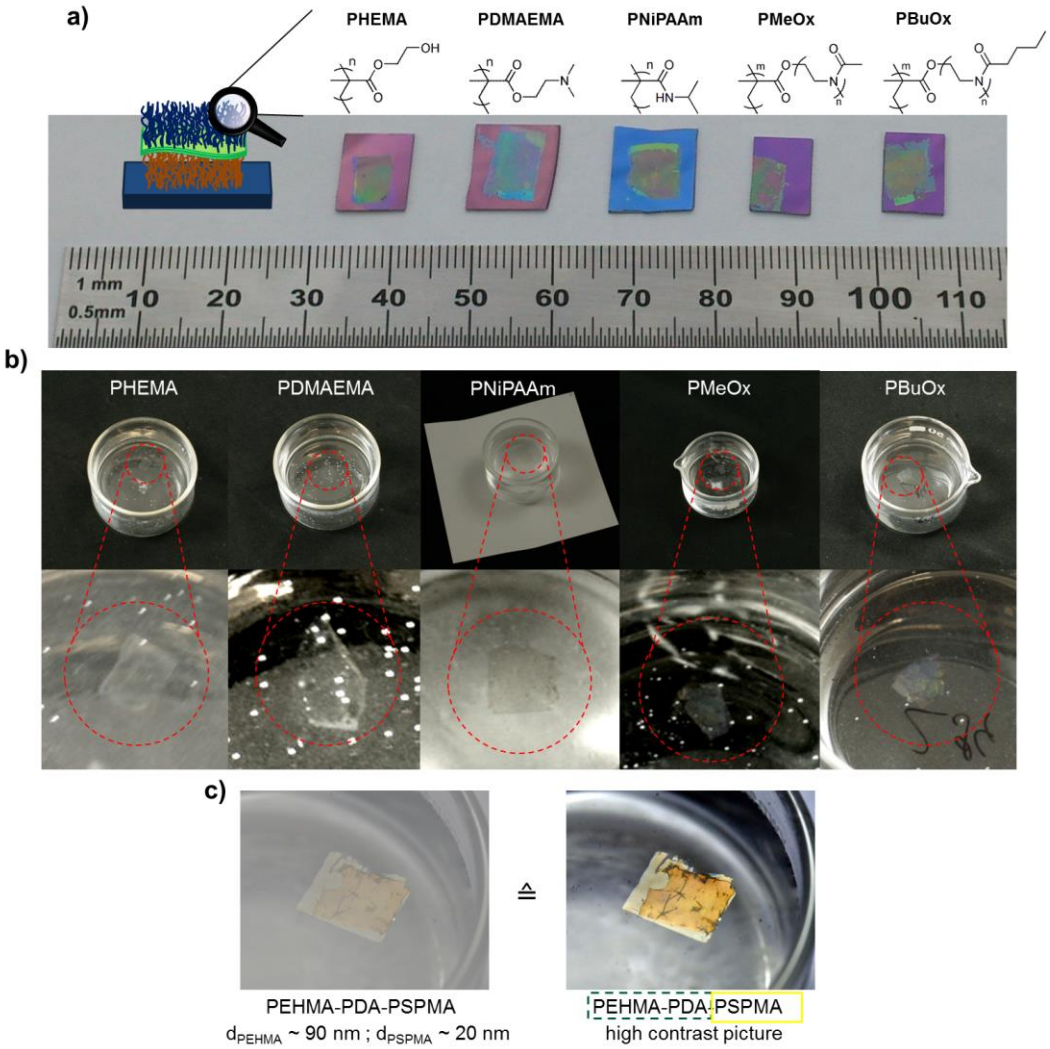

Figure 4.25: Photographs of Janus polymer carpets from flipped PDA-g-PEHMA as fabricated on SiO_2 (a) and floating on water after subsequent etching of the substrate (b). High resolution photograph of a PSPMA Janus polymer carpet (c) shows the two single polymer sheets sticking together after detachment from the substrate.

Additionally, poly(methyloxazoline) (PMeOx) and poly(butyloxazoline) (PBuOx) bottle-brush brushes were synthesized in a previously reported way (see experimental) and used for the fabrication.[269] Thus, different types of Janus systems were received including membranes that are hydrophobic/hydrophilic (all, but PBuOx), non-responsive/T-responsive (PDMAEMA, PNiPAAm), non-responsive/pH-responsive (PDMAEMA) or have

polymer brush/bottle-brush brush architecture (PMeOx, PBuOx). Overall thickness of the so synthesized membranes lies in between 100 nm and 200 nm (compare **Tab. 4.2**). Taking into account their lateral size of 0.5 - 1 cm huge aspect ratios of 10^4 to 10^5 can be calculated. Furthermore, all Janus polymer carpets exhibit excellent stability after detachment from the support. Owing to the exceptional adhesion of the PDA layers no delamination of the individual polymer carpets was observed **(Fig. 4.25 b, c)** even after letting them float on water for months. It can be therefore concluded that the presented synthesis route is an effective, straight forward method to fabricate Janus membranes with desired properties at clearly separated sides.

4.2.4 Patterned Janus polymer carpets

To demonstrate the versatility of the systems and to further explore on wrinkling behavior patterned Janus polymer carpets were fabricated. As found by Amin *et al.* patterning of polymer carpets can be used to produce directed buckling originating from anisotropic stress release.[10] Control of such buckling/wrinkling can be achieved by shape and size of the used pattern.[10,270] Therefore, the initiator bearing layer was exposed to UV-light (200 W) through different photomasks to selectively remove Br. Then, SI-CuCRP of DMAEMA was conducted giving polymer brushes with the desired structure of the used mask **(Fig. 4.26)**.

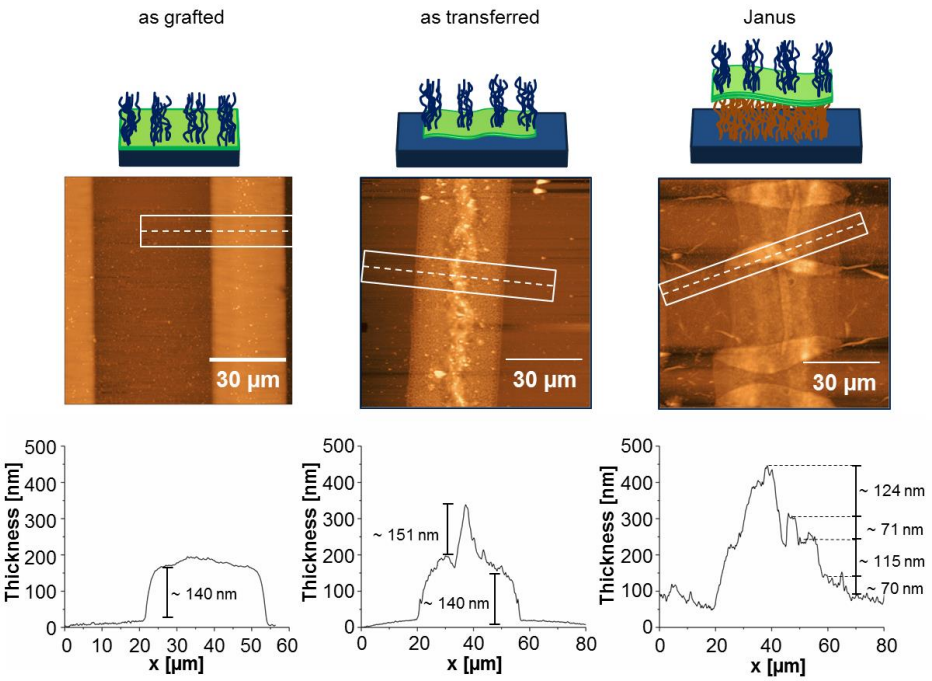

Figure 4.26: AFM images and profiles of patterned polymer brushes (left), polymer carpets (middle) and Janus polymer carpets (right). The samples display stronger wrinkling after transfer onto a flipped PDA-g-PEHMA carpet (Janus). White squares indicate where the profiles were taken.

As can be seen from the AFM scan of the still grafted PDMAEMA brushes on PDA **(Fig. 4.26)** the polymerized areas are smooth and well defined. Small inhomogeneities in the projected patterns result from incomplete coverage of the sample by the photomask during application of UV-light and from damages in the used photomask. Upon transfer onto a SiO_2 wafer wrinkling along the polymer pattern can be observed with a wrinkle height of approximately 151 nm. Besides that, unordered buckling was found everywhere in the polymerized areas with buckles size mostly ranging from 20 nm to 70 nm. The very same sample was transferred onto a flipped PDA-g-PEHMA carpet using the procedure described above. As a result the received Janus polymer carpet displayed morphology with even more pronounced wrinkling and height steps from 70 nm to 124 nm **(Fig. 4.26)**. This can be attributed to the above mentioned anisotropic stress release and contraction of the polymer carpet. Curiously, two main directions of wrinkling are seen in the AFM scans for this sample: one still following the pattern of the polymer brushes and the second forming orthogonally to it. Furthermore, wrinkles in the non-polymerized area are appearing reaching heights of 150 - 250 nm. In both cases wrinkling is directed. From these observations it also becomes obvious that the underlying material plays a key role in the formation of the wrinkles and the PDA-g-PEHMA carpet enables a stronger relaxation than SiO_2. Different patterns also provide different buckling behavior **(Fig. 4.27)**.

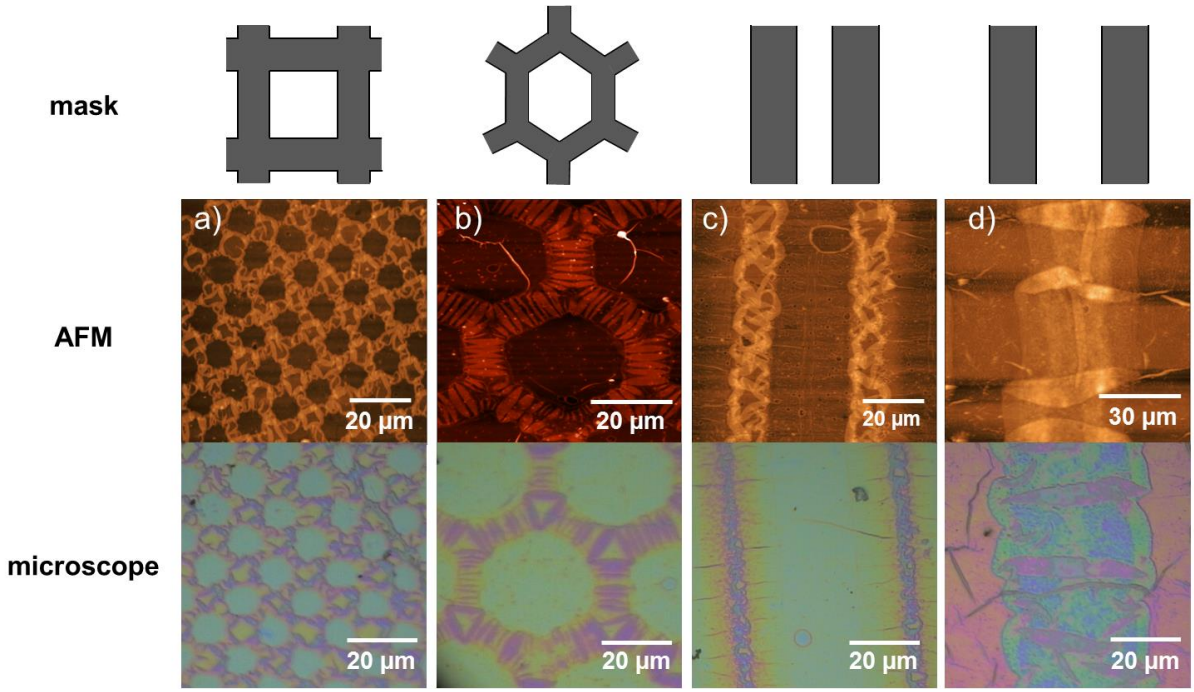

Figure 4.27: AFM images (middle) and photomicrographs (bottom) of the fabricated patterned Janus polymer carpets. All carpets show anisotropic or directed wrinkling depending on the used patterning mask (top).

However, all of the used shapes are marked by well-defined and ordered wrinkles. More importantly directed wrinkling was observed for all of the patterned samples with the only exception being rectangular shape. Considering that buckling wavelength (λ) must be considerably lower than the patterns dimension[10,270] to be directed, this results are somewhat expected. The rectangular shape gave a $\lambda = 1.25 \pm 0.31$ µm while having a structure size of 9 µm. This difference was significantly bigger for the other structures showing $\lambda = 1.40 \pm 0.40$ µm for hexagonal pattern (37 µm) and $\lambda = 2.54 \pm 0.32$ µm or $\lambda = 6.50 \pm 1.7$ µm for the parallel patterns (30 µm and 50 µm, respectively). Wrinkle heights were determined to be 50 - 100 nm for hexagons and rectangles **(Fig. 4.27 a, b)** and 120 - 180 nm for stripes **(Fig. 4.27 c)**. Besides the influences of solvent and underlying material, which were discussed above, the initial thickness as well as mechanical properties of the patterned polymer brush will affect the formation of buckles and wrinkles.[270–274] The results still clearly demonstrate that underlying polymer carpet enhances wrinkling and buckling in the patterned polymer sheet transferred on top.

Concluding it can be said that the flexibility of PDA surface chemistry merged with the durability and versatility of SI-CuCRP provide a simple strategy for Janus membrane synthesis. While the robust nature of adhesion and cross-linking of PDA stabilizes the material, the structural variety offered by SI-CuCRP gives rise to a high number of different Janus functionalities. In addition, patterning is achievable by straightforward photolithography and enables strong and directed wrinkling through anisotropic stress release. Thereby Janus polymer carpets are received being interesting for directed transport, movement or controlled deformation. As the fabrication is done by sequential transfer of polymer carpets, an incorporation of further materials between the layers can also be easily realized. Finally, it should be noted that the presented Janus polymer carpets typically exhibit a size of ca. 1 cm^2. Since both SI-CuCRP and PDA deposition can be carried out on large areas, the dimension of resulting Janus carpets can be scaled up to overcome the herein obtained aspect ratios of 10^5. Thus, the developed approach gives access to a series of novel 2D materials with adjustable properties.

4.3 Strain-engineering of graphene by polymer grafting

After demonstrating the potential of SI-CuCRP in combination with PDA surface chemistry for controlled, specific surface functionalization and material synthesis, it was targeted to exploit it for modification and strain-engineering of graphene (G). By deposition of PDA, initiator can be bound in the previously applied procedure and polymer brushes can be grafted *via* SI-CuCRP **(Fig. 4.28)**. High grafting density of so synthesized polymer brushes on graphene will lead to a sterically induced, high chemo-mechanical force, which should induce deformation and eventually band gap opening.

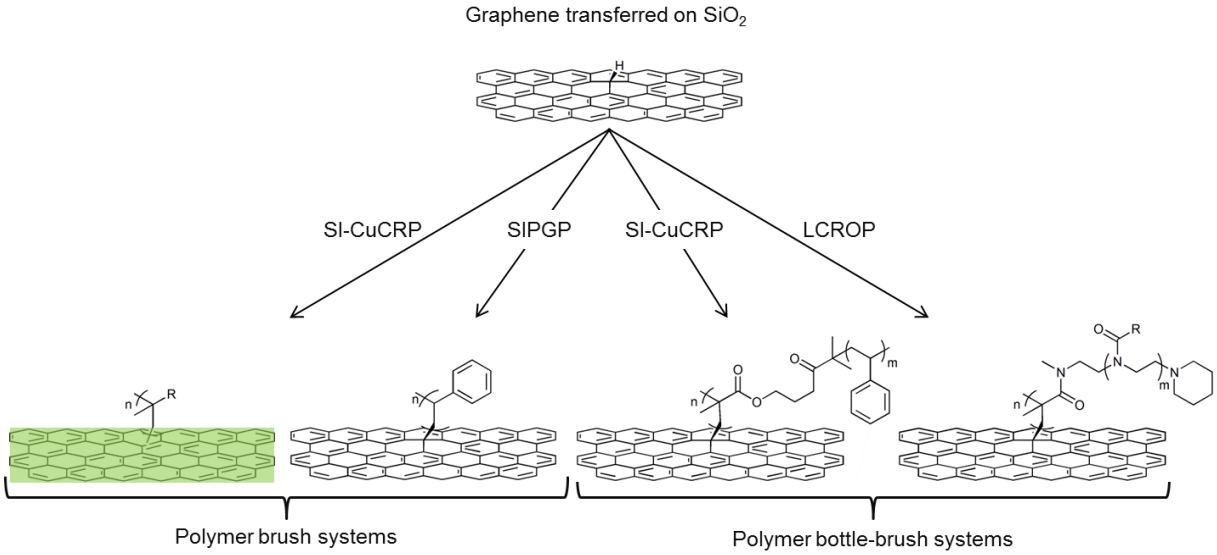

Figure 4.28: Schematic illustration of applied grafting routes for introduction of strain in graphene by chemo-mechanical force. After transfer of graphene on SiO_2 support polymer brushes are grafted by SIPGP or SI-CuCRP (initiating PDA/BiBB layer is indicated by green color). Polymer BBBs are grafted by SIPGP of a precursor polymer and subsequent SI-CuCRP or LCROP (for POx BBBs).

Since such band gap opening in graphene is of biggest interest for material science, other grafting approaches were also applied **(Fig. 4.28)** to achieve this goal. Beside SI-CuCRP, SIPGP was used to synthesize polymer brushes. Furthermore, BBB systems were synthesized either by SI-CuCRP or living cationic ring-opening polymerization (LCROP) of 2-oxazolines. In both cases a precursor polymer brush was grafted *via* SIPGP. HEMA was grafted for subsequent SI-CuCRP and 2-isopropenyl-2-oxazoline (iPOx) for following LCROP. Bottle-brush brushes allow for an efficient transfer of steric pressure onto the graphene sheet and lead to strong wrinkling and buckling, especially observed in POx BBB carpets. Eventually, samples were patterned to promote anisotropic stress release and induce directed wrinkling.

In all experiments single layer CVD graphene on Cu-foil from Graphene Supermarket was used. The obtained graphene was transferred onto SiO_2 support for subsequent analysis and modifications. For this procedure PMMA was spin-coated to stabilize the monolayer and the Cu-foil was dissolved with $NH_4S_2O_8$ solution. This transfer process is a standard procedure well known from lieterature.[217,243,275]

Acetone was used to wash away the resist after transfer and should effectively remove all of the PMMA. Still, the transferred G-sheets often have little residues of PMMA sticking to the surface (**Fig. 4.29**, white circles). It is not possible to obtain completely clean samples, when transfer is applied, even if other solvents like concentrated acetic acid are used. In addition, black, worm-like structures can be seen under microscope **(Fig. 4.29)**. These are found especially in areas, where the graphene is ruptured or at the edges of the transferred sheet. It was hypothesized that these are rolled up graphene layers, which originate from the mechanical stress during transfer.[276] In fact, Raman spectra on these structures show both G- and 2 D-band characteristic for graphene multi layers, since the G-band normally has higher intensity than the 2 D-band on the respective measuring spot.[277,278]

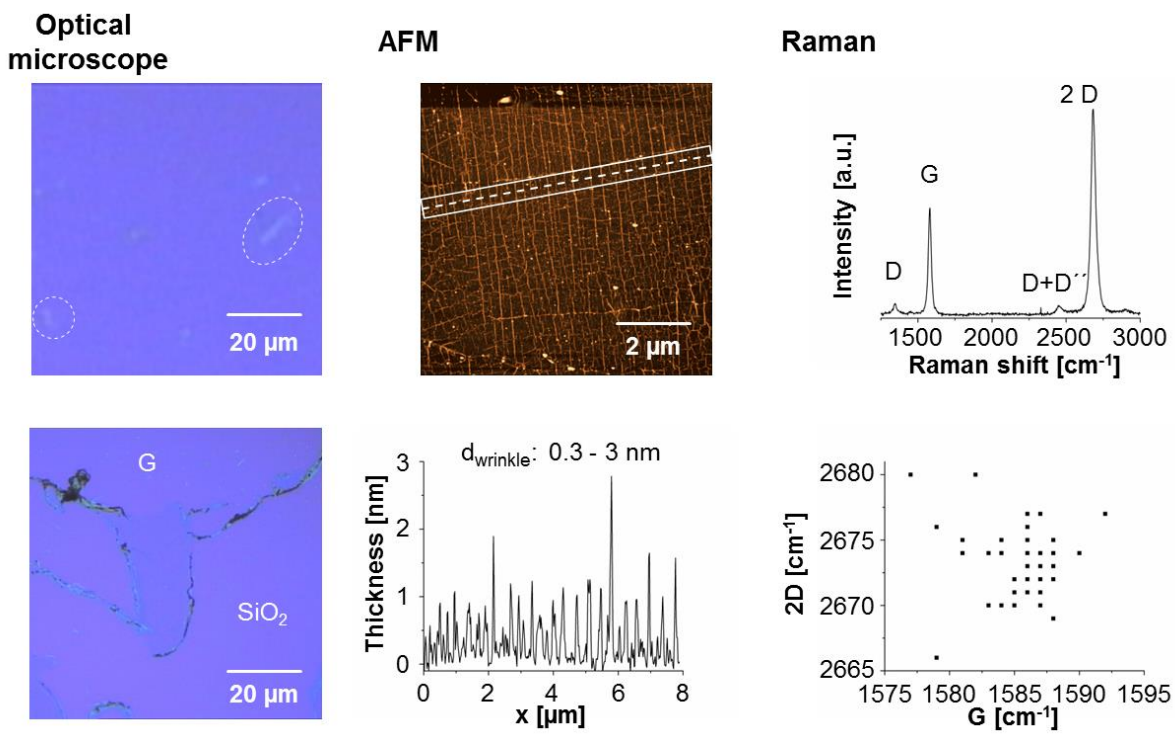

Figure 4.29: Optical microscopy pictures (left) and AFM scan with corresponding profile (middle) of graphene transferred onto SiO_2. Residues of PMMA (white circles) and rolled up graphene can be found on the sample. Regular and directed wrinkles are already visible on the pristine graphene monolayer. Raman spectra (right) show typical G- and 2 D-band, which vary in their exact position (± 3 cm^{-1} for both signals). Some samples exhibit small D- and D+D´´- bands.

As they can be found on other spots of intact graphene as well, the "worms" might also be residues from the CVD production process. When monolayers are fabricated, graphene starts to grow in isles on the copper support. While growth proceeds, these isles will eventually meet and form grain boundaries, which might lead to such rolling up of graphene at their edges. Furthermore, precursor could be also deposited directly on the already formed single layer. Despite the found residues the main part of the transferred sheets is clean. As can be seen from the AFM images **(Fig. 4.29)** graphene exhibits small wrinkles on SiO_2 mostly ranging between 0.3 - 3 nm. This observation can also be ascribed to the mechanical stress during transfer as well as the production process.[279] Interestingly, the observed wrinkles are often directed, which indicates anisotropically applied stress. However, this cannot be controlled or experimentally prevented and the obtained wrinkles are comparably low (highest measured = 10 nm). Raman spectra of the transferred sheets **(Fig. 4.29)** exhibit typical signals for single layer graphene with the G-band and 2 D-band being most prominent. Some spots also display a small D-band (1345 - 1350 cm^{-1}) and D+D´´-band (~ 2460 cm^{-1}) indicating little defects within the structure. Since these bands have relatively low intensity (Intensity ratio $I_D/I_G \leq 0.08$) and the D-band is only found occasionally, it can be concluded that the used graphene has a high quality and mainly consists of sp^2-hybridized C-atoms. It was noticed that the exact position of the characteristic bands varies strongly (± 3 nm for G- and 2 D-band, **Fig. 4.29**) even within one sample. Exemplarily, one graphene sheet was transferred onto SiO_2 and 19 different areas of the sheet (100 x 100 µm) were scanned. Three spots from these areas were randomly chosen to measure Raman spectra. The so obtained 57 spectra show that G-band lies within a range of 1575 cm^{-1} to 1592 cm^{-1} **(Fig. 4.29)**. Similarly, the Raman shift of the 2 D-band can be found between 2666 cm^{-1} and 2682 cm^{-1}. This inconsistency in signal position can be explained by doping effects originating from charge carriers on the substrate due to adsorbates or resist residues. As documented by Ferrari *et al*. charges can not only strongly influence the position of the signals, but also the full width at half maximum of the G-peak (7 - 16 cm^{-1}).[280] Furthermore, they show that the G-peak can be asymmetric and its ratio to the 2 D-band varied from 0.14 to 1. Therefore, clear prove of a possible band gap opening is only obtained, if a signal splitting is observed (see **chapter 2.3.2**). In consequence prove of uniform, biaxial strain will be difficult as no break of symmetry and thus no change of scattering paths will occur. Only shifts in peak position would be detectable in that case. Considering the anisotropic nature of wrinkling on polymer carpets observed by Amin *et al.* such preservation of geometry seems implausible for the investigated systems.[9,10] Hence, band splitting should be observed if the chemo-mechanically applied strain is sufficient.

4.3.1 Grafting of polymer brushes on graphene

Polymer brushes on graphene were synthesized with SIPGP or SI-CuCRP **(Fig. 4.30)**. The graphene single layer was transferred onto SiO_2 support for all further reactions. For SI-CuCRP a PDA layer was deposited on graphene before transfer and subsequent conversion with BiBB. The experimental set-up for polymerizations remained the same as before.

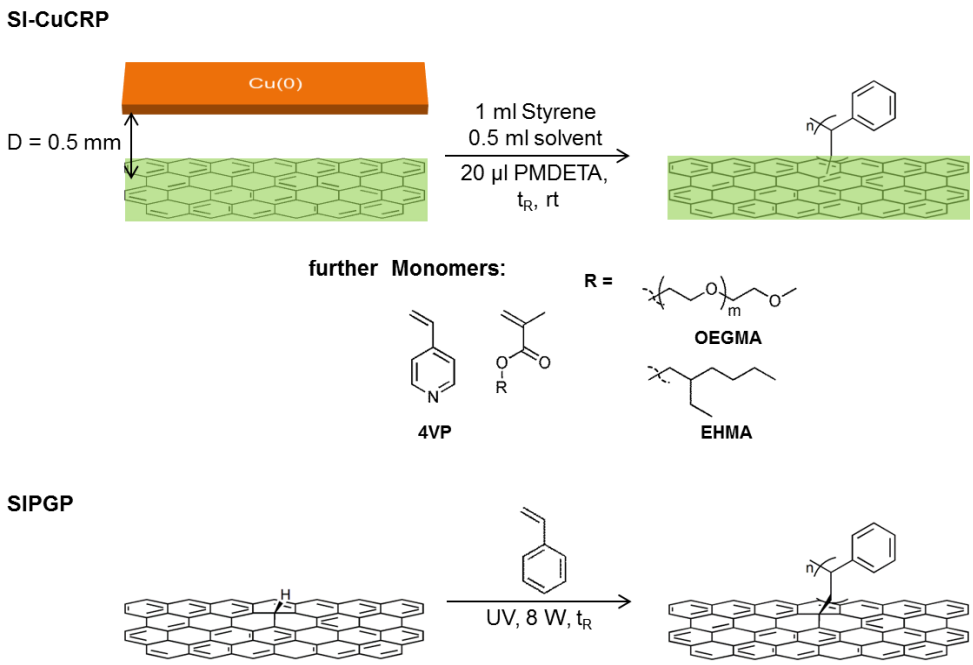

Figure 4.30: Schematic illustration of the synthetic procedure to obtain polymer brushes on graphene. SI-CuCRP is performed on graphene modified with PDA/BiBB (indicated by green color). SIPGP is used to graft St directly on graphene. All reactions are processed with pristine graphene or PDA/BiBB modified graphene transferred onto SiO_2 support (not shown).

Expectedly, SI-CuCRP resulted in rapid polymer brush growth giving 20 - 50 nm thick polymer layers for styrenic monomers after only 20 min of reaction **(Tab. 4.6)**. POEGMA and PEHMA brushes reached thicknesses up to 100 nm. Moreover, while PDA modified graphene (G/PDA) shows a θ_S value of ca. 48°, all of synthesized graphene based polymer carpets exhibit θ_S typical for the respective polymer brush. In addition, PEHMA brushes were grafted for longer time (45 min) and resulted in 500 - 1200 nm layer thickness **(Tab. 4.6)**. Most of the samples are very rough and height determination was performed with AFM, since ellipsometry could not be accurate due to insufficient reflection. In consequence, the shown thicknesses represent only strongly localized properties, especially for the thickest polymer carpets as they are inhomogeneous. Since mostly smooth surface is obtained with SI-CuCRP on rigid surface, this inhomogeneity probably originates from the buckling of the flexible graphene to locally release stress, which is induced by the grafting of the polymer brushes.

Table 4.6: Results of SI-CuCRP of different monomers on PDA/BiBB modified graphene. Successful grafting is proved by AFM measurements and change in θ_S. Raman signals of pristine G on SiO_2 already exhibit strong fluctuation before polymerization and no significant change can be observed after grafting. Ligand: PMDETA.

Polymer	Solvent	t_R [min]	d_{AFM} [nm]	θ_S [°]	Raman shift [cm^{-1}] G	2 D
G (on SiO_2)	-	-	-	90	**1575 - 1592**	**2666 - 2682**
G/PDA	-	-	18	48	n.d.	n.d.
PSt	DMSO	20	30 - 50	92	1588	2677
P4VP		20	20 - 50	68	1581	2669
POEGMA	iPrOH in H_2O (1:2)	20	50 - 100	60	1576	2682
PEHMA	Tol in DMSO (0.75:1)	20	~ 100	99	1585	2680
		45	**500 - 1200**	103	1582	2672

As can be seen in **Fig. 4.31**, G/PDA-g-PEHMA carpets actually buckle strongly reaching up to 470 nm high buckles. Similarly, G/PDA-g-POEGMA carpets wrinkles and buckles range between 20 - 220 nm in height. The thinner carpets from PSt and P4VP on the other hand exhibit regular and directed wrinkles ($d_{wrinkle}$ = 2 - 10 nm, **Fig. 4.31**). Their form leads to the assumption that they origin from the wrinkles observed in the graphene single layer. On one hand these might be enhanced by the grafting of polymer, on the other hand the wrinkling might enhance the grafting due to higher reactivity in this region. In any case neither these samples nor the carpets from PEHMA and POEGMA display significant changes in the Raman spectra in regard to the position or form of the G- and 2 D-band of pristine graphene on SiO_2 **(Tab. 4.6, Fig. 4.31)**. G-band of the samples ranges from 1576 cm^{-1} to 1588 cm^{-1} and 2 D-band from 2669 cm^{-1} to 2682 cm^{-1} falling into the mean variation of graphene. Furthermore, a baseline increase is observed for all samples. This can be ascribed to the fluorescence of the PDA layer. Since no band splitting is observed, no prove for modification of electronic properties in graphene is found. However, insufficient chemo-mechanical force is improbable regarding the wrinkling height and frequency. In contrast, the applied mechanical forces could be so strong that the underlying graphene sheet is destroyed by the grafting. As can be seen in the AFM scans of G/PDA-g-PSt and G/PDA-g-P4VP **(Fig. 4.31)**, small ruptures and defects can be observed even with low polymer brush thickness. Of course these are already present in the transferred graphene monolayer and not necessarily the result of grafting.

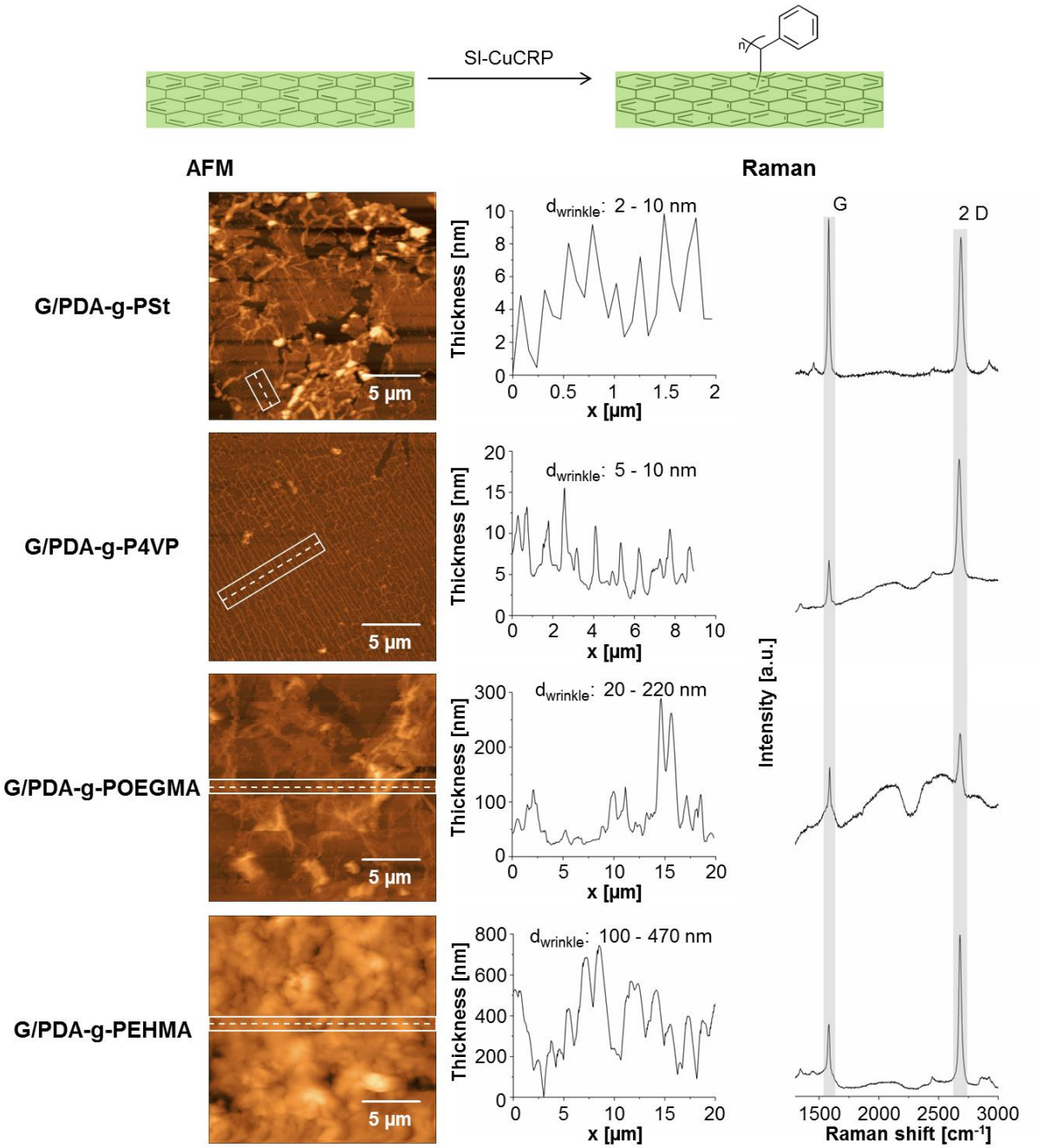

Figure 4.31: AFM scans (left), respective height profile (middle) and Raman spectra (right) of different polymer brushes on graphene synthesized by SI-CuCRP. For low thicknesses small directed wrinkles can be seen and defects are already observed in the layers. Wrinkles up to 470 nm are obtained with PEHMA brushes. Typical G-band and 2 D-band of graphene can be found in the Raman spectra and baseline increase is observed due to fluorescence of PDA. No band splitting is detected.

Still, the assumption that the graphene sheet is partly destroyed during polymerization is supported by the fact that G- and 2 D-band were often difficult to find on the samples and low in intensity. Especially for samples with thick polymer brushes it is often impossible to detect the graphene specific peaks in a lot of areas. The measured signals might therefore arise from residues of intact and stress-free graphene flakes on top of the polymer sheet or from non-

polymerized spots. Likewise, the above mentioned "worms" of residues lying on top of the sample might be measured. This would also explain why the intensity of the G-peak in the spectrum of G/PDA-g-PSt is higher than the intensity of the 2 D-peak (I_G/I_{2D} = 1.1) as it then comes from multi-layered graphene. Another explanation for overall low intensities may lie in the layer thickness of polymer on graphene. If the laser light cannot penetrate through the polymer layer well enough, the resulting Raman signals will be considerably low. Fluorescence of the PDA layer will additionally disturb the detection. To test this hypothesis the thick G/PDA-g-PEHMA carpet was transferred onto a TEM-grid and Raman spectra were measured from graphene side **(Fig. 4.32)**.

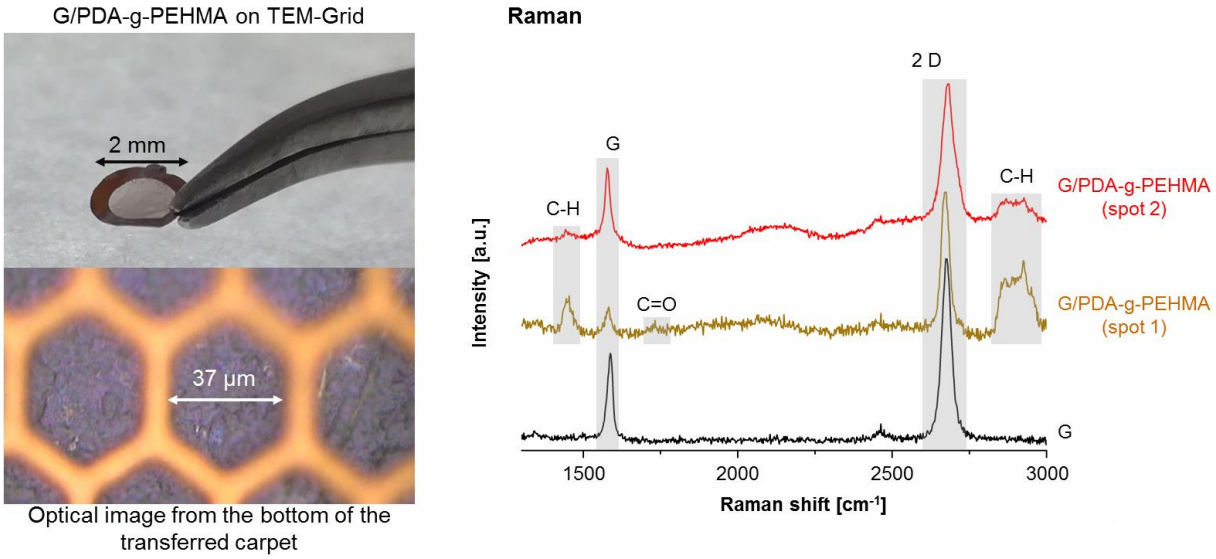

Figure 4.32: Optical images of a G/PDA-g-PEHMA carpet transferred on TEM grid (left). Raman spectra (right) were obtained by measurements from graphene exposing side. Similar to previous results baseline increase is visible. Signals from polymer brush are found with inconstant intensity, while no significant change of graphene bands is detectable.

The obtained spectra are dominated by polymer signals from C-H stretching (ca. 2850 - 3000 cm^{-1}) and deformation modes (1450 cm^{-1}) and vary in intensity. In some cases even a small signal from C=O stretching (1725 cm^{-1}) of the ester group is detectable. Graphene signals, however, were as difficult to find as before and do not show significant changes in comparison to pristine graphene (**Fig. 4.32** exemplarily shows two spectra with detected G- and 2 D-band). This finding reinforces the assumption of graphene being destroyed during grafting and that only residues are detected. If the monolayer was not damaged by the polymerization, then G- and 2 D-band should be detectable on each spot of the scanned area. This is further supported by very recent results of Goldsche and coworkers.[257] They used a device to mechanically apply strain on a single sheet of graphene.

Contrary to theoretical calculations, they observed rupture of the sheet already at low strain of 2 - 3 %. The main reason for this behavior was determined to be defects at the edges of the used graphene flakes through which cracks can propagate causing mechanical failure. As no graphene sheet is a perfectly assembled single layer, this explanation is also applicable for the herein investigated systems. However, Goldsche *et al.* also observed G-band spitting at even lower deformations of the graphene. Therefore, if grafting is performed in such a manner that graphene stays intact the chemo-mechanically applied strain should be still sufficient to observe such band splitting.

SIPGP is known to be applicable for the polymer brush synthesis on graphene.[11] In comparison to SI-CuCRP grafting density achieved with SIPGP is much lower and thus the resulting chemo-mechanical stress should be significantly less. At the same time the I_D/I_G ratio remains constant meaning no additional defects are introduced through the grafting.[11] PSt was grafted on graphene, as it is one of the best known monomers for SIPGP. To follow the formation of wrinkles different reaction times were used. As can be seen in **Figure 4.33**, polymer brush thickness increases slowly with increasing t_R and results in the formation of partly oriented wrinkles. Analogously, these grow in size as polymerization proceeds reaching 20 nm to 50 nm after 8 h. Interestingly, further grafting results in carpet buckling with comparable thickness (20 - 60 nm after 16 h) rather than building of wrinkles. These results are similar to the previous findings and suggest that the observed wrinkles are predetermined by those of pristine graphene in the early stages of the reaction. When polymer brushes grow further and grafting density rises the additional anisotropic stress might be released through stronger buckling and very rough polymer carpets are received. After 16 - 18 h of SIPGP carpets even tend to detach from the SiO_2 support. Additionally, AFM measurements of samples polymerized for long time often proved to be impossible, as the polymer carpet was dragged by the cantilever because of the weak adhesion to the SiO_2 surface. Similar results can be achieved with EHMA (0.5 - 2 h) as monomer (data not shown). The detachment might be explained by strong repulsion forces as a consequence of high chemo-mechanical forces induced by the grafting. The unavoidable cross-linking within the growing polymer brushes during SIPGP could even stabilize the layer and prevent destruction of the graphene sheet thereby enabling high strain. However, polymer grafted directly to the SiO_2 can also be found and might explain the detachment as well. Zhang demonstrated that graphene can be "transparent" to monomer and grafting can start beneath, if initiator is present.[281] Equally, Steenackers *et al.* saw polymerization between the sheets of multi-layered graphene.[11] Such polymer growth can weaken adhesion to surface and eventually break the graphene sheets.

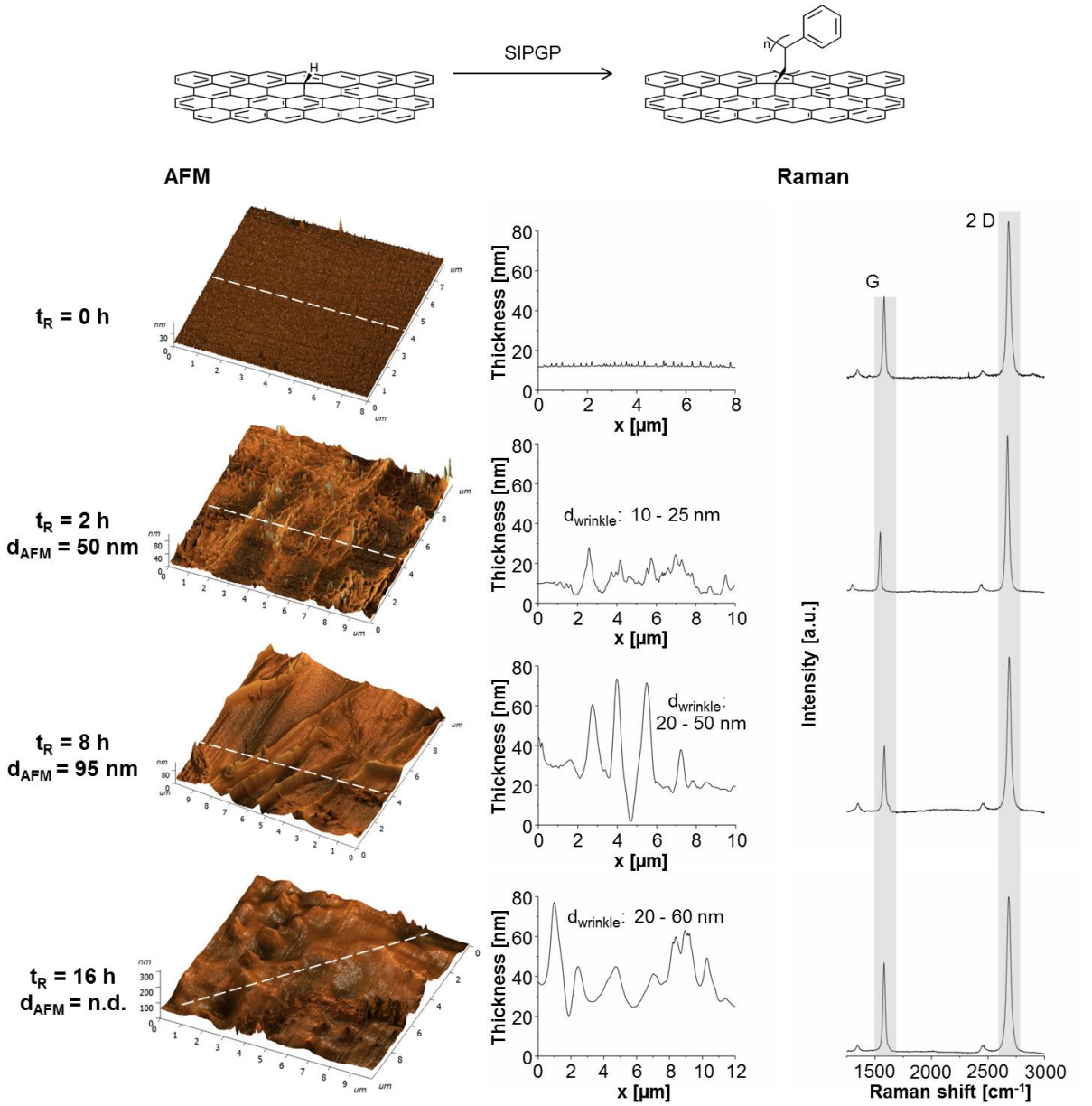

Figure 4.33: AFM scans (left), respective height profile (middle) and Raman spectra (right) of PSt brushes on graphene synthesized by SIPGP. AFM displays the arising of wrinkles, increasing in size with increasing grafting time. Typical G-band and 2 D-band of graphene without significant changes in signal position, width or form are found in the Raman spectra.

The latter is again supported by the difficulties to find graphene signals in the Raman spectra of thick polymer carpets. The detected G- and 2 D-bands do not differ from signals of the Raman spectra of pristine graphene. At 1600 - 1615 cm^{-1} the C=C stretching of PSt can be found (**Fig. 4.33**, t_R = 8 h) in some samples. Other than that neither signal splitting can be seen nor significant red shifts and thus no prove is obtained for a possible straintronic effect. Beside the possible destruction by the polymer grafting described above, the laser used for the Raman measurements could be a reason that no changes are observable. On one hand the resolution could be a limiting factor prohibiting the characterization of localized strain due to

overlaying signals of stress-free graphene. On the other hand intensity of G^- and G^+-band as well as 2 D^- and 2 D^+-band is strongly dependent on laser polarization in relation to strain axis.[205,207] Considering the non-uniform nature of the buckles and wrinkles of the graphene based carpets it is impossible to find the optimal orientation of the sample towards the laser in a controllable way. Hence, a high resolution of the band splitting might be problematic.

In summary, grafting of polymer brushes on graphene *via* both SI-CuCRP and SIPGP expectedly leads to formation of wrinkles (for thinner polymer brushes) and buckles (for thicker polymer brushes). Evidence for a straintronic effect could not be provided, although a range of wrinkle and buckle height from tens to hundreds of nanometers is covered. However, it is suspected that the induced strain leads to rupture and destruction of the graphene sheet, while grafting density and polymer brush thickness increase during reaction.

4.3.2 Grafting of polymer bottle-brush brushes on graphene

As stated above polymer BBBs should enable an effective transfer of steric repulsion force onto the graphene sheet. Even though polymer brushes are suspected to destroy the underlying single layer, the well-defined shape of wrinkles observed with POx BBBs on PDA based carpets promises to be a suited system for introduction of chemo-mechanical force for strain-engineering. As can be seen in **Figure 4.34**, SIPGP was first applied to graft polymer brushes from iPOx. These were converted *via* LCROP to give POx BBBs from 2-methyl-2-oxazoline (MeOx), 2-ethyl-2-oxazoline (EtOx), 2-isopropyl-2-oxazoline (iPrOx), 2-propyl-2-oxazoline (nPrOx) or 2-butyl-2-oxazoline (BuOx). Similarly, SI-CuCRP was applied to synthesize PSt and PEHMA BBBs on graphene after SIPGP of HEMA and subsequent conversion with BiBB **(Fig. 4.34)**.

The successful polymerization on graphene was proved by static water contact angle measurement and AFM **(Tab. 4.7)**. Both monomers used for SIPGP showed typical θ_S for the respective polymer brush, which is 60° for PHEMA and ~ 50° for poly(2-isopropenyl-2-oxazoline) (PiPOx). Typically, thickness of G-g-PiPOx lies between 40 - 60 nm after 24 h of grafting, while PHEMA brushes were 30 - 60 nm in height after 2 h **(Tab. 4.7)**. The chosen reaction times depend on the used monomer, as the viscosity increase caused by the polymerization in substance prohibits further grafting. Additionally, BBB synthesis will lead to height increase due to steric repulsion of the polymeric side-chains, so that higher polymer brush thickness is not desired in regard to possible rupture of graphene. To exclude polymerization beneath the graphene, SIPGP was also carried out with graphene on Cu-foil.[11] This approach also ensures the absence of PMMA residues as no transfer is needed.

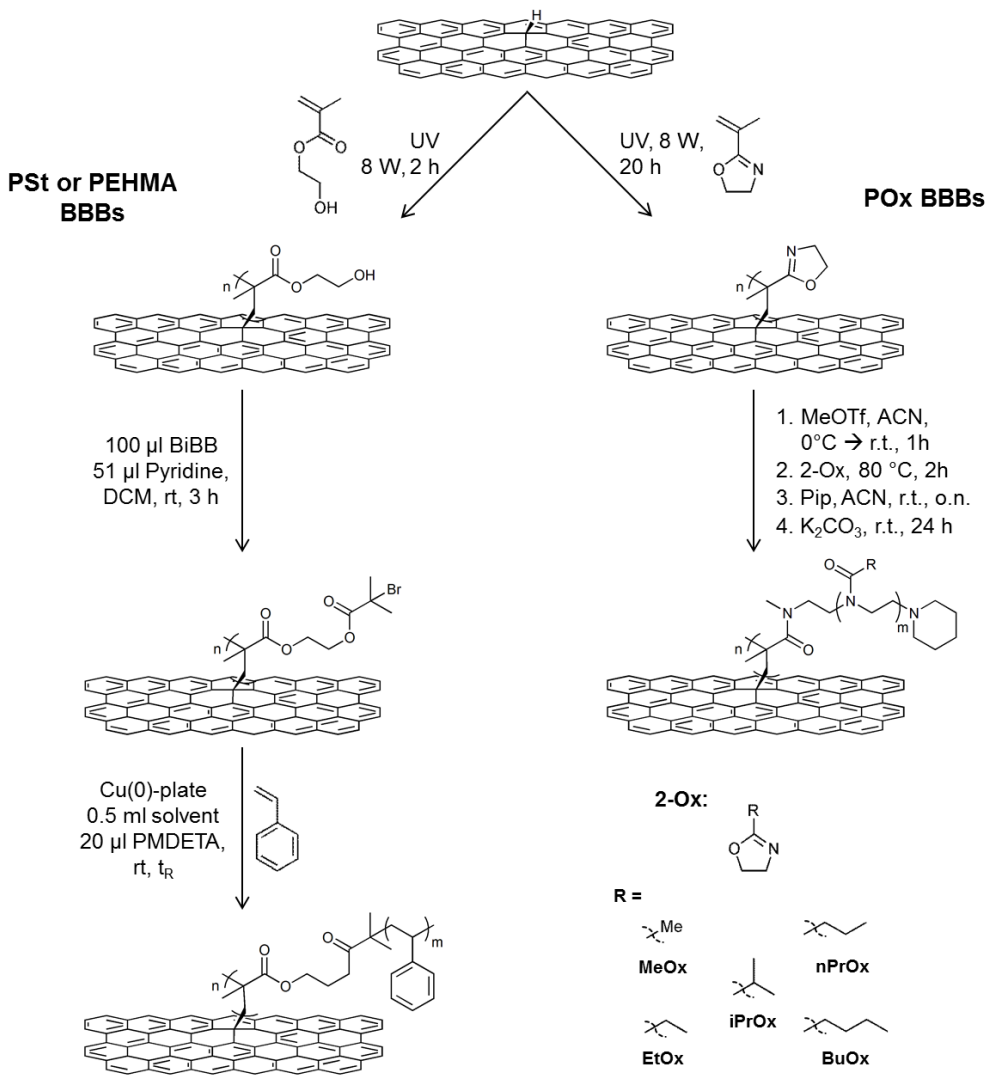

Figure 4.34: Schematic illustration of the synthetic procedure to obtain polymer BBBs on graphene. SIPGP is used to graft HEMA or iPOx directly on graphene. Subsequently, LCROP is carried out with PiPOx brushes for synthesis of POx BBBs. PHEMA brushes are converted with BiBB and SI-CuCRP is performed to obtain BBBs from St and EHMA. All reactions are processed on SiO_2 support (not shown).

Grafting efficiency of SIPGP is reduced, when performed on Cu-foil due to reduced reflectivity and lack of constructive interference. Therefore, achieved thicknesses are noticeably lower and inhomogeneous G-g-PHEMA carpets are received with θ_S between 70 - 90°. To overcome this issue, sequential SIPGP (6 x 30 min) was applied and results in 20 - 50 nm thick PHEMA brushes on graphene (analyzed with AFM after transfer onto SiO_2). In comparison to SIPGP on SiO_2 support, however, this method did not prove to be advantageous and gives comparable results in the following steps. Due to the relatively low polymer brush thickness a possible destruction of graphene probably does not play a role at that stage of the synthesis.

Table 4.7: Synthesis results of different BBBs on graphene. PHEMA was synthesized *via* SIPGP and converted with BiBB. SI-CuCRP of St and EHMA leads to strong thickness increase reaching polymer brush heights of over 1 µm. Ligand: PMDETA.

Polymer	Solvent	t_R [min]	d_{AFM} [nm]	θ_S [°]	Raman shift [cm^{-1}] G	Raman shift [cm^{-1}] 2 D
G (on SiO_2)	-	-	-	90	**1575 - 1592**	**2666 - 2682**
PHEMA (SIPGP)	-	120	30 - 60	60	1578	2678
PSt BBB	DMSO	5	20 - 150	98	1580	2667
		10	50 - 140	97	1580	2682
		20	50 - 250	96	1582	2684
		40	**> 500**	100	1580	2671
PEHMA BBB	Tol in DMSO (0.75:1)	5	50 - 80	80	1580	2666
		10	150 - 250	100	1582	2678
		15	**200 - 1800**	100	1580	2670
		40	**1000 - 5000**	117	1585	2678

After functionalization with initiator PSt and PEHMA side-chains were grafted on the PHEMA carpets *via* SI-CuCRP. Depending on t_R layer thickness increases because of the high steric pressure on the polymer backbone **(Tab. 4.7)**. The so synthesized PSt BBBs reach overall thickness of over 500 nm after 40 min of polymerization, which corresponds to a height increase of more than 1000 %. Analogously, PEHMA BBBs grow to a thickness of up to 1800 nm after only 15 min (3000 %) and 1 - 5 µm (1600 - 9000 %) after 40 min of SI-CuCRP. The BBB carpets possess a very inhomogeneous and rough surface **(Fig. 4.35)**.

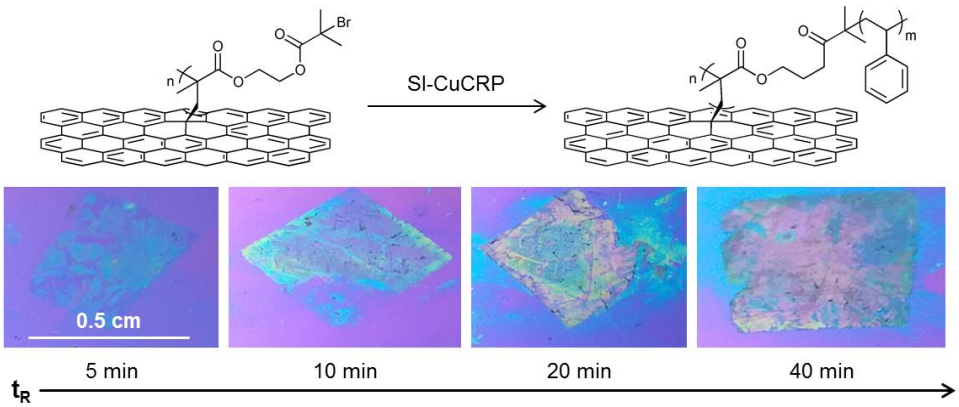

Figure 4.35: Photographs of PSt BBBs on graphene after different grafting times of the PSt side chain. Layer thickness of the BBB increases with increasing reaction time. The received polymer carpets are often inhomogeneous and are partly destroyed during the SI-CuCRP.

The shown thicknesses represent typical values determined with AFM and are difficult to evaluate as they strongly vary even locally due to strong buckling **(Fig. 4.36)**. The noticeably faster growth of PEHMA BBBs can be explained by faster polymerization of the monomer in SI-CuCRP and the sterically demanding side-chain of EHMA. Still, both monomers expose buckles from hundreds of nanometers to ca. 2000 nm after 40 - 45 min, which is a huge enhancement of the wrinkles in PHEMA carpets ($d_{wrinkle}$ = 2 - 18 nm, **Fig. 4.36**) and the highest values achieved so far.

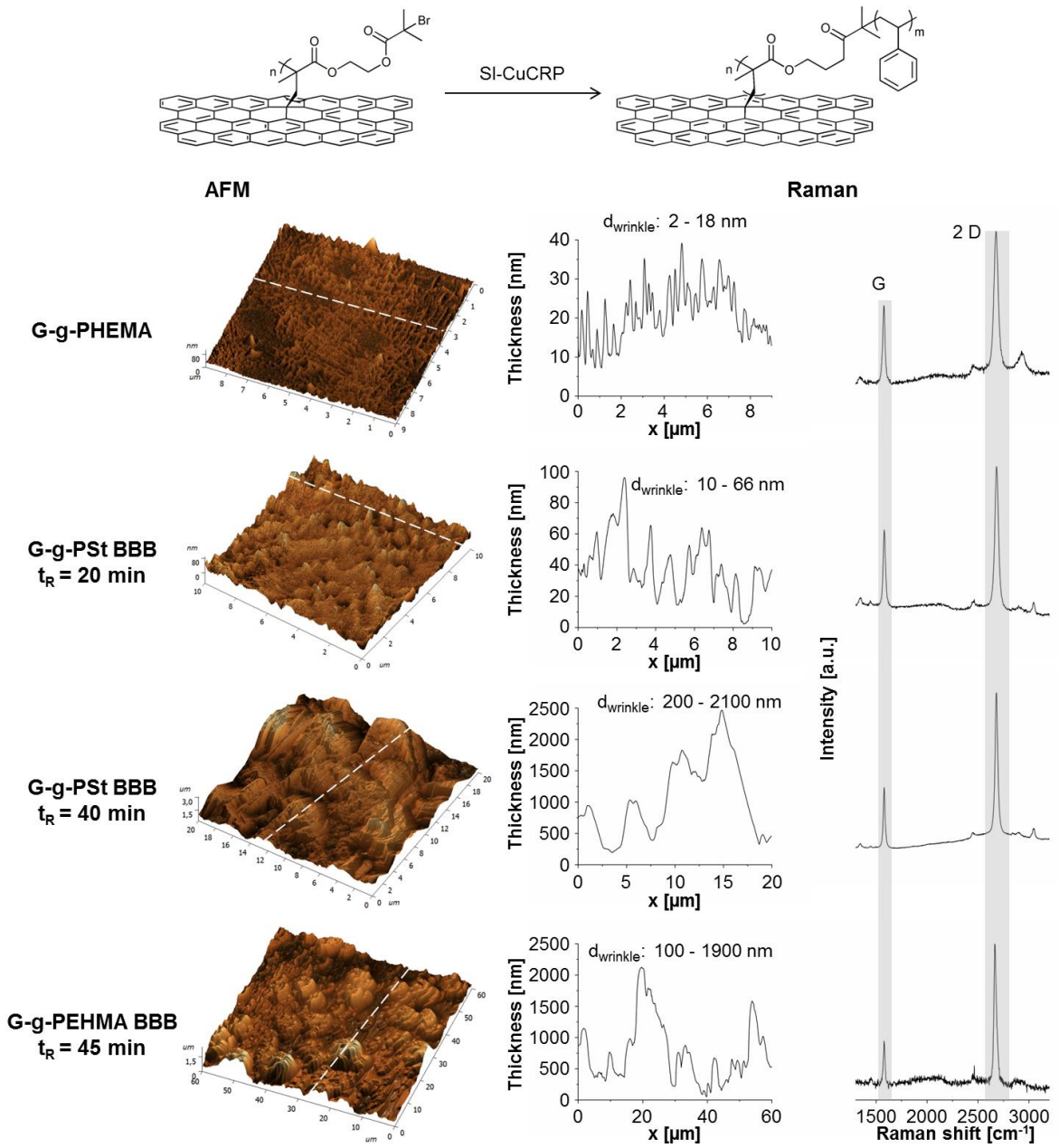

Figure 4.36: AFM scans (left), respective height profile (middle) and Raman spectra (right) of BBBs on graphene synthesized by SI-CuCRP. BBB thicknesses and wrinkles ranging from hundreds of nanometers to micrometers are achieved. G-band and 2 D-band of graphene are often difficult to find in the Raman spectra. No significant changes in signal position, width or form are observed when spots with clear graphene signals are measured.

Grafting of PHEMA brushes introduces large quantity of functional groups, which then are converted with BiBB. If the following SI-CuCRP is nearly as effective as on surface-bound initiator and polymer chain length is comparable, the immense height increase and buckling is well-founded. Consequently, the steric pressure on the polymeric backbone and thus resulting strain on the graphene sheet are extremely high.

The photographs in **Fig. 4.35** display non-polymerized and destroyed areas within the polymer carpets. In case of $t_R = 5$ min such large defects are probably the consequence of stress during transfer processes. However, black particles can be seen on all carpets as well and could be residues of destroyed graphene, which was ruptured during the grafting of the BBB side-chains. Looking back at the results achieved with polymer brushes on graphene and considering the measured thicknesses on the BBB carpets such destruction seems most likely. Once again this assumption is reflected in the Raman spectra where G- and 2 D-band were difficult to detect. The found signals are inconsistent in intensity and lie in the range of 1580 cm^{-1} to 1585 cm^{-1} for the G peak and from 2666 cm^{-1} to 2684 cm^{-1} for the 2 D peak **(Tab. 4.7, Fig. 4.36)**. Furthermore, polymer signals from alkyl C-H stretching at ~ 2900 cm^{-1} and deformation at ~ 1450 cm^{-1} as well as aromatic C-H stretching (for PSt BBBs) at ~ 3050 cm^{-1} are prominent. Evidence for a change in electronic properties of graphene is not obtained within the detected spectra of all synthesized BBB carpets. Beside graphene destruction the same reasons can be listed for these results as for the polymer brush systems, i.e. laser resolution and polarization limitations. One more problem of signal detection in Raman spectroscopy might arise from the applied strain itself. Raman scattering mechanism is promoted by bond vibration. If the steric pressure is transferred from polymer brushes to the graphene layer, the induced deformation could lead to "stiffening" of the carbon bonds. Thereby vibrations would be limited and thus signal generation would be suppressed in intact graphene. This explanation can be specifically applied to BBB carpets, since the polymeric side-chains produce extreme steric repulsion. Moreover, it is another rationalization why detection of G- and 2 D-band was challenging, even when Raman spectra were measured on the graphene exposing side **(Fig. 4.32)**. As discussed previously the acquired spectra then come from residual graphene flakes on the sample and signals from the modified single sheet remain undetectable. Unfortunately, that would also label the verification of band gap opening *via* Raman spectroscopy nearly impossible for graphene with densely grafted polymers.

POx BBB synthesis by LCROP of 2-oxazolines was equally successful. In comparison to the BBBs synthesized *via* SI-CuCRP thickness gain is lower and overall height of the carpets after 2 h of polymerization reaches ca. 200 nm ($d/d_0 = 500$ %), 500 nm ($d/d_0 = 800 - 900$ %)

and 170 nm (d/d_0 = 300 %) for BBBs from MeOx, EtOx and iPrOx, respectively **(Fig. 4.37)**. The different degree of thickness increase can be explained by different reaction rates of the monomers, different steric demand of the alkyl groups as well as different swelling behavior at ambient conditions. Just as before POx BBB carpets are very rough and inhomogeneous. AFM measurements for characterization only give localized properties and therefore the received values can differ depending on the scanning spot. It still becomes obvious that wrinkling and buckling is enhanced after LCROP **(Fig. 4.37)**.

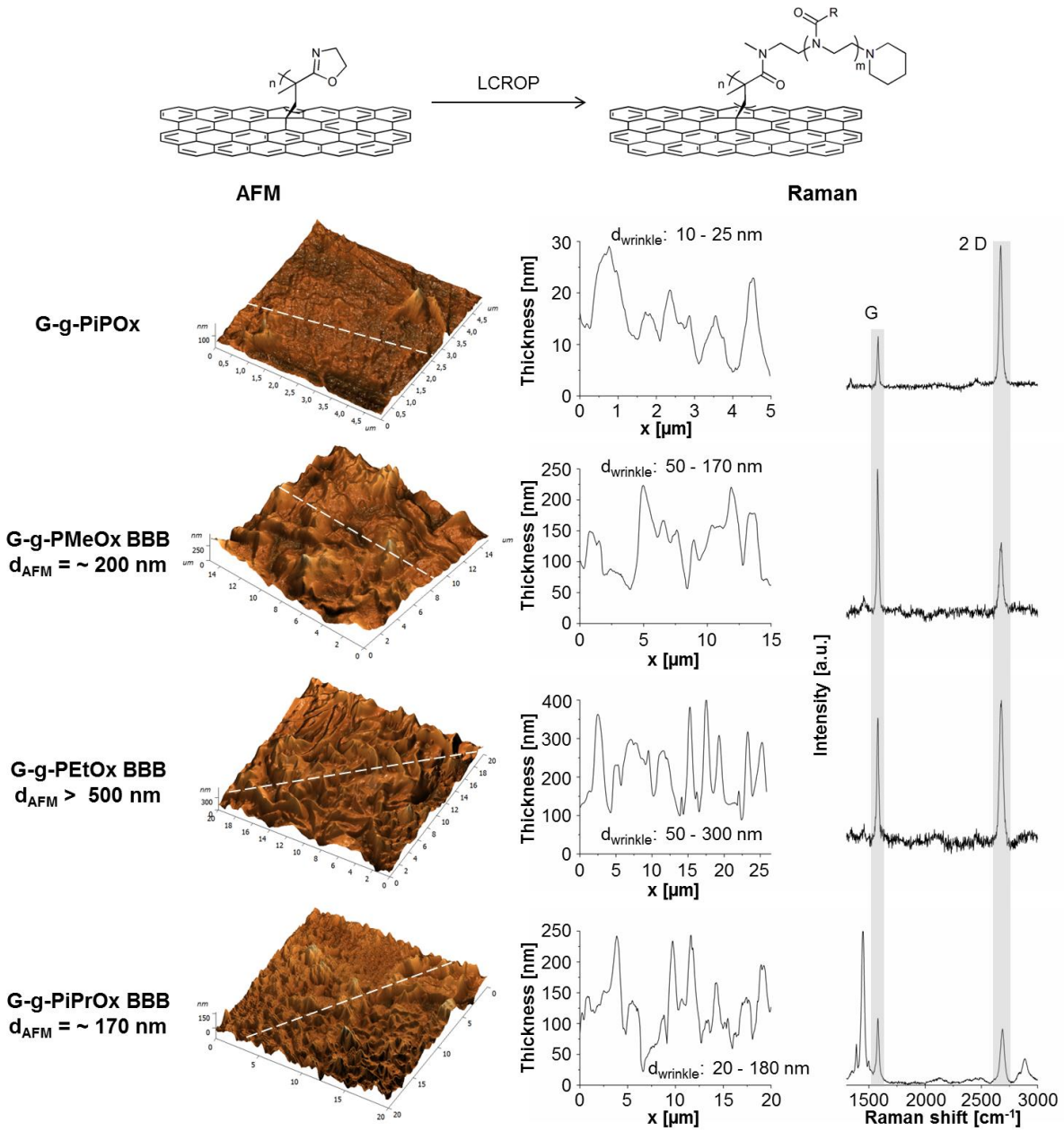

Figure 4.37: AFM scans (left), respective height profile (middle) and Raman spectra (right) of POx BBBs on graphene synthesized by LCROP. BBB thicknesses and wrinkles within a range of hundreds of nanometers are achieved. Typical G-band and 2 D-band of graphene can be found in the Raman spectra. However, no significant changes in signal position, width or form are observed.

The height of the wrinkles and buckles can be found between tens (20 - 50 nm) and hundreds of nanometers (170 - 300 nm). In comparison to the foregoing systems all of the POx BBBs showed a higher tendency to build actual wrinkles instead of buckles although polymer carpets already were thick. That can particularly be seen in the AFM scan and profile of BBBs from EtOx (G-g-PEtOx in **Fig. 4.37**). On that sample the wrinkles are well-defined and comparably frequent, which was aimed for with the utilization of POx. Despite the observed tendency wrinkle shaping is not as defined on graphene based systems as on POx BBB carpets from PDA. Bearing in mind that the deformation of the carpet will be also determined by the mechanical properties of the polymer brush (or BBB) exposing scaffold, this result is not surprising. In literature the Young´s modulus of PDA can be found to lie in the range of 4 - 10 GPa[76,159], while graphene reportedly exhibits a value of 1 TPa[185]. This difference of at least two orders of magnitude plausibly explains, why PDA is stronger deformed by the sterically induced chemo-mechanical forces than graphene.

The stronger wrinkling in comparison to the other investigated graphene BBB carpets does not bring about detectable band gap opening. Polymer signals can be detected with Raman spectroscopy **(Fig. 4.37)** at ca. 1450 cm^{-1} (δ C-H) and 2900 cm^{-1} (ν C-H). In case of BBBs from iPrOx (G-g-PiPrOx BBB in **Fig. 4.37**) these signals even dominate the spectrum. With the previously named problems G- and 2 D-band can also be found, but do not differ significantly from pristine graphene in signal position. Interestingly, the intensity ratio I_G/I_{2D} is often comparably high for POx BBB carpets (0.9 - 1.9). While inconsistency of the ratio is known to occur in pristine graphene[280], it is not observable to such extent for the other systems, which were synthesized from the same graphene batch (I_G/I_{2D} = 0.5 - 1.1). Since an increase of I_G/I_{2D} indicates multi-layered graphene[277,278], it can be concluded that grafting of POx BBBs and the consequential wrinkling might lead to efficient deformation and thereby overlapping of graphene. A small shoulder can be seen in the 2 D-band of G-g-PiPrOx BBBs at around 2620 cm^{-1} **(Fig. 4.38 d)**. As Ferrari *et al*. pointed out, the 2 D peak in multi-layer graphene originates from inequivalent scattering pathways due to the multi-layered energetic structure of the Dirac cones **(Fig. 4.38 a, b)**.[277] Consequently, 4 different signals, i.e. 2 D_{1B}, 2 D_{1A}, 2 D_{2A} and 2 D_{2B}, can be fitted into the 2 D peak of bilayer graphene **(Fig. 4.38 c)**. This was accordingly done for the 2 D-band of G-g-PiPrOx BBBs **(Fig. 4.38 d)**. Similar to the finding of Ferrari *et al.* the peaks arising from scattering paths 1B and 2B have lower intensity than from 1A and 2A. In addition, the distances between the fitted curves are 52 cm^{-1} (2 D_{1B} - 2 D_{1A}), 13 cm^{-1} (2 D_{1A} - 2 D_{2A}) and 15 cm^{-1} (2 D_{2A} - 2 D_{2B}) and match well with those observed for bilayer graphene (44 - 55 cm^{-1}, 10 cm^{-1} and 25 - 30 cm^{-1}, respectively)[277].

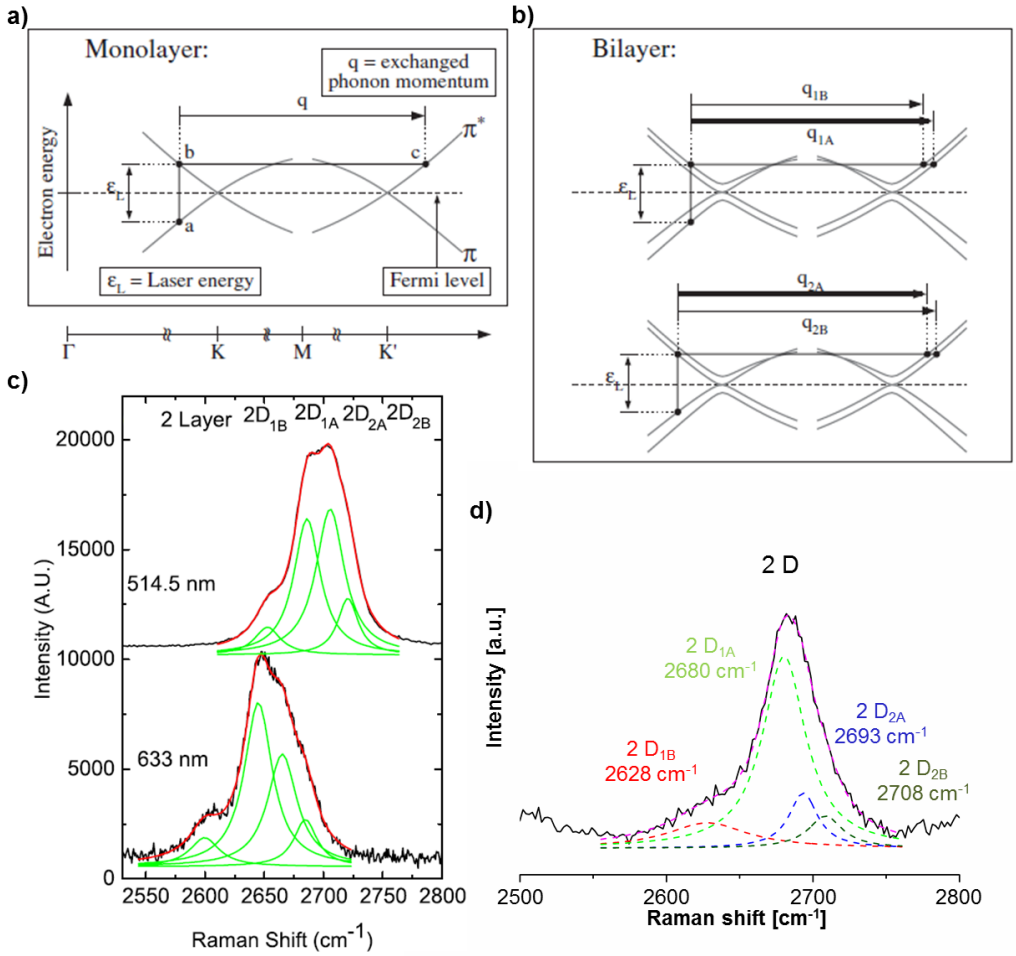

Figure 4.38: Schematic illustration of possible electron scattering paths in the Dirac cones of a graphene single layer (a) and bilayer (b). Arising from inequivalent scattering paths 1B, 1A, 2A and 2B, the 2 D-band of bilayer graphene splits into four signals 2 D_{1B}, 2 D_{1A}, 2 D_{2A} and 2 D_{2B} (c) (taken from Ref.[277] and modified). Likewise, four signals can be fitted into the 2 D-band of the synthesized G-g-PiPrOx BBBs (d).

These results further support the assumption of overlapping graphene and it can be hypothesized that the formed bilayers are seen in the Raman spectrum. However, no similar features concerning the 2 D signal are found in the spectra of the other POx BBBs and background noise as well as inconsistency of the baseline in all of the samples´ spectra **(Fig. 4.37)** cannot be neglected. Therefore, an evaluation of this hypothesis is difficult. Furthermore, evidence of sufficiently strained graphene, which is expected after strong deformation, is not provided as no band splitting can be seen in the Raman spectra. Hence, the obtained signals may arise from residual graphene on top of the samples as it was speculated before and as supported by the recurring difficulties of detection. The discussed possible limitations of Raman spectroscopy considering resolution, polarization and hindrance of signal generation are also applicable for POx BBBs on graphene.

All in all, BBB carpets based on graphene were successfully synthesized *via* a combination of SIPGP and SI-CuCRP or LCROP of 2-oxazolines. Introduction of wrinkles and buckles ranging from tens of nanometers up to several micrometers is possible with these systems due to strong steric repulsion of the polymeric side-chains. Especially, POx BBBs deliver more defined wrinkles than other BBBs or polymer brushes and Raman spectra suggest that graphene may be stacked by the deformation. Still, no straintronic effect could be confirmed. Like before it cannot be excluded that graphene is destructed during the grafting process.

4.3.3 Patterning of graphene based polymer carpets

Patterning of polymer carpets leads to anisotropic stress release, which results in pronounced and directed wrinkling. This was demonstrated by Amin *et al*. on cross-linked 4'-amino-1,1'-biphenyl-4-thiol[10] and also proved to be true for patterned polymer carpets from PDA (see **chapter 4.2.4**). To explore the influence of patterning on graphene based carpets, different photolithographic approaches were applied during the synthesis of the afore investigated systems. For negatively patterned brushes, SIPGP was carried out with a TEM-grid fixed on the graphene sheet, so that covered regions would not initiate grafting. LCROP of MeOx on so prepared G-g-PiPOx results in negatively patterned PMeOx BBBs. Positive patterns were received by selectively cleaving Br-initiator *via* UV exposure (200 W, 45 min) using a TEM-grid as photomask. Then, SI-CuCRP was performed on the so prepared surface. For positively patterned BBBs, PHEMA was grafted on graphene *via* SIPGP and functionalized with BiBB. After selectively cleaving initiator with UV-light, SI-CuCRP was performed.

The synthesis of polymer brushes on graphene was successful *via* SIPGP and SI-CuCRP and gave the desired pattern predetermined by the used TEM-grid **(Fig. 4.39)**. It has to be stated that different geometries of the photomasks as well as different grafting times were screened for the polymer brush synthesis. The herein displayed samples were chosen to represent the most intriguing results considering their morphology or Raman spectrum. In general, SI-CuCRP of EHMA leads to polymer brushes comparably inhomogeneous as without pattern. However, stronger wrinkling can be observed with wrinkle height between 100 nm and 350 nm **(Fig. 4.39)** within polymer grafted regions. Furthermore, the wrinkles are partly directed orthogonally to the polymer pattern. Interestingly, directed wrinkling can also be seen within non-polymerized areas (scan with enhanced contrast, **Fig. 4.39**). In these parts the measured values ($d_{wrinkle}$ = 2 - 35 nm) are comparable with wrinkles obtained on non-patterned carpets with low polymer brush thickness ($d_{wrinkle}$ = 2 - 25 nm, **Fig. 4.31 and 4.33**) and are similar in shape to those in pristine graphene.

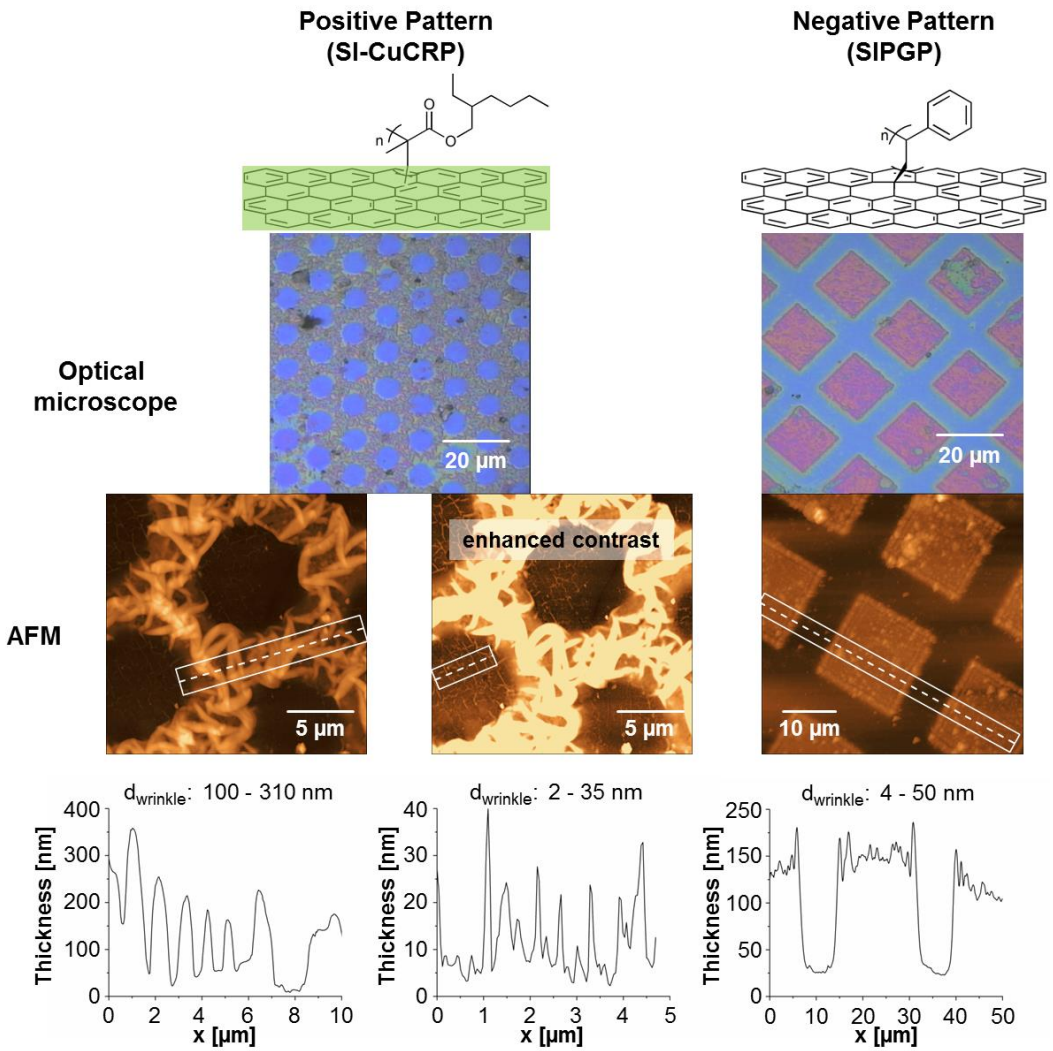

Figure 4.39: Optical microscopy pictures and AFM scans with corresponding profiles of patterned polymer brushes on graphene. SI-CuCRP on patterned initiator layer was applied to obtain positively patterned brushes and SIPGP was used for negative pattern. Strong and partly directed wrinkling was observed for brushes patterned *via* SI-CuCRP even in non-polymerized area.

That the higher thickness arises because of enhanced reactivity of the wrinkles can be ruled out in this case, since no grafting is possible in these initiator-free spaces. PDA used to bind the initiator will also not affect their height, as dopamine deposition is known to form homogeneous layers independent of substrate. As hypothesized previously this type of wrinkles are a result of chemo-mechanical force and enhancement of graphene folding. In addition, the directed wrinkling in the polymerized parts of the sample indicates the desired anisotropic stress release due to the patterning. This is supported by the fact that wrinkling wavelength ($\lambda = 0.5 \pm 0.2$ µm) is much lower than the dimension of the pattern (~ 15 µm) and might contribute to a stronger folding of graphene.

Negative patterns from PSt grafted *via* SIPGP (200 W, 2 h) on graphene look somewhat different. Although 120 nm thick polymer brushes are synthesized, the morphology of the polymerized regions is relatively smooth in comparison to SI-CuCRP samples. Fluctuations in thickness ($d_{wrinkle}$ in **Fig. 4.39**) lie between 4 nm and 50 nm, display no actual wrinkling and can be attributed to different polymer chain lengths. Moreover, no wrinkling between the polymer brushes can be detected and grafting through a different photomask did not lead to substantial changes. These differences most probably come from different grafting densities achieved with both methods. While SI-CuCRP can reach outstanding grafting density of ~ 1 chain/nm^2[12], the SIPGP as a free radical polymerization cannot match this value. So, induced steric pressure is significantly lower and the chemo-mechanically applied force does not result in wrinkling of the polymer carpet. To overcome this limitation, PDA was deposited on graphene before SIPGP. In fact, SIPGP under otherwise identical conditions gives patterned polymer carpets of G/PDA-g-PSt with thickness of around 950 nm (profile 3, **Fig. 4.40**). In contrast to samples without PDA strong folding can be seen in the polymerized areas with wrinkle heights comparable to those reached with SI-CuCRP ($d_{wrinkle}$ = 40 - 360 nm, profile 1, **Fig. 4.40**).

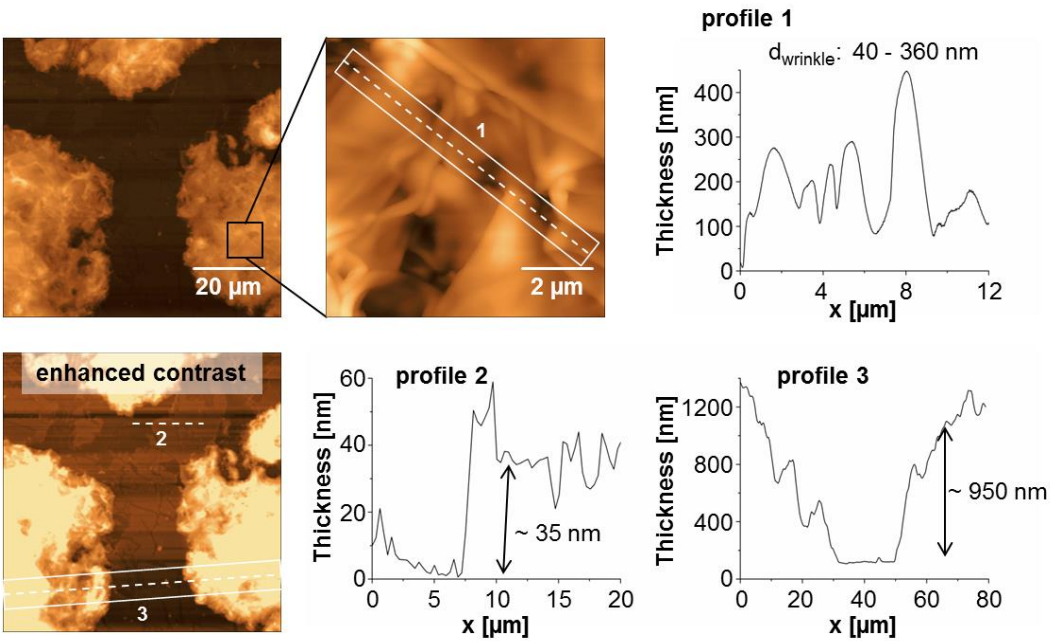

Figure 4.40: AFM scans with corresponding profiles for negatively patterned PSt brushes on G/PDA. SIPGP is strongly enhanced by use of PDA. Strong wrinkling with thicknesses comparable to those achieved with SI-CuCRP can be partly seen in the scans. Moreover, cracks in the non-polymerized area display destruction of the graphene layer.

By deposition of PDA functionalities including primary and secondary amines are introduced on the surface. Bond dissociation energies (BDEs) of N-H normally lie within 350 - 400 kJ/mol depending on the chemical structure of the component.[282] Graphene on the other hand offers C-H bonds of sp^3-hybridized C-atoms found in the defects of the layer. These BDE values are typically higher than 400 kJ/mol.[283] Since hydrogen abstraction is necessary to form surface-bound radicals and start grafting, initiation on PDA surface will be therefore more efficient. Even if sp^2-carbon of graphene may stabilize a formed radical, thereby decreasing the BDE, the quantity of functional groups suited to start grafting remains sufficiently higher in PDA. However, neither wrinkling between the polymer brush regions nor directed wrinkling is observed with positive patterns. Instead cracks appear in the non-patterned parts as well as in the rim of the pattern (AFM scan with enhanced contrast, **Fig. 4.40**). The height of these defects is around 35 nm (profile 2, **Fig. 4.40**) and corresponds with the PDA layer thickness. Similar results are achieved with rectangular photomask.

It was previously stated that the applied strain arising from steric repulsion of the grafted polymer brushes may be high enough to destroy the underlying graphene sheet. This would also explain the observed holes within the layer. Most intriguingly cracks are not as frequent and large in the positively patterned sample. In best case such pattern provides a continuous polymer brush layer and non-polymerized “isles”. Chemo-mechanical stress can therefore spread through the material, effectively pulling and compressing the whole polymer carpet. In negatively patterned samples, however, the isles are built by the polymer grafted parts. Hence, compressive strain is strictly localized. As a result the non-polymerized areas between the isles of polymer brushes are strongly pulled apart, which eventually leads to rupture of the sheet. In any case, the strain should be visible in Raman spectra.

For the spectroscopic characterization of the samples shown in **Figure 4.41** reflectivity measurements using a photomultiplier tube (PMT) as well as Raman mapping were performed. The obtained scans expectedly display inverse intensity distribution of reflectivity and Raman signal for the negatively patterned brushes **(Fig. 4.41 a, b)**. Since the polymer carpet is supported by a SiO_2 wafer, the background excellently reflects the laser light. Polymer grafted spots on the other hand can effectively absorb and scatter the light. Raman signals in these areas are more intense due to the signals and slight fluorescence of the PSt brushes. For positively patterned carpets the distinction becomes more problematic because of dissimilar scattering within the polymer brushes and wrinkles. PDA fluorescence, which is evident from baseline increase in the Raman spectra of G/PDA-g-PSt **(Fig. 4.41 c)** and carpets patterned *via* SI-CuCRP (3 and 4 in **Fig. 4.41 c**), further reduces contrast in the scans.

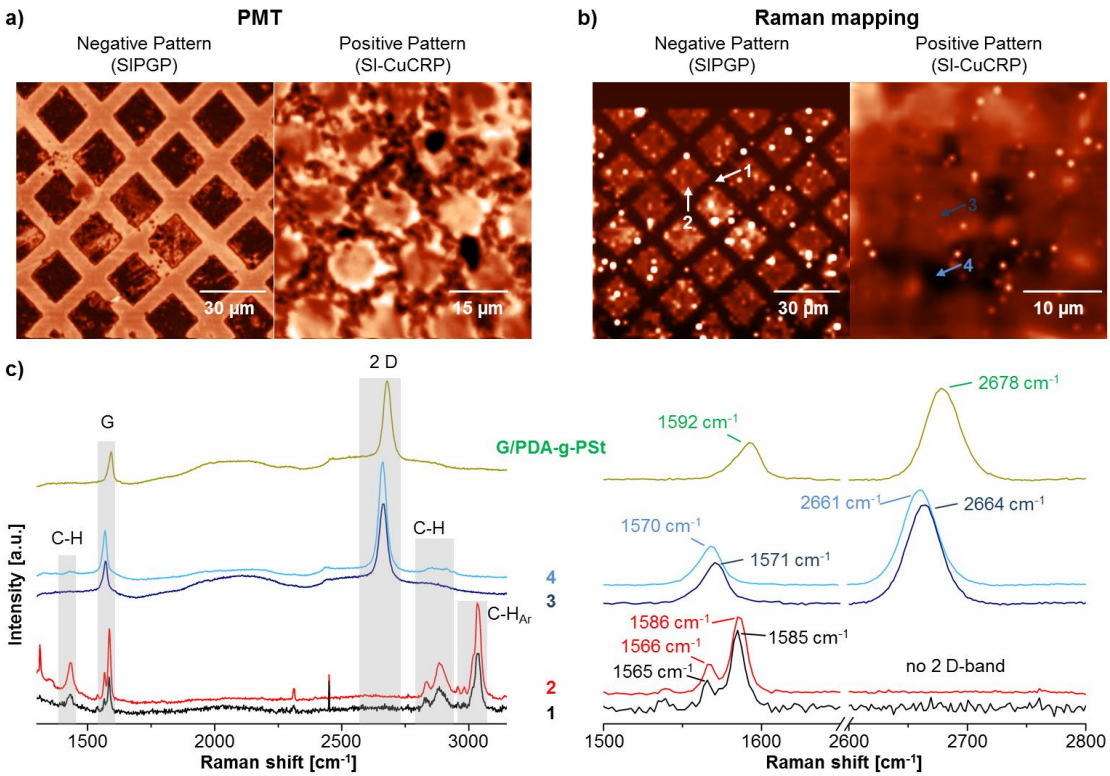

Figure 4.41: Scans of PMT (a) and Raman mapping (b) of patterned polymer brushes with corresponding Raman spectra (c) as indicated by the numbers. PMT and Raman scans display inverse intensity distribution. No significant changes in signal position can be observed between patterned and non-patterned areas and range within the mean variation of pristine graphene. Patterned G-g-PSt carpets (1, 2 in c) mainly exhibit polymer signals.

Obviously the spectra of all samples (G/PDA-g-PSt included) do not differ significantly between polymerized (2 and 4 in **Fig. 4.41 c**) and non-polymerized spots (1 and 2 in **Fig. 4.41 c**). This observation is somewhat surprising for the negatively patterned G-g-PSt carpets (1 and 2 in **Fig. 4.41 c**), since both spectra are dominated by polymer signals, i.e. aliphatic (2833 cm^{-1}, 2885 cm^{-1}) and aromatic (3033 cm^{-1}) C-H stretching as well as C-H deformation (1435 cm^{-1}). No polymer should be present in areas which were covered by the photomask during synthesis (SIPGP). The reason for the detected signals may lie in the diffusion of monomer beneath the used TEM-grid. Then, styrene could be ineffectively grafted by scattered UV-light or promoted by π-π stacking rather robustly stick to graphene. Likewise, polymer formed in solution could be deposited. Such residues might withstand the cleaning process, since no ultrasonication was applied to prevent carpet destruction. At a Raman shift of ca. 1585 cm^{-1} and 1565 cm^{-1} two peaks can also be seen in the spectrum of G-g-PSt (1 and 2 in **Fig. 4.41 c**). While their position corresponds with G-band position and might indicate strong strain and resulting signal splitting, PSt exhibits the same double-peak pattern in its spectrum at around 1602 cm^{-1} and 1582 cm^{-1}[284–287]. Similar to graphene,

position shifts can be explained by doping effects from surface and residues. The total absence of the 2 D-band further supports this assumption and suggests that graphene signals are not observable on this sample. The other polymer carpets display G- and 2 D-bands without significant changes in comparison to pristine graphene (3 and 4 in **Fig. 4.41 c**). Though their position red shifts comparably strong to ~ 1570 cm^{-1} (G) and 2861 cm^{-1} (2 D) in the negative pattern, no prove of a straintronic effect is provided as long as no band splitting is observed (as argued in **chapter 4.3**). A slight shoulder in the G-band can be explained by the baseline fluctuation due to the PDA fluorescence.

All in all, same reasons can be named for the lack of band splitting as in previous experiments. Still, strong wrinkling, that hints towards efficient anisotropic stress relief, is generated by patterning of polymer brushes if PDA is deposited as interlayer. It is well researched in literature that adhesion of PDA is dependent on substrate type.[164–167,169] The linkage to graphene will be mainly realized by π-π stacking and dispersion interaction. The adhesion energy of the latter was determined to be ~ 0.2 mJ/m^2 for PDA on CH_3-terminated surface[167], while π-π stacking in poly(norepinephrine) (PDA analogue) exhibited a value of ~ 6.4 mJ/m^2[169]. Goldsche *et al.* observed rupture of graphene single sheets at ca. 412.5 mJ/m^2.[257] Even if the numbers for interaction of PDA and graphene do not represent exact values, it becomes obvious that required energies for layer separation and graphene destruction lie apart at least two orders of magnitude. So, if the chemo-mechanical stress applied by polymer brushes is sufficient enough to destroy graphene, it is also sufficient enough to overcome the adhesion energy of PDA. Thus, the observed wrinkling may be resulting from breach of respective interaction motifs and subsequent deformation of the PDA layer. The graphene sheet, however, remains unstressed and Raman spectra are not affected.

Eventually, patterned BBBs from PMeOx (negative) and PEHMA (positive) on graphene were investigated. For these samples no PDA was used as interlayer, so that the polymer backbone was directly grafted from the graphene sheet. As could be suspected from the foregoing results the following synthesis of polymer side-chains gives thick and inhomogeneous BBBs **(Fig. 4.42)**. G-g-PEHMA BBBs as well as G-g-PMeOx BBBs expose thicknesses between tens of nanometers (30 - 60 nm) up to ~ 1 µm in the polymerized areas. Formation of well-defined or directed wrinkles is not observed. Instead, the pattern appears to be scrunched up and big parts of non-grafted regions are clearly destroyed (optical microscope, **Fig. 4.42**). Similarly to negatively patterned polymer brushes the used patterns do not build a continuous polymer BBB layer. The resulting compressive strain might be therefore localized in the polymerized areas pulling the layer in-between in opposite direction

and causing its mechanical failure. In addition, the steric pressure within the BBBs is much higher than in polymer brushes, so that the tearing should be even more forceful. It might also explain why use of a positive hexagonal pattern did not bring about different morphology and samples are equally inhomogeneous. Precise control of the overall thickness is difficult to achieve, since SI-CuCRP is extremely rapid and gives BBBs of several hundreds of nanometers after only 5 - 10 min of grafting (see **Tab. 4.7**). Therefore, patterning of BBBs on graphene does not seem to be a suited system for large-area strain-engineering. Still, the compression within grafted regions might induce a local straintronic effect.

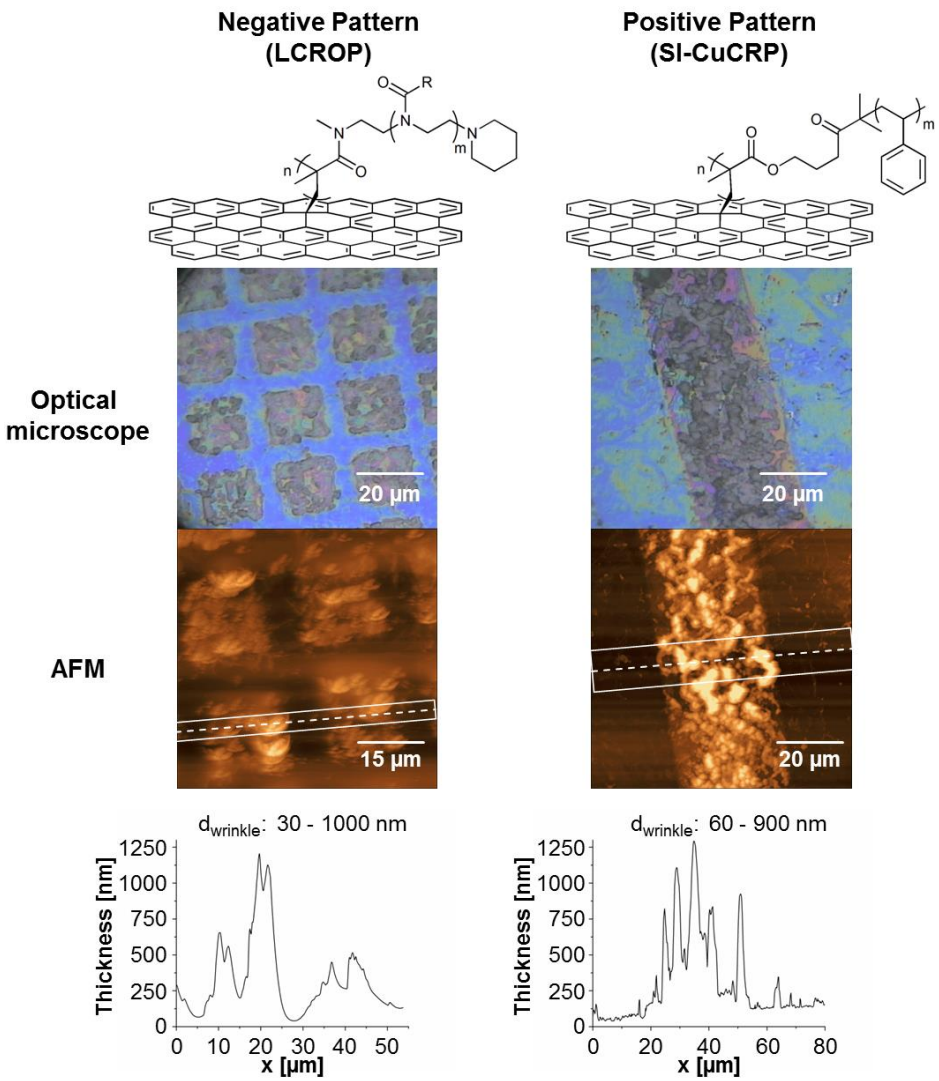

Figure 4.42: Optical microscopy pictures and AFM scans with corresponding profiles of patterned BBBs on graphene. SIPGP was applied to obtain negatively patterned brushes and LCROP or SI-CuCRP was used for synthesis of BBBs. Inhomogeneous polymer layers are received and strong destruction of the layer between polymerized areas can be seen.

Raman measurements were conducted within polymerized (red and green, **Fig. 4.43**) and non-polymerized (black and blue, **Fig. 4.43**) spots of the samples. The obtained spectra resemble

previous results. Polymer signals from C-H stretching (~ 2900 cm^{-1}) and deformation (~ 1450 cm^{-1}) are present on both samples, but are inconsistent in intensity. G- and 2 D-band can be found in patterned and non-patterned spots. In case of PMeOx BBBs (top spectra, **Fig. 4.43**) the G-peak at ca. 1568 cm^{-1} displays higher intensity than the 2 D signal (~ 2676 cm^{-1}), as it was already observed for non-patterned POx BBBs. It was hypothesized that overlapping layers of graphene could be formed due to wrinkling and crumbling of the carpet. However, the spectra lack a clear prove of sufficient strain, since no band splitting occurs. Likewise, grafting of PEHMA BBBs does not lead to an obvious straintronic effect (bottom spectra, **Fig. 4.43**). Similarly to positively patterned polymer brushes G- and 2 D-band display a slightly stronger red shift to 1565 cm^{-1} and 2657 cm^{-1}, respectively. This would correspond to ca. 1 % of strain.[207] Whether this is true, remains questionable because of the observed destruction of layers and previously listed limitations of Raman spectroscopy. Band splitting is not observed either. Graphene signals could merely arise from residues located on top of the BBBs.

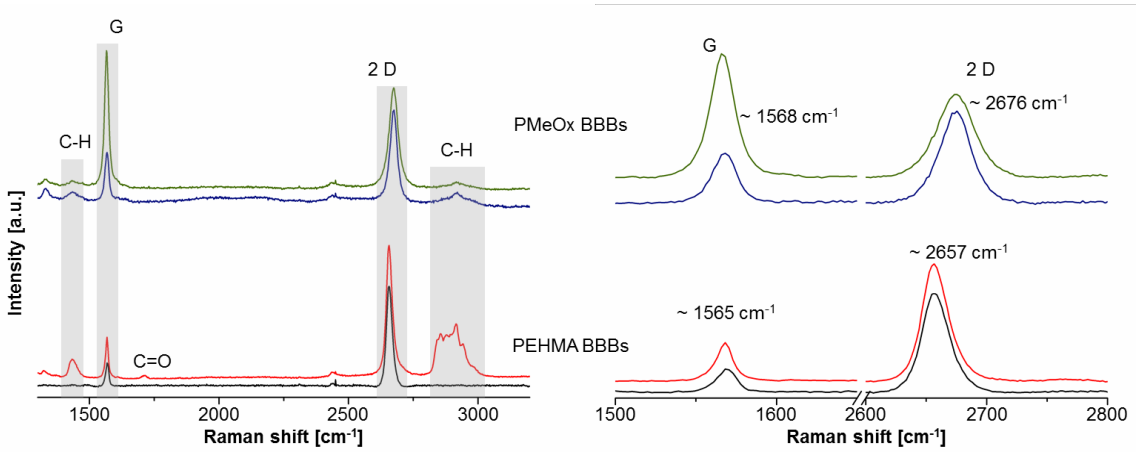

Figure 4.43: Raman spectra of patterned PMeOx (negative) and PEHMA (positive) BBBs on graphene. No significant changes in signal position can be observed between polymerized (red, green) and non-polymerized areas (black, blue). Intensities of polymer signals vary strongly on different spots on the sample.

To sum up, different approaches of graphene patterning were demonstrated using polymer brushes and BBBs. As was suspected from preceding data, destruction of the layers can be observed after grafting. Especially, negative patterns and BBBs seem to allow for rupturing by localized and strong chemo-mechanical forces. Positively patterned polymer brushes on the other hand display pronounced and partly directed wrinkling. Here, it is suspected that the used PDA interlayer promotes anisotropic stress release as adhesive interactions are overcome and graphene is not involved in the deformation. In any case no prove for a strong straintronic effect can be found by means of Raman spectroscopy.

4.3.4 Janus polymer carpets based on graphene

In the next experiments, Janus polymer carpets from graphene were synthesized. The different mechanical properties and mismatch in wettability of the grafted polymer brushes can lead to a higher effective stress within the material thereby enabling band gap opening in graphene. Furthermore, the direct synthesis of Janus polymer carpets from graphene contributes to material science. So far, most fabrication methods of graphene based Janus membranes are difficult to scale up or limited to modification of (reduced) graphene oxide or graphene hybrid materials.[24,288] In this work PSt was grafted *via* SIPGP (8 W, 15 h) directly on graphene supported by SiO_2 **(Fig. 4.44)**. Subsequently, the support was etched by HF-solution and the freestanding polymer carpet (no PMMA coating was applied) was transferred onto a solution of DMAEMA in water (0.5 : 3). Then, a second SIPGP was carried out by irradiation through the monomer solution. To ensure effective grafting a 200 W UV-lamp was used and reaction was allowed to proceed for 4 hours. An IR-filter was attached to the lamp and the distance of the polymer carpet was adjusted to 20 - 25 cm to prevent heating of the solution. This is necessary, as PDMAEMA built in solution otherwise precipitates due to lower critical solution temperature (LCST) and inhibits further grafting.

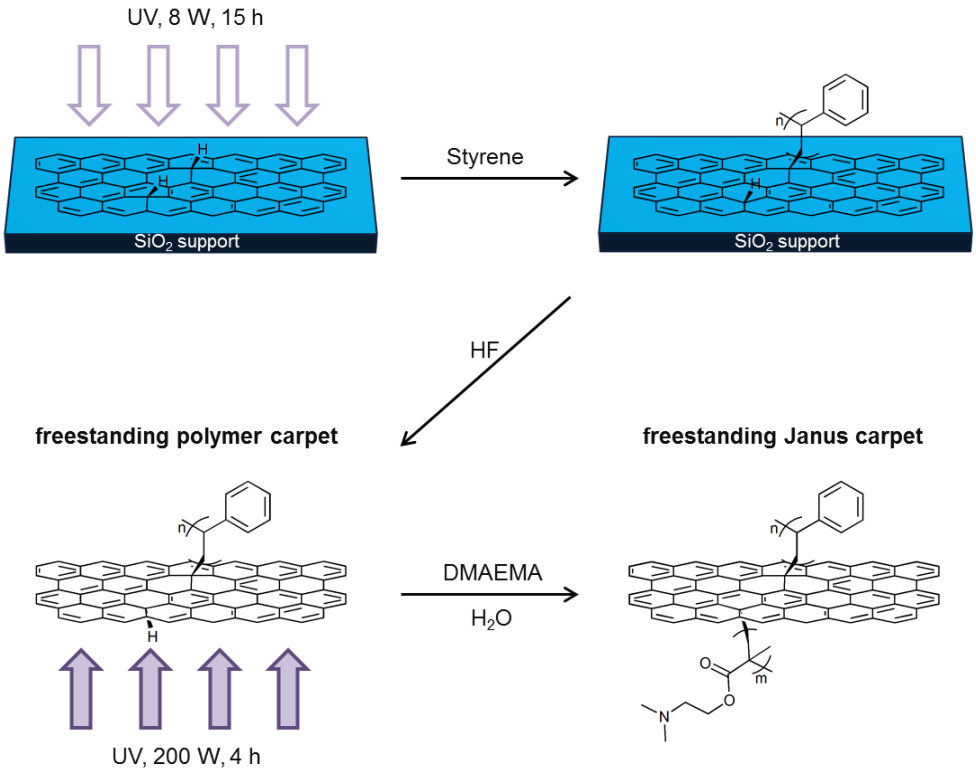

Figure 4.44: Synthesis scheme for fabrication of Janus polymer carpets from graphene. SIPGP is performed on SiO_2 support (8 W UV-lamp). Subsequently, the carpet is detached and transferred onto a solution of DMAEMA in water and irradiated with intense UV-light (200 W) through the solution to give polymer brushes on the other side.

Expectedly, the first grafting of PSt on graphene results in thick polymer brushes (160 nm, **Fig. 4.45**) exposing a hydrophobic θ_S of 100°. The success of the second grafting was confirmed by means of AFM, FT-IR and θ_S measurements after transfer of the freestanding polymer carpet onto a SiO_2 support. A thickness gain of 117 nm can be seen in the AFM **(Fig. 4.45)** after polymerization of DMAEMA. Since no grafting can take place on the up-facing PSt side, θ_S did not change. To analyze the backside, the carpet was again detached from the SiO_2. After fishing, an adhesive tape was carefully placed on top of the carpet. Then, it was peeled off and dried, so that the carpet side exposing PDMAEMA brushes could be characterized. Due to the hydrophilic nature of PDMAEMA the θ_S exhibits 56° **(Fig. 4.45)**, which is in good agreement with literature values[81] and confirms that a Janus type material (hydrophobic/hydrophilic) is received by this fabrication method. Similar to the Janus polymer carpets from PDA a material is obtained with lateral dimension of centimeters and only hundreds of nanometers in height. Considering the typical sample size of ca. 1 cm^2 and the overall thickness of 217 nm a great aspect ratio of ~ 0.5 x 10^5 can be calculated.

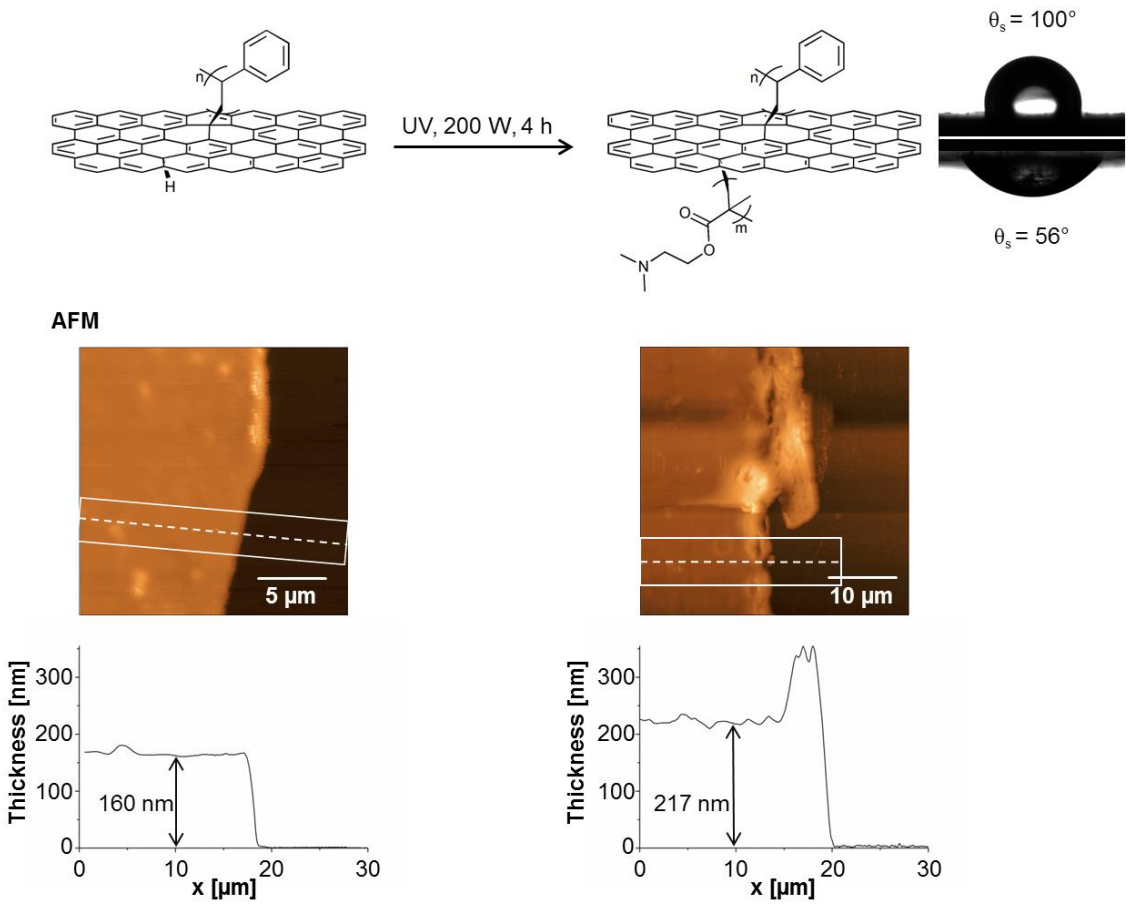

Figure 4.45: Static water contact angle of the synthesized Janus polymer carpet measured on both sides. θ_S exhibits typical values of the respective polymer and AFM displays thickness gain after grafting of the second polymer brush.

ATR FT-IR further verifies the direct grafting of polymer on the graphene sheet **(Fig. 4.46)**. Signals from stretching of aromatic C-H (3102 - 3000 cm^{-1}) and alkyl CH_2 (2921 cm^{-1} and 2850 cm^{-1}) are detected on G-g-PSt. Moreover, different deformation vibrations resulting from the aromatic ring, i.e. δ $(C\text{-}H)_{Ar}$ at 1493 cm^{-1} and 1452 cm^{-1}, δ $(C\text{-}H)_{ring}$ at 758 cm^{-1} and δ_{ring} at 701 cm^{-1}, as well as typical C=C stretching mode (1602 cm^{-1}) are observed. After grafting of the second polymer brush two signals at 2820 cm^{-1} and 2770 cm^{-1} arise from the tertiary amino group in PDMAEMA. In addition, characteristic ν (C=O) from the ester group appears at 1718 cm^{-1} clearly proving the successful synthesis of PDMAEMA-g-G-g-PSt.

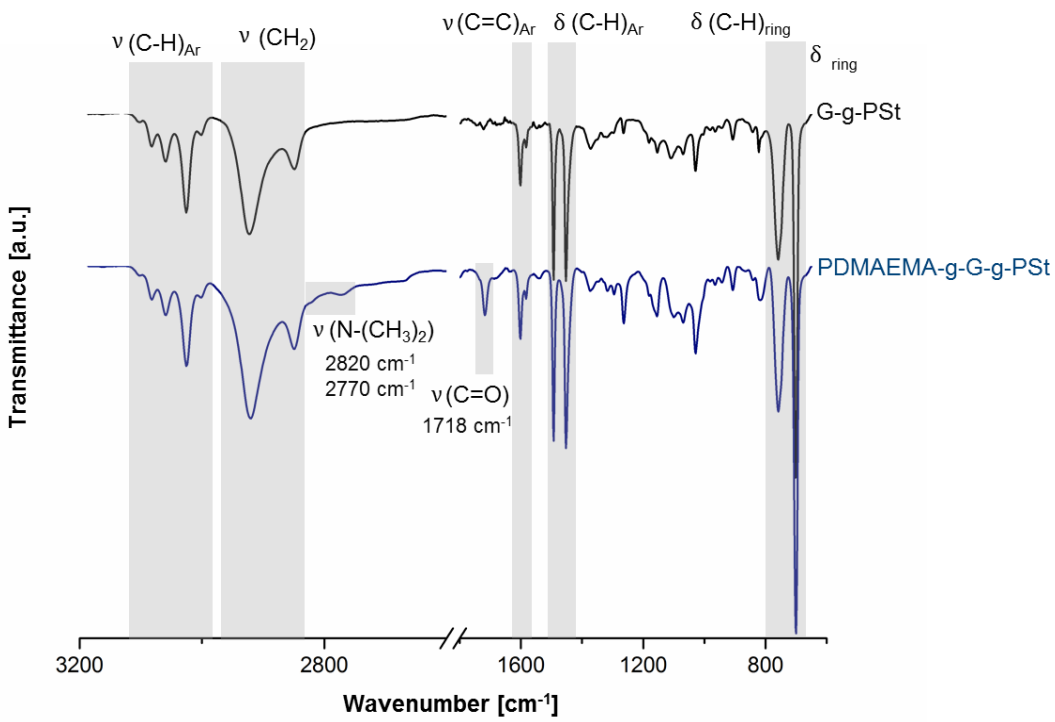

Figure 4.46: ATR FT-IR spectra of PSt brush on graphene and Janus polymer carpet from PSt and PDMAEMA. The spectra display signals from aromatic stretching modes of PSt and introduction of ester vibration as well as stretching of the tertiary amino group after grafting of PDMAEMA.

Apparently, the surface of the received Janus polymer carpet is fairly homogeneous (AFM, **Fig. 4.45**). However, the measuring spots were intentionally chosen to be smooth to ensure correct height determination. In general, the morphology of G-g-PSt resembled results achieved with polymer brushes grafted *via* SIPGP (compare **Fig. 4.33**). The grafting of PDMAEMA does not lead to formation of defined wrinkles or strongly enhanced buckling because of the mismatch in polymer brush wettability. Overall buckling height and frequency is comparable to that obtained for polymer brush carpets with similar thickness. Hence, it comes as little surprise that Raman spectroscopy does not deliver new results.

As before patterned samples were synthesized to promote anisotropic stress release in the Janus polymer carpets. For that, the first polymer brush (PSt) was grafted *via* SIPGP through a TEM-grid (photomask). Afterwards the polymer carpet was detached from support and PDMAEMA was grafted from beneath as described above. Since polymer cannot grow on the covered areas during the first SIPGP, the synthesized G-g-PSt carpet retains a non-polymerized ring in the middle of the sample, which is predetermined by the shape of the TEM-grid. This ring builds a weak point which leads to crumbling and destruction of the polymer carpet during the required transfer processes and makes the second polymerization impossible. To address this issue PMMA resist was spin-coated as stabilizing layer before detachment of the patterned G-g-PSt. The resist remained on the carpet until the end of the second SIPGP and was subsequently washed off with acetone. In that manner patterned Janus polymer carpets are reproducibly obtained from graphene. Problems with PMMA dissolution due to UV-induced cross-linking are not observed and signals from the ester group are not present in the FT-IR spectrum of a blank sample. AFM scans and optical pictures **(Fig. 4.47 a,b)** of the synthesized carpets display quite inhomogeneous patterns and wrinkling within the pattern as well as in-between. Wrinkle height is noticeably higher in polymerized regions (50 - 760 nm) than in non-polymerized (20 - 180 nm), as chemo-mechanical stress should be considerably higher in those areas. Average thickness determination is somewhat difficult because of the strong wrinkling, but lay within 150 nm to 250 nm thus being similar in height to patterned G-g-PSt (compare **Fig. 4.39**). That wrinkling is stronger and more pronounced on the Janus systems may be explained by the mismatch of polymer brush wettability as well as synthesis procedure. After the first grafting the resulting polymer carpet is detached from support, which already can promote relaxation within the material. Moreover, the polymer carpet is not bound to a support for the second grafting. Further effective stress release can therefore occur right during the synthesis, since it is not limited by the rigidity of a substrate. Mechanical stress from transfer processes also contributes to the final morphology. Curiously, wrinkling is not directional, although wrinkling wavelength λ is 1.1 ± 0.4 µm ($\lambda = 0.6 \pm 0.2$ µm for non-grafted areas) and differs keenly from the pattern dimension of ca. 30 µm. However, directed wrinkling was so far only existent on PDA containing samples. It can be hypothesized that limitations may arise from the high Young´s modulus of graphene prohibiting comparable development. Nevertheless, the achieved wrinkle heights and form are promising in regard to possible modification of graphene´s electronic structure.

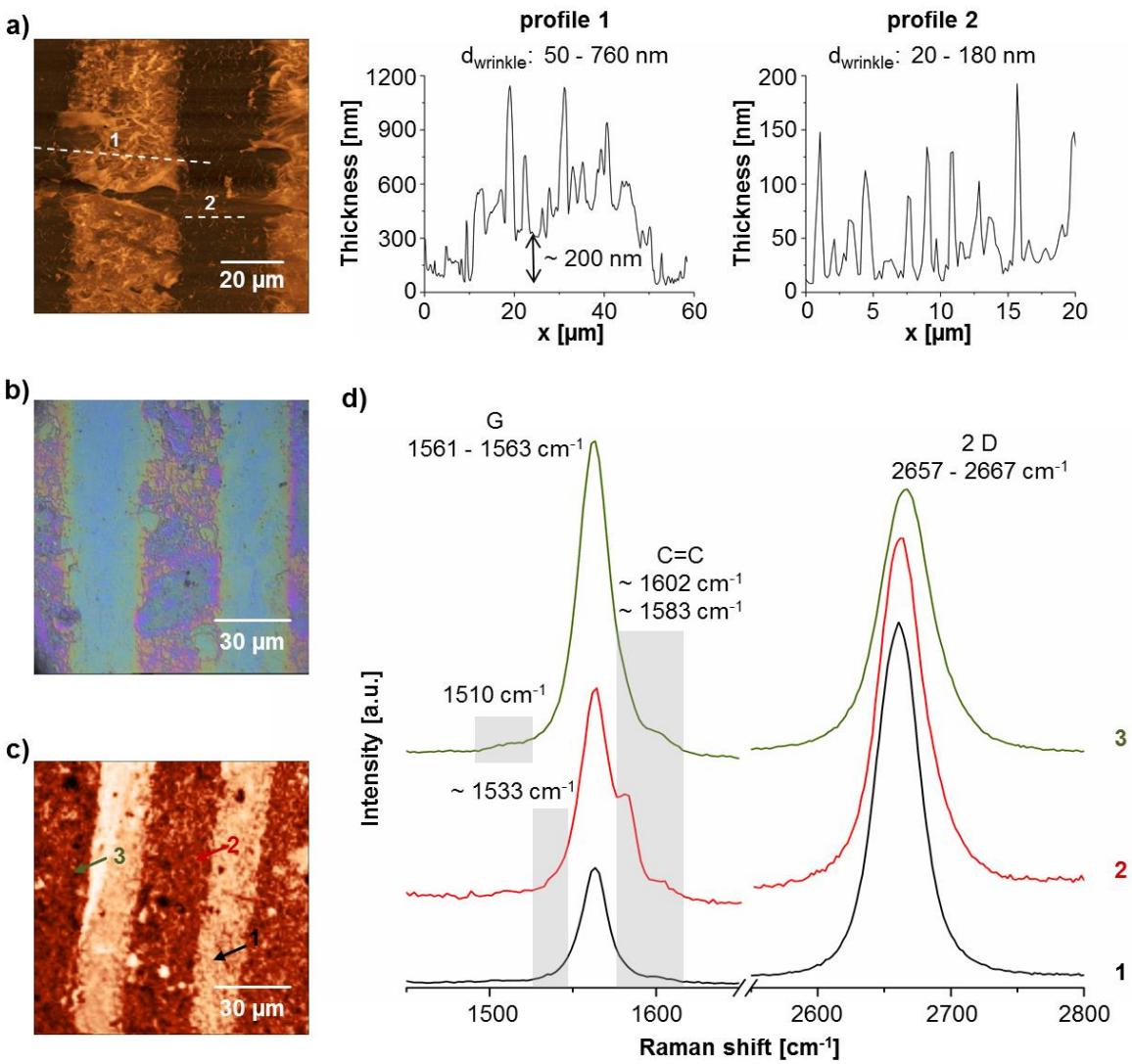

Figure 4.47: AFM of patterned graphene based Janus polymer carpet (a) with corresponding profiles as indicated by the numbers. Strong wrinkling can be seen with wrinkle heights up to 760 nm. Optical image (b) and PMT scans (c) were taken and Raman spectra (d) reveal small shoulders at 1510 cm^{-1} and 1533 cm^{-1}. Signal intensity of graphene and polymer brushes are varying strongly on the entire sample.

Raman spectra were measured on different spots of the sample including non-polymerized (1 in **Fig. 4.47 d**) and polymerized (2 and 3 in **Fig. 4.47 d**) regions. Usually signal intensity varies independent of the measuring spot and PSt peaks can be always found at 1602 cm^{-1} and 1583 cm^{-1} (both $\nu\,(C{=}C)_{Ar}$) as well as 3030 cm^{-1} ($\nu\,(C\text{-}H)_{Ar}$). In addition, signals from stretching modes and deformation vibration of alkyl CH_2 can be often found at 2880 cm^{-1}, 2730 cm^{-1} and 1430 cm^{-1}, respectively. As discussed previously the polymer signals in non-polymerized areas may come from residual polymer deposited from solution or ineffective grafting due to scattered UV-light during the first SIPGP.

The detected G- and 2 D-band of graphene lie in the range of 1561 - 1563 cm^{-1} and 2657 - 2667 cm^{-1}, respectively **(Fig. 4.47 d)**. Equivalent to patterned PEHMA brushes and

BBBs this slightly higher red shift would correspond to ~ 1% of strain.[205,207] In the G-band small shoulders at ~ 1533 cm^{-1} or 1510 cm^{-1} might indicate beginning band splitting. However, this is not expected to be very prominent at such low strain and could not be described with a fitting mathematical function. Furthermore, the distance between G^- and G^+ would be 30 - 53 cm^{-1} and rather correspond to 4 - 8 % of strain.[205] In that case actual signal position would be expected at ca. 1532 - 1482 cm^{-1} for G^- and 1560 - 1536 cm^{-1} for G^+ (if G = 1582 cm^{-1} for unstrained graphene). While this is represented for 4 % of strain in the measured spectra, the 2 D-peak does neither shift accordingly (to at least 2580 cm^{-1})[207,210] nor shows evolution of a second band. Therefore, the small shoulders are probably not a result of high mechanical force, but rather arise from certain fluorescence of PSt.

Spots with high I_G/I_{2D} are also existent (3 in **Fig. 4.47 d**). Same as in POx BBB systems this could be a consequence of overlapping graphene caused by the wrinkle formation. Yet, clear spectroscopic evidence of chemo-mechanically realized stress is not found because of the absence of distinct band splitting and low significance of Raman signal shifts in supported graphene (see **chapter 4.3**). Even if observed red shifts can be ascribed to strain, it is not sufficient to open a band gap within graphene´s electronic structure.

At last, patterned Janus polymer carpets from PDA were combined with graphene. PDA-g-PEHMA carpets were flipped onto a SiO_2 support as described in **chapter 4.2.1**. Sequentially, a graphene sheet and a patterned PDA-g-PDMAEMA carpet were transferred on top with the help of PMMA resist for stabilization. In that way a graphene based Janus material ("Janus sandwich", **Fig. 4.48**) is obtained without risk of possible destruction by covalent grafting. In contrast to direct patterning of polymer brushes on G/PDA the anisotropic stress release during transfer might lead to strain and deformation in graphene. Alternatively the graphene sheet was placed on top of a prior fabricated patterned Janus polymer carpet to promote strain by already formed winkles.

The wrinkling behavior of the Janus sandwich is similar to that observed on positively patterned graphene polymer carpets and even partly directed in polymer brush areas **(Fig. 4.48)**. However, in comparison to patterned Janus polymer carpets without graphene (wrinkling wavelength $\lambda = 1.25 \pm 0.3$ µm, compare **Fig. 4.27**) wrinkling is somewhat finer for the same pattern ($\lambda = 0.5 \pm 0.1$ µm). Similar observations are also made for parallel bar patterns. This can be explained by the interaction of PDA based polymer carpets with the graphene sheet, that prevents an equally strong stress relief because of its high Young´s modulus (1 TPa). The inherent tension is then released through locally confined deformation.

Still, the build wrinkles reach 15 - 120 nm (profile 1, **Fig. 4.48**), which falls into the same range as for patterned Janus polymer carpets from PDA (compare **Fig. 4.26** and profile 2 and 3 in **Fig. 4.48**).

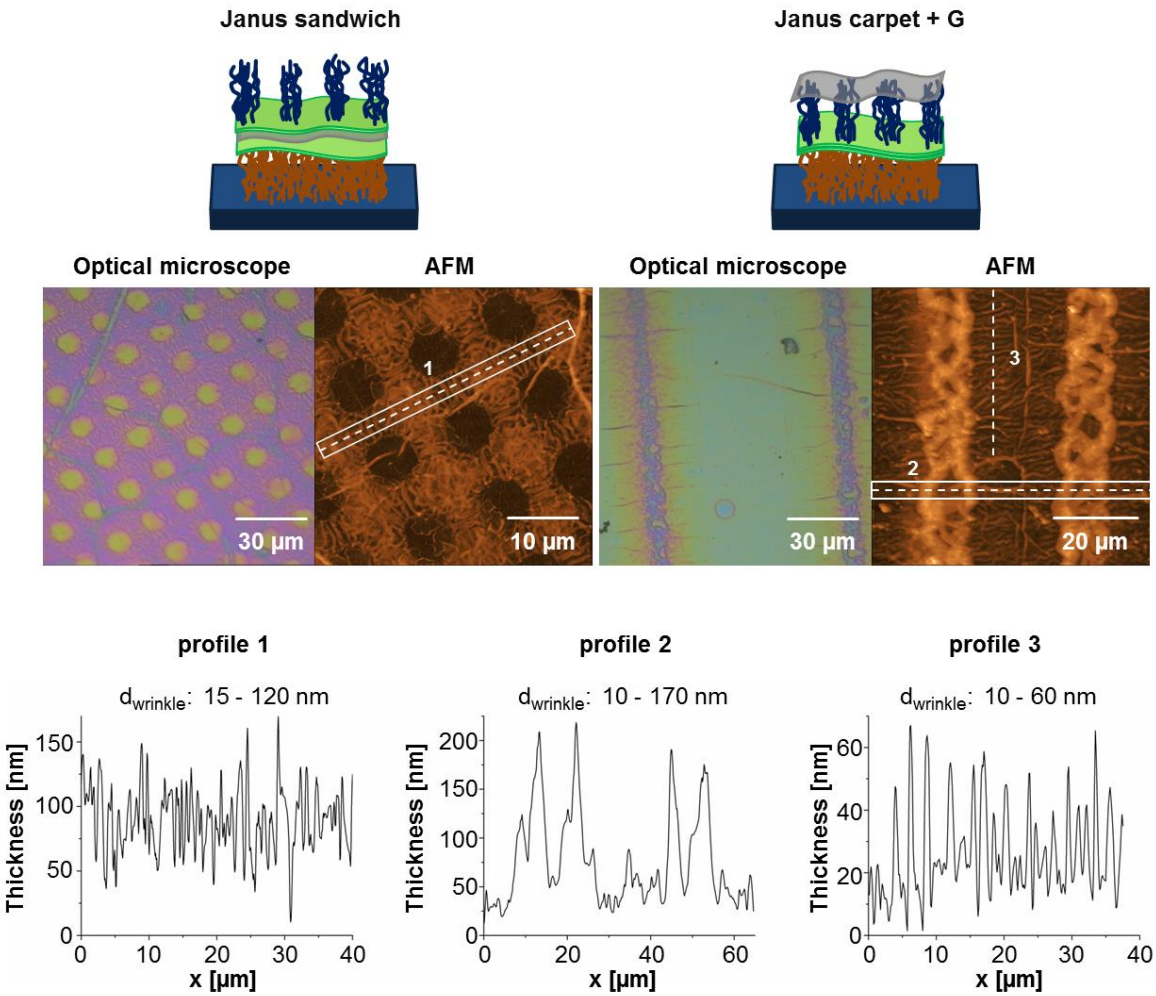

Figure 4.48: Optical pictures and AFM scans with corresponding height profile of patterned Janus polymer carpets with graphene sheets within ("Janus sandwich") and on top. Transfer of patterned polymer carpets onto graphene leads to building of wrinkles. The bottom row displays the AFM profiles as indicated by the numbers in the AFM scans.

The Janus polymer carpet, which was used to transfer a graphene single layer on top, exhibits wrinkles up to 170 nm in polymerized regions (profile 2 in **Fig. 4.48**) and directed wrinkles in-between with thicknesses from 10 nm to 60 nm (profile 3 in **Fig. 4.48**). Note that AFM scans and profiles were taken after graphene transfer. The wrinkles are still resolved in the measurements without big difference to AFM scans of pure Janus polymer carpet (compare **Fig. 4.27**). Only wrinkling between the patterns seems slightly stronger, which can be ascribed to further swelling and deswelling during dissolution of PMMA resist after the

transfer. Therefore, graphene might be adapted to the morphology of the pattern and wrinkles of the sample.

Raman spectra of these samples **(Fig. 4.49)** do not display noticeable change in the graphene specific signals. Most prominent feature of the spectra is the strong baseline increase due to the fluorescence of the PDA layers. This is even stronger than on other samples, since the Janus polymer carpets possess a double layer of PDA. Additionally, the fluorescence can be enhanced by the graphene layer[289–291]. As Ling *et al.* demonstrated, graphene is able to improve Raman signal intensity of underlying materials by the so called chemical enhancement mechanism (graphene enhanced Raman spectroscopy).[289,290] Analogously, Weng *et al.* achieved increase of fluorescence by application of graphene.[291] Consequently, the detection of G- and 2 D-band is difficult even when the graphene sheet lies on top of the Janus polymer carpet. The found Raman shifts are 1583 - 1590 cm^{-1} for the G-band and 2671 - 2684 cm^{-1} for the 2 D-band, which lies within the mean variation for signal position of pristine graphene. Splitting of the signals is not visible either. Hence, it can be said that possible deformation of the graphene is not sufficient enough to result in a detectable straintronic effect.

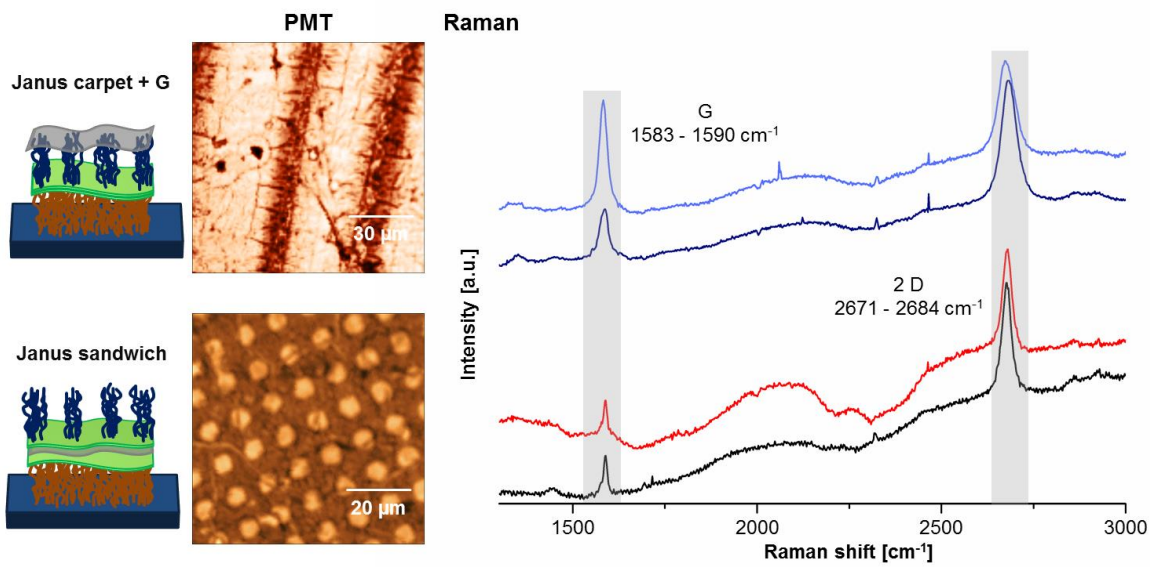

Figure 4.49: PMT scans and Raman spectra of graphene polymer carpet hybrid materials. No significant changes in signal position or form can be observed on different spots of the samples (different color in the spectra). Strong baseline increase due to fluorescence of PDA layer can be observed.

In conclusion, two new methods of Janus membrane synthesis from graphene were successfully performed. Direct grafting of polymer brushes by sequential SIPGP from both sides of the graphene sheet gives Janus polymer carpets with aspect ratios around 10^5. These

can be patterned using an established photolithographic process. The previously described transfer and flipping procedures of PDA polymer carpets can also be applied for fabrication by simply placing a graphene sheet between the facing PDA layers. In both cases the electronic structure of the graphene single layer stays intact, since no significant change in I_D/I_G is detected. In regard to strain-engineering the received Janus materials do not provide a noticeable improvement in comparison to the graphene polymer carpets synthesized before. However, both synthetic approaches can be applied directly to graphene and scaled up, as PDA deposition, CVD of graphene and used grafting techniques (SIPGP and SI-CuCRP) can be realized on large substrates. In combination with the structural variety of polymer brushes and BBBs the presented methods offer a unique pathway to a whole palette of new graphene based materials for directed chemistry.

5. Summary

In this work, different materials were synthesized by grafting of polymer brushes on poly(dopamine) (PDA) and graphene (G). Special attention was put on strain-engineering of graphene and synthesis of Janus membranes.

Firstly, the combination of PDA surface chemistry and surface-initiated Cu(0)-mediated controlled radical polymerization (SI-CuCRP) was established as a robust and versatile method for polymer brush synthesis. The initiator 2-bromoisobutyryl bromide (BiBB) can be bound after deposition of PDA on substrate. PDA does not affect the SI-CuCRP in any way and gives similar results as on a typical surface-bound initiator (APTES-BiBB). Owing to its adhesive nature, PDA enables substrate-independent controlled polymerization without complex experimental set-up **(Fig. 5.1)**.

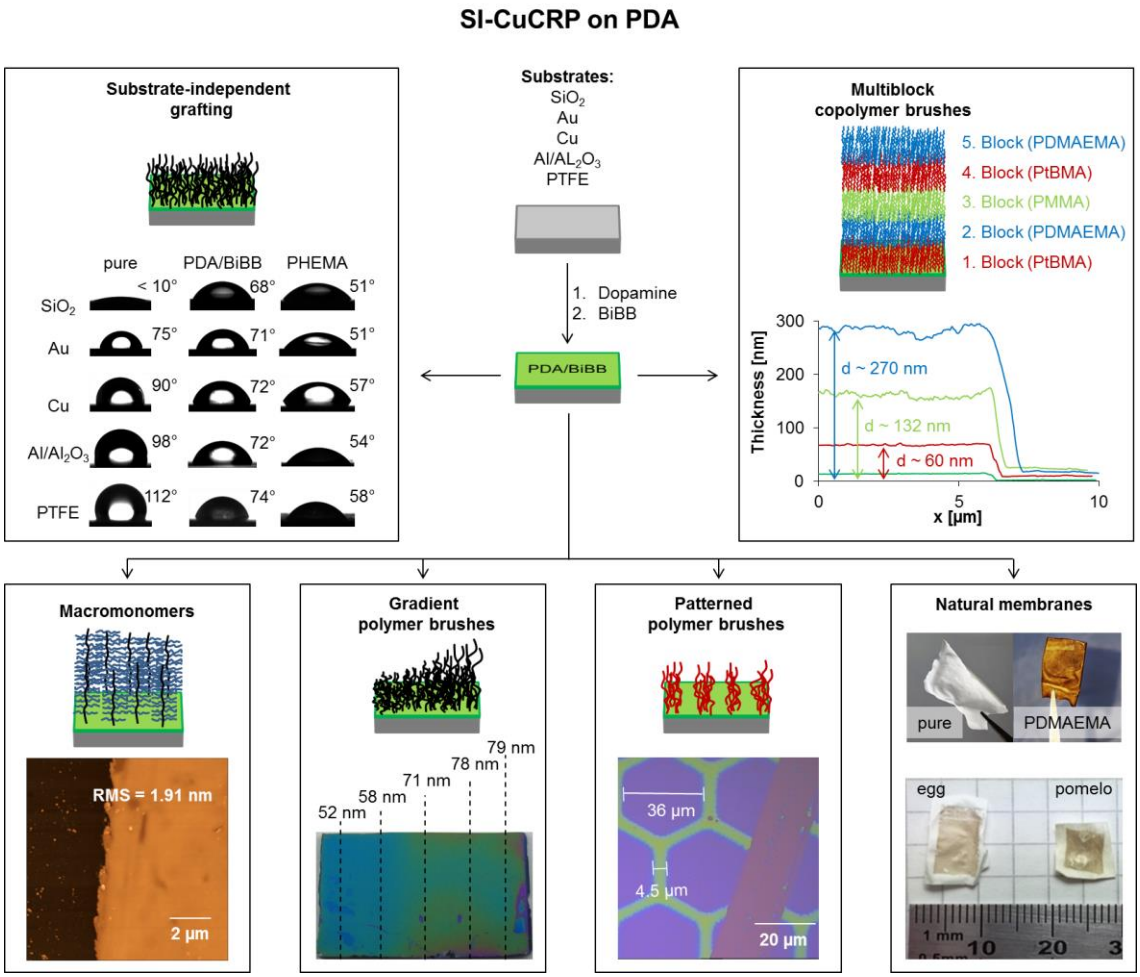

Figure 5.1: Overview of synthetic results achieved by SI-CuCRP on PDA modified surface. Besides patterning and gradient synthesis, substrate-independent grafting of polymer brushes is possible due to the adhesive nature of PDA. Moreover, the reaction is highly effective and robust, so that macromonomers and multiblock copolymers can be grafted.

Polymer brush from hydrophilic, hydrophobic and sterically demanding monomers can be produced and reach thicknesses of hundreds of nanometers within 1 h **(Fig. 5.1)**. Outstanding end group preservation is observed allowing synthesis of pentablock copolymer brushes **(Fig. 5.1)**, which represents the highest copolymer block number for surface-bound polymer up to date. Additionally, SI-CuCRP gives rise to straight forward and highly effective synthesis of defined patterned and gradient polymer brushes as well as functionalization of natural membranes **(Fig. 5.1)**. Hence, a general method for manifold, controlled surface functionalization starting from a PDA/BiBB initiating layer is obtained.

In the second part of this work this method was applied to functionalize single sheet graphene with polymer brushes **(Fig. 5.2)**. As the steric repulsion within these brushes is high, resulting chemo-mechanical stress should lead to graphene deformation and the straintronic effect.

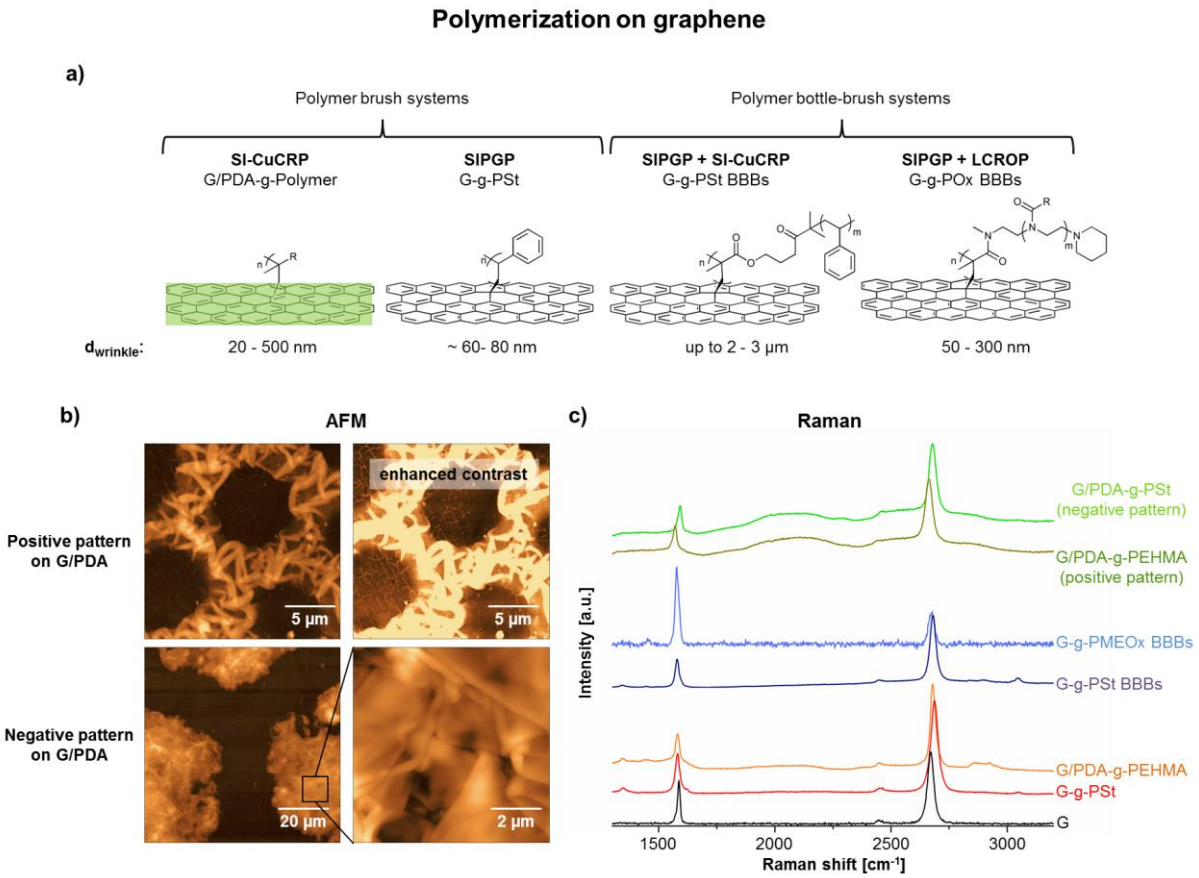

Figure 5.2: Scheme of the synthesized graphene polymer carpets with the achieved wrinkle and buckle heights (a). Patterning of PDA modified graphene results in strong and partly directed wrinkling (b). Obtained G- and 2 D-bands of the samples do not differ significantly from pristine graphene on SiO_2, but fluctuate in intensity and are often difficult to detect.

Synthesis of polymer brushes *via* SI-CuCRP or Self-initiated photografting and photopolymerization (SIPGP) graphene samples expectedly leads to formation of wrinkles

which lie within a range of 20 nm to 500 nm **(Fig. 5.2 a)**. However, Raman spectra do not show significant changes in G- and 2 D-band (G-g-PSt and G/PDA-g-PEHMA in **Fig. 5.2 c**) and evidence for a straintronic effect is not found. Similar results were achieved with bottle-brush brush (BBB) carpets **(Fig. 5.2 a,c)**, although wrinkles and buckles reach up to several micrometers for these systems due to strong steric repulsion of the polymeric side-chains. Since patterning can provide anisotropic stress release, patterned polymer brushes and BBBs on graphene were synthesized. Although some samples display pronounced and partly directed wrinkling in the AFM **(Fig. 5.2 b)**, no evidence for a straintronic effect is obtained. Evaluation and quantification of chemo-mechanically induced strain remains problematic with Raman spectroscopy. It is suspected that the induced strain leads to rupture and destruction of the graphene sheet, while grafting density and polymer brush (or BBB) thickness increase during reaction. This assumption is supported by recent literature.[257,292] Still, a whole palette of polymer modifications on graphene is presented to obtain (directed) wrinkles and buckles on different scales.

In the context of material synthesis Janus polymer carpets (or Janus membranes) were fabricated from both PDA and graphene **(Fig. 5.3)**. In the first step, PDA polymer carpets can be flipped on SiO_2 support to expose the adhesive layer. Due to the mechanically demanding process, polymer brush adhesion energy to the support must be sufficiently high to withstand the procedure. This is achieved by use of monomers with low bulk glass transition temperature ($Tg \leq 0°C$, **Fig. 5.3 a**).[266] In a second step, readily synthesized polymer carpets can be transferred on top of the flipped carpet. The two facing PDA sides stabilize the material and subsequent detachment from support gives freestanding Janus membranes with lateral dimension of centimeters and thickness of nanometers (PEHMA-PDA-PSPMA in **Fig. 5.3 a**). In this work, Janus membranes were fabricated, which are hydrophobic/hydrophilic, non-responsive/T-responsive, non-responsive/pH-responsive or possess polymer brush/bottle-brush brush architecture. This series can be easily extended.

Patterned Janus polymer carpets undergo effective anisotropic stress release and display directed wrinkling if the pattern dimension is considerably higher than the wrinkling wavelength **(Fig. 5.3 c)**. This behavior is promoted by the soft nature of the underlying carpet, as wrinkling is noticeably stronger than on on rigid SiO_2.

The sequential transfer of polymer carpets also enables incorporation of other materials like graphene between the layers **(Fig. 5.3 c)**. Synthesis of (patterned) Janus polymer carpets directly from graphen was realized by the sequential SIPGP from both sides of the graphene

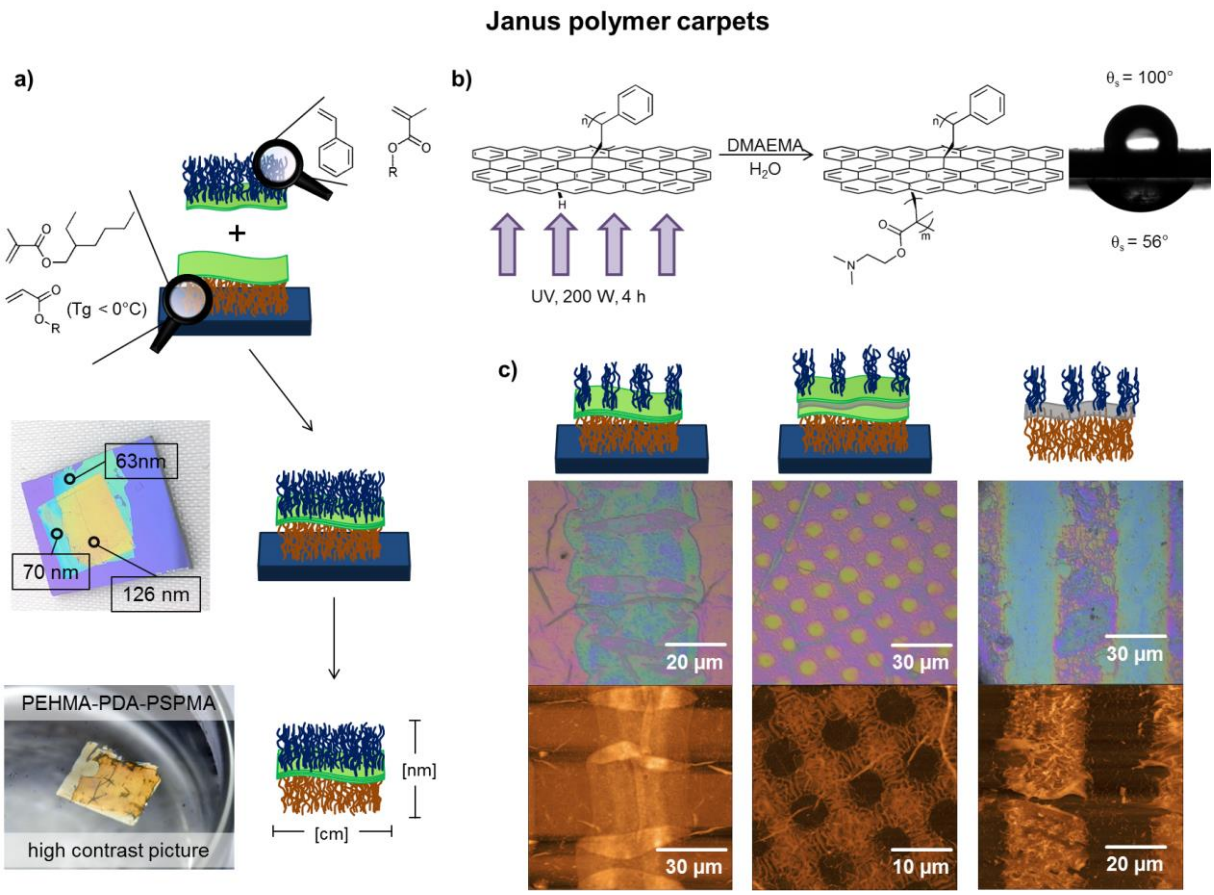

Figure 5.3: Scheme of the synthesized Janus polymer carpets from PDA (a). The synthesized polymer carpets are robustly held together by facing PDA layers and can be made freestanding. Janus polymer carpets from graphene can be received by second grafting from the backside (b). Patterned Janus polymer carpets (c) display enhanced and partly directed wrinkling from both PDA and graphene.

sheet **(Fig. 5.3 b)**. To the best of our knowledge, this is the first example of the synthesis of a Janus membrane directly from a single layer graphene. Effects on the electronic structure of the graphene single layer are not detected after synthesis of the Janus membrane.

Finally, all the presented Janus polymer carpets typically exhibit a size of ca. 1 cm^2. Taking into account their thickness, which ranges from tens to hundreds of nanometers, aspect ratios lie between 10^4 and 10^5. Each synthetic approach can be applied directly and scaled up, as PDA deposition and chemical vapor deposition (CVD) of graphene can be carried out on large areas. As used grafting techniques (SIPGP and SI-CuCRP) can be realized on large substrates as well, Janus carpets can overcome the herein obtained aspect ratios of 10^5. In combination with the structural variety of polymer brushes and BBBs the presented methods offer a unique pathway to a series of novel 2D materials with adjustable properties. The outstanding wrinkling behavior of patterned Janus polymer carpets will make them especially interesting for directed transport and movement or controlled deformation.

6. Zusammenfassung

In dieser Arbeit wurden verschiedene Materialien durch das Pfropfen von Polymerbürsten auf Poly(dopamin) (PDA) und Graphen (G) synthetisiert. Ein besonderes Augenmerk wurde dabei auf sog. *strain-engineering* von Graphen und Synthese von Janus-Membranen gelegt.

Die Kombination aus PDA-Oberflächenchemie und oberflächeninitiierter Cu(0)-vermittelter kontrolliert radikalischer Polymerisation (SI-CuCRP) wurde als robuste und vielseitige Methode zur Synthese von Polymerbürsten etabliert. Nach Abscheidung von PDA auf einem Substrat kann der Initiator 2-Bromisobutyrylbromid (BiBB) gebunden werden. Die SI-CuCRP auf PDA liefert vergleichbare Ergebnisse wie auf einem typischen, oberflächengebundenem Initiator (APTES-BiBB). Die universelle Haftkraft des PDA ermöglicht substratunabhängige, kontrollierte Polymerisation ohne komplexen experimentellen Aufbau **(Abb. 6.1)**.

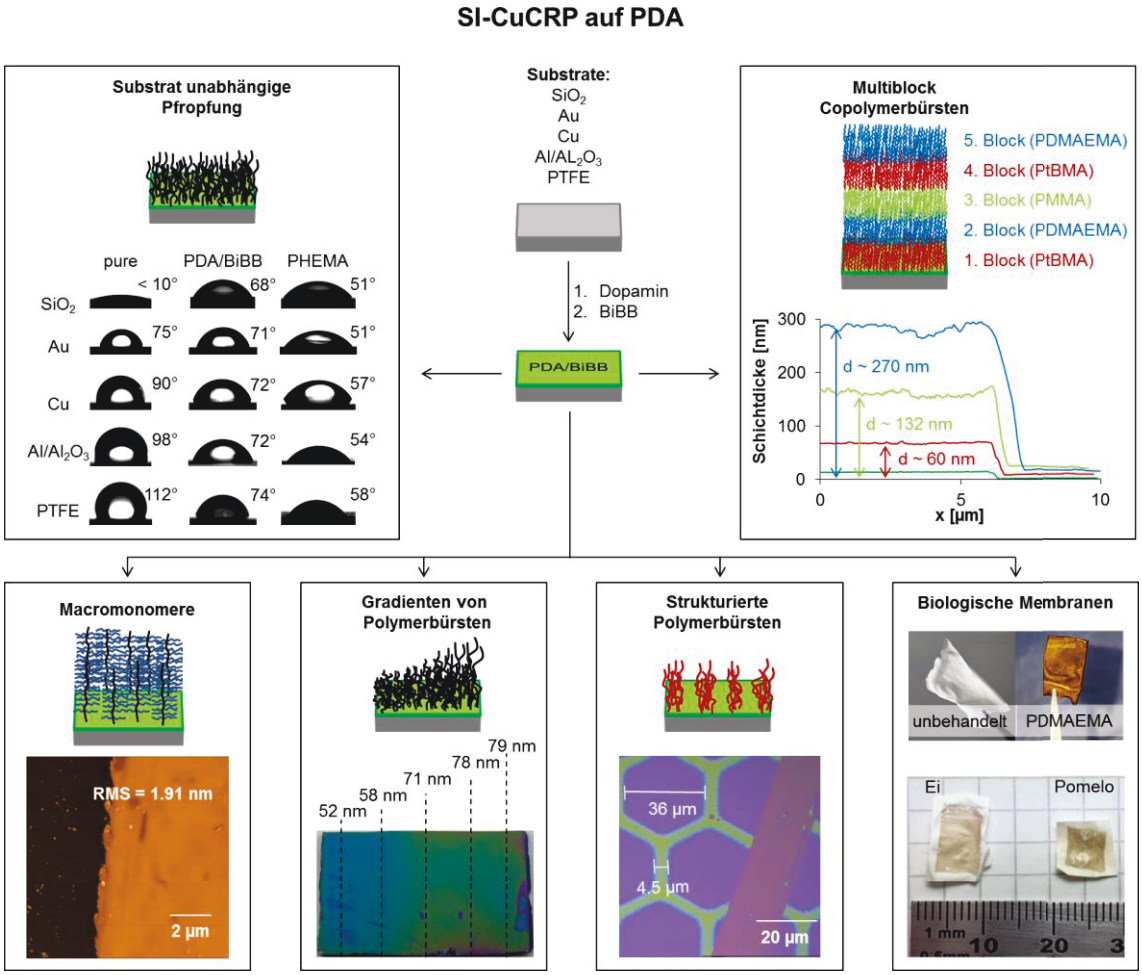

Abbildung 6.1: Syntheseergebnisse der SI-CuCRP auf PDA-modifizierten Oberflächen. Neben der Strukturierung und Gradientensynthese ist eine substratunabhängige Synthese von Polymerbürsten möglich. Darüber hinaus ist die Reaktion effizient und robust, so dass Makromonomere und Multiblockcopolymere gepfropft werden können.

Es können Polymerbürsten aus hydrophilen, hydrophoben oder sterisch anspruchsvollen Monomeren synthetisiert werden. Dabei können Schichtdicken von einigen hundert Nanometern innerhalb 1 h erreicht werden. Die Zugänglichkeit der Endgruppen bleibt erhalten, was die Synthese von Pentablockcopolymerbürsten ermöglicht **(Abb. 6.1**). Dies stellt die bis dato höchste Blockzahl für oberflächengebundenes Copolymer dar. Zudem erlaubt die SI-CuCRP eine einfache und hocheffiziente Synthese von Polymerbürsten mit definierten Gradienten und Strukturen sowie die Funktionalisierung von natürlichen Membranen **(Abb. 6.1)**. Somit dient die Kombination von SI-CuCRP und PDA als eine allgemeine Methode zur vielfältigen, kontrollierten Oberflächenfunktionalisierung.

Im zweiten Teil der Arbeit wurde diese Methode zur Funktionalisierung von Graphen mit Polymerbürsten angewendet **(Abb. 6.2)**. Aufgrund des hohen sterischen Drucks innerhalb der Bürsten, sollte die resultierende chemisch-mechanische Beanspruchung zu einer Deformation des Graphens und einem *straintronic*-Effekt führen.

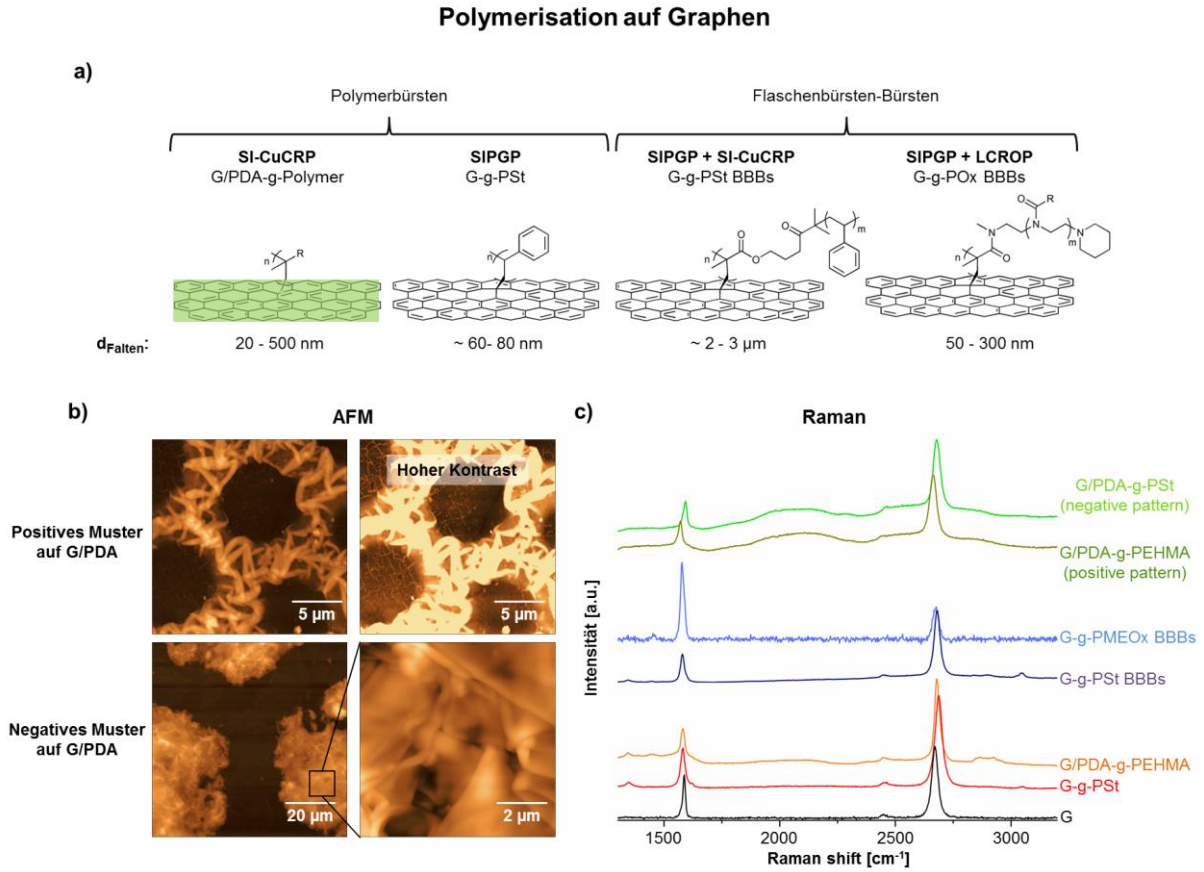

Abbildung 6.2: Schema der von Graphen synthetisierten Polymerteppiche mit den erzielten Falten- und Wölbungshöhen (a). Die Strukturierung von PDA-modifiziertem Graphen führt zu starker und teilweise gerichteter Faltenbildung (b). Erhaltene G- und 2D-Banden der Proben unterscheiden sich nicht signifikant von reinem Graphen auf SiO_2, schwanken jedoch in der Intensität und sind oft schwer zu detektieren.

Die Synthese von Polymerbürsten über SI-CuCRP oder Selbst-initiierte Photopfropfung und Photopolymerisation (SIPGP) auf Graphen führt erwartungsgemäß zur Bildung von Falten, deren Dicke in einem Bereich von 20 nm bis 500 nm liegt **(Abb. 6.2 a)**. Raman-Spektren (G-g-PSt und G/PDA-g-PEHMA in **Abb. 6.2 c**) zeigen jedoch keine signifikanten Veränderungen in der G- und 2 D-Bande und liefern keine Hinweise auf einen *straintronic*-Effekt, obwohl die Falten auf starke Deformation hinweisen. Ähnlich Ergebnisse werden mit sog. Flaschenbürsten-Bürsten (BBBs) erzielt, obwohl die Faltendicke bei diesen Systemen aufgrund der starken sterischen Abstoßung der polymeren Seitenketten bis zu mehreren Mikrometern erreichen kann **(Abb. 6.2 a)**.

Da die Strukturierung polymerer Bürsten einen anisotropen Spannungsabbau bewirken kann, wurden strukturierte Polymerbürsten und BBBs auf Graphen synthetisiert. Obwohl einige Proben eine ausgeprägte und gerichtete Faltenbildung im AFM **(Abb. 6.2 b,c)** zeigen, wurde kein Hinweis auf die Ausprägung eines *straintronic*-Effekts gefunden. Die Bewertung und Quantifizierung der chemisch-mechanisch induzierten Belastung mittels Raman-Spektroskopie ist jedoch problematisch. Vermutlich führt die induzierte mechanische Spannung zum Bruch bzw. Reißen der Graphenschicht, wenn die Pfropfungsdichte und Schichtdicke der Polymerbürsten (oder BBBs) zunimmt. Diese Annahme wird durch neueste Literatur gestützt.[257,292] Dennoch wurde eine ganze Reihe von Polymermodifikationen auf Graphen erhalten, um (gerichtete) Faltenbildung verschiedener Größenordnungen zu erzielen.

Im Zusammenhang der Materialsynthese wurden sowohl aus PDA als auch aus Graphen Janus-Membranen, sog. *Janus polymer carpets*, hergestellt. Im ersten Schritt konnten PDA-Polymerteppiche auf einen SiO_2-Träger umgedreht werden. Somit bildet das adhäsive PDA die obere Schicht. Aufgrund der hohen mechanischen Belastung während des Prozesses sollte die Haftung der Polymerbürsten an den Träger ausreichend hoch sein, damit sie durch das Verfahren nicht zerstört werden. Dies wird durch Verwendung von Monomeren mit niedriger Glassübergangstemperatur ($Tg \leq 0°C$, **Abb. 6.3 a**) gewährleistet.[266]. In einem zweiten Schritt kann ein bereits synthetisierter Polymerteppich darauf transferiert werden. Die beiden aneinander haftenden PDA-Schichten stabilisieren das Material, sodass nach Ablösen vom Träger freistehende Janus-Membranen erhalten werden (PEHMA-PDA-PSPMA in **Abb. 6.3 a**). Deren laterale Ausdehnung liegt im Bereich von Zentimetern, während sich ihre Gesamtdicke im Nanometerbereich befindet. In dieser Arbeit wurden Janus-Membranen aus hergestellt, die hydrophob/hydrophil, nicht-sensitiv/T-sensitiv oder nicht-sensitiv/pH-sensitiv sind oder eine Polymerbürsten/Flaschenbürsten-Architektur besitzen. Diese kann allerdings Reihe auf einfache Weise erweitert werden.

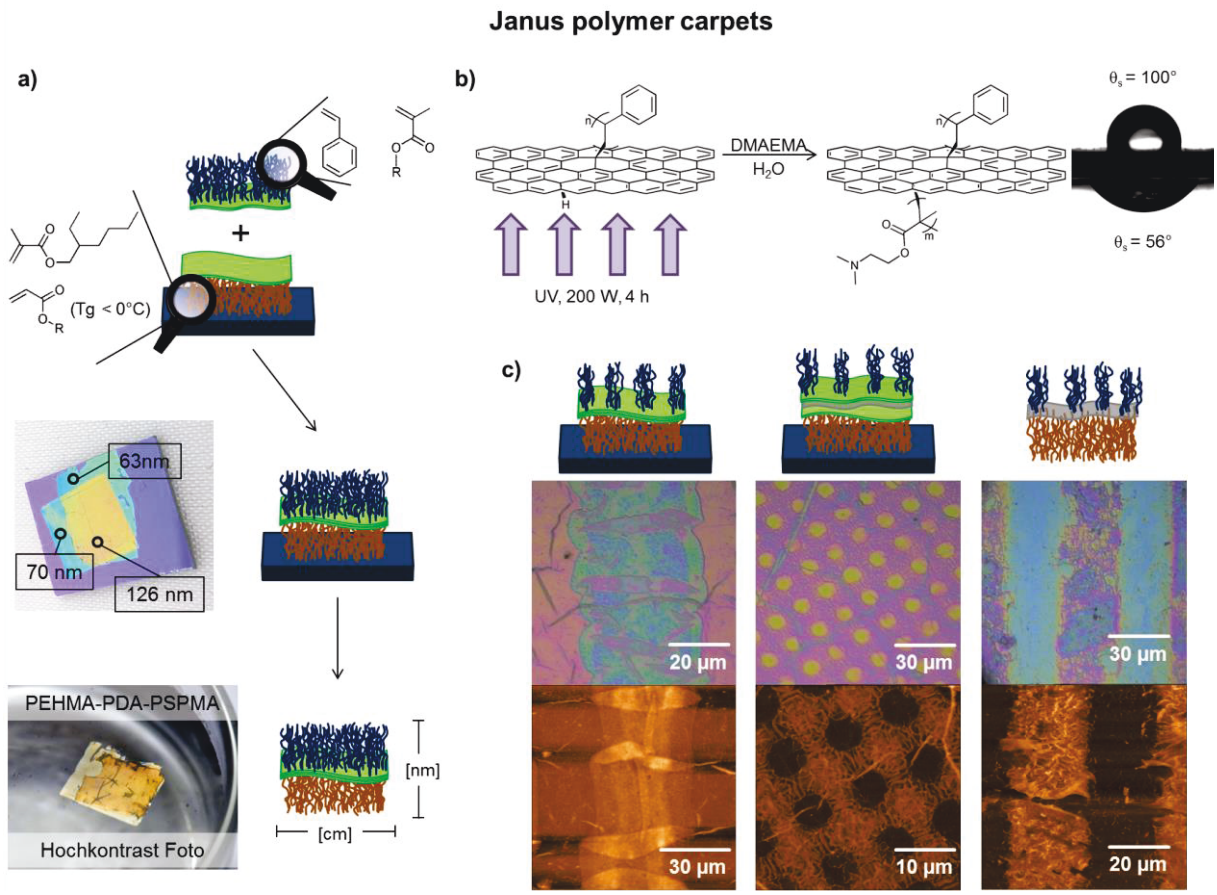

Abbildung 6.3: Schema zur Synthese von *Janus polymer carpets* aus PDA (a). Die synthetisierten Polymerteppiche werden durch aneinander haftende PDA-Schichten zusammengehalten und können vom Substrat abgelöst werden. *Janus polymer carpets* aus Graphen können durch eine zweite Pfropfung von der Rückseite synthetisiert werden (b). Sowohl strukturierte *Janus polymer carpets* von PDA als auch von Graphen (c) zeigen eine verstärkte und teilweise gerichtete Faltenbildung.

In strukturierten *Janus polymer carpets* findet ein effektiver, anisotroper Spannungsabbau statt und es kommt zu einer gerichteten Faltenbildung, wenn die Abmessung des Musters beträchtlich höher ist als die Wellenlänge der Falten **(Abb. 6.3 c)**. Dieses Verhalten wird durch den darunter liegenden, weichen Polymerteppich unterstützt, da die Faltenbildung merklich stärker ausfällt als auf starrem SiO_2.

Der sequentielle Transfer von Polymerteppichen erlaubt auch die Integration anderer Materialien wie Graphen zwischen den Schichten **(Abb. 6.3 c)**. Die direkte Synthese von Janus-Membranen ausgehend von Graphen wurde durch sequentielle SIPGP auf beiden Seiten des Graphens realisiert **(Abb. 6.3 b)**.Nach unserem Kenntnisstand stellt dies das erste Beispiel für die direkte Synthese einer Janus-Membran ausgehend von einlagigem Graphen dar. Effekte auf die elektronische Struktur der Graphen-Einzelschicht wurden nach Synthese der Janus-Membranen nicht beobachtet.

Alle hergestellten *Janus polymer carpets* weisen typischerweise eine Größe von ca. 1 cm^2 auf. Unter Berücksichtigung ihrer Gesamtdicken, die im Bereich von max. einigen hundert Nanometern liegen, betragen die Aspektverhältnisse zwischen 10^4 und 10^5. Jeder synthetische Ansatz kann direkt angewendet und hochskaliert werden, da die Abscheidung von PDA sowie chemische Gasphasenabscheidung (CVD) von Graphen auf großen Flächen durchgeführt werden können. Da auch die verwendeten Pfropftechniken (SIPGP und SI-CuCRP) auf großen Substraten realisierbar sind, können *Janus polymer carpets* die in dieser Arbeit erreichten Aspektverhältnisse von 10^5 noch übertreffen. In Kombination mit der strukturellen Vielfalt von Polymerbürsten und BBBs bieten die vorgestellten Methoden einen einzigartigen Weg zu einer ganzen Palette neuartiger 2D-Materialien mit einstellbaren Eigenschaften. Das hervorragende Faltverhalten von strukturierten *Janus polymer carpets* macht sie besonders interessant für gerichteten Transport und Bewegung oder kontrollierte Verformung.

7. Experimental

7.1 Materials

Methyl methacrylate (MMA), 2-(dimethylamino)ethyl methacrylate (DMAEMA), 2-hydroxyethyl methacrylate (HEMA), N-isopropyl acrylamide (NiPAAm), 2-ethylhexyl methacrylate (EHMA), tert-butyl methacrylate (tBMA) and styrene (St) were purchased from Sigma-Aldrich (Weinheim, Germany) and purified before use by passing through a basic alumina column to remove the inhibitor. 2-bromoisobutyryl bromide (BiBB), 3-aminopropyltriethoxysilane (APTES), 1,1,4,7,7-pentamethyldiethylenetriamine (PMDETA, 99%), acetonitrile (ACN, dry), pyridine (99%), octadecyltrichlorosilane (ODS), tris(hydroxymethyl) aminomethane (Tris, > 99.8%), ammonium persulfate, dichloromethane (DCM, dry), dimethyl sulfoxide (DMSO) and isopropanol (iPrOH) as well as toluene (all from Sigma-Aldrich) were used as received. Methyl triflate (MeOTf), 2-methyl-2-oxazoline (MeOx, 98 %), 2-ethyl-2-oxazoline (EtOx, 98%), 2-isopropyl-2-oxazoline (iPrOx, 98%), 2-isopropenyl-2-oxazoline (iPOx, 98 %) and piperidine (Pip) were purchased from Sigma-Aldrich (Weinheim, Germany) and dried via distillation over CaH_2 before use. 2-Butyl-2-oxazoline (BuOx) was synthesized in a previously reported way.[293] Dopamine as HCl salt (DA·HCl) and ethylacetate (99.5 %) were purchased from Acros Organics and used as received. Hydrofluoric acid (38 - 40 %) was purchased from Merck (Darmstadt, Germany) and used as received. Poly(methyl methacrylate) (PMMA, 950 K) e-beam resist for spin-coating was provided by Allresist (Strausberg, Germany) and used as received. Deionized water was used for reactions and contact angle measurements.

4-inch Silicon wafers with a 300 nm oxide layer were obtained from Wacker AG (Burghausen, Germany). A diamond cutter was used to obtain the desired sample size. An oxygen plasma cleaning system (PDC-002, 200 W) from Harrick (USA) was used to clean the surface of the silicon wafer. The oxygen source of the chamber was supplied by a flow of air of 10 ml/min in 5 min for each wafer. Ethanol and water were used to rinse the wafers after plasma treatment.

4-inch Copper wafers were from MicroChemicals GmbH, Germany: Prime CZ-Si wafer 4 inch, 1-side polished, p-type (boron) TTV < 10 µm, 1 - 10 Ohm cm; 10 nm Ti adhesion layer; 200 nm Cu (purity > 99.9 %), RMS < 10 nm. The copper coated side of the wafer was

consecutively washed with portions of water and ethanol under ultrasonication (5 min). The cleaned Cu plate was immediately used.
Monolayers of chemical vapor deposition (CVD) graphene (G) on Cu-foil were purchased from Graphene Supermarket.

7.2 Methods and devices

Atomic force microscopy (AFM) was performed on a customized Ntegra Aura/Spectra from NT-MDT (Moscow, Russia) with a SMENA head in semicontact mode. The probes have a typical curvature radius of 6 nm, a resonant frequency of 140 - 235 kHz, and a force constant of 3.5 - 12 N/m. Typically AFM scans were performed at a frequency of 0.5 Hz consisting of 256 x 256 or 512 x 512 points. For thickness measurement the polymer layer were scratched with a cannula. Editing, height determination and calculation of the surface roughness was performed with the software Nova Px 3.2.5 from NT-MDT.
Raman spectroscopy was performed on a customized Ntegra Spectra from NT-MDT (Moscow, Russia) equipped with a 532 nm laser in upright configuration. Signals were measured at ambient conditions for 2 seconds and 50 - 500 scans were accumulated. Evaluation of the raw data was done with Nova Spectra software.
Ellipsometry measurements of the optical thickness, d, were performed with a SE800 ellipsometer from SENTECH Instruments GmbH equipped with a He-Ne laser source (λ = 632.8 nm) and a fixed angle of incidence of 60° at ambient conditions. The accumulated spectra were modeled using SpectraRay 3 software. The d-value was determined from three individual series of measurements utilizing the refractive index of the respective monomer.
X-ray photoelectron spectroscopy (XPS) was performed on an Omicron Multiprobe spectrometer using monochromatic aluminum Kα radiation. The spectra were calibrated by setting the Si 2p signal to 102.0 eV. Spectra were fitted by symmetric Voigt functions with a Shirley background correction.
Attenuated total reflection Fourier transform infrared spectroscopy (ATR FT-IR) was measured with a Nicolet 5700 (Thermo) IR-spectrometer with MCT detector. For the measurement a GladiATR set-up from PIKE Technologies with a diamond crystal was used and operated under OMNIC software. Before collection of sample spectra the device was flushed with nitrogen for 30 min and the respective substrate was scanned to obtain background. Then, IR of the polymer brush was obtained by summing up 256 or 512 scans for each sample.

Static water contact angle (θ_S) measurements were carried out with the Drop Shape Analysis System DSA 10 from Kruss to characterize the wettability of the polymer layers. For each sample, individual measurements at three different spots were performed and averaged. The measurements were performed at RT with bidestilled water. The contact angles were obtained using the tangent method fitting.

UV-lamps used for UV-induced polymerizations or photolithographic process were from Hitachi (FL8BL-B) with a maximum wavelength at 350 nm and a total power of 8 W or a Hg arc source from LOT Quantum Design (λ_{max} = 350 nm, 200 W).

A spin-coater from the company Setcas Electronis (China) model KW-4A was used to coat PMMA resist on samples before transfer. Typically the spin-coating was performed by dropping PMMA resist (1 - 2 drops) on the sample and spinning at 3000 rpm at ambient conditions.

A glovebox UniLab from MBraun (Klempner, Germany) was used to work under inert conditions and storage of oxygen and moisture sensitive chemicals. Concentration of O_2 and H_2O was at least under 20 ppm.

7.3 Procedures and Syntheses

7.3.1 Transfer of graphene

Cu-supported graphene sheets were spin-coated with PMMA and placed onto a freshly prepared 5 % solution of ammonium persulfate in water. After dissolution of the Cu-foil the freestanding PMMA/graphene sheets were fished with the help of a SiO_2 wafer and transferred onto a water reservoir for cleaning (2 x 5 min). Then, the sheets were transferred onto a clean SiO_2 substrate and dried with a moderate stream of N_2. Finally, PMMA was dissolved by placing the samples into acetone (3 x 5 min) and ethanol (1 x 5 min). The so transferred graphene sheets were dried with a jet of nitrogen and used for further reactions and modifications. Transfer of graphene onto polymer carpets or Janus polymer carpets was carried out analogously.

7.3.2 Self-assembled monolayer (SAM) of APTES on SiO_2 wafer

Clean SiO_2 surfaces were functionalized by ultrsonication of the wafers in a 5 %-(v/v) APTES solution in dry acetone for 30 min at room temperature and under dry argon atmosphere. After SAM formation, the samples were extensively rinsed with dry acetone and dried with a stream of nitrogen. Then, the samples were put into oven at 120°C for 2 h and rinsed with water,

acetone and ethanol. After drying with a flow of N_2 the APTES modified substrates typically exhibit a θ_S of 50 - 55°.

7.3.3 SAM of ODS on SiO_2 wafer

Clean SiO_2 surfaces were functionalized by CVD process. In the glovebox the substrate was placed at an equal distance to four containers with ODS. This set-up was closed and heated to 80°C for 24 h in the oven. After SAM formation, the samples were extensively rinsed with toluene and heptane and ultrsonicated in each solvent for 1 minute. After drying with a flow of N_2, the ODS modified substrates typically exhibit a θ_S of 90 - 100°.

7.3.4 Deposition of PDA on different substrates

Poly(tetrafluoroethylene) (PTFE), Au, Cu and Al/Al_2O_3 were extensively rinsed with deionized water and ethanol and ultrasonicated for 5 min each. SiO_2 was cleaned as described above. Deposition on graphene was carried out before transferring onto SiO_2 support.

DA·HCl (12.4 mg) was dissolved in 10 ml of Tris/HCl-buffer (10 mM, pH = 8.5) and the substrates were immersed into the freshly prepared solution. Deposition was allowed to proceed for approximately 24 h. Then, the samples were washed with deionized water and ethanol and ultrasonicated for 5 min each. In case of graphene the samples were only thoroughly rinsed with ethanol and water. Eventually, all the samples were blow dried by nitrogen.

7.3.5 Binding of BiBB-initiator on surface

In argon atmosphere the PDA or APTES modified surface was immersed in dry DCM (5 ml). Pyridine (51 µL) was added, followed by addition of 100 µL BiBB. The reaction was allowed to complete under stirring at RT within 3 h. The substrate was removed, washed with portions of DCM, water and ethanol and then dried by a jet of nitrogen. The resulting layer thickness was determined by ellipsometry or AFM and lay within the range of $d \approx 20$ - 35 nm for PDA/BiBB. The APTES-Br layer typically exhibited a thickness of $d \approx 2$ nm.

7.3.6 Surface-initiated Cu(0)-mediated controlled radical polymerization (SI-CuCRP)

A silicon wafer piece modified with APTES-Br or a substrate modified with PDA/BiBB was sandwiched with a copper plate at a typical distance of D = 0.5 mm using two spacers. This assembly was put into a degassed solution of monomer (1 ml or 0.1 g), solvent and PMDETA (20 µL) and closed with a rubber septum.

Hydrophilic monomers were typically dissolved in 1 ml of water and 0.5 ml of iPrOH. For monomers not soluble in water 0.5 ml DMSO was used as solvent. EHMA and styrene were dissolved in 1 ml DMSO and 0.75 ml toluene. The assembly was left in the reaction solution at RT for different amounts of time. The plates were separated and the substrate immediately washed with a fresh solvent appropriate for the respective monomer and ultrasonicated for 1 min. Finally, the substrates were dried by a jet of dry nitrogen and analyzed. In case of polymerization on graphene ultrasonication was not applied.

7.3.7 Self-initiated photografting and photopolymeriaztion (SIPGP)

The substrates were immersed into freshly degassed monomer in a standard glass reaction tubes. Next, the samples were irradiated with UV-light (λ_{max} = 350 nm, 8 W) for different amounts of time at a distance of approximately 2 cm to the UV-lamp. Reaction times were limited by viscosity increase due to polymerization in bulk and thus were strongly dependent on the used monomer. After polymerization the samples were rinsed with good solvent for the respective monomer and treated with ultrasound for 1 min. Eventually, the polymer brushes were dried by a jet of nitrogen. In case of polymer brushes on graphene ultrasonication was not applied.

7.3.8 Grafting of block copolymer brushes on PDA/BiBB

First, SI-CuCRP was performed with tBMA on PDA/BiBB as described above. The polymer brush was washed with DMSO and ethanol und ultrasonicated for 1 min. Then, a layer of PDMAEMA was grafted, followed by a third layer of PMMA. Both were rinsed with ethanol and ultrasonicated for 1 min each. The whole process was repeated for another block of PtBMA and PDMAEMA. Each resulting polymer brush was analyzed with AFM and contact angle measurement.

7.3.9 Patterning of polymer brushes

Two different approaches were used for the patterning of polymer brushes. Transmission electron microscopy grids (TEM-grids) were fixed on the substrates and used as photomask during SIPGP to obtain a polymer brush with negative pattern, as polymerization only takes place in uncovered areas.

Substrates with bound BiBB-initiator were exposed to UV-light (200 W) through a photomask for 1 h to selectively remove Br-moieties from surface. As photomasks different TEM-grids were carefully placed on the surface and covered with a quartz glass slide.

After UV exposure the samples were rinsed and ultrasonicated in water and ethanol for 1 min each and dried by a jet of nitrogen. No ultrasound was applied in case of graphene samples. Subsequently, the so patterned initiating layer was used for SI-CuCRP to obtain polymer brushes with positive pattern.

7.3.10 Synthesis of poly(2-oxazoline) (POx) bottle-brush brushes

First, PiPOx brushes were grafted on PDA or graphene *via* SIPGP and analyzed by means of ellipsometry or AFM and contact angle measurement.

In the glovebox 3 ml of ACN and 20 µl of MeOTf were put into a dry Schlenck-tube. Then, the solution was cooled to 0°C and a PiPOx grafted sample was immersed under a dry argon atmosphere. After stirring at 0°C for 30 min the solution was allowed to stir at room temperature for another 30 min. 1 ml of monomer was added to the tube and the reaction was stirred at 80°C for 2 h. Subsequently, the reaction was then cooled to room temperature and 40 µl of piperidine in 1 ml ACN were added under an argon atmosphere. The solution was stirred at room temperature over night. Afterwards, an excess of potassium carbonate was added and also stirred overnight. The substrate was removed from the reaction solution and cleaned with deionized water, ethanol and ethylacetate. Eventually, they were dried with a stream of nitrogen. Beside the thickness increase and change of θ_S, ATR FT-IR confirmed successful synthesis; signals from ring stretching (988 cm^{-1}, 956 cm^{-1}) disappeared after reaction and the signal from C=N stretching (1659 cm^{-1}) shifted due to formation of the poly(oxazoline) amid group (1645 cm^{-1}).

7.3.11 Fabrication of polymer carpets and Janus polymer carpets from PDA

Polymer brushes were detached from substrate by etching of the SiO_2 layer. The substrate was placed on a freshly prepared 5 - 10 % HF-solution in water. Prior to etching a PMMA resist was spin-coated on the samples to stabilize hydrophilic polymer brushes. After detachment of the polymeric layer, another SiO_2 wafer was used to fish out the polymer carpet and transfer it onto a water reservoir. The polymer carpet was left floating on the water for 5 minutes to ensure removal of residual HF molecules. This process was repeated with fresh water. Eventually, the polymer carpet was fished out with another wafer and dried under ambient conditions and with a moderate stream of nitrogen. If necessary, PMMA resist was washed off by placing the sample in acetone (3 x 5 min) and ethanol (1 x 5 min). The so transferred polymer carpets were dried with a jet of nitrogen.

For fabrication of Janus polymer carpets the freestanding layers were fished and a second SiO_2 wafer (support) was placed on top of the still wet carpet. Then, the support was carefully slid off to give a flipped polymer carpet attached to its surface. A moderate stream of N_2 was applied to dry the flipped carpet. Other polymer brushes were made freestanding as described above and transferred on top of the previously flipped samples by fishing them with the respective sample. The so prepared Janus polymer carpets were dried with a moderate stream of nitrogen and the PMMA was washed off with acetone and ethanol. Finally, the SiO_2 was etched again to obtain freestanding Janus polymer carpets floating on water.

7.3.12 Fabrication of Janus polymer carpets from graphene

First, poly(styrene) brushes were grafted on SiO_2-supported graphene *via* SIPGP (8 W UV-lamp). The resulting polymer carpet was etched from the support by use of 5 - 10 % HF-solution in water. After detachment the freestanding sheet was transferred onto a freshly degassed solution of 0.5 ml DMAEMA in 3 ml water. Subsequently, the floating polymer carpet was irradiated with UV-light (200 W UV-lamp) through the monomer solution for 4 h. The distance between polymer carpet and UV source was adjusted to 20 - 25 cm and an IR-filter was used to prevent strong heating in the reaction solution. After reaction, the carpet was fished from the reaction solution and transferred onto water to enable diffusion of unreacted monomer. This cleaning procedure was repeated twice. Finally, the received Janus polymer carpet was transferred onto another SiO_2 support and dried with a moderate stream of nitrogen.

For backside analysis of the graphene based Janus carpets, samples were detached from the support by etching. After fishing with another wafer, a scotch tape was placed on top of the Janus carpet and carefully peeled off. Sticking to the scotch tape the sample was let dry under ambient conditions. In that way the whole carpet was turned around enabling characterization of the backside by contact angle measurements.

Bibliography

[1] A. K. Geim, *Angew. Chemie - Int. Ed.* **2011**, *50*, 6966.

[2] I. Bojanova, *IT Prof.* **2014**, *16*, 8.

[3] R. Debjani, *Int. J. Interdiscip. Multidiscip. Stud.* **2014**, *1*, 107.

[4] R. Hodson, *Nat. Outlook* **2018**, *563*, 131.

[5] E. Brynjolfsson, A. McAfee, *Race Against The Machine: How the Digital Revolution Is Accelerating Innovation, Driving Productivity, and Irreversibly Transforming Employment and the Economy*, Digital Frontier Press, **2011**.

[6] C. Casagrande, P. Fabre, E. Raphael, M. Veyssie, *Europhys. Lett.* **1989**, *9*, 251.

[7] H. C. Yang, J. Hou, V. Chen, Z. K. Xu, *Angew. Chemie - Int. Ed.* **2016**, *55*, 13398.

[8] H. C. Yang, Y. Xie, J. Hou, A. K. Cheetham, V. Chen, S. B. Darling, *Adv. Mater.* **2018**, *30*, 1801495.

[9] I. Amin, M. Steenackers, N. Zhang, A. Beyer, X. Zhang, T. Pirzer, T. Hugel, R. Jordan, A. Gölzhäuser, *Small* **2010**, *6*, 1623.

[10] I. Amin, M. Steenackers, N. Zhang, R. Schubel, A. Beyer, A. Gölzhäuser, R. Jordan, *Small* **2011**, *7*, 683.

[11] M. Steenackers, A. M. Gigler, N. Zhang, F. Deubel, M. Seifert, L. H. Hess, C. H. Y. X. Lim, K. P. Loh, J. a Garrido, R. Jordan, M. Stutzmann, I. D. Sharp, *J. Am. Chem. Soc.* **2011**, *133*, 10490.

[12] T. Zhang, Y. Du, J. Kalbakova, R. Schubel, R. D. Rodriguez, T. Chen, D. Zahn, R. Jordan, *Polym. Chem.* **2015**, *6*, 8176.

[13] T. Zhang, E. M. Benetti, R. Jordan, *ACS Macro Lett.* **2019**, *8*, 145.

[14] T. Zhang, Y. Du, F. Müller, I. Amin, R. Jordan, *Polym. Chem.* **2015**, *6*, 2726.

[15] K. S. Novoselov, A. K. Geim, S. V. Morozov, D. Jiang, Y. Zhang, S. V. Dubonos, I. V. Grigorieva, A. A. Firsov, *Science (80-.).* **2004**, *306*, 666.

[16] K. S. Novoselov, *Angew. Chemie - Int. Ed.* **2011**, *50*, 6986.

[17] E. J. Boyd, D. Uttamchandani, S. Member, *J. Microelectromechanical Syst.* **2012**, *21*, 243.

[18] X. Zhang, B. R. S. Rajaraman, H. Liub, S. Ramakrishna, *RSC Adv.* **2014**, *4*, 28987.

[19] G. Yang, L. Li, W. B. Lee, M. C. Ng, *Sci. Technol. Adv. Mater.* **2018**, *19*, 613.

[20] C. Si, Z. Sun, F. Liu, *Nanoscale* **2016**, *8*, 3207.

[21] "Janus-Statue," can be found under https://de.wikipedia.org/wiki/Janus_(Mythologie),

2018.

[22] S. Gangwal, O. J. Cayre, O. D. Velev, *Langmuir* **2008**, *24*, 13312.

[23] X. Tian, H. Jin, J. Sainio, R. H. A. Ras, O. Ikkala, *Adv. Funct. Mater.* **2014**, *24*, 6023.

[24] J. Gu, P. Xiao, J. Chen, J. Zhang, Y. Huang, T. Chen, *ACS Appl. Mater. Interfaces* **2014**, *6*, 16204.

[25] D. M. Andala, S. H. R. Shin, H.-Y. Lee, K. J. M. Bishop, *ACS Nano* **2012**, *6*, 1044.

[26] C. Wang, C. Xu, H. Zeng, S. Sun, *Adv. Mater.* **2009**, *21*, 3045.

[27] T. Chen, G. Chen, S. Xing, T. Wu, H. Chen, *Chem. Mater.* **2010**, *22*, 3826.

[28] P.-G. de Gennes, *Science (80-.).* **1992**, *256*, 495.

[29] A. Walther, A. H. E. Mu, *Chem. Rev.* **2013**, *113*, 5194.

[30] L. Zhang, J. Yu, M. Yang, Q. Xie, H. Peng, Z. Liu, *Nat. Commun.* **2013**, *4*, DOI 10.1038/ncomms2464.

[31] J. G. Gibbs, Y. P. Zhao, *Appl. Phys. Lett.* **2009**, *94*, DOI 10.1063/1.3122346.

[32] A. Walther, M. Hoffmann, A. H. E. Müller, *Angew. Chemie - Int. Ed.* **2008**, *47*, 711.

[33] T. Tanaka, M. Okayama, Y. Kitayama, Y. Kagawa, M. Okubo, *Langmuir* **2010**, *26*, 11732.

[34] S. Gangwal, O. J. Cayre, M. Z. Bazant, O. D. Velev, *Phys. Rev. Lett.* **2008**, *100*, 1.

[35] K. C. Bryson, T. I. Löbling, A. H. E. Müller, T. P. Russell, R. C. Hayward, *Macromolecules* **2015**, *48*, 4220.

[36] G. Stoychev, L. Guiducci, S. Turcaud, J. W. C. Dunlop, L. Ionov, *Adv. Funct. Mater.* **2016**, *26*, 7733.

[37] Z. Cao, G. Wang, Y. Chen, F. Liang, Z. Yang, *Macromolecules* **2015**, *48*, 7256.

[38] F. S. Ou, M. M. Shaijumon, P. M. Ajayan, *Nano Lett.* **2008**, *8*, 1853.

[39] S. N. Yin, C. F. Wang, Z. Y. Yu, J. Wang, S. S. Liu, S. Chen, *Adv. Mater.* **2011**, *23*, 2915.

[40] T. Nisisako, T. Torii, T. Takahashi, Y. Takizawa, *Adv. Mater.* **2006**, *18*, 1152.

[41] S. Bhaskar, J. Hitt, S. W. L. Chang, J. Lahann, *Angew. Chemie - Int. Ed.* **2009**, *48*, 4589.

[42] J. R. Howse, R. A. L. Jones, A. J. Ryan, T. Gough, R. Vafabakhsh, R. Golestanian, *Phys. Rev. Lett.* **2007**, *99*, 8.

[43] L. Y. Wu, B. M. Ross, S. G. Hong, L. P. Lee, *Small* **2010**, *6*, 503.

[44] A. Kirillova, C. Schliebe, G. Stoychev, A. Jakob, H. Lang, A. Synytska, *ACS Appl. Mater. Interfaces* **2015**, *7*, 21224.

[45] S. H. Hu, X. Gao, *J. Am. Chem. Soc.* **2010**, *132*, 7234.

[46] C. Xu, J. Xie, D. Ho, C. Wang, N. Kohler, E. G. Walsh, J. R. Morgan, Y. E. Chin, S. Sun, *Angew. Chemie - Int. Ed.* **2008**, *47*, 173.

[47] H. Y. Hsieh, T. W. Huang, J. L. Xiao, C. S. Yang, C. C. Chang, C. C. Chu, L. W. Lo, S. H. Wang, P. C. Wang, C. C. Chieng, C. H. Lee, F. G. Tseng, *J. Mater. Chem.* **2012**, *22*, 20918.

[48] Q. Cheng, M. Li, Y. Zheng, B. Su, S. Wang, L. Jiang, *Soft Matter* **2011**, *7*, 5948.

[49] A. Synytska, L. Ionov, *Part. Part. Syst. Charact.* **2013**, *30*, 922.

[50] Z. Zhang, X. Sui, P. Li, G. Xie, X. Y. Kong, K. Xiao, L. Gao, L. Wen, L. Jiang, *J. Am. Chem. Soc.* **2017**, *139*, 8905.

[51] S. Liu, C. Wu, W. S. Hung, X. Lu, K. R. Lee, *J. Mater. Chem. A* **2017**, *5*, 22988.

[52] F. Ren, G. Li, Z. Zhang, X. Zhang, H. Fan, C. Zhou, Y. Wang, Y. Zhang, C. Wang, K. Mu, Y. Su, D. Wu, *J. Mater. Chem. A* **2017**, *5*, 18403.

[53] X. Sheng, Z. Liu, R. Zeng, L. Chen, X. Feng, L. Jiang, *J. Am. Chem. Soc.* **2017**, *139*, 12402.

[54] M. B. Wu, H. C. Yang, J. J. Wang, G. P. Wu, Z. K. Xu, *ACS Appl. Mater. Interfaces* **2017**, *9*, 5062.

[55] H. Wang, H. Zhou, H. Niu, J. Zhang, Y. Du, T. Lin, *Adv. Mater. Interfaces* **2015**, *2*, 1400506.

[56] H. C. Yang, J. Hou, L. S. Wan, V. Chen, Z. K. Xu, *Adv. Mater. Interfaces* **2016**, *3*, 1500774.

[57] Y. S. Oh, G. Y. Jung, J. H. Kim, J. H. Kim, S. H. Kim, S. K. Kwak, S. Y. Lee, *Adv. Funct. Mater.* **2016**, *26*, 7074.

[58] J. Gao, W. Guo, D. Feng, H. Wang, D. Zhao, L. Jiang, *J. Am. Chem. Soc.* **2014**, *136*, 12265.

[59] J. Wu, N. Wang, L. Wang, H. Dong, Y. Zhao, L. Jiang, *Soft Matter* **2012**, *8*, 5996.

[60] L. Hu, S. Gao, Y. Zhu, F. Zhang, L. Jiang, J. Jin, *J. Mater. Chem. A* **2015**, *3*, 23477.

[61] Y. Zhang, M. Barboiu, *Chem. Commun.* **2015**, *51*, 15925.

[62] J. Chen, Y. Liu, D. Guo, M. Cao, L. Jiang, *Chem. Commun.* **2015**, *51*, 11872.

[63] Z. Wang, Y. Wang, G. Liu, *Angew. Chemie - Int. Ed.* **2016**, *55*, 1291.

[64] B. D. Ratner, A. F. Hoffman, F. J. Schoen, J. E. Lemons, *Biomaterials Science An Introduction to Materials in Medicine*, Academic Press, Inc., **1996**.

[65] M. Cichomski, J. Grobelny, G. Celichowski, *Appl. Surf. Sci.* **2008**, *254*, 4273.

[66] M. E. Buck, D. M. Lynn, *Langmuir* **2010**, *26*, 16134.

[67] N. C. Estillore, R. C. Advincula, *Macromol. Chem. Phys.* **2011**, *212*, 1552.

[68] K. B. Blodgett, *J. Am. Chem. Soc.* **1935**, *57*, 1007.

[69] N. Meyerbröker, M. Zharnikov, *Adv. Mater.* **2014**, *26*, 3328.

[70] Y. Okamura, K. Kabata, M. Kinoshita, H. Miyazaki, A. Saito, T. Fujie, S. Ohtsubo, D. Saitoh, S. Takeoka, *Adv. Mater.* **2013**, *25*, 545.

[71] G. Dearnaley, J. H. Arps, *Surf. Coatings Technol.* **2005**, *200*, 2518.

[72] M. Steenackers, R. Jordan, A. Küller, M. Grunze, *Adv. Mater.* **2009**, *21*, 2921.

[73] M. Steenackers, A. Kü ̈ ler, S. Stoycheva, *Langmuir* **2009**, *25*, 2225.

[74] A. Wang, H. Tang, T. Cao, S. O. Salley, K. Y. S. Ng, *J. Colloid Interface Sci.* **2005**, *291*, 438.

[75] J. Schlenoff, M. Li, H. Ly, *J. Am. Chem. Soc.* **1995**, *117*, 12528.

[76] D. Hafner, L. Ziegler, M. Ichwan, T. Zhang, M. Schneider, M. Schiffmann, C. Thomas, K. Hinrichs, R. Jordan, I. Amin, *Adv. Mater.* **2016**, *28*, 1489.

[77] N. G. Patel, G. Zhang, *Organogenesis* **2013**, *9*, 93.

[78] Z. Tang, T. Okano, *Regen. Biomater.* **2014**, *1*, 91.

[79] Z. Ma, X. Jia, G. Zhang, J. Hu, X. Zhang, Z. Liu, H. Wang, F. Zhou, *J. Agric. Food Chem.* **2013**, *61*, 5474.

[80] Z. Ma, X. Jia, J. Hu, G. Zhang, F. Zhou, Z. Liu, H. Wang, *Langmuir* **2013**, *29*, 5631.

[81] S. Gupta, M. Agrawal, M. Conrad, N. A. Hutter, P. Olk, F. Simon, L. M. Eng, M. Stamm, R. Jordan, *Adv. Funct. Mater.* **2010**, *20*, 1756.

[82] Z. Guo, L. L. Henry, V. Palshin, E. J. Podlaha, *J. Mater. Chem.* **2006**, *16*, 1772.

[83] Z. Fang, A. Ito, A. C. Stuart, H. Luo, Z. Chen, K. Vinodgopal, W. You, T. J. Meyer, D. K. Taylor, *ACS Nano* **2013**, 7992.

[84] S. T. Milner, *Science (80-.).* **1991**, *251*, 905.

[85] S. Alexander, *J. Phys.* **1977**, *38*, 983.

[86] P. G. De Gennes, P. G. D. G. Scaling, J. De Physique, *J. Phys.* **1976**, *37*, 1445.

[87] W. L. Chen, R. Cordero, H. Tran, C. K. Ober, *Macromolecules* **2017**, *50*, 4089.

[88] S. T. Milner, T. A. Witten, M. E. Cates, *Macromolecules* **1989**, *22*, 853.

[89] S. T. Milner, T. A. Witten, M. E. Cates, *Macromolecules* **1988**, *21*, 2610.

[90] E. B. Zhulina, O. V. Borisov, V. A. Pryamitsyn, T. M. Birshtein, *Macromolecules* **1991**, *24*, 140.

[91] D. Dukes, Y. Li, S. Lewis, B. Benicewicz, L. Schadler, S. K. Kumar, *Macromolecules* **2010**, *43*, 1564.

[92] Y. Tran, P. Auroy, L. T. Lee, *Macromolecules* **1999**, *32*, 8952.

[93] P. Pincus, *Macromolecules* **1991**, *24*, 2912.

[94] E. B. Zhulina, T. M. Birshtein, O. V. Borisov, *Macromolecules* **1995**, *28*, 1491.

[95] P. Mansky, Y. Liu, E. Huang, T. P. Russell, C. Hawker, *Solutions* **2009**, *1458*, 1458.

[96] D. J. Dyer, *Adv. Polym. Sci.* **2006**, *197*, 47.

[97] O. Kir, W. H. Binder, *Eur. Polym. J.* **2013**, *49*, 3078.

[98] R. Jordan, A. Ulman, J. F. Kang, M. H. Rafailovich, J. Sokolov, *J. Am. Chem. Soc.* **1999**, *121*, 1016.

[99] R. Jordan, A. Ulman, *J. Am. Chem. Soc.* **1998**, *120*, 243.

[100] K. Matyjaszewski, D. Hongchen, W. Jakubowski, J. Pietrasik, A. Kusumo, *Langmuir* **2007**, *23*, 4528.

[101] C. A. Kuliasha, R. L. Fedderwitz, P. R. Calvo, B. S. Sumerlin, A. B. Brennan, *Macromolecules* **2018**, *51*, 306.

[102] M. F. Z. Lerum, W. Chen, *Langmuir* **2011**, *27*, 5403.

[103] O. Prucker, J. Rühe, *Langmuir* **1998**, *14*, 6893.

[104] O. Prucker, J. Rühe, *Macromolecules* **1998**, *31*, 602.

[105] L. Pemberton, R. De Jaeger, *Chem. Mater.* **1996**, *8*, 1391.

[106] K. Kildal, K. Olafsen, A. Stori, *J. Appl. Polym. Sci.* **1992**, *44*, 1893.

[107] N. V. Bhat, D. J. Upadhyay, *J. Appl. Polym. Sci.* **2002**, *86*, 925.

[108] H. Mohapatra, M. Kleiman, A. P. Esser-Kahn, *Nat. Chem.* **2017**, *9*, 135.

[109] W. T. Yang, B. Rånby, *J. Appl. Polym. Sci.* **1996**, *62*, 533.

[110] S. J. Li, C. G. Li, T. Li, J. J. Cheng, *Polymer Photochemistry Principles and Applications*, Fudan University Press, Shanghai, **1993**.

[111] J. P. Deng, W. T. Yang, B. Rånby, *Macromol. Rapid Commun.* **2001**, *22*, 535.

[112] M. Steenackers, S. Q. Lud, M. Niedermeier, P. Bruno, D. M. Gruen, P. Feulner, M. Stutzmann, J. A. Garrido, R. Jordan, *J. Am. Chem. Soc.* **2007**, *129*, 15655.

[113] N. Zhang, M. Steenackers, R. Luxenhofer, R. Jordan, *Macromolecules* **2009**, *42*, 5345.

[114] C. J. Hawker, G. G. Barclay, A. Orellana, J. Dao, W. Devonport, *Macromolecules* **1996**, *29*, 5245.

[115] J. S. Wang, K. Matyjaszewski, *J. Am. Chem. Soc.* **1995**, *117*, 5614.

[116] R. Barbey, L. Lavanant, D. Paripovic, N. Schuwer, C. Sugnaux, S. Tugulu, H.-A. Klok, *Chem. Rev.* **2009**, *109*, 5437.

[117] D. Gieseler, R. Jordan, *Polym. Chem.* **2015**, *6*, 4678.

[118] T. Zhang, T. Chen, I. Amin, R. Jordan, *Polym. Chem.* **2014**, *5*, 4790.

[119] K. Matyjaszewski, *Macromolecules* **2012**, *45*, 4015.

[120] K. Matyjaszewski, M. Wei, J. Xia, S. G. Gaynor, *Macromol. Chem. Phys.* **1998**, *199*,

2289.

[121] H. Zhang, B. Klumperman, W. Ming, H. Fischer, R. Van der Linde, *Macromolecules* **2001**, *34*, 6169.

[122] D. R. D'Hooge, D. Konkolewicz, M. F. Reyniers, G. B. Marin, K. Matyjaszewski, *Macromol. Theory Simulations* **2012**, *21*, 52.

[123] N. Bortolamei, A. A. Isse, A. J. D. Magenau, A. Gennaro, K. Matyjaszewski, *Angew. Chemie Int. Ed.* **2011**, *50*, 11391.

[124] C. Y. Hsiao, H. A. Han, G. H. Lee, C. H. Peng, *Eur. Polym. J.* **2014**, *51*, 12.

[125] V. Percec, T. Guliashvili, J. S. Ladislaw, A. Wistrand, A. Stjerndahl, M. J. Sienkowska, M. J. Monteiro, S. Sahoo, *J. Am. Chem. Soc.* **2006**, *128*, 14156.

[126] F. Sven, B. M. Rosen, P. Virgil, *J. Polym. Sci. Part A Polym. Chem.* **2010**, *48*, 1190.

[127] C. Waldron, Q. Zhang, Z. Li, V. Nikolaou, G. Nurumbetov, J. Godfrey, R. McHale, G. Yilmaz, R. K. Randev, M. Girault, K. McEwan, D. M. Haddleton, M. Droesbeke, A. J. Haddleton, P. Wilson, A. Simula, J. Collins, D. J. Lloyd, J. a. Burns, C. Summers, C. Houben, A. Anastasaki, M. Li, C. R. Becer, J. K. Kiviaho, N. Risangud, *Polym. Chem.* **2014**, *5*, 57.

[128] B. M. Rosen, V. Percec, *Chem. Rev.* **2009**, *109*, 5069.

[129] D. Konkolewicz, Y. Wang, P. Krys, M. Zhong, A. a. Isse, A. Gennaro, K. Matyjaszewski, *Polym. Chem.* **2014**, *5*, 4396.

[130] M. E. Levere, N. H. Nguyen, X. Leng, V. Percec, *Polym. Chem.* **2013**, *4*, 1635.

[131] N. H. Nguyen, B. M. Rosen, G. Lligadas, V. Percec, *Macromolecules* **2009**, *42*, 2379.

[132] B. M. Rosen, X. Jiang, C. J. Wilson, N. H. Nguyen, M. J. Monteiro, V. Percec, *J. Polym. Sci. Part a-Polymer Chem.* **2009**, *47*, 5606.

[133] M. E. Levere, N. H. Nguyen, V. Percec, *Macromolecules* **2012**, *45*, 8267.

[134] N. H. Nguyen, M. E. Levere, V. Percec, *J. Polym. Sci. Part A Polym. Chem.* **2012**, *50*, 860.

[135] T. Guliashvili, V. Percec, *J. Polym. Sci. Part a-Polymer Chem.* **2007**, *45*, 1607.

[136] C. Y. Lin, M. L. Coote, A. Gennaro, *J. A. Chem. Soc.* **2008**, *130*, 12762.

[137] D. Konkolewicz, Y. Wang, M. Zhong, P. Krys, A. a. Isse, A. Gennaro, K. Matyjaszewski, *Macromolecules* **2013**, *46*, 8749.

[138] Y. Wang, M. Zhong, W. Zhu, C.-H. Peng, Y. Zhang, D. Konkolewicz, N. Bortolamei, A. A. Isse, A. Gennaro, K. Matyjaszewski, *Macromolecules* **2013**, *46*, 3793.

[139] F. Alsubaie, A. Anastasaki, V. Nikolaou, A. Simula, G. Nurumbetov, P. Wilson, K. Kempe, D. M. Haddleton, *Macromolecules* **2015**, *48*, 5517.

[140] F. Alsubaie, A. Anastasaki, V. Nikolaou, A. Simula, G. Nurumbetov, *Macromolecules* **2015**, *48*, 6421.

[141] Z. Liu, S. Zhu, Y. Li, Y. Li, P. Shi, Z. Huang, X. Huang, *Polym. Chem.* **2015**, *6*, 311.

[142] S. Ding, J. A. Floyd, K. B. Walters, *J. Polym. Sci. Part A Polym. Chem.* **2009**, *47*, 6552.

[143] Y. Che, T. Zhang, Y. Du, I. Amin, C. Marschelke, R. Jordan, *Angew. Chemie - Int. Ed.* **2018**, *57*, 16380.

[144] E. S. Dehghani, Y. Du, T. Zhang, S. N. Ramakrishna, N. D. Spencer, R. Jordan, E. M. Benetti, *Macromolecules* **2017**, *50*, 2436.

[145] H. Lee, S. M. Dellatore, W. M. Miller, P. B. Messersmith, *Science* **2007**, *318*, 426.

[146] R. Zangmeister, T. Morris, M. Tarlov, *Langmuir* **2013**, *29*, 8619.

[147] M. Kohri, Y. Shinoda, H. Kohma, Y. Nannichi, M. Yamauchi, S. Yagai, T. Kojima, T. Taniguchi, K. Kishikawa, *Macromol. Rapid Commun.* **2013**, *34*, 1220.

[148] H. Watanabe, A. Fujimoto, R. Yamamoto, J. Nishida, M. Kobayashi, A. Takahara, *ACS Appl. Mater. Interfaces* **2014**, *6*, 3648.

[149] F. Yu, S. Chen, Y. Chen, H. Li, L. Yang, Y. Chen, Y. Yin, *J. Mol. Struct.* **2010**, *982*, 152.

[150] J. Tian, D. Xu, M. Liu, F. Deng, Q. Wan, Z. Li, K. Wang, X. He, X. Zhang, Y. Wei, *J. Polym. Sci. Part A Polym. Chem.* **2015**, *53*, 1872.

[151] Q. Wan, M. Liu, J. Tian, F. Deng, G. Zeng, Z. Li, K. Wang, Q. Zhang, X. Zhang, Y. Wei, *Polym. Chem.* **2015**, *6*, 1786.

[152] W. Wang, X. Ji, H. Bin Na, M. Safi, A. Smith, G. Palui, J. M. Perez, H. Mattoussi, *Langmuir* **2014**, *30*, 6197.

[153] A. Lak, J. Dieckhoff, F. Ludwig, J. M. Scholtyssek, O. Goldmann, H. Lünsdorf, D. Eberbeck, A. Kornowski, M. Kraken, F. J. Litterst, K. Fiege, P. Mischnick, M. Schilling, *Nanoscale* **2013**, *5*, 11447.

[154] W. Sheng, B. Li, X. Wang, B. Dai, B. Yu, X. Jia, F. Zhou, *Chem. Sci.* **2015**, *6*, 2068.

[155] J. H. Ryu, P. B. Messersmith, H. Lee, *ACS Appl. Mater. Interfaces* **2018**, *10*, 7523.

[156] F. Bernsmann, V. Ball, F. Addiego, A. Ponche, M. Michel, J. J. D. A. Gracio, V. Toniazzo, D. Ruch, *Langmuir* **2011**, *27*, 2819.

[157] J. Liebscher, R. Mró czyń ki, H. Scheidt, *Langmuir* **2013**, *29*, 10539.

[158] D. Dreyer, D. Miller, B. Freeman, *Langmuir* **2012**, *28*, 6428.

[159] S. Lin, C.-T. Chen, I. Bdikin, V. Ball, J. Grácio, M. J. Buehler, *Soft Matter* **2014**, *10*, 457.

[160] N. F. Della Vecchia, R. Avolio, M. Alfè, M. E. Errico, A. Napolitano, M. d'Ischia, *Adv. Funct. Mater.* **2013**, *23*, 1331.

[161] N. F. Della Vecchia, A. Luchini, A. Napolitano, G. Derrico, G. Vitiello, N. Szekely, M. Dischia, L. Paduano, *Langmuir* **2014**, *30*, 9811.

[162] O. Z. Fisher, B. L. Larson, P. S. Hill, D. Graupner, M. T. Nguyen-Kim, N. S. Kehr, L. De Cola, R. Langer, D. G. Anderson, *Adv. Mater.* **2012**, *24*, 3032.

[163] K. Y. Ju, Y. Lee, S. Lee, S. B. Park, J. K. Lee, *Biomacromolecules* **2011**, *12*, 625.

[164] J. Yu, Y. Kan, M. Rapp, E. Danner, W. Wei, S. Das, D. R. Miller, Y. Chen, J. H. Waite, J. N. Israelachvili, *Proc. Natl. Acad. Sci.* **2013**, *110*, 15680.

[165] T. Utzig, P. Stock, M. Valtiner, *Angew. Chemie - Int. Ed.* **2016**, *55*, 9524.

[166] H. Lee, N. F. Scherer, P. B. Messersmith, *Proc. Natl. Acad. Sci.* **2006**, *103*, 12999.

[167] C. Zhang, L. Gong, L. Xiang, Y. Du, W. Hu, H. Zeng, Z. K. Xu, *ACS Appl. Mater. Interfaces* **2017**, *9*, 30943.

[168] Q. Lu, E. Danner, J. H. Waite, J. N. Israelachvili, I. Jn, H. Zeng, H. Ds, *J. R. Soc. Interface* **2013**, *10*, 20120759.

[169] C. Lim, J. Huang, S. Kim, H. Lee, H. Zeng, D. S. Hwang, *Angew. Chemie - Int. Ed.* **2016**, *55*, 3342.

[170] G. P. Maier, M. V. Rapp, J. H. Waite, J. N. Isrealachvili, A. Butler, *Science (80-.).* **2015**, *349*, 628.

[171] X. Zhang, J. Ji, X. Zhang, B. Yang, M. Liu, W. Liu, L. Tao, Y. Chen, Y. Wei, *RSC Adv.* **2013**, *3*, 21817.

[172] A. K. Roy, B. Park, K. S. Lee, S. Y. Park, I. In, *Nanotechnology* **2014**, *25*, 445603.

[173] C. Li, Z. Liu, P. Yao, *RSC Adv.* **2016**, *6*, 33083.

[174] R. Gu, W. Z. Xu, P. a. Charpentier, *J. Polym. Sci. Part A Polym. Chem.* **2013**, *51*, 3941.

[175] S. P. Le-Masurier, G. Gody, S. Perrier, A. M. Granville, *Polym. Chem.* **2014**, *5*, 2816.

[176] H. Li, L. Shen, K. Yin, J. Ji, J. Wang, X. Wang, X. Zhang, *J. Mater. Chem. A* **2013**, *1*, 7270.

[177] J. Kong, W. A. Yee, L. Yang, Y. Wei, S. L. Phua, H. G. Ong, J. M. Ang, X. Li, X. Lu, *Chem. Commun.* **2012**, *48*, 10316.

[178] K. Ai, Y. Liu, C. Ruan, L. Lu, G. Lu, *Adv. Mater.* **2013**, *25*, 998.

[179] M. Liu, G. Zeng, K. Wang, Q. Wan, L. Tao, X. Zhang, Y. Wei, *Nanoscale* **2016**, *8*, 16819.

[180] X. Zhang, Q. Huang, F. Deng, H. Huang, Q. Wan, M. Liu, Y. Wei, *Appl. Mater. Today* **2017**, *7*, 222.

[181] M. Krogsgaard, V. Nue, H. Birkedal, *Chem. - A Eur. J.* **2016**, *22*, 844.

[182] Y. Liu, K. Ai, L. Lu, *Chem. Rev.* **2014**, *114*, 5057.

[183] K. Balasubramanian, M. Burghard, *Chemie Unserer Zeit* **2011**, *45*, 240.

[184] G. E. Volovik, *JETP Lett.* **2018**, *107*, 115.

[185] C. Lee, X. Wei, J. W. Kysar, J. Hone, *Science (80-.).* **2008**, *321*, 385.

[186] S. V Morozov, K. S. Novoselov, M. I. Katsnelson, F. Schedin, D. C. Elias, J. A. Jaszczak, A. K. Geim, *Phys. Rev. Lett.* **2008**, *100*, 016602.

[187] R. Murali, Y. Yang, K. Brenner, T. Beck, J. D. Meindl, *Appl. Phys. Lett.* **2009**, *94*, 243114.

[188] M. Cai, D. Thorpe, H. Adamson, H. C. Schniepp, *J. Mater. Chem.* **2012**, *22*, 24992.

[189] B. N. Liu, F. Luo, H. Wu, Y. Liu, C. Zhang, J. Chen, *Afdanced Funct. Mater.* **2008**, *18*, 1518.

[190] L. Jiao, L. Zhang, X. Wang, G. Diankov, H. Dai, *Nature* **2009**, *458*, 877.

[191] D. V Kosynkin, A. L. Higginbotham, A. Sinitskii, J. R. Lomeda, A. Dimiev, B. K. Price, J. M. Tour, *Nature* **2009**, *458*, 872.

[192] W. S. Hummers, R. E. Offeman, *J. Am. Chem. Soc.* **1958**, *80*, 1339.

[193] G. Montambaux, F. Piéchon, J. N. Fuchs, M. O. Goerbig, *Eur. Phys. J. B* **2009**, *72*, 509.

[194] J. M. Garcia, R. He, M. P. Jiang, J. Yan, A. Pinczuk, Y. M. Zuev, K. Soo, P. Kim, K. Baldwin, K. W. West, L. N. Pfeiffer, *Solid State Commun.* **2010**, *150*, 809.

[195] C. Berger, Z. Song, T. Li, X. Li, A. Y. Ogbazghi, R. Feng, Z. Dai, A. N. Marchenkov, E. H. Conrad, P. N. First, W. A. De Heer, *J. Phys. Chem. B* **2004**, *108*, 19912.

[196] X. Li, W. Cai, J. An, S. Kim, J. Nah, D. Yang, L. Colombo, R. S. Ruoff, *Science (80-.).* **2009**, *324*, 1312.

[197] K. S. Kim, Y. Zhao, H. Jang, S. Y. Lee, J. M. Kim, K. S. Kim, J. Ahn, P. Kim, J. Choi, B. H. Hong, *Nature* **2009**, *457*, 706.

[198] Q. Yu, L. A. Jauregui, W. Wu, R. Colby, J. Tian, Z. Su, H. Cao, Z. Liu, D. Pandey, D. Wei, T. F. Chung, P. Peng, N. P. Guisinger, E. A. Stach, J. Bao, S.-S. Pei, Y. P. Chen, *Nat. Mater.* **2011**, *10*, 443.

[199] A. Reina, X. Jia, J. Ho, D. Nezich, H. Son, V. Bulovic, M. S. Dresselhaus, J. Kong, *Nano Lett.* **2009**, *9*, 30.

[200] A. H. Neto Castro, F. Guinea, N. M. R. Peres, K. S. Novoselov, A. K. Geim, *Rev. Mod. Phys.* **2009**, *81*, 109.

[201] Y. Zhang, F. Liu, *Appl. Phys. Lett.* **2011**, *99*, 241908.

[202] V. M. Pereira, A. H. C. Neto, N. M. R. Peres, *Phys. Rev. B* **2009**, *80*, 045401.

[203] S. Choi, S. Jhi, Y. Son, *Phys. Rev. B* **2010**, *81*, 081407.

[204] G. Cocco, E. Cadelano, L. Colombo, C. Neto, *Phys. Rev. B* **2010**, *81*, 241412.

[205] M. Huang, H. Yan, C. Chen, D. Song, T. F. Heinz, J. Hone, *Proc. Natl. Acad. Sci.* **2009**, *106*, 7304.

[206] T. M. G. Mohiuddin, A. Lombardo, R. R. Nair, A. Bonetti, G. Savini, R. Jalil, N. Bonini, D. M. Basko, C. Galiotis, N. Marzari, K. S. Novoselov, A. K. Geim, A. C. Ferrari, *Phys. Rev. B* **2009**, *79*, 205433.

[207] M. Huang, H. Yan, T. F. Heinz, J. Hone, *Nano Lett.* **2010**, *10*, 4074.

[208] A. C. Ferrari, *Solid State Commun.* **2007**, *143*, 47.

[209] D. Yoon, Y. W. Son, H. Cheong, *Nano Lett.* **2011**, *11*, 3227.

[210] D. Yoon, Y. W. Son, H. Cheong, *Phys. Rev. Lett.* **2011**, *106*, 1.

[211] F. Ding, H. Ji, Y. Chen, A. Herklotz, K. Do, Y. Mei, A. Rastelli, O. G. Schmidt, *Nano Lett.* **2010**, *10*, 3453.

[212] A. Castellanos-Gomez, R. Roldán, E. Cappelluti, M. Buscema, F. Guinea, H. S. J. Van Der Zant, G. A. Steele, *Nano Lett.* **2013**, *13*, 5361.

[213] N. Ferralis, R. Maboudian, C. Carraro, *Phys. Rev. Lett.* **2008**, *101*, 156801.

[214] H. Mi, Z. Ma, J. P. Blanchard, *Raman Spectroscopy and Applications*, **2017**.

[215] W. Eck, A. Küller, M. Grunze, B. Völkel, A. Gölzhäuser, *Adv. Mater.* **2005**, *17*, 2583.

[216] L. H. Hess, A. Lyuleeva, B. M. Blaschke, M. Sachsenhauser, M. Seifert, J. A. Garrido, F. Deubel, *ACS Appl. Mater. Interfaces* **2014**, *6*, 9705.

[217] M. Ai, S. Shishatskiy, J. Wind, X. Zhang, C. T. Nottbohm, N. Mellech, A. Winter, H. Vieker, J. Qiu, K.-J. Dietz, A. Gölzhäuser, A. Beyer, *Adv. Mater.* **2014**, *26*, 3421.

[218] A. Turchanin, A. Gölzhäuser, *Prog. Surf. Sci.* **2012**, *87*, 108.

[219] X. Zhang, C. Neumann, P. Angelova, A. Beyer, A. Gölzhäuser, *Langmuir* **2014**, *30*, 8221.

[220] W. T. S. Huck, A. D. Stroock, G. M. Whitesides, *Angew. Chemie Int. Ed.* **2000**, *39*, 1058.

[221] A. Stroock, R. Kane, M. Weck, *Langmuir* **2003**, 2466.

[222] H. Xu, W. Goedel, *Langmuir* **2002**, 2363.

[223] F. Mallwitz, W. Goedel, *Angew. Chemie Int. Ed.* **2001**, *2*, 2645.

[224] N. C. Estillore, R. C. Advincula, *Langmuir* **2011**, *27*, 5997.

[225] M. Seifert, A. H. R. Koch, F. Deubel, T. Simmet, L. H. Hess, M. Stutzmann, R. Jordan, J. a. Garrido, I. D. Sharp, *Chem. Mater.* **2013**, *25*, 466.

[226] Z. Guangjian, C. Tingting, H. Long, L. Meiying, J. Ruming, W. Qing, D. Yanfeng, W. Yuanqing, Z. Xiaoyong, W. Yen, *J. Taiwan Inst. Chem. Eng.* **2018**, *82*, 205.

[227] M. Salehirad, M. Mohammad, A. Nikje, *Iran. Polym. J.* **2017**, *26*, 467.

[228] Z. Cui, A. P. Martinez, D. H. Adamson, *Nanoscale* **2015**, *7*, 10193.

[229] A. Badri, M. R. Whittaker, P. B. Zetterlund, *J. Polym. Sci. Part A Polym. Chem.* **2012**, *50*, 2981.

[230] W. Sheng, No Title, Dissertation Technische Universität Dresden, **2019**.

[231] D. Hou, S. Zhu, H. Tian, H. Wei, X. Feng, Y. Mai, *ACS Appl. Mater. Interfaces* **2018**, *10*, 40800.

[232] S. Mishra, T. G. Lohr, C. A. Pignedoli, J. Liu, R. Berger, J. I. Urgel, K. Mu, X. Feng, P. Ru, R. Fasel, *ACS Nano* **2018**, *12*, 11917.

[233] M. Richter, S. Hahn, E. Dmitrieva, F. Rominger, *Chem. - A Eur. J.* **2019**, *25*, 1345.

[234] J. Sakamoto, J. van Heijst, O. Lukin, A. D. Schlüter, *Angew. Chem. Int. Ed. Engl.* **2009**, *48*, 1030.

[235] H. Yang, W. Xu, Y. Du, J. Wu, Z. Xu, *RSC Adv.* **2014**, *4*, 45415.

[236] C. Ohm, C. K. Ober, *RSC Adv.* **2013**, *3*, 18482.

[237] T. Fujie, H. Haniuda, S. Takeoka, *J. Mater. Chem.* **2011**, *21*, 9112.

[238] T. Fujie, J. Y. Park, A. Murata, N. C. Estillore, M. C. R. Tria, S. Takeoka, R. C. Advincula, *ACS Appl. Mater. Interfaces* **2009**, *1*, 1404.

[239] T. Gao, S.-W. Ng, X. Liu, L. Niu, Z. Xie, R. Guo, C. Chen, X. Zhou, J. Ma, W. Jin, Y.-S. Chui, W. Zhang, F. Zhou, Z. Zheng, *NPG Asia Mater.* **2014**, *6*, e130.

[240] J. Comrie, W. Huck, *Langmuir* **2007**, *23*, 1569.

[241] T. S. Kelby, M. Wang, W. T. S. Huck, *Adv. Funct. Mater.* **2011**, *21*, 652.

[242] M. E. Welch, C. K. Ober, *J. Polym. Sci. Part B Polym. Phys.* **2013**, *51*, 1457.

[243] M. Welch, C. Ober, *ACS Macro Lett.* **2013**, *2*, 2741.

[244] S. Edmondson, W. T. S. Huck, *Adv. Mater.* **2004**, *16*, 1327.

[245] D.-H. Kim, J.-H. Ahn, W. M. Choi, H.-S. Kim, T.-H. Kim, J. Song, Y. Y. Huang, Z. Liu, C. Lu, J. A. Rogers, *Science (80-.).* **2008**, *320*, 507.

[246] M. C. LeMieux, Z. Bao, *Nature* **2008**, *3*, 585.

[247] J. J. K. Iv, J. Imbrogno, G. Belfort, *ACS Appl. Mater. InterfacesApplied Mater.* **2016**, *8*, 28383.

[248] Y. Han, Z. Xu, C. Gao, *Adv. Funct. Mater.* **2013**, *23*, 3693.

[249] D. F. Stamatialis, B. J. Papenburg, M. Giron, S. N. M. Bettahalli, S. Schmitmeier, M. Wessling, *J. Memb. Sci.* **2008**, *308*, 1.

[250] T. Zhang, R. D. Rodriguez, I. Amin, J. Gasiorowski, M. Rahaman, W. Sheng, J. Kalbacova, E. Sheremet, D. R. T. Zahn, R. Jordan, *J. Mater. Chem. C* **2018**, *6*, 4919.

[251] S. Günes, H. Neugebauer, N. S. Sariciftci, *Chem. Rev.* **2007**, *107*, 1324.

[252] M. Wang, J. E. Comrie, Y. Bai, X. He, S. Guo, W. T. S. Huck, *Adv. Funct. Mater.* **2009**, *19*, 2236.

[253] F. Greco, A. Bellacicca, M. Gemmi, V. Cappello, V. Mattoli, P. Milani, *Appl. Mater. Interfaces* **2015**, *7*, 7060.

[254] C. M. González-Henríquez, M. A. Vallejos Sarabia, J. Rodriguez-Hernández, *Wrinkled Polymer Surfaces*, Springer International Publishing, **2019**.

[255] R. C. Advincula, W. J. Brittain, K. C. Caster, J. Rühe, *Polymer Brushes: Synthesis, Characterization and Applications*, Wiley-VHC, **2004**.

[256] W. Senaratne, L. Andruzzi, C. K. Ober, S. Monolayers, P. Brushes, W. Senaratne, L. Andruzzi, C. K. Ober, S. Monolayers, P. Brushes, *Biomacromolecules* **2005**, *6*, 2427.

[257] M. Goldsche, J. Sonntag, G. J. Verbiest, S. Reichardt, C. Neumann, N. V. Den Driesch, D. Buca, C. Stampfer, *Nano Lett.* **2018**, *18*, 1707.

[258] Y. C. Chiang, Y. Chang, A. Higuchi, W. Y. Chen, R. C. Ruaan, *J. Memb. Sci.* **2009**, *339*, 151.

[259] B. Zhu, S. Edmondson, *Polymer (Guildf).* **2011**, *52*, 2141.

[260] N. H. Nguyen, J. Kulis, H.-J. Sun, Z. Jia, B. van Beusekom, M. E. Levere, D. A. Wilson, M. J. Monteiro, V. Percec, *Polym. Chem.* **2013**, *4*, 144.

[261] M. Liu, G. Luo, Y. Wang, R. Xu, Y. Wang, W. He, J. Tan, M. Xing, J. Wu, *Sci. Rep.* **2017**, *7*, 1.

[262] F. Guarderas, Y. Leavell, T. Sengupta, M. Zhukova, T. L. Megraw, *Adv. Skin Wound Care* **2016**, *29*, 131.

[263] L. Chen, J. Kang, S. Sukigara, *Biomed. Mater. Eng.* **2014**, *24*, 1979.

[264] J.-Y. Yang, S.-S. Chuang, W.-G. Yang, P.-K. Tsay, *Chang Gung Med. J.* **2003**, *26*, 153.

[265] E. Ohto-Fujita, T. Konno, M. Shimizu, K. Ishihara, T. Sugitate, J. Miyake, K. Yoshimura, K. Taniwaki, T. Sakurai, Y. Hasebe, Y. Atomi, *Cell Tissue Res.* **2011**, *345*, 177.

[266] W. Xia, S. Keten, *Langmuir* **2013**, *29*, 12730.

[267] "Thermal Transitions of Homopolymers: Glass Transition & Melting Point," can be found under https://www.sigmaaldrich.com/technical-documents/articles/materials-science/polymer-science/thermal-transitions-of-homopolymers.html, **2018**.

[268] "PEHMA: Poly(2-ethylhexyl methacrylate)," can be found under https://www.polychemistry.com/pehma, **2018**.

[269] N. Zhang, T. Pompe, I. Amin, R. Luxenhofer, C. Werner, R. Jordan, *Macromol. Biosci.* **2012**, *12*, 926.

[270] N. Bowden, S. Brittain, A. G. Evans, J. W. Hutchinson, G. M. Whitesides, *Nature* **1998**, *393*, 146.

[271] C. M. Stafford, C. Harrison, K. L. Beers, A. Karim, E. J. Amis, M. R. Vanlandingham, H. Kim, W. Volksen, R. D. Miller, E. V. A. E. Simonyi, *Nat. Mater.* **2004**, *3*, 545.

[272] J. Y. Chung, A. J. Nolte, C. M. Stafford, *Adv. Funct. Mater.* **2011**, *23*, 349.

[273] Y. Ebata, B. Croll, A. J. Crosby, *Soft Matter* **2012**, *8*, 9086.

[274] A. Karim, J. F. Douglas, B. P. Lee, S. C. Glotzer, J. A. Rogers, R. J. Jackman, E. J. Amis, G. M. Whitesides, *Phys. Rev. E* **1998**, *57*, 6273.

[275] P. Liu, Q. Chen, L. Li, S. Lin, J. Shen, *J. Mater. Chem. B* **2014**, *2*, 7222.

[276] P. Förster, Kovalente Und Nicht-Kovalente Funktionalisierung von Graphen Mit Polymerbürsten, Dissertation Technische Universität Dresden, **2019**.

[277] A. C. Ferrari, J. C. Meyer, V. Scardaci, C. Casiraghi, M. Lazzeri, F. Mauri, S. Piscanec, D. Jiang, K. S. Novoselov, S. Roth, A. K. Geim, *Phys. Rev. Lett.* **2006**, *97*, 1.

[278] A. Das, B. Chakraborty, A. K. Sood, *Bull. Mater. Sci.* **2008**, *31*, 579.

[279] W. Chen, X. Gui, S. Li, L. Yang, B. Liang, H. Zhu, J. She, Z. Tang, *Carbon N. Y.* **2018**, *129*, 646.

[280] C. Casiraghi, S. Pisana, K. S. Novoselov, A. K. Geim, A. C. Ferrari, *Appl. Phys. Lett.* **2007**, *91*, 1.

[281] T. Zhang, Surface Modification Strategies for Grafting Polymer Brushes from Silicon and Graphene, Dissertation Technische Universität Dresden, **2015**.

[282] J. Lalevée, X. Allonas, J. P. Fouassier, *J. Am. Chem. Soc.* **2002**, *124*, 9613.

[283] Y. R. Luo, *Comprehensive Handbook of Chemical Bond Energies*, CRC Press, Boca Raton, FL, **2007**.

[284] D. Bertoldo Menezes, A. Reyer, A. Marietta, M. Musso, *Mater. Res. Express* **2017**, *4*, 015303.

[285] N. M. Reynolds, S. Ling Hsu, *Macromolecules* **1990**, *23*, 3463.

[286] F. J. Torres, B. Civalleri, C. Pisani, P. Musto, A. R. Albunia, G. Guerra, *J. Phys. Chem. B* **2007**, *111*, 6327.

[287] W. Winkler, M. Musso, E. C. Kirchner, *J. Raman Spectrosc.* **2003**, *34*, 157.

[288] S. W. Ng, N. Noor, Z. Zheng, *NPG Asia Mater.* **2018**, *10*, 217.

[289] X. Ling, L. Xie, Y. Fang, H. Xu, H. Zhang, J. Kong, M. S. Dresselhaus, J. Zhang, Z. Liu, *Nano Lett.* **2010**, *10*, 553.

[290] X. Ling, J. Zhang, *Small* **2010**, *6*, 2020.

[291] W. Weng, X. Sun, B. Liu, J. Shen, *J. Mater. Chem. C* **2018**, *6*, 4400.

[292] A. Juneja, G. Rajasekaran, *IOP Conf. Ser. Mater. Sci. Eng.* **2018**, *402*, 012020.

[293] C. Taubmann, R. Luxenhofer, S. Cesana, R. Jordan, *Macromol. Biosci.* **2005**, *5*, 603.

Danksagung

Zu guter Letzt ist es an der Zeit all denjenigen zu danken, die den Weg bis zu dieser Arbeit geebnet und zur erfolgreichen Umsetzung ebendieser beigetragen haben.
Am Anfang steht natürlich der Dank an meinen Doktorvater Prof. Dr. Rainer Jordan für die Aufnahme in seinen Arbeitskreis und die damit verbundene Möglichkeit meine Dissertation anzufertigen. Seine wissenschaftliche Betreuung fördert zielorientiertes, selbstständiges Arbeiten und hat mir ermöglicht, mich mit den ebenso spannenden wie aktuellen Themen der „2D Welt“ auseinanderzusetzen. Zudem haben sein Vertrauen, seine Denkanstöße und Ideen stets zu dieser Promotion beigetragen und boten Hilfe, wo diese gebraucht wurde.
Da wir einmal bei der Anerkennung von Hilfe aus der Chefetage sind, möchte ich auch Frau Schulze meinen herzlichsten Dank aussprechen. Sie war/ist die gute Seele des Arbeitskreises und wird dies mit Sicherheit auch in Zukunft bleiben. Auf ihren organisatorischen Überblick war immer Verlass, egal ob bei Vertragsunterzeichnungen, Rechnungszahlungen oder Boßel-Turnieren. Vielen Dank für die Unterstützung in den letzten Jahren.
Noch nicht ganz in der Chefetage angekommen, aber ebenso eine gute Seele, ist Matthias Kluge. Ihm gilt ein besonderer Dank als Beschaffer und Entsorger sowie für die technische Unterstützung im Labor. Außerdem hat er mir insbesondere gegen Ende meiner Promotion durch seine generöse Art Rätsel zu teilen, sehr geholfen, meinen Wortschatz zu erweitern. Du bleibst trotzdem der Rätsel-Master 2019!
Ein riesiger Dank geht raus an alle „Makros“. Egal ob ehemalige, aktive oder zukünf ige – ihr habt eine tolle Arbeitsatmosphäre etabliert und unaufhörlich mit aller fachlichen Kompetenz geholfen. Zahlreiche produktive „Subgroup meetings“, Seminare und intensive Gespräche haben stets dazu beigetragen, dass man seine Arbeit erfolgreich gestaltete. Im Einzelnen ist da zunächst Dr. Lisa Holz, unsere hauseigene Sicherheitsbeauftragte und Tränensammlerin. Sie ist während meiner Promotion nicht nur eine Kollegin gewesen, sondern auch eine gute Freundin geworden. Nicht zuletzt war sie außerdem ein klasse Coach, Hutmacher und wird vermutlich auch erfolgreiche Comedy-Autorin („Allein unter Affen“ kommt!). Dr. Erik „Berliner Blau ist nicht rot!“ Wegener, dem einzigen richtigen Gitarrenspieler der Gruppe, sei für seine zitierfertigen Weisheiten und die Übernahme der Leitung von Subgoup Meetings gedankt. Im Grunde bist du ja auch einer der „Surface Guys“. Im Weiteren wäre da noch unser Schaffner Clemens „Klecker“ Sachse. Neben regelmäßiger Dokumentkontrolle ist er auch mit aufmunternden Aphorismen („Wir sind doch alle Hacke-Strakke-Lamm.“) und

Gleichungen (Zwerg-Parabel) stets hilfreich gewesen. Danke auch für die Beförderung zum "Chief Assistent to the Bad Gag Administration Committee and Executive Sheriff for Joke Prohibition/Persecution". In diesem Zusammenhang sei auch unserem Vogelfänger Hagen Sekulla ein großer Dank ausgesprochen, der mit seiner Kreativität immer etwas zu dieser Tätigkeit beisteuerte. Er ist ein wahrer Barde…oder heißt das Bardierer? Sarah „Mad Eye" Naumann gilt ebenso ein besonderer Dank für die weiterführenden Gespräche unter den „Heads of Education Center Course Distribution and Knowledge Navigation". Vor allem ob dieser Kooperation konnte die „Tradition des Vor-Kaffees" begründ t werden. Mir zuliebe legte sie außerdem den Besen beiseite und nahm das Fahrrad.

At this point, I have to switch languages to thank our international colleagues Wei Li, Wenbo Sheng and Yunhao Du. Thank you for being my lab mates and part of the "Surface Guys" in the last years. You not only brought your chemical competence to the table, but also some exotic and tasty food – thank you for that cultural contribution as well.

Den inzwischen "Ehemaligen" seien auch die wärmsten Worte zugesendet. Ihr habt meiner Entwicklung und Forschung gerade zur Anfangszeit entscheidende Impulse gegeben. Allen voran sei hier – wie soll ich sagen – Dr. Ihsan Amin gedankt, der mich bereits während meiner Master-Zeit betreute und in die Oberflächen-Chemie einführte. Meinem langjährigen Laborkollegen und „Herrn der Raupen" Michael Schiffmann gilt ein großer Dank für die vielen Gespräche, den wissenschaftlichen Austausch und seine Freundschaft. Außerdem ist er ein hervorragender Tandem-Fahrer. Ein weiterer Dank geht an Paul „Pepe" Nagelschneider, der, thematisch betrachtet, mein Nächster war und dementsprechend der erste Ansprechpartner in Sachen Graphen. Ferner ist er Miterfinder der „Scotch tape for Hafner-Nagelschneider Adhesion, Peel and Swap"-Methode (kurz: ScHNAPS). Und wo ein Dank an Paul formuliert ist, kann ebendieser an seinen kongenialen Trainingspartner Dan Gieseler nicht weit sein. Es gibt niemanden, dem ich lieber Spieße mache. Desgleichen geht ein herzlicher Dank an „Maxi" Schneider, Jannik „Die Rub " Sonntag, Jonas „Die Nase" Nawroth und René „Die Wade" Schubel.

Meinen Studenten danke ich für das Beisteuern von Ergebnissen sowie die Ausbildung des Lehrers in mir. Da wäre mein erster Bachelor Nic Gürtler zu nennen sowie Fred Lange, deren Leistung nicht nur aus dem Kochen von Eiern und Mitbringen von Zucchini bestand. Besonders danke ich auch den Graphen-Pionieren Niclas Weigel und (Me)-Talika Neuendorf ("Witzig! Den habe ich noch nie gehört!") für ihre geduldige und fleißige Arbeit in unseren Faltversuchen. Lisa Ziegler, der Master-Studentin der ersten Stunde, gilt großer Dank für das Mitlernen der SI-CuCRP. Selbiger gilt auch allen von mir betreuten MRC-Studenten.

Dr. Enrico Langer danke ich für seine freundliche Unterstützung bei den XPS-Messungen.
Ich möchte einen extra großen Dank an alle richten, die diese Arbeit zur Korrektur gelesen haben, um die kleinen und nicht so kleinen Fehler auszumerzen. Falls ihr noch nicht namentlich erwähnt wurdet, kommt das noch.
Darüber hinaus möchte ich meine Dankbarkeit an alle Freunde zum Ausdruck bringen, die während des Studiums bei mir waren und so manche harte Lernstunde erleichtert haben. Da ist zum einen die „Clique des 10-Järigen Jubiläums“ a.k.a. die „Donnertags-Runde“: Anton, Christina, David und Marta, G!, Hildegard-Marika und Steffen, Marcus und Ronny. Zum anderen gibt es noch die „Clique der Dresdener“: Albi, Dustin und Susi, Mandy, Martina und Meike. Ich danke euch allen für die nötige Ablenkung in den richtigen Momenten und gegenseitige Unterstützung während der gesamten Zeit.
Ein gesonderter Dank richtet sich an Alex. Danke für die vielen tollen Erinnerungen, die Möglichkeit darin zu schwelgen und unseren nicht enden wollenden Email-Verkehr aus nicht enden wollenden Satzgeflechten, der mich zu dieser nicht enden wollenden Danksagung inspiriert ebenso wie dieser längsten (versprochen! (vermutlich auch klammerreichsten)) Formulierung und uns mit Sicherheit einen ganz bestimmten Preis einbringen wird. Meine rhetorische Grenzbegabung hat bereits jetzt davon profitiert.
Ein weiterer Dank geht an das „Falkenbrunnen-Duo“: Sven und Gina a.k.a. Theofrastus Bombastus. Mit euch kann man stets neue Kraft tanken und lachen (HGA for ever!).
Robert, Felix und Rafa gilt als den „ewigen Freunden“ genauso mein Dank wie Elke Mu̇ ler samt Gemahl. Die „höflichen“ Erinnerungen werden immer bleiben.
Ich möchte Regine, Michael und Stephan Polnick herzlich für die letzten Jahre danken. Ihr habt mich bei euch aufgenommen und immer unterstützt und geholfen, wo es ging. Speziell für Michael flechte ich daher den folgenden Satz ein: „Der Schuss knallte und die Leiche sprang über die Mauer.“ So, bitte schön!
Ein Danke, dessen Wichtung sich nicht in einfachen Worten ausdrücken lässt, geht an meine Eltern, meinen Bruder und seine Familie. Спасибо за то, что всегда были рядом со мной и поддерживали меня в финансовом и в моральном плане. Без вас, вашего воспитание и вашей любви я никогда бы этого не достиг. Спасибо за ваше терпение и за то, что я всегда могу положиться на вас. Ach ja, und noch ein „Hallo Jan!“ und „Hallo Sophie!“
Zum Abschluss danke ich meiner Uli. In den letzten Jahren warst du meine größte Motivation, meine treuste Konstante und teuerste Zuflucht. Danke für jede Stunde, in der du mich emotional ge- und ertragen hast, selbst wenn es stressig wurde. Ich verspreche, dass ich immer versuchen werde, wenigstens im Ansatz ein ähnlich guter Partner zu sein.

Erklärung

Hiermit versichere ich, dass ich die vorliegende Arbeit ohne unzulässige Hilfe Dritter und ohne Benutzung anderer als der angegebenen Hilfsmittel angefertigt habe; die aus fremden Quellen direkt oder indirekt übernommenen Gedanken sind als solche kenntlich gemacht. Die Arbeit wurde bisher weder im Inland noch im Ausland in gleicher oder ähnlicher Form einer anderen Prüfungsbehörde vorgelegt.

Die vorliegende Arbeit wurde in der Zeit vom Januar 2015 bis Juni 2019 unter wissenschaftlicher Betreuung von Herrn Prof. Dr. Rainer Jordan an der Professur für Makromolekulare Chemie an der Technischen Universität Dresden angefertigt.

Dresden, ...

Daniel Hafner